



INSA

N°d'ordre NNT : 2018LYSEI020

THESE de DOCTORAT DE L'UNIVERSITE DE LYON
opérée au sein de
L'INSA de Lyon

Ecole Doctorale N° 162
Mécanique, Energétique, Génie civil, Acoustique (MEGA)

Spécialité/ discipline de doctorat :
Génie Mécanique

Soutenue publiquement le 23/03/2018, par :
Pauline Cusseau

The role of polymer additives on the behavior of engine lubricants in elastohydrodynamic and thin film regimes: from rheology to tribology

Devant le jury composé de :

Chassenieux, C	Prof. des Universités	U. du Mans	Président
Fernandez, J	Prof. des Universités	U. of Santiago de C.	Rapporteuse
Fillon, M	Directeur de recherche	U. de Poitiers	Rapporteur
Martinie, L	Maître de Conférences	INSA de Lyon	Examinatrice
Philippon, D	Maître de Conférences	INSA de Lyon	Co-directeur de thèse
Vergne, P	Directeur de recherche	INSA de Lyon	Directeur de thèse
Briand, F	Ingénieur recherche	TOTAL	Invitée

Département FEDORA – INSA Lyon - Ecoles Doctorales – Quinquennal 2016-2020

SIGLE	ÉCOLE DOCTORALE	NOM ET COORDONNEES DU RESPONSABLE
CHIMIE	CHIMIE DE LYON http://www.edchimie-lyon.fr Sec. : Renée EL MELHEM Bât. Blaise PASCAL, 3e étage secretariat@edchimie-lyon.fr INSA : R. GOURDON	M. Stéphane DANIELE Institut de recherches sur la catalyse et l'environnement de Lyon IRCELYON-UMR 5256 Équipe CDFA 2 Avenue Albert EINSTEIN 69 626 Villeurbanne CEDEX directeur@edchimie-lyon.fr
E.E.A.	ÉLECTRONIQUE, ÉLECTROTECHNIQUE, AUTOMATIQUE http://edeea.ec-lyon.fr Sec. : M.C. HAVGOUDOUKIAN ecole-doctorale.eea@ec-lyon.fr	M. Gérard SCORLETTI École Centrale de Lyon 36 Avenue Guy DE COLLONGUE 69 134 Écully Tél : 04.72.18.60.97 Fax 04.78.43.37.17 gerard.scorletti@ec-lyon.fr
E2M2	ÉVOLUTION, ÉCOSYSTÈME, MICROBIOLOGIE, MODÉLISATION http://e2m2.universite-lyon.fr Sec. : Sylvie ROBERJOT Bât. Atrium, UCB Lyon 1 Tél : 04.72.44.83.62 INSA : H. CHARLES secretariat.e2m2@univ-lyon1.fr	M. Fabrice CORDEY CNRS UMR 5276 Lab. de géologie de Lyon Université Claude Bernard Lyon 1 Bât. Géode 2 Rue Raphaël DUBOIS 69 622 Villeurbanne CEDEX Tél : 06.07.53.89.13 cordey@univ-lyon1.fr
EDISS	INTERDISCIPLINAIRE SCIENCES- SANTÉ http://www.ediss-lyon.fr Sec. : Sylvie ROBERJOT Bât. Atrium, UCB Lyon 1 Tél : 04.72.44.83.62 INSA : M. LAGARDE secretariat.ediss@univ-lyon1.fr	Mme Emmanuelle CANET-SOULAS INSERM U1060, CarMeN lab, Univ. Lyon 1 Bâtiment IMBL 11 Avenue Jean CAPELLE INSA de Lyon 69 621 Villeurbanne Tél : 04.72.68.49.09 Fax : 04.72.68.49.16 emmanuelle.canet@univ-lyon1.fr
INFOMATHS	INFORMATIQUE ET MATHÉMATIQUES http://edinfomaths.universite-lyon.fr Sec. : Renée EL MELHEM Bât. Blaise PASCAL, 3e étage Tél : 04.72.43.80.46 Fax : 04.72.43.16.87 infomaths@univ-lyon1.fr	M. Luca ZAMBONI Bât. Braconnier 43 Boulevard du 11 novembre 1918 69 622 Villeurbanne CEDEX Tél : 04.26.23.45.52 zamboni@maths.univ-lyon1.fr
Matériaux	MATÉRIAUX DE LYON http://ed34.universite-lyon.fr Sec. : Marion COMBE Tél : 04.72.43.71.70 Fax : 04.72.43.87.12 Bât. Direction ed.materiaux@insa-lyon.fr	M. Jean-Yves BUFFIÈRE INSA de Lyon MATEIS - Bât. Saint-Exupéry 7 Avenue Jean CAPELLE 69 621 Villeurbanne CEDEX Tél : 04.72.43.71.70 Fax : 04.72.43.85.28 jean-yves.buffiere@insa-lyon.fr

<p>MEGA</p>	<p>MÉCANIQUE, ÉNERGÉTIQUE, GÉNIE CIVIL, ACOUSTIQUE</p> <p>http://edmega.universite-lyon.fr Sec. : Marion COMBE Tél : 04.72.43.71.70 Fax : 04.72.43.87.12 Bât. Direction mega@insa-lyon.fr</p>	<p>M. Philippe BOISSE INSA de Lyon Laboratoire LAMCOS Bâtiment Jacquard 25 bis Avenue Jean CAPELLE 69 621 Villeurbanne CEDEX Tél : 04.72.43.71.70 Fax : 04.72.43.72.37 philippe.boisse@insa-lyon.fr</p>
<p>ScSo</p>	<p>ScSo*</p> <p>http://ed483.univ-lyon2.fr Sec. : Viviane POLSINELLI Brigitte DUBOIS INSA : J.Y. TOUSSAINT Tél : 04.78.69.72.76 viviane.polsinelli@univ-lyon2.fr</p>	<p>M. Christian MONTES Université Lyon 2 86 Rue Pasteur 69 365 Lyon CEDEX 07 christian.montes@univ-lyon2.fr</p>

*ScSo : Histoire, Géographie, Aménagement, Urbanisme, Archéologie, Science politique, Sociologie, Anthropologie

Abstract

The development of high-performance lubricants to reduce engine friction and consequently fuel consumption remains a major challenge for oil manufacturers. Viscosity Index Improvers (VII) are polymer additives used for decades to limit the dependency of the lubricant's viscosity on temperature, to maintain an acceptable hydrodynamic lubrication at high temperature, without experiencing excessive frictional and thermal losses at low temperature. This work focuses on understanding the role of VII in engine lubricants with the aim to bridge their tribological response with their rheological behavior. Simplified lubricants are studied, composed of various polymers of different molecular weights and conformations added to a mineral base oil.

In a first part, the viscosity-temperature-pressure dependence of these lubricants is investigated. Their rheological behavior is shown to result from mechanisms occurring at molecular scale, by considering the notions of solubility, hydrodynamic radii and conformation effects.

In a second part, the viscosity-shear stress dependence is discussed according to the polymers structure and predicted on a large range of temperatures and pressures through a conventional model. However, the strong assumptions behind this model lead us to propose a more appropriate relationship which takes into account the viscoelastic properties of the lubricants.

Finally, film thickness measurements are conducted to explore how the polymer addition affects the lubricant's response in the Elastohydrodynamic and Thin Film regimes. They are compared with analytical predictions based on the rheological models established previously. It is shown that i) there is a good agreement between predictions and measured film thicknesses in the EHD regime and ii) at lower thickness, i.e. in the Thin Film regime, some polymers show a critical thickness from which the film thickness significantly departs from the predictions. Several explanations are considered, among them the non-Newtonian behavior of the lubricants and the adsorption of polymers on the solid bodies.

Résumé

Le développement de lubrifiants haute performance pour réduire le frottement dans les moteurs et limiter la consommation de carburant, demeure un défi majeur pour les fabricants d'huiles. Les améliorants d'indice de viscosité (VII) sont des polymères couramment utilisés pour réduire la dépendance en température de la viscosité du lubrifiant, afin de maintenir une lubrification hydrodynamique acceptable à haute température. Ce travail se concentre sur la compréhension du rôle des VII dans les lubrifiants moteur afin de relier leur réponse tribologique et leur comportement rhéologique. Des lubrifiants simplifiés sont étudiés, composés de divers polymères de différents poids moléculaires et conformations, ajoutés à une huile de base minérale.

Premièrement, la dépendance de la viscosité à la température et la pression de ces lubrifiants est étudiée. Il est montré que leur comportement rhéologique résulte de mécanismes se produisant à l'échelle moléculaire, en considérant les notions de solubilité, rayon hydrodynamique et d'effets de conformation.

Ensuite, la dépendance viscosité-cisaillement est discutée en fonction de la structure des polymères et prédite sur une large gamme de températures et de pressions à travers un modèle conventionnel. Cependant, les hypothèses qui sous-tendent ce modèle nous amènent à proposer une relation plus appropriée prenant en compte la viscoélasticité des lubrifiants.

Enfin, des mesures d'épaisseur de film sont effectuées pour explorer comment l'addition de polymère affecte la réponse du lubrifiant dans les régimes élastohydrodynamique et thin film. Elles sont comparées aux prévisions analytiques basées sur les modèles rhéologiques établis précédemment. Il est montré i) une bonne adéquation entre les prévisions et les données expérimentales dans le régime EHD et ii) la présence d'une épaisseur critique pour certains polymères à partir de laquelle les résultats s'écartent significativement des prévisions. Ce régime thin film, aux faibles épaisseurs, est expliqué par le comportement non newtonien des lubrifiants et l'adsorption des polymères aux surfaces.

Remerciements

L'étude présentée dans ce mémoire a été réalisée au sein du Laboratoire de Mécanique des Contacts et Structures (LaMCoS) de l'INSA de Lyon et au Centre de recherche de Solaize (CReS, TOTAL).

J'aimerais tout d'abord remercier les membres du jury, Christophe Chassenieux, Josefa Fernandez et Michel Fillon, pour l'intérêt et le temps qu'ils ont consacré à la lecture de ce manuscrit, ainsi que pour nos échanges lors de la soutenance.

Je remercie bien évidemment Philippe Vergne, David Philippon et Laetitia Martinie, mes directeurs de thèse, qui ont encadré ce travail et su m'initier au métier de chercheur. Un grand merci pour votre disponibilité et vos conseils. Ces trois années à vos côtés ont été riches en enseignements.

Je remercie également Fanny Briand, mon encadrante industriel, pour sa grande disponibilité et nos discussions. Merci aussi à Grégory Descroix de m'avoir fait bénéficier de son expertise technique. Un grand merci aux personnes impliquées au CReS qui ont permis à ce travail d'aboutir.

Je tenais également à remercier nos collègues de l'IMMM (Institut des Molécules et Matériaux du Mans, Université du Maine), à savoir Jean-François Tassin, Christophe Chassenieux (de nouveau) et leur doctorante Justine Dorengé pour les caractérisations des polymères étudiés et leurs interventions lors de nos réunions.

Je remercie mon binôme Nicolas Devaux, sans qui les mesures sur Jerotrib n'auraient pu être réalisées. Merci également pour nos discussions qui auront rendu ce travail agréable. Je tiens également à remercier Lionel Lafarge, une autre personne indispensable à la réalisation de ces travaux et qui a maintenu les rhéomètres hautes pressions en état de fonctionnement tout au long de cette thèse.

Un grand merci à Nathalie Bouscharain, de m'avoir formée, soutenue et remonté le moral, et pour nos nombreux échanges sur les sujets les plus divers et variés. Merci, merci.

Je tiens également à remercier les doctorants du laboratoire (que je ne nommerai pas, de peur d'en oublier), devenus des amis au fil des années. Nos échanges de nature non scientifiques à la salle de pause, Kfet ou autre Kolok vont grandement me manquer.

Merci aux Faidherbards et CPÉeins, pour votre soutien sans faille tout au long de cette thèse et depuis pas mal d'années maintenant. Merci également à la Cacophonie et aux Krapos d'avoir rythmé mes semaines et fait voyager. Une nouvelle fanfare clermontoise sera bientôt présente pour vous accueillir.

Merci à ma famille. Il y aura finalement un autre docteur Cusseau. Merci pour votre soutien. Je vous dois beaucoup.

Enfin, un merci particulier à mon fiancé Romain.

Résumé étendu

Introduction générale

Réduire la consommation de carburant dans le secteur du transport est un enjeu majeur de l'industrie automobile considérant le contexte actuel de réchauffement climatique. Un tiers des émissions des gaz à effets de serre provient en effet du secteur du pétrole et du gaz, qui comprend les secteurs de la construction, de l'industrie, de la production et du transport. Ce dernier est identifié comme le plus gros contributeur des émissions liées au pétrole et au gaz à près de 40%. De nouvelles réglementations européennes visent ainsi à limiter les émissions de dioxyde de carbone à moins de 95 gCO₂.km⁻¹ d'ici à 2021. Augmenter l'efficacité énergétique et limiter la consommation de carburant sont les défis actuels auxquels les constructeurs automobiles et pétroliers doivent faire face.

Plusieurs solutions techniques existent pour diminuer la consommation de carburant. Une des pistes d'actions envisagées est de réduire les pertes par frottements au sein des moteurs d'automobiles par l'utilisation de lubrifiants haute performance. Selon Holmberg et al. [1], 11% des pertes énergétiques d'un véhicule de tourisme sont attribuées aux frottements au sein du moteur. Récemment [2], Holmberg a également établi que réduire l'usure et les pertes par frottements pour le secteur du transport impliquerait une réduction des émissions de CO₂ de près de 620 MtCO₂ et des économies de 180 000 million d'euros sur le court terme (8 ans).

Le développement de lubrifiant à haute valeur ajoutée est primordial pour répondre à ces enjeux environnementaux et économiques. Le lubrifiant moteur est un produit complexe, composé principalement d'une huile de base et d'un mélange varié d'additifs. Sa fonction principale est de séparer les surfaces glissantes en contact par un film, afin de minimiser les pertes d'énergies liées au frottement. Cette épaisseur de film est directement liée à la viscosité du lubrifiant (et plus généralement à son comportement rhéologique) qui doit donc être contrôlée et ajustée pour faire face aux différentes variations de température, pression et contrainte rencontrées au sein d'un moteur. Pour ce faire, des polymères appelés améliorants d'indice de viscosité (ou Viscosity Index Improvers VIIs) sont formulés avec l'huile de base. Leur rôle est de réduire la diminution de viscosité de l'huile de base à haute température pour maintenir une lubrification hydrodynamique acceptable, tout en limitant leur contribution à basse température pour ne pas augmenter les pertes de frottements à froid dues à un fluide trop visqueux.

Les conditions de hautes températures, pressions et contraintes rencontrées au sein d'un moteur peuvent amener le lubrifiant à être dans le régime dit élastohydrodynamique (EHD), où les pressions considérées sont telles (supérieures à 300MPa) que les surfaces en contact sont déformées élastiquement. De nombreuses études ont été menées sur ce régime de lubrification depuis plus de 60 ans [3][4]. Les progrès dans ce domaine sont notamment le résultat de l'amélioration des caractérisations et prédictions des profils rhéologiques des lubrifiants à hautes pressions et contraintes [5][6], qui améliorent la prédiction des épaisseurs de film [6][7][8]. L'établissement de modèles rhéologiques précis pour prédire et ajuster la viscosité d'un lubrifiant est donc essentiel pour aider le formulateur dans le choix du meilleur VII possible selon le cahier des charges préétabli, et sans passer par des essais sur banc moteur. Cette

approche, qui est celle de nos recherches, permet ainsi d'optimiser le processus de formulation en diminuant son temps et son coût.

L'objectif de ces recherches est d'aider le formulateur dans le choix du meilleur VII en liant les réponses à l'échelle moléculaire (liées à la structure et à la chimie du polymère) aux réponses à l'échelle du contact. La démarche est la suivante:

- Les comportements rhéologiques et leur prédiction en conditions réalistes de température, pression et contrainte de cisaillement pour des lubrifiants simplifiés, composés d'un mélange d'huile de base et de polymères uniquement sont tout d'abord établis.
- La compréhension des mécanismes moléculaires et leur impact sur les réponses rhéologiques des lubrifiants est ensuite considérée.
- Enfin, une étude tribologique pour comprendre comment la rhéologie, donc la physico-chimie des polymères, impacte la formation d'épaisseur de film d'un lubrifiant, est menée.

La Fig. 1 montre les différentes étapes de la démarche scientifique suivie au cours de la thèse

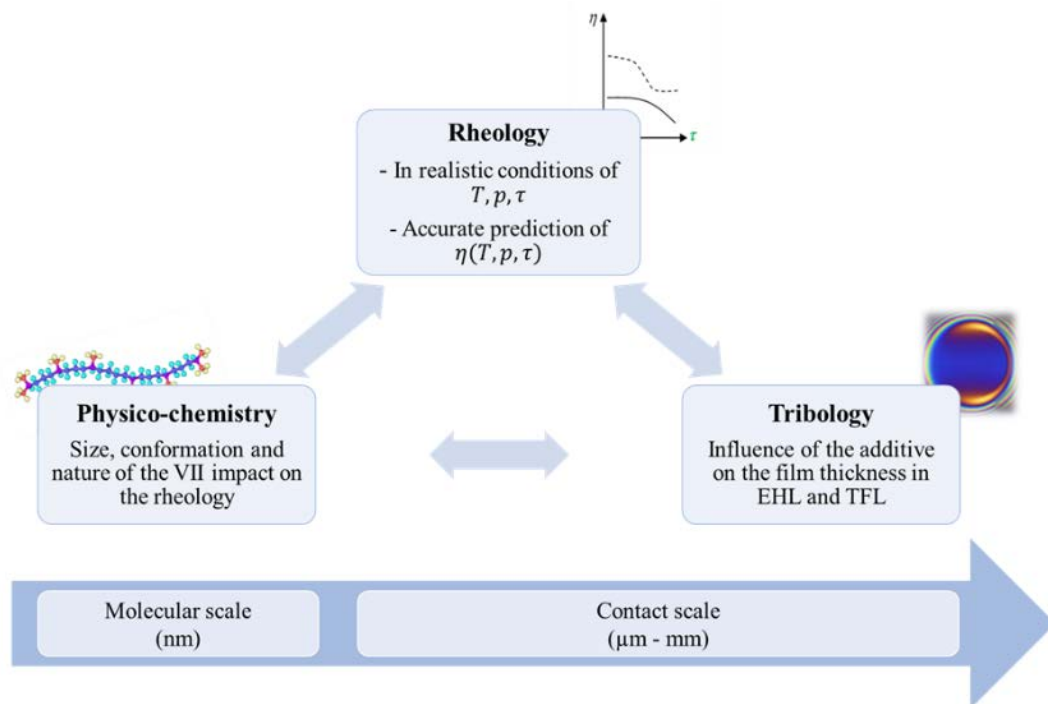


Fig. 1 : Démarche de la thèse aux différentes échelles considérées.

Ce document est composé de quatre chapitres. Le premier introduit les notions nécessaires à la compréhension du rôle et des actions des VIIs. Les bases nécessaires sur la lubrification, la physico-chimie des polymères et polymères en solutions, ainsi que la rhéologie des lubrifiants et des modèles étudiés y sont décrits. Les chapitres II and III sont consacrés à l'étude rhéologique complète des solutions de polymères. L'originalité de ce travail est d'utiliser deux rhéomètres haute pression non-commerciaux. Le chapitre II se concentre sur l'influence de la température et de la pression à faible taux de cisaillement.

La relation entre les réponses rhéologiques observées et l'échelle moléculaire est établie par l'étude des variations (en fonction de la température et pression) des rayons hydrodynamiques des polymères, déterminés ici par la loi d'Einstein appliquée à haute pression. La dépendance viscosité-cisaillement est ensuite discutée dans le chapitre III en fonction de la structure des polymères et prédite sur une large gamme de températures et de pressions à travers un modèle conventionnel. Cependant, les hypothèses qui sous-tendent ce modèle nous amènent à proposer une relation plus appropriée prenant en compte la viscoélasticité des lubrifiants. Dans le dernier chapitre, des mesures d'épaisseur de film sont effectuées pour explorer comment l'addition de polymère affecte la réponse du lubrifiant dans les régimes élastohydrodynamique et film mince. Elles sont comparées aux prévisions analytiques basées sur les modèles rhéologiques établis précédemment. Il est montré i) une bonne adéquation entre les prévisions et les données expérimentales dans le régime EHD et ii) la présence d'une épaisseur critique pour certains polymères à partir de laquelle les résultats s'écartent significativement des prévisions. Ce régime dit en film mince (thin film regime), aux faibles épaisseurs, est expliqué par le comportement non newtonien des lubrifiants et l'adsorption des polymères aux surfaces.

Chap. I : Etat de l'art: lubrification, physico-chimie des polymères et rhéologie.

Cette partie fournit les bases sur la lubrification moteur (notamment les régimes de lubrification, le rôle et la composition d'un lubrifiant moteur), la physico-chimie des polymères en solution ainsi que les modèles rhéologiques couramment utilisés pour les lubrifiants moteurs.

Lubrification moteur

La grande diversité des pièces métalliques d'un moteur de voiture amène le lubrifiant à fonctionner dans différentes conditions de températures, de pressions et de contraintes de cisaillement. Le lubrifiant unique doit ainsi assurer plusieurs rôles critiques, comme le nettoyage des surfaces, l'équilibre thermique du moteur, et surtout la réduction des pertes d'énergie par frottement et du risque d'usure des surfaces en séparant ces dernières par un film d'huile.

Les différentes conditions rencontrées au sein du moteur impliquent également la pluralité des régimes de lubrification. Ces différents régimes sont différenciés par le mécanisme de formation de l'épaisseur de film, qui est déterminé par la vitesse d'entraînement moyenne des surfaces dans le cas où la pression est constante. À faibles vitesses, l'épaisseur de film est insuffisante et la charge est directement supportée par les aspérités du contact. Les coefficients de frottement en résultant sont alors élevés : il s'agit du régime limite. Lorsque la vitesse augmente, un fin film d'huile se forme et sépare partiellement les surfaces. La transition vers la lubrification mixte est donc visible par une réduction du coefficient de frottement. Ce dernier atteint son minimum en régime élastohydrodynamique (où les pressions élevées supportées par un film complet de lubrifiant induisent la déformation élastique des surfaces) avant d'atteindre le régime hydrodynamique aux plus hautes vitesses. La zone transitoire entre le régime EHD et le régime mixte peut également abriter le régime en film mince (TFL pour Thin Film

Lubrification), où l'épaisseur de film est du même ordre de grandeur que les polymères en solution et où les contributions moléculaires ne sont plus négligeables.

La majorité des fonctions du lubrifiant est assurée par l'huile de base, qui crée un film séparant les surfaces en contact. Les huiles de base peuvent être d'origines minérales, synthétiques ou végétales et sont le composé majoritaire d'un lubrifiant moteur à près de 70 à 80%. Les 20 à 30% restants sont constitués d'additifs, ayant pour fonction d'améliorer les propriétés des huiles de base. Ces additifs sont variés et comprennent les détergents, dispersants, antioxydants, antirouille/anticorrosion, antimousse, antiusure, extrême pression, modificateur de frottements, abaisseur de point d'écoulement et améliorants d'indice de viscosité. Ces derniers sont au centre de ces recherches. Leur fonction est de réduire la dépendance en température de la viscosité de l'huile de base, en épaississant cette dernière aux hautes températures sans l'affecter à basses températures. Le mécanisme d'action supposé des VII repose sur le potentiel gonflement des pelotes de polymères avec la température [9]. En effet, la solubilité du polymère augmente avec la température, privilégiant ainsi les interactions entre l'huile et le polymère. Les pelotes gonflent, le frottement intermoléculaire entre solvant et solution augmente et provoque ainsi une augmentation de la viscosité. Lorsque la température diminue, la solubilité est moindre et les interactions intramoléculaires sont alors préférées. Les pelotes se contractent et contribuent peu à la viscosité de l'huile de base. L'utilisation de paramètres comme l'indice de viscosité VI ou le facteur épaississant Q permet d'évaluer la performance de ces VII.

Polymères et polymères en solutions

Différentes notions nécessaires pour la compréhension des phénomènes étudiés à l'échelle moléculaire sont introduites dans cette partie. Les polymères sont des macromolécules caractérisés par leur masse moléculaire, leur conformation, leur solubilité et également leur taille. Cette dernière peut être définie de différentes manières, à savoir le rayon de giration R_g ou le rayon hydrodynamique R_h .

Ce dernier est une des notions les plus étudiées de la thèse et représente la taille effective du polymère dans son environnement et varie avec la température et la pression. Pour un milieu dilué composé de polymères considérés comme des sphères dures, ce rayon hydrodynamique est déterminé à partir des mesures rhéologiques à hautes pressions et faibles taux de cisaillement, grâce à la loi d'Einstein appliquée aux hautes pressions [10][11]:

$$\begin{aligned}\eta_{solution} &= \eta_{solvent}(1 + 2.5\phi) \\ \phi &= \frac{c}{M} \frac{4}{3} \pi R_{coil}^3\end{aligned}\tag{Eq. (1)}$$

où $\eta_{solution}$ et $\eta_{solvent}$ correspondent respectivement à la viscosité de la solution de polymère et à celle de l'huile de base, c la concentration et M la masse molaire moyenne d'une molécule. ϕ correspond à la fraction volumique de sphères dures de rayon R_{coil} . Ce dernier est considéré équivalent au rayon hydrodynamique R_h .

Rhéologie des lubrifiants

La viscosité est une propriété essentielle du lubrifiant, étroitement liée à sa capacité à réduire le frottement au sein d'un moteur par la formation d'un film d'huile. La rhéologie correspond à l'étude de l'écoulement des matériaux, principalement à l'état liquide, suite à leur déformation par cisaillement. De plus, la rhéologie explore la relation entre la viscosité et les influences combinées de la température, la pression et la contrainte (ou taux) de cisaillement. Lorsque la viscosité du fluide η est indépendante de la contrainte de cisaillement τ , le fluide est dit Newtonien. Cependant, les lubrifiants sont connus pour être des fluides dits rhéofluidifiants. En effet, l'ajout de polymères modifie considérablement les propriétés rhéologiques de l'huile de base. À faibles contraintes de cisaillement, les pelotes de polymères sont peu impactées et restent dans leur état. La viscosité de la solution de polymère n'est pas affectée et est dite « viscosité de premier plateau Newtonien ». Lorsque la contrainte de cisaillement augmente, elle engendre une distorsion et un alignement des macromolécules, qui favorisent l'écoulement et réduisent donc la viscosité. Une fois les chaînes des polymères complètement « étirées », le second plateau Newtonien est atteint. Ce phénomène est réversible uniquement si les chaînes de polymères ne sont pas dégradées par un cisaillement trop élevé (voir Fig. 2) et son ampleur dépend de la structure, de la composition et de la masse moléculaire du polymère. Différentes réponses rhéologiques peuvent donc être attendues selon le produit étudié.

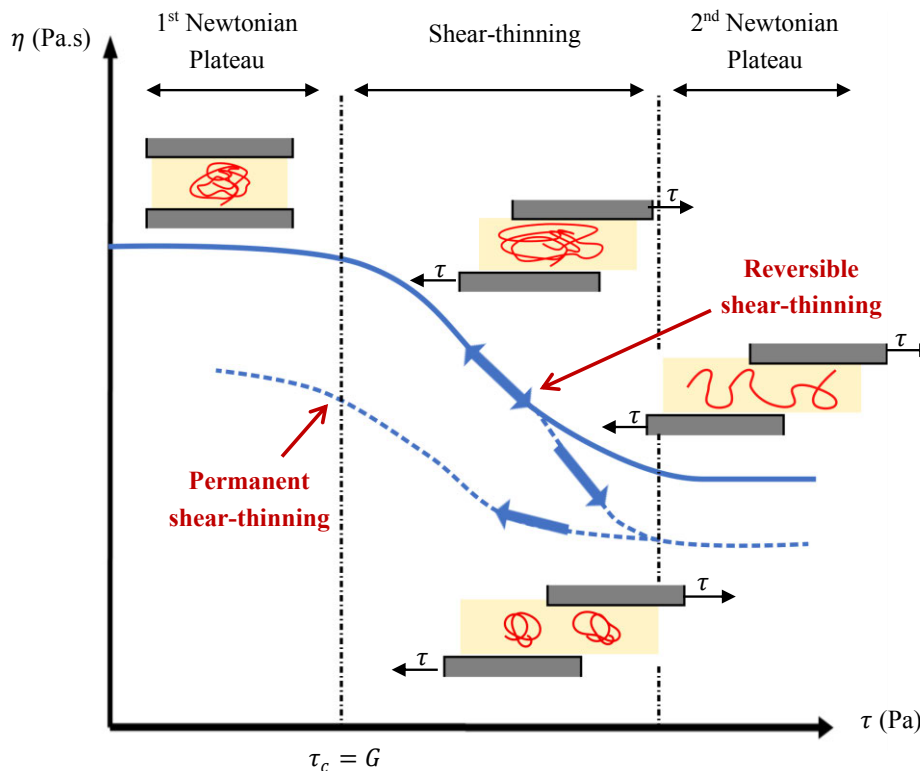


Fig. 2 : Comportement rhéofluidifiant des lubrifiants

Divers modèles existent pour décrire le comportement rhéologique des lubrifiants à n'importe quelles conditions de température et de pression. Les modèles utilisés dans les chapitres II et III sont décrits à la suite.

La loi de Vogel, Tammann et Fulcher (VTF)[12] décrit la dépendance en température de la viscosité:

$$\text{VTF} \quad \eta_0(T) = \eta_\infty \exp\left(\frac{D_F T_\infty}{T - T_\infty}\right) \quad \text{Eq. (2)}$$

où D_F est le paramètre de fragilité, η_∞ est la viscosité extrapolée à la température infinie et T_∞ , la température de Vogel pour laquelle la viscosité diverge.

La loi de Williams, Landel, Ferry modifiée par Yasutomi [13] et Bair [14] décrit la dépendance en température et pression :

$$\begin{aligned} \text{Modified WLF-} & \quad \eta_0(T, p) = \eta_g \exp \left[\ln 10 \frac{-C_1 (T - T_g(p)) F(p)}{C_2 + (T - T_g(p)) F(p)} \right] \\ \text{Yasutomi} & \quad T_g(p) = T_g(0) + A_1 \ln(1 + A_2 p) \\ & \quad F(p) = (1 + B_1 p)^{B_2} \end{aligned} \quad \text{Eq. (3)}$$

où $T_g(p)$ est la température de transition vitreuse à la pression p , F est l'expansion thermique relative du volume libre, adimensionnée, η_g est la viscosité à la transition vitreuse et $A_1, A_2, B_1, B_2, C_1, C_2$ sont les constantes numériques du modèle pour un fluide donné.

L'équation généralisée issue de Carreau-Yasuda [15] et modifiée par Bair [16] décrit la dépendance de la viscosité en fonction de la contrainte de cisaillement :

$$\begin{aligned} \text{Carreau-Yasuda modifié par} & \quad \eta(\tau) = \eta_2 + \frac{\eta_0 - \eta_2}{\left(1 + \left(\frac{\tau}{G}\right)^a\right)^{\frac{1}{n}-1}} \\ \text{Bair} & \end{aligned} \quad \text{Eq. (4)}$$

où η_0 et η_2 sont respectivement les viscosités du premier et second plateau Newtonien, G le module de cisaillement apparent, n l'exposant de la loi puissance et a le paramètre influant sur la transition du régime Newtonien au régime rhéofluidifiant.

Enfin, l'équation de Zhang [17] décrit la dépendance de la viscosité en fonction du taux de cisaillement, en prenant en compte les variations du module de cisaillement et sans faire d'hypothèse sur la viscosité du second plateau Newtonien :

$$\begin{aligned} \text{Zhang} & \quad \eta(\dot{\gamma}) = \frac{\eta_0}{\left(1 + \left[\frac{\eta_0 \dot{\gamma}}{2 \cdot G(T, p, \dot{\gamma})}\right]^2\right)} \\ & \quad G(T, p, \dot{\gamma}) = G_0 + \beta \eta_0(T, p) \dot{\gamma} \end{aligned} \quad \text{Eq. (5)}$$

où $\dot{\gamma}$ correspond au taux de cisaillement, G le module de cisaillement, G_0 le module de cisaillement à faibles contraintes de cisaillement et β une constante adimensionnée.

Lubrifiants simplifiés

Des solutions d'huiles et de polymères, sans autres additifs, sont considérées pour l'étude de lubrifiants simplifiés. L'huile de base étudiée, la Yubase 4+, est une huile minérale hydrocraquée de groupe III (selon la classification API). Six polymères de différentes chimies, deux PAMAs (polyalkylméthacrylate), deux PISHs (polyisoprène styrène hydrogéné), deux OCPs (copolymère d'oléfine) et de différentes conformations (peigne, étoilé et linéaire) sont considérés. Ces polymères sont formulés à iso HTHS 2,6 mPa.s, indiquant une formulation à iso-viscosité à 150 °C et haut taux de cisaillement (10^6 s^{-1}). Les caractéristiques des polymères sont précisées dans le Tableau 1 ci-dessous.

Polymer	PAMA		PISH		OCP		
	Nom	PAMA-C	PAMA-L	PISH-S	PISH-L	OCP-HE	OCP-LE
Structure moléculaire		Comb	Linear	Star	Linear	Linear	Linear
M_w (g.mol ⁻¹)		678 800	332 000	689 600	113 000	86 700	87 300
Polydispersité		3,2	2,3	2,2	1,6	1,1	1,0
Concentration en matière active (% _{w/w})		3,36	4,67	1,18	1,49	1,19	1,28

Tableau 1 : Caractéristiques des polymères étudiés

Chap. II : Etude rhéologique à faibles cisaillements : effet de la pression et température.

L'établissement de profils rhéologiques précis pour les solutions de polymère à haute température, haute pression et haut taux de cisaillement est de la plus haute importance pour prédire correctement la réponse tribologique du lubrifiant et guider les fabricants d'huile dans la sélection des améliorants d'indices de viscosité (VIIs). Ce chapitre est consacré à l'étude de l'impact de la température et de la pression sur la viscosité des mélanges huile-polymère, et ce à faible cisaillement.

Effet de la température à pression atmosphérique.

La dépendance de la viscosité en température, à pression atmosphérique et faible contrainte de cisaillement est mesurée grâce au rhéomètre Physica MCR301 (Anton-Paar). Différentes réponses sont obtenues selon le polymère étudié, qui épaississent néanmoins tous l'huile de base, et sont modélisées par le modèle VTF décrit précédemment (Eq. (2), p.x)[12]. La Fig. 3 permet de différencier les comportements VIIs des comportements épaississants, par un changement de pente traduisant un changement de pouvoir épaississant du polymère, plus important à haute température qu'à basse température. Le PAMA-C est ici identifié comme le VII le plus performant. Le PISH-S et le PAMA-L (non représenté) sont considérés également comme VIIs. Les OCPs et PISH-L sont quant à eux des épaississants. Toutes ces observations ne sont valables qu'à pression atmosphérique et faible contrainte de cisaillement.

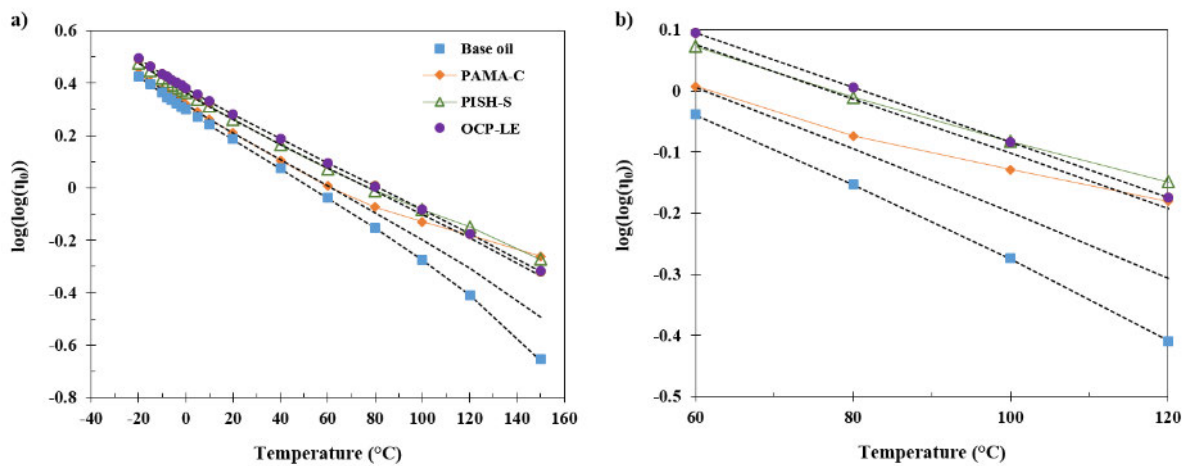


Fig. 3 : Viscosité à faible cisaillement, exprimée en $\text{Log}(\text{Log}(\eta_0))$, de l'huile de base et des solutions de PAMA-C, PISH-S et d'OCP-LE en fonction de la température et modélisée par la loi VTF – a) entre 40 °C et 160 °C, b) zoomée entre 60 et 120 °C

La modélisation VTF permet également de déterminer la température de transition vitreuse à pression atmosphérique $T_g(0)$ nécessaire au modèle WLF-Yasutomi modifié (équation WLF par la suite) utilisé dans le prochain paragraphe. Cette température est calculée pour une viscosité de $\eta_g = 10^{12}$ Pa.s, conventionnellement considérée comme la viscosité du lubrifiant à sa transition vitreuse [18].

Comportement à haute pression

La dépendance en température-pression-viscosité des solutions étudiées est obtenue grâce au viscosimètre à chute de corps, de 40 à 120 °C et de la pression. La Fig. 4 ci-dessous présente le comportement piezo-visqueux de l'huile de base en fonction de la pression à plusieurs températures, et dont la viscosité est modélisée par l'équation WLF (Eq. (3), p. x) [14]. L'allure des courbes des solutions de polymère est très similaire.

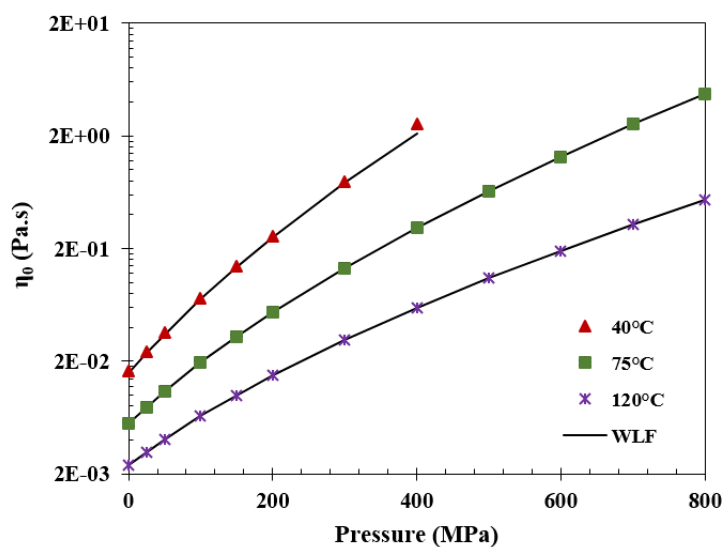


Fig. 4 : Comportement piezo-visqueux de l'huile de base à plusieurs températures.

Influence de la pression sur les propriétés des VIIs

Différents outils sont utilisés pour évaluer les performances des différents polymères en fonction de la température et de la pression. L'étude de la viscosité réduite en fonction de la température et de la pression est une première étape qui permet de distinguer différentes tendances. C'est en revanche l'utilisation du facteur épaississant Q [9] en fonction de la pression qui permet de conclure sur la nature du polymère étudié, à savoir VII ou épaississant (voir Fig. 5).

$$Q = \frac{\eta_{sp}(100\text{ }^{\circ}\text{C}, p)}{\eta_{sp}(40\text{ }^{\circ}\text{C}, p)} \quad \text{Eq. (6)}$$

où η_{sp} correspond à la viscosité spécifique de la solution de polymère.

Les VIIs présentent un pouvoir épaississant plus important à haute température qu'à basse température. Leur facteur Q devrait être strictement supérieur à 1. Tout autre résultat définit un épaississant. Les précédentes observations faites à pression atmosphérique quant à la distinction entre VII et épaississant sont ici toujours valables. Le PAMA-C est le produit présentant le facteur le plus élevé, et est confirmé comme le VII le plus performant dans le cadre de ces recherches. Le PAMA-L et le PISH-S sont également considérés comme des VIIs, de performance moindre. Les OCPs ont des facteurs inférieurs à un et des propriétés correspondantes à celles d'épaississants. Les produits précédemment cités ne voient pas leurs propriétés en tant que VII ou épaississant changer en fonction de la pression, ce qui n'est pas le cas du PISH-L. Ce polymère ayant un facteur proche de un peut facilement être considéré soit comme un VII soit comme un épaississant. La pression affecte ici ses propriétés, le polymère ayant celle d'un VII pour des pressions supérieures à 300 MPa uniquement.

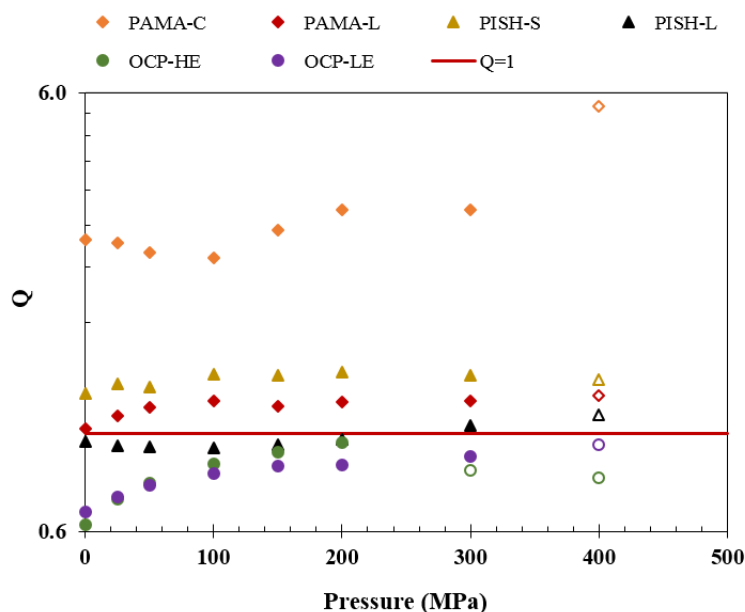


Fig. 5 : Variations du facteur épaississant Q en fonction de la pression pour toutes les solutions.

Relation entre l'échelle moléculaire et la dépendance en température-pression-viscosité des polymères.

Il est nécessaire de s'intéresser aux mécanismes ayant lieu à l'échelle moléculaire pour comprendre les différentes réponses rhéologiques observées et d'identifier les mécanismes expliquant la performance du PAMA-C. Cette sous-partie est donc consacrée à l'étude des variations de la taille des polymères en fonction de la température et de la pression, via le calcul de leur rayon hydrodynamique R_h . La loi d'Einstein (Eq. (11), p. 41) permet de calculer ce rayon à différentes températures et pressions, à partir des mesures de viscosité issues du viscosimètre haute pression à chute de corps et des viscosités calculées avec le modèle WLF. La Fig. 6 présente les résultats obtenus pour le PAMA-C. Les variations de R_h sont comprises entre 10 et 16 nm pour le PAMA-C, entre 20 et 24 nm pour le PISH-S. Le R_h reste aux alentours de 11 nm pour le PAMA-L (légère variation du même ordre de grandeur que les incertitudes expérimentales) et 12 nm pour le PISH-L. Enfin, le R_h diminue de 12 à 10 nm pour les OCPs.

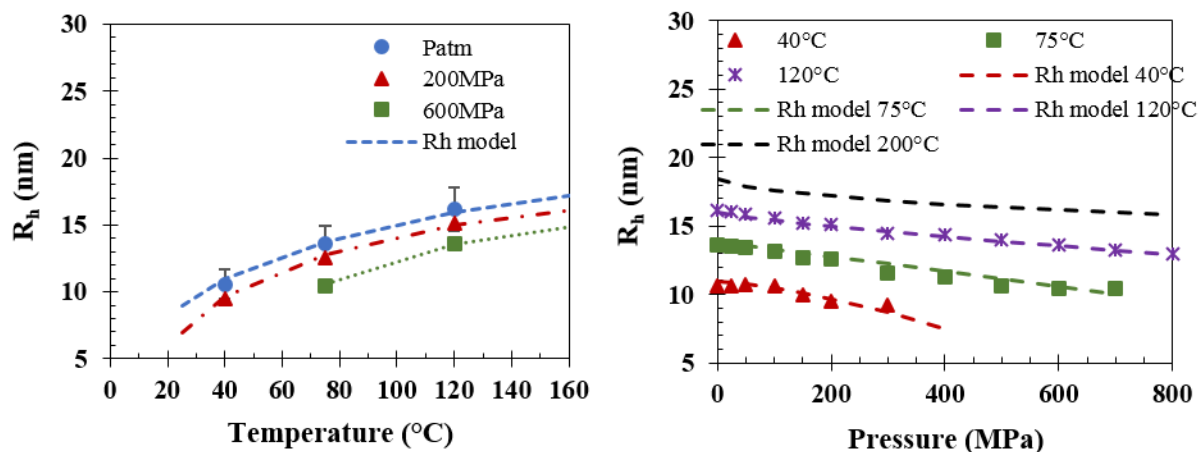


Fig. 6 : Variation du rayon hydrodynamique R_h (dédit de la loi d'Einstein) en fonction de la température (gauche) et de la pression (droite) pour la solution de PAMA-C

L'effet de la température sur le PAMA-C induit une augmentation de 53 % à pression atmosphérique de la taille de ses molécules. Ce phénomène est également visible dans une moindre mesure pour le PISH-S et le PAMA-L, dont les molécules voient leur taille augmenter de près de 15 % et 10 % respectivement, à pression atmosphérique. La variation de solubilité de ces espèces permet d'expliquer ce phénomène. En effet, ces deux polymères sont en conditions de θ solvant à 25 °C. Leurs molécules sont repliées sur elles-mêmes et les interactions intramoléculaires sont préférées. Cependant, l'augmentation de température favorise l'agitation thermique et augmente la solubilité des espèces, qui interagissent plus avec le solvant et donc gonflent. Le gonflement des pelotes est plus marqué pour le PAMA-C de par son caractère amphiphile. Ce polymère présentant des propriétés polaires et non polaires, de par sa conformation peigne, est donc plus sensible que le PISH-S et le PAMA-L au changement de qualité de solvant [19][20]. Le gonflement visible des pelotes contribue donc à améliorer les performances du VII (PAMA-C), sans pour autant être indispensable (PAMA-L, PISH-S). Les OCPs, identifiés comme épaississants, sont en revanche en bonne condition de solvant à basse température, étant des molécules apolaires en solvant apolaire. Ils ne sont donc pas sensibles au changement de qualité de solvant, ce qui explique leur légère diminution de R_h . Les cas du PISH-L est

particulier. En effet, ce polymère est également en condition thêta solvant. Une réponse similaire à celle du PISH-S pourrait être attendue avec une légère augmentation de la taille des molécules en fonction de la température. Cependant, ce polymère forme des micelles une fois en solution [20][21]. Un réarrangement de ces dernières a lieu lors du gonflement de son cœur styrène, amenant le volume global des micelles à rester constant avec l'augmentation de température.

En ce qui concerne l'influence de la pression, le R_h du PAMA-C diminue de près de 20% à chaque température, tandis qu'il reste constant pour le PAMA-L, le PISH-S et les OCPs et augmente pour le PISH-L (+ 10 % à 40 °C et 15 % à 120 °C). La pression implique une augmentation de la densité de solvant. Il est donc plus difficile pour des macromolécules de s'entourer de molécules de solvant. La pression a donc peu d'influence sur des polymères peu sensibles au changement de qualité de solvant, ce qui est le cas pour le PAMA-L, le PISH-S et les OCPs. Ce n'est en revanche pas le cas du PAMA-C et explique la contraction de ses molécules. La réponse du PISH-L est en revanche plus difficile à expliquer et doit être liée à la dynamique de réarrangement des micelles qui doit être impactée par la pression.

La Fig. 7 ci-dessous résume les différents comportements observés selon les polymères.

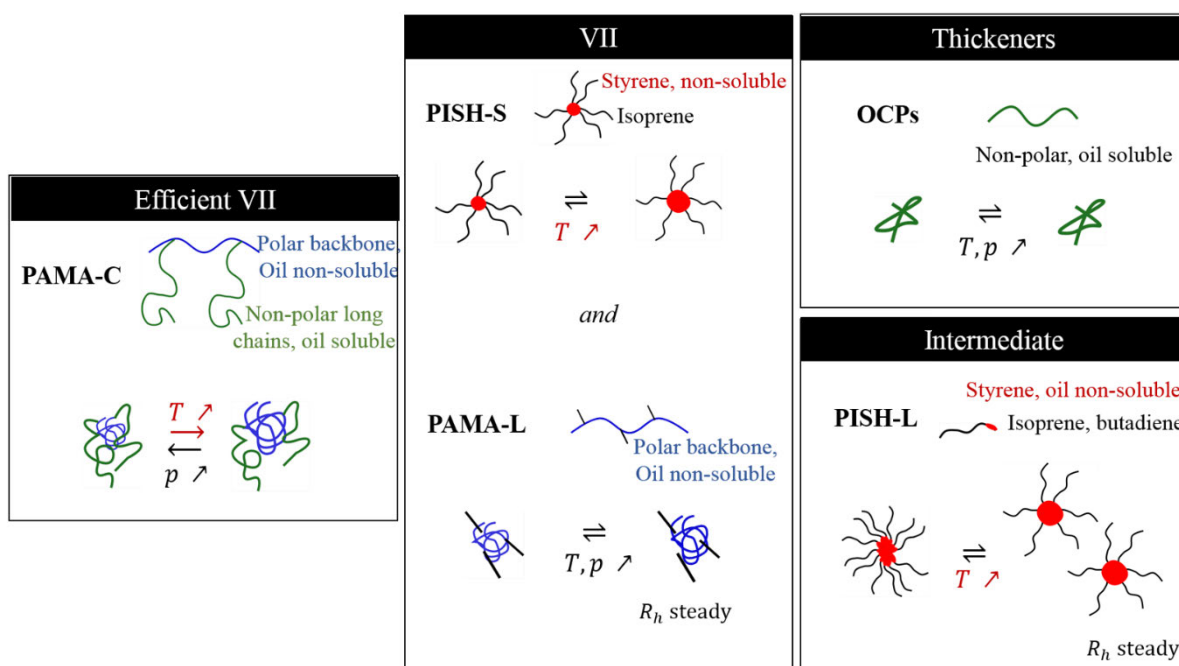


Fig. 7 : Représentation schématique de la relation entre les propriétés VII des polymères et leurs rayons hydrodynamiques.

L'étude de l'influence de la température et de la pression sur la viscosité des solutions de polymère a pu être établie de manière précise par l'utilisation de rhéomètres fonctionnant à très hautes pressions. Ces comportements ont enfin pu être liés à la structure moléculaire des polymères par les variations de leurs rayons hydrodynamiques avec la température et la pression.

Chap. III : Etude rhéologique à haute contrainte de cisaillement des solutions de polymères.

Dans la précédente partie, le PAMA-C a été identifié comme le VII le plus performant étudié, mais à faible contrainte. Ce chapitre se concentre donc sur l'influence de la contrainte de cisaillement sur la viscosité des solutions de polymère et leur propriété VII. Une fois de plus, les considérations à l'échelle moléculaire permettent d'expliquer les différents comportements observés.

Différents comportements rhéologiques

L'influence de la contrainte de cisaillement sur la viscosité est obtenue grâce au rhéomètre haute pression, de 30 °C à 60 °C, de 200 à 400 MPa. La Fig. 8 présente le comportement du mélange PISH-S, ainsi que sa prédiction calculée par la relation de Carreau-Yasuda généralisée par Bair (Eq. (31), p. 48) [16]. Les viscosités mesurées à faible cisaillement avec le viscosimètre à haute pression sont également reportées pour attester de la bonne cohérence des mesures entre les deux appareils et modèles.

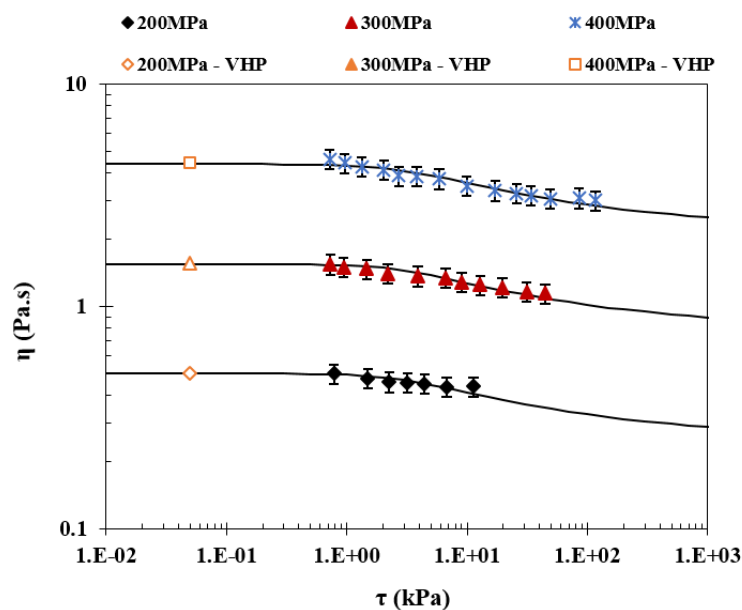


Fig. 8 : Variations de la viscosité du PISH-S en fonction de la contrainte de cisaillement à 40 °C, de 200 MPa à 400 MPa et modélisées par le modèle de Carreau-Yasuda (ligne noire)

Différentes réponses rhéologiques sont observées selon le mélange étudié. L'huile de base se comporte comme un fluide Newtonien. L'OCP-LE et les PISHs présentent des comportements rhéofluidifiants, le début d'un second plateau Newtonien étant même observé pour ces derniers. En revanche les deux PAMAs rhéofluidifient peu, en particulier le PAMA-C qui a un comportement quasi Newtonien (-10 % sur le domaine expérimental exploré). Ce résultat est surprenant sachant que le comportement non-Newtonien des lubrifiants est attribué à la présence de tels polymères en solution. L'OCP-HE n'a en revanche pu être étudié en raison de son comportement thixotrope, impliquant une viscosité dépendante du temps de sollicitation.

De nouveau, les considérations à l'échelle moléculaire permettent d'expliquer ces phénomènes. Dans [22], Mary *et al.* ont mis en avant les effets de conformations et de tailles pour expliquer les différents comportements rhéologiques des mélanges de polymères.

À tailles de polymères comparables, les effets de conformation prédominent comme en témoignent les résultats de l'OCP-LE et des deux PAMAs. Le comportement quasi-Newtonien du PAMA-C est attribué à sa conformation peigne couplée aux fortes interactions intramoléculaires présentes à basses températures. Ces molécules sont donc très peu flexibles comparées à celles de l'OCP-LE, molécule linéaire et en bon solvant (interactions molécules et solvant préférées). Le PAMA-L a un comportement entre ces deux extrêmes, en raison de ses molécules moyennement flexibles et présentant de plus faibles interactions intramoléculaires (Fig. 9).

Deux polymères ayant des encombrements stériques semblables peuvent néanmoins présenter des comportements rhéologiques différents (PAMA-C et PISH-S). Ces différences peuvent dans ce cas être expliquées par la taille du polymère. Les molécules du PISH-S font en effet le double de la taille celles du PAMA-C (20 nm contre 10 nm respectivement). Les molécules de plus grandes tailles sont plus sensibles au cisaillement, ce qui explique la chute de viscosité du PISH-S.

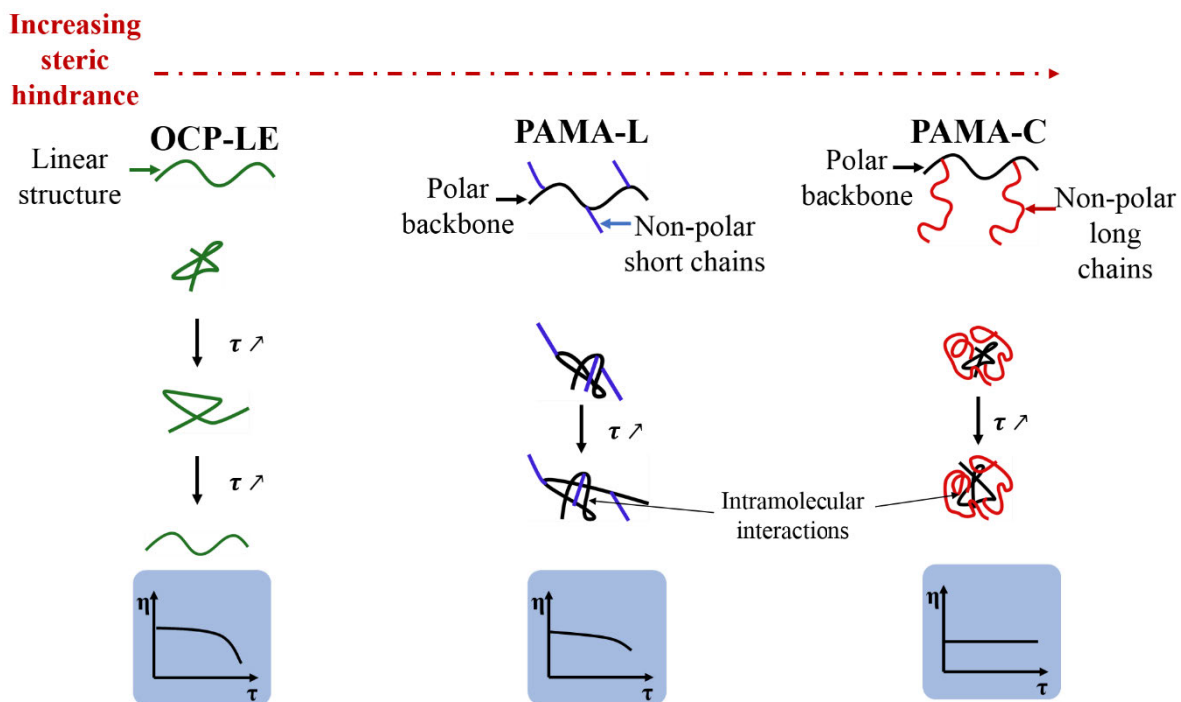


Fig. 9 : Schéma de la relation entre la réponse rhéologique des polymères en regard de leur encombrement stérique et des interactions intramoléculaires.

Il est rappelé cependant que les molécules de PAMA-C gonflent avec la température. Tenant compte des observations et commentaires fait sur le PISH-S, une réponse rhéofluidifiante plus ou moins importante peut être attendue pour le PAMA-C une fois ses pelotes gonflées à haute température. Cette chute de viscosité (correspondant au ratio entre premier et second plateau Newtonien variable avec la température ne peut en revanche être représentée par le modèle de Carreau-Yasuda dont l'une des hypothèses est de considérer le ratio entre les deux plateaux constant. Le modèle de Zhang (Eq. (32), p. 49)[17], prenant en compte la viscoélasticité des solutions, est alors proposé. Les résultats obtenus sont probants mais mettent également en avant les limites de la modélisation. En effet, la viscosité calculée

et extrapolée à haute contrainte de cisaillement diffère selon le modèle rhéologique considéré, en raison notamment de l'impossibilité actuelle de caractériser expérimentalement la viscosité du second plateau Newtonien.

Néanmoins, une étude rhéologique complète a pu être mise en place dans les conditions réalistes d'un moteur en fonctionnement, à haute température, haute pression et haute contrainte de cisaillement. Les différentes réponses des solutions de polymère ont également pu être rationalisées en considérant le rayon hydrodynamique et la conformation des polymères.

Chap. IV : Réponse tribologique des polymères en régime élastohydrodynamique et films minces

L'objectif de ce chapitre est de fournir une étude tribologique des solutions de polymère. Les mesures d'épaisseurs de films sont ainsi comparées aux prédictions d'épaisseurs issues de modèles analytiques. Cette section présente aussi la relation entre la rhéologie, la tribologie et la physico-chimie des polymères.

Mesures d'épaisseurs de films

Les mesures d'épaisseurs de films en régime EHD sont réalisées sur le tribomètre Jerotrib en configuration bille disque. Le contact EHD est reproduit par la mise en charge et la rotation d'une bille en acier 100C6 contre un disque en verre. Ce dernier peut être, soit un disque BK7 revêtu uniquement d'une couche de chrome semi-réfléchissante pour des mesures d'épaisseurs de films supérieures à 100 nm, soit un disque en S-BSL7 recouvert d'une couche de chrome ainsi que d'une cale optique de dioxyde de silice pour des mesures à très faibles épaisseurs (inférieures à 100 nm). Le principe de la mesure d'épaisseur de film, développé par Molimard [23][24], se base sur l'interférométrie optique en lumière blanche. L'épaisseur centrale h_c et minimale h_{min} sont issues du traitement de cinq interférogrammes pour une condition donnée de vitesse d'entraînement, de température et pression.

Les profils d'épaisseurs en fonction de la vitesse d'entraînement sont obtenus pour l'huile de base et une sélection de solutions de polymère. Uniquement le PAMA-C, VII le plus performant et peu rhéofluidifiant, l'OCP-LE, épaississant très rhéofluidifiant, et le PAMA-L et PISH-S, VII aux propriétés intermédiaires, sont étudiés. Les courbes d'épaisseur de film sont tracées en fonction de la vitesse d'entraînement en échelle log-log et comparées aux modèles semi-analytiques de Chittenden [25], et Moes Chevalier [26][27]. À 25 et 75 °C, les résultats de l'huile de base sont en accord avec les résultats des prédictions analytiques, confirmant ainsi son comportement Newtonien sur le domaine expérimental exploré. En revanche, toutes les solutions de polymères présentent un écart entre les résultats expérimentaux et les prédictions semi-analytiques (Fig. 10 pour le cas du PAMA-L). Ces déviations sont attribuées au comportement des solutions de polymères mis en évidence dans le troisième chapitre.

Cependant, la rhéologie du lubrifiant seule ne permet pas d'expliquer les écarts visibles aux prédictions aux faibles épaisseurs dans le cas des PAMAs (en dessous de 40 nm). Dans de telles conditions, le film

de lubrifiant a une épaisseur du même ordre de grandeur que la taille de quelques couches de polymères. Les effets intervenant à l'échelle moléculaire ne sont plus négligeables et doivent être pris en compte parmi les facteurs influençant l'épaisseur de film.

Les prédictions effectuées avec les modèles semi-analytiques précédents sont donc corrigées avec la viscosité réelle à l'entrée du contact. Cette dernière est calculée via le modèle de Carreau-Yasuda précédemment établi, afin de prendre en compte les effets de rhéofluidification. Les résultats expérimentaux sont en accord avec les nouvelles prédictions et permettent une bonne estimation de l'épaisseur de film (Fig. 11).

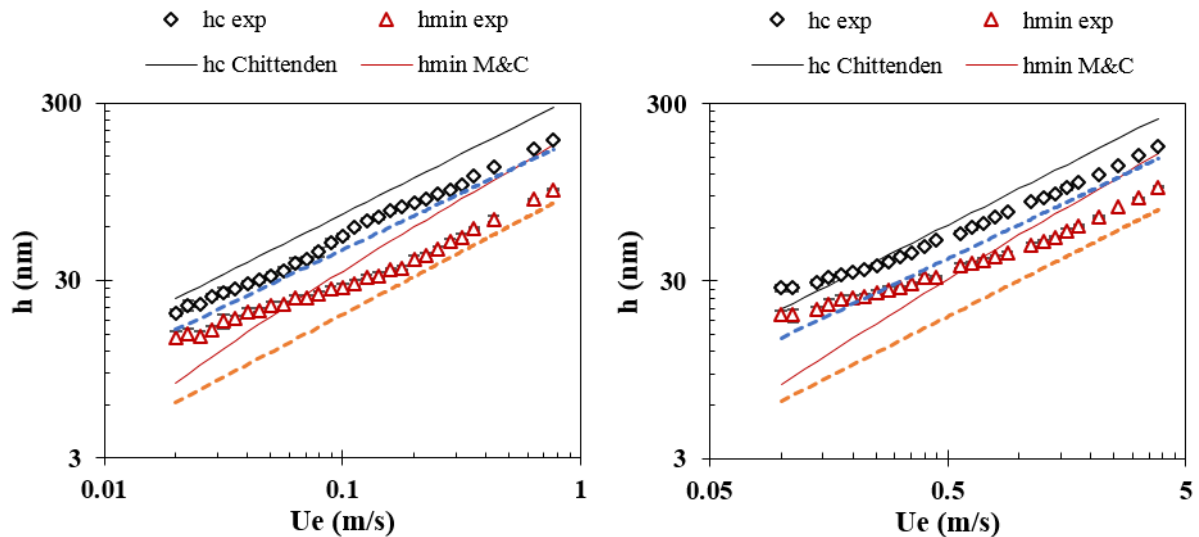


Fig. 10 : Epaisseur de film centrale et minimale, expérimentale et prédite par les modèles semi analytiques pour la solution de PAMA-L à 25 °C et 75 °C

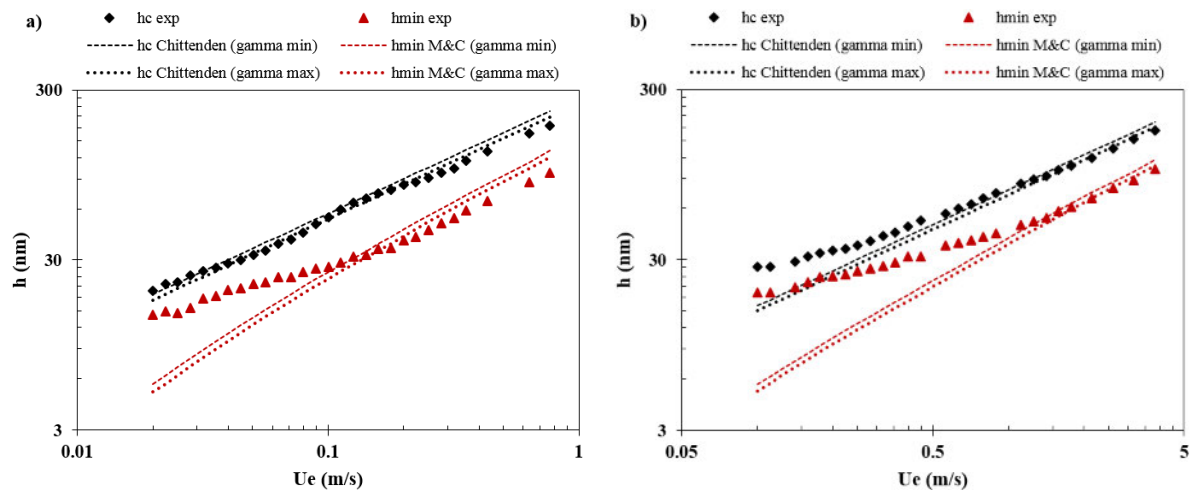


Fig. 11 : Epaisseur de film centrale et minimale, expérimentale et prédite par les modèles semi analytiques corrigés avec la viscosité issue de Carreau-Yasuda à $\dot{\gamma}_{inlet}$, pour la solution de PAMA-L à 25 °C et 75 °C.

La présence (supposée) de molécules adsorbées aux surfaces a également été mise en évidence dans le cas des PAMAs uniquement. La polarité de ces macromolécules explique leur possible adsorption aux surfaces en contact [28]. Cette épaisseur limite de molécules adsorbées a par ailleurs été évaluée par régression polynomiale des points expérimentaux. Elle correspond aux doubles du rayon de

giration R_g dans le cas du PAMA-L et à un seul rayon dans le cas du PAMA-C. Il semblerait donc que le premier PAMA cité s'adsorbe sur les deux surfaces en contact contre une pour le PAMA-C (Fig. 12). Etant donné la nature différente des surfaces, un disque en verre contre une bille en acier, ce résultat est envisageable.

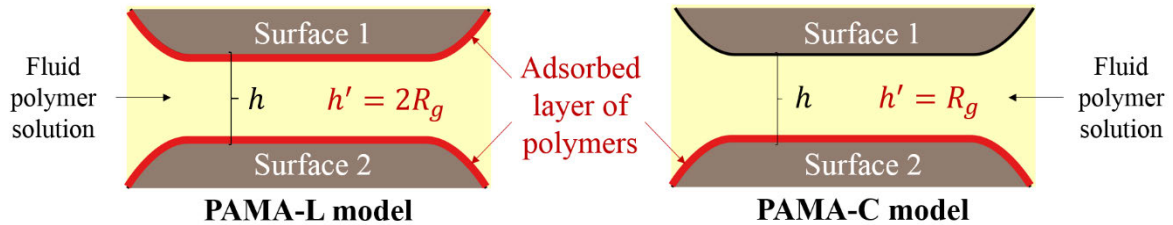


Fig. 12 : Représentation schématique des solutions de PAMAs en régime films minces.

Par ailleurs, les résultats du PISH-S posent de nouvelles questions. Les mesures d'épaisseurs de films de ce polymère ont en effet mis en évidence sa faible contribution à l'épaisseur de la solution. De plus ce polymère apolaire ne s'adsorbait pas aux surfaces. Des épaisseurs de films inférieures aux dimensions des pelotes du PISH-S (environ 20 nm) sont également atteintes. Ces résultats posent question sur le passage ou non dans le contact de molécules de grande tailles (et ne pouvant s'adsorber aux surfaces). Des mesures in-situ (spectroscopie Raman ou infra-rouge par exemple) peuvent être envisagées pour visualiser le passage, l'alignement et l'adsorption de molécules aux surfaces en contact.

Conclusion générale et recommandations

Le développement de lubrifiants haute performance pour réduire le frottement dans les moteurs et limiter la consommation de carburant, demeure un défi majeur pour les fabricants d'huiles. L'objectif des recherches entreprises au cours de cette étude est de comprendre le rôle et l'action des polymères dits améliorants d'indice de viscosité dans la formulation de lubrifiants moteurs. Pour ce faire, une étude multi-échelle a été mise en place, de l'échelle moléculaire à la tribologie, en passant par la rhéologie.

En premier lieu, une étude bibliographique fournit les éléments essentiels à la compréhension des points abordés dans ces recherches. Les notions de frottements et régimes de lubrification, ainsi que le rôle et la composition des lubrifiants y sont abordés. Des généralités sur la physico-chimie des polymères et polymères en solutions sont expliquées, avec les notions de conformation, de rayon de giration et d'hydrodynamique, et des considérations de solubilité nécessaires à la compréhension des mécanismes intervenant à l'échelle moléculaire. Enfin, la rhéologie des lubrifiants ainsi que les modèles rhéologiques classiquement employés sont présentés.

Les chapitres II et III sont consacrés à l'étude rhéologique complète du lubrifiant, à haute température, haute pression et haute contrainte de cisaillement. Dans le chapitre II la dépendance de la viscosité à la température et la pression de ces lubrifiants est étudiée. Il est montré que leur comportement rhéologique résulte de mécanismes se produisant à l'échelle moléculaire, en considérant les notions de solubilité, de rayon hydrodynamique et d'effets de conformation. Les deux OCPs sont considérés comme des épaississants, tandis que les PAMAs et le PISH-S ont des propriétés VII. Le PAMA-C est par ailleurs le polymère le plus performant étudié ici. Le PISH-L quant à lui peut être considéré comme un épaississant à pression atmosphérique et présente des propriétés de VII au-delà de 300 MPa.

Le chapitre III est consacré à l'étude de la dépendance de la viscosité en fonction de la contrainte de cisaillement, ainsi qu'à l'extrapolation de la réponse rhéologique mesurée sur une large gamme de températures et de pressions à travers un modèle de Carreau-Yasuda. Différents comportements rhéologiques sont observés et directement liés aux effets de conformation et taille des polymères en solutions. À taille comparable, les molécules les plus flexibles et présentant peu d'interactions intramoléculaires, comme le polymère linéaire apolaire OCP-LE, présentent un comportement rhéofluidifiant de large amplitude, contrairement au PAMA-C, encombré stériquement et favorisant les interactions entre ses chaînes. À conditions de solvatation et encombrement stérique comparables (cas du PISH-S et PAMA-C), les effets de tailles prédominent. Les molécules de plus grandes tailles (PISH-S), sont plus sensibles au cisaillement. Une réponse rhéofluidifiante est alors observée, ce qui pourrait également arriver pour la solution de PAMA-C une fois ses molécules complètement gonflées à haute température. Cette dernière hypothèse met également en avant les limites du modèle de Carreau-Yasuda et nous amène à proposer une relation plus appropriée prenant en compte la viscoélasticité des lubrifiants.

Le dernier chapitre présente les mesures d'épaisseur de film effectuées pour explorer l'impact de l'addition de polymère sur la réponse du lubrifiant dans les régimes élastohydrodynamiques et films minces. Elles sont comparées aux prévisions analytiques basées sur les modèles rhéologiques établis

précédemment. Il est montré i) une bonne adéquation entre les prévisions et les données expérimentales dans le régime EHD et ii) la présence d'une épaisseur critique pour les PAMAs à partir de laquelle les résultats s'écartent significativement des prévisions. Ce régime dit thin film, aux faibles épaisseurs, est expliqué par le comportement non newtonien des lubrifiants et l'adsorption des polymères aux surfaces.

L'étude approfondie du rôle et des fonctions des améliorants d'indice de viscosité a soulevé plusieurs questions. Plusieurs directions possibles sont à considérer pour approfondir la compréhension de la relation entre les propriétés physico-chimiques des VIIs et les réponses des lubrifiants moteurs en conditions de fonctionnement.

Les différentes hypothèses émises lors de ces recherches doivent tout d'abord être vérifiées. Les modèles rhéologiques peuvent être améliorés pour prendre en compte la potentielle rhéofluidification du PAMA-C à haute température. Des études de simulations en dynamique moléculaire pourraient également être intéressantes pour améliorer notre compréhension des mécanismes intervenant à l'échelle moléculaire. La dégradation du lubrifiant après plusieurs cycles moteurs pourrait également être étudiée. Des mesures in-situ sont à envisager pour visualiser la trajectoire des polymères dans le contact, ainsi que des analyses de surfaces pour confirmer l'adsorption de polymères aux surfaces en contact.

Enfin d'autres chimies de polymères, de masses moléculaires, de conformation sont également à envisager. Une huile polaire pourrait être étudiée, ainsi qu'un PAMA étoilé et présentant des fonctions dispersantes polaires.

Tables of contents

Abstract	i
Remerciements	iii
Résumé étendu	v
Tables of contents	1
List of tables	5
List of figures	5
Nomenclature	9
General introduction	13
Chapter I – Literature overview on engine lubrication, polymer solutions and rheology	17
I.1 Engine Lubrication	19
I.1.1 Friction and role of engine lubricants.....	19
I.1.2 Lubrication regimes.....	21
I.2 Nature and composition of engine lubricants	26
I.2.1 Base oils	26
I.2.1.a Mineral base oils	26
I.2.1.b Synthetic base oils	29
I.2.2 Additives	30
I.2.3 Viscosity index improvers (VIIs)	31
I.2.3.a Mechanism of action and properties affecting VII	31
I.2.3.b Polymers families and synthesis	32
I.2.4 Distinction between VIIs and thickeners.....	34
I.3 Polymers and polymer solutions	36
I.3.1 Generalities.....	36
I.3.2 Conformation and sizes	36
I.3.2.a Molecular architecture.....	36
I.3.2.b Solvency regimes	38
I.3.2.c Characteristics size	38
I.3.3 Concentration regimes.....	40
I.3.3.a Critical concentration	40
I.3.3.b Einstein’s law	41
I.4 Rheology of lubricants	42
I.4.1 Generalities and definitions	42
I.4.2 Non-Newtonian rheological behavior	43
I.4.3 Rheological models for lubricants.....	45
I.4.3.a Temperature dependence.....	45

I.4.3.b	Pressure dependence	46
I.4.3.c	Combined temperature and pressure dependences	47
I.4.3.d	Shear stress dependence	47
I.5	Simplified Lubricants	50
I.6	Conclusion	52
Chapter II - Low-stress rheology of polymer solutions: effect of pressure and temperature.....		53
II.1	VIIIs against thickeners at atmospheric pressure	55
II.2	Behavior at high pressure	58
II.2.1	Temperature and pressure dependence at low shear stress.....	58
II.2.2	Pressure-viscosity coefficients variations against temperature	62
II.3	Pressure influence on the VII properties	63
II.3.1	Comparative study using the reduced viscosity η_{red}	63
II.3.2	Distinction between VIIIs and thickeners at high pressure.....	65
II.4	Impact of the molecular structure on the pressure-viscosity dependence.....	67
II.4.1	Concentration regime and determination of R_h at atmospheric pressure.....	67
II.4.2	Determination of R_h at high pressure using the Einstein's law	69
II.4.2.a	Temperature variations at constant pressure.....	72
II.4.2.b	Pressure variations at constant temperature.....	74
II.5	Conclusion	76
Chapter III - High shear stress response of polymer solutions		77
III.1	Rheological response at high shear stress	79
III.1.1	Thixotropy of the OCP-HE solution.....	79
III.1.2	Shear-thinning response of all solutions.....	80
III.2	Relationship between the additive's structures and their rheological responses	86
III.2.1	Mass average molecular weight effects.....	87
III.2.2	Conformation effect.....	87
III.2.3	Size effect	88
III.2.4	Limits of the Carreau model.....	89
III.3	Zhang model for low viscoelastic solutions.....	91
III.3.1	Model and experiments	91
III.3.2	Comparison to Carreau predictions	92
III.4	Conclusion	95

Chapter IV – Tribological response of polymer solutions in elastohydrodynamic and thin film regimes..... 97

IV.1 Films thickness measurements method..... 99

IV.1.1 Differential colorimetric interferometry principle..... 99

IV.1.2 Description of the classical EHL analytical models 102

IV.1.3 Operating conditions 103

IV.2 Film thickness results 104

IV.2.1 Tribological response of the base oil 104

IV.2.2 Tribological behavior of polymer solutions 106

IV.3 Thin film lubrication regime 111

IV.3.1 Approach 111

IV.3.2 Discussion on the PAMA-L in TFL 112

IV.3.3 Discussion on the PAMA-C in TFL 115

IV.3.4 Discussion on the OCP-LE and parameters influencing the thin layer formation..... 118

IV.3.5 Discussion on the PISH-S limitations 120

IV.4 Conclusion 122

Summary and conclusion..... 125

Recommendations for future works 129

References 131

Appendix 1 - Physica MCR301 rheometer (Anton-Paar) 139

Appendix 2 - Ultra-Shear Viscometer (USV) 140

Appendix 3 – High pressure falling-body viscometer 141

Appendix 4 - High pressure Couette rheometer. 142

Appendix 5 – Analytical tools 143

Appendix 6 – Viscosity-pressure dependence of all solutions 144

Appendix 7 - Reduced viscosity variations against temperature and pressure for all solutions..... 145

Appendix 8 - Rheological study of the “PAMA-C low” 148

Appendix 9 - Zhang results 151

Appendix 10 - Comparison Carreau-Yasuda and Zhang modeling 153

Appendix 11 - Jerotrib test-rig description..... 155

Appendix 12 - The Hertz theory..... 157

List of tables

Table 1: Lubrication regimes in function of the film thickness ratio λ [23].....	24
Table 2: API classification of base oils [44].....	26
Table 3: Chemical and physical properties of mineral and synthetic (PAO) oils components.....	29
Table 4: Flory exponent, gyration radius, form factor and nature of the interaction of polymers as a function of the solvent quality	39
Table 5: Main characteristics of the polymers studied in this work	50
Table 6: Extrapolated (from the VTF model) and measured (from DSC) glass transition temperatures at atmospheric pressure with the Viscosity index (VI, see Figure 9) of all solutions	58
Table 7: Parameters of the WLF, reciprocal asymptotic isoviscous pressure coefficients computed from the WLF model and VI, for the base oil and all polymer solutions.....	60
Table 8: Variations of the reduced viscosity η_{red} calculated by the WLF model between 40 to 150 °C at ambient pressure and between 75 to 150 °C at 600 MPa.....	65
Table 9: Hydrodynamic radii and critical concentrations of polymer solutions in theta and good solvent conditions using the Flory equations. Results at the chosen solvency regime are bolded. The polymers weight concentration in the solution is indicated in the extreme right side colusmn.	67
Table 10: hydrodynamic radii from different methodologies at atmospheric pressure – in bold the solvent quality chosen for the Flory equations	69
Table 11: Parameters of the Carreau-Yasuda model with ($\eta_2 \neq 0$) or without ($\eta_2 = 0$) a second Newtonian plateau	81
Table 12: Characteristics of the polymers to apprehend the relationship between the VII structure and its rheological response - Hydrodynamic radii calculated from 25 to 120 °C at atmospheric pressure using the Einstein’s law, the mass average molar mass of each VII and the viscosity decrease calculated between shear stresses from 10^{-2} and 10^3 kPa.....	86
Table 13: Parameters of the Zhang model.....	91
Table 14: Material properties of the ball and discs used in Jerotrib [38]	101
Table 15: Experimental conditions for film thickness measurements	103
Table 16: Power law parameters for the log-log plot of h_c for all solutions	107
Table 17: Comparison between the actual viscosities at the inlet determined, from the Chittenden equation and h_c measurements and the low shear viscosity from the modified WLF-Yasutomi model	110
Table 18: Actual viscosity calculated at the inlet with the Carreau-Yasuda model $\eta_{inlet,CY}$ at the minimal and maximal shear strain rate evaluated at the inlet.	112
Table 19: Comparison of fluid layer thicknesses to hydrodynamic radii R_g at 25 °C and 75 °C for PAMA solutions.....	116
Table 20: Shearing gaps and resulting shear stresses range covered of the cylinders sets.....	142
Table 21: Main characteristics of the two comb polyalkylmethacrylates.....	148
Table 22: Parameters of the WLF, reciprocal asymptotic isoviscous pressure coefficients computed from the WLF model and VI of comb polyalkylmethacrylates	149
Table 23: Jerotrib operating ranges and accuracy	155

List of figures

Figure 1: Key technologies for reduction of CO ₂ emissions [29].....	13
Figure 2: Energy losses in a passenger car, according to Holmberg et al. [1]	14
Figure 3: Approach of the study at different scales	15
Figure 4: Severe conditions of temperature and pressure in a combustion engine [30]	19
Figure 5: Description of the lubrication system in a combustion engine [31]	20

List of tables and figures

Figure 6: Stribeck curve associated with automotive engine parts	22
Figure 7: Film thickness and pressure profiles in an EHD contact	23
Figure 8: Lubrication map proposed by Luo et al [39]	24
Figure 9: Viscosity Index determination [10]	27
Figure 10: Simplified refining process of mineral base oils.....	28
Figure 11: Schematic coil expansion model to explain viscosity index improvement by polymers [19]	32
Figure 12: Chemical structures of viscosity index improvers	33
Figure 13: Schematic distinction between a viscosity index improver and a thickener	35
Figure 14: Various polymer architectures.....	37
Figure 15: Comb polymer, a combination of PAMA and polyolefin chemistries [52].....	37
Figure 16: Micelle formation of amphiphilic copolymer [20]	38
Figure 17: Crossover between dilute and semi-dilute solutions (from left to right: dilute, onset of interact and semi-dilute) [11].....	40
Figure 18: Scaling relationship between specific viscosity and concentration for 6FDA- TFDB PI/DMF solutions at 20 °C [68].....	41
Figure 19: Description of simple shear flow.....	42
Figure 20: Maxwell model – where η_{real} is the real viscosity and E is the elastic modulus	44
Figure 21: Shear-thinning behavior of lubricants.....	44
Figure 22: Viscosity of the base oil and the OCP-HE solution at different temperatures and fitted by the VTF equation (plotted as the black line).	55
Figure 23: Low shear viscosity, expressed as $\text{Log}(\text{Log}(\eta_0))$ of the base oil, PAMA-C, PISH-S and OCP-LE solutions versus temperature and fitted by the VTF expression plotted as the dotted black line, between - a) 40°C and 160°C and b) zoomed between 60 and 120°C to highlight the slope change of PAMA-C and PISH-S.....	57
Figure 24: Viscosity-pressure dependence of the base oil (experimental data as colored dots) at different temperatures and regressed to the WLF expression (black line)	60
Figure 25: Master curves of the base oil and the polymer solutions – Top) PAMA solutions, Bottom left) PISH solutions, Bottom right) OCP solutions	61
Figure 26: Pressure viscosity coefficient α^* variations against temperature for the base oil and each polymer family – Top) PAMA, Bottom left) PISH, Bottom right) OCP	63
Figure 27: Reduced viscosity η_{red} calculated from the modified WLF equation plotted against temperature for all solutions at left) atmospheric pressure, right) 600 MPa	64
Figure 28: Reduced viscosity η_{red} calculated from the modified WLF equation plotted against pressure for all solutions at left) 40 °C, right) 120 °C.	64
Figure 29: Thickening factor Q versus pressure for all polymer solutions – full colored dots for thickening factor from experimental data and empty colored dots for Q extrapolated at 400 MPa using the WLF model	66
Figure 30: Hydrodynamic radius variations versus temperature (left) and pressure (right) for PAMA-C (top) and PAMA-L (bottom) - R_h determined from experimental values plotted as color dots and R_h calculated by the WLF equation plotted as dotted lines.	70
Figure 31: H Hydrodynamic radius variations versus temperature (left) and pressure (right) for PISH-S (top) and PISH-L (bottom) - R_h determined from experimental values plotted as color dots and R_h calculated by the WLF equation plotted as dotted lines.	71
Figure 32: Hydrodynamic radius variations versus temperature (left) and pressure (right) for OCP-HE (top) and OCP-LE (bottom) - R_h determined from experimental values plotted as color dots and R_h calculated by the WLF equation plotted as dotted lines.	71
Figure 33: Molecular behavior of PISH according to their structure, star-shape or micellar shape [20].....	74
Figure 34: Summary on the relationship between the VII/thickeners and their molecular properties, at low shear stress.	75

Figure 35: Raw data of the OCP-HE solution acquired from the different cylinders sets of the high pressure Couette rheometer at 40 °C and 400 MPa and showing thixotropy at low shear stress. The Carreau-Yasuda model is fitted to the experimental data (black line).	79
Figure 36: Viscosity of the base oil versus shear stress at 40 °C, from 200 MPa to 400 MPa and fitted by the Carreau-Yasuda model (black line)	82
Figure 37: Viscosity of the OCP-LE solution versus shear stress at 40 °C, from 200 MPa to 400 MPa and fitted by the Carreau-Yasuda model (black line)	82
Figure 38: Viscosity of the PISHs solutions versus shear stress at 40 °C, from 200 MPa to 400 MPa and fitted by the Carreau-Yasuda model (black lines) – a) PISH-S, b) PISH-L	83
Figure 39: Viscosity of the PAMAs solutions versus shear stress at 40 °C, from 200 MPa to 400 MPa and fitted by the Carreau-Yasuda model (black lines) – a) PAMA-C, b) PAMA-L.....	84
Figure 40: Comparison of the rheological response of the base oil and polymer solutions at 40 °C and 400 MPa – experimental data as colored dots and predicted viscosities as colored lines.	85
Figure 41: Summary of the rheological behaviors of the base oil and polymer solutions.	86
Figure 42: Schematic representation of the polymers responses with respect to the steric hindrance of their macromolecules and the intramolecular interactions	88
Figure 43: Experimental viscosity against shear strain rate from different devices – from the Physica MCR301 (empty colored dots), the USV (colored dots). Experiments were carried out from 40 °C up to 150 °C at atmospheric pressure. The colored lines stand for the first Newtonian plateau η_0 extrapolation in order to appreciate the viscosity decrease, which is calculated between η_0 and the highest shear-rate USV value – a) PISH-S, b) PAMA-C	90
Figure 44: Viscosity of the PISH-S solution versus shear strain rate at 40 °C, from 200 MPa to 400 MPa and fitted by the Zhang model (black line)	92
Figure 45: Comparison between the Carreau-Yasuda predictions, the Zhang’s results and the master curve resulting from the experiments carried out at different temperatures and pressures for the PAMA-C solution.	93
Figure 46: Comparison between the Carreau-Yasuda predictions, the Zhang’s results and the master curve resulting from the experiments carried out at different temperatures and pressures for the PAMA-C solution.	93
Figure 47: Basic principle of monochromatic optical interferometry [100]	100
Figure 48: Block diagram of the film thickness evaluation process.	101
Figure 49: Experimental and analytical central and minimum film thicknesses of the base oil at – a) 25 °C; b) 75 °C.	105
Figure 50: Experimental and analytical central and minimum film thicknesses of the OCP-LE solution at 25 °C (left) and 75 °C (right), along with the base oil film thicknesses (colored dashed lines)	107
Figure 51: Experimental and analytical central and minimum film thicknesses of the PISH-S solution at 25 °C (left) and 75 °C (right), along with the base oil film thicknesses (colored dashed lines)	108
Figure 52: Experimental and analytical central and minimum film thicknesses of the PAMA-C solution at 25 °C (left) and 75 °C (right), along with the base oil film thicknesses (colored dashed lines)	109
Figure 53: Experimental and analytical central and minimum film thicknesses of the PAMA-L solution at 25 °C (left) and 75 °C (right), along with the base oil film thicknesses (colored dotted lines).....	109
Figure 54: Specific viscosity at the inlet against the central film thickness for the PAMA-L solution at 25 °C and 75 °C.	113
Figure 55: Experimental h_c and h_{min} of the PAMA-L solution shown along with their analytical predictions using the η_{inlet} calculated with the Carreau-Yasuda model, at either the minimal or maximal shear rate encountered at the inlet – a) at 25 °C; b) at 75 °C.	114
Figure 56: Specific viscosity at the inlet against the central film thickness for the PAMA-C solution at 25 °C and 75 °C.	115
Figure 57: Experimental h_c and h_{min} of the PAMA-C solution shown along with their analytical predictions using the η_{inlet} calculated with the Carreau-Yasuda model, at either the minimal or maximal shear rate encountered at the inlet – a) at 25 °C; b) at 75 °C.	117

List of tables and figures

Figure 58: Specific viscosity at the inlet against the central film thickness for the OCP-LE solution at 25 °C and 75 °C.	119
Figure 59: Experimental h_c and h_{min} of the OCP-LE solution shown along with their analytical predictions using the η_{inlet} calculated with the Carreau-Yasuda model, at either the minimal or maximal shear rate encountered at the inlet – a) at 25 °C; b) at 75 °C.	119
Figure 60: Specific viscosity at the inlet against the central film thickness for the PISH-S solution at 25 °C and 75 °C.	120
Figure 61: Experimental h_c and h_{min} of the PISH-S solution shown along with their analytical predictions using the η_{inlet} calculated with the Carreau-Yasuda model, at either the minimal or maximal shear rate encountered at the inlet – a) at 25 °C; b) at 75 °C.	121
Figure 62: Schematic representation of the PAMA solutions in thin film regime.....	122
Figure 63: Physica MCR301 rheometer (Anton-Paar) [10].....	139
Figure 64: Anton-Paar geometries (plate-plate; cone-plate, coaxial cylinders) [10]	139
Figure 65: Picture of the USV from PCS Instruments [10].....	140
Figure 66: Schematic view of the USV	140
Figure 67: Description of the high pressure viscometer	141
Figure 68: Description of the high pressure Couette rheometer.....	142
Figure 69: Viscosity-pressure dependence of all solutions at different temperatures.....	144
Figure 70: Reduced viscosity variations versus temperature (left) and pressure (right) for PAMAs – PAMA-C top left and right, PAMA-L bottom left and right – η_{red} determined from experimental values plotted as color dots and calculated with Eq. (26) as dotted lines.	145
Figure 71: Reduced viscosity variations versus temperature (left) and pressure (right) for PISH-S – PISH-S top left and right, PISH-L bottom left and right - η_{red} determined from experimental values plotted as color dots and calculated with Eq. (26) as dotted lines.	146
Figure 72: Reduced viscosity variations versus temperature (left) and pressure (right) for OCPs – OCP-HE top left and right, OCP-LE bottom left and right - η_{red} determined from experimental values plotted as color dots and calculated with Eq. (26) as dotted lines.	146
Figure 73: Hydrodynamic radius variations versus temperature (left) and pressure (right) for PAMA-C low....	149
Figure 74: Viscosity of the PAMA-C low solution versus shear stress from 40 °C to 60 °C and from 200 MPa to 400 MPa, along with the Newtonian viscosity at the considered temperature and pressure (colored dotted line)	150
Figure 75: Viscosity of the OCP-LE solution versus shear strain rate at 40 °C, from 200 MPa to 400 MPa and fitted by the Zhang model (black line)	151
Figure 76: Viscosity of the PISH-L solution versus shear strain rate at 40 °C, from 200 MPa to 400 MPa and fitted by the Zhang model (black line)	151
Figure 77: Viscosity of the PAMA-C solution versus shear strain rate at 40 °C, from 200 MPa to 400 MPa and fitted by the Zhang model (black line)	152
Figure 78: Viscosity of the PAMA-L solution versus shear strain rate at 40 °C, from 200 MPa to 400 MPa and fitted by the Zhang model (black line)	152
Figure 79: Comparison of Carreau-Yasuda predictions and Zhang’s results for the PAMA-L solution by looking at the master curve and experimental results obtained at different temperatures and pressures. .	153
Figure 80: Comparison of Carreau-Yasuda predictions and Zhang’s results for the PISH-S solution by looking at the master curve and experimental results obtained at different temperatures and pressures ..	154
Figure 81: Comparison of Carreau-Yasuda predictions and Zhang’s results for the PISH-L solution by looking at the master curve and experimental results obtained at different temperatures and pressures ..	154
Figure 82: Picture of the Jerotrib test-rig along with its scheme while running.....	155
Figure 83: Typical calibration curve used for the interferogram acquired with the Jerotrib test-rig	156

Nomenclature

Acronyms

API	American petroleum institute
BL	boundary lubrication
DCI	differential colorimetric interferometry
DLS	dynamic light scattering
DSC	differential scanning calorimetry
EHD	elastohydrodynamic
EHL	elastohydrodynamic lubrication
EP	extreme pressure additive
HD	hydrodynamic
HL	hydrodynamic lubrication
HTHS	high temperature high shear stress test
ML	mixed lubrication
OCP	olefin copolymer
OCP-HE	OCP of high ethylene content
OCP-LE	OCP of low ethylene content
PAMA	polyalkylmethacrylate
PAMA-C	comb polyalkylmethacrylate
PAMA-L	linear polyalkylmethacrylate
PAO	polyalphaolefin
PBSH	polyhydrogenated butadiene-styrene copolymer
PDI	polydispersity index
PIB	polyisobutene
PISH	polyhydrogenated isoprene-styrene copolymer
PISH-L	linear PISH
PISH-S	star PISH
PPD	pour point depressant
RMS	root mean square roughness
SANS	small angle neutron scattering
SEC	size exclusion chromatography
TFL	thin film lubrication
USV	ultra shear viscometer
VI	viscosity index
VTF	Vogel, Tamman and Fulcher (model)
VII	viscosity index improver
WLF	Williams, Landel and Ferry (model)

Latin letters

a	Carreau-Yasuda parameter
a_H	radius of the Hertzian contact (m)
c	concentration in weight of active ingredient (g.cm^{-3})
c^*	critical concentration (g.cm^{-3})
c_p	specific heat capacity ($\text{J.kg}^{-1}.\text{K}^{-1}$)
C	calibration constant for the falling body viscometer
$C_1, C_2, A_1, A_2, B_1, B_2$	WLF constants
C_∞	Flory characteristic ratio
D_F	fragility parameter in the VTF equation
DP_n	number average degree of polymerization
E	elastic modulus in the Maxwell model (GPa)
E'	Young modulus (GPa)
E_a	thermal activation energy (J.mol^{-1})
E_{eq}	reduced Young elastic modulus of the contacting bodies (GPa)
F	dimensionless relative thermal expansion function in WLF
F_{ext}	external force in the simple shear flow description (N)
G	effective shear modulus (kPa)
G_C	Chittenden dimensionless material properties parameter
G_0	equivalent shear modulus at low shear rate (kPa)
h	film thickness (nm)
h'	film thickness of the adsorbed layer at the surfaces (nm)
h_0	film thickness at atmospheric pressure
h_c	central film thickness (nm)
h_i	height of inner cylinder (m)
h_{min}	minimal central thickness (nm)
$h(p)$	film thickness at the pressure p (nm)
H_C	Chittenden dimensionless film thickness
H_{Moes}	Moes dimensionless film thickness
H_{Moes}^{center}	central Moes dimensionless film thickness
I	intensity of light captured by the detector
I_0	intensity of the incident light beams
I_1 to I_n	intensity of the reflected light beams
k_H, k_K, k_M	Huggins, Kraemer, Martin constants
k	liquid thermal conductivity ($\text{W.m}^{-1}.\text{K}^{-1}$)
K	Chittenden parameter
l	mean monomer size (cm)
L_{Moes}	Moes dimensionless material properties parameter
m_i	units of mass (g)
M	molar mass of one molecule
M_0	molar mass of one monomer unit (g.mol^{-1})
M_{Moes}	Moes dimensionless load parameter

M_n	number average molar mass (g.mol ⁻¹)
M_t	torque applied to the inner cylinder (N.m)
M_w	mass average molar mass (g.mol ⁻¹)
n	power law exponent
n_0	refractive index at atmospheric pressure
n_i	mole fraction of molecules i
$n(p)$	refractive index at the pressure p
N	number of monomers
Na	Nahme-Griffith number
N_a	the Avogadro number (6.022 * 10 ²³ mol ⁻¹)
$N_{experiment}, N_{parameters}$	number of experiments performed and parameters in the considered model
N_i	number of molecules i
p	pressure (MPa)
p_{atm}	atmospheric pressure (MPa)
p_H	maximum Hertzian pressure (MPa)
Q	thickening factor
r	distance from the contact center (m)
rms	root mean square deviation
r_i	distance of an atom from the center of mass of a polymer (nm)
R	ideal gas constant (8.314 J.mol ⁻¹ .K ⁻¹)
R_{ball}	curvature radii of the ball (m)
R_{coil}	coil radius (nm)
R_{eq}	reduced radii of curvature (m)
R_g	gyration radius (nm)
R_h	hydrodynamic radius (nm)
R_i, R_{ot}	radius of the inner cylinder and outer cylinders in a rheometer (m)
R_q	root mean square (RMS) roughness of materials
R_x, R_y	curvature radii in the x-direction and y-direction respectively (m)
R_1, R_2	curvature radii of the surfaces (m)
SRR	slide-to-roll ratio
t	falling time of the sinker in the falling body viscometer (s)
T	temperature (°C)
$T_g(p)$	glass transition temperature at the pressure p (°C)
$T_g(0)$	glass transition temperature at atmospheric pressure (°C)
T_∞	Vogel temperature at which the temperature diverge (°C)
u	velocity of the flow (m.s ⁻¹)
U_{ball}	ball speed (m.s ⁻¹)
U_c	Chittenden dimensionless speed
U_{disc}	disc speed (m.s ⁻¹)
U_e	entrainment velocity (m.s ⁻¹)
V_{coil}	volume of a polymer coil (m ³)
W	external normal applied load (N)

Nomenclature

W_C	Chittenden dimensionless load parameter
w_i	weight fraction of molecules i

Greek letters

α	pressure-viscosity coefficient (GPa ⁻¹)
α^*	reciprocal asymptotic isoviscous pressure coefficient (GPa ⁻¹)
β	Zhang model dimensionless constant
β_{Na}	temperature-viscosity coefficient (K ⁻¹)
$\dot{\gamma}$	shear strain rate (s ⁻¹)
$\dot{\gamma}_{inlet}$	shear strain rate calculated at the contact inlet (s ⁻¹)
η	dynamic viscosity (Pa.s)
η_0	viscosity at low shear stress (Pa.s)
η_∞	viscosity extrapolated to infinite temperature (Pa.s)
$\eta_{experiment}$	experimental viscosity (Pa.S)
η_{model}	calculated viscosity from the considered model (Pa.s)
η_g	viscosity at the glass transition (Pa.s)
η_r	relative viscosity
η_{inlet}	real viscosity calculated at the contact inlet (Pa.s)
η_{real}	real viscosity in the Maxwell model
η_{red}	reduced viscosity (cm ³ .g ⁻¹)
$\eta_{solution}, \eta_{solvent}$	viscosity of the solution or the solvent respectively (Pa.s)
η_{sp}	specific viscosity
$\eta_{sp,inlet}$	specific viscosity calculated at the contact inlet
$[\eta]$	intrinsic viscosity (cm ³ .g ⁻¹)
λ	film thickness ratio
λ_i	incident light wavelength (m)
λ_r	relaxation time (s)
μ	friction coefficient
ν	kinematic viscosity (mm ² .s ⁻¹)
ν_p	Poisson's coefficient
ξ	Flory exponent
ρ	volumetric mass density (g.cm ⁻³)
ρ_0	mass density at atmospheric pressure (g.cm ⁻³)
ρ_f	ratio, or form factor, between the gyration and hydrodynamic radii
ρ_s	mass density of the sinker in the falling body viscometer (g.cm ⁻³)
$\rho(p)$	mass density at the pressure p (g.cm ⁻³)
σ	composite RMS roughness of a couple of materials (nm)
τ	shear stress (kPa)
τ_c	characteristic shear stress (kPa)
ϕ	volume fraction
Ω	applied angular speed

General introduction

Reducing fuel consumption in transportation is a main challenge of the automotive industry, regarding the current context of global warming. All of oil and gas consumptions – including transport, building, industry and production – account for one third of greenhouse gases emissions. Among those, the main contribution is attributed to the rising transportation, which represents almost 40 % of all oil and gas emissions (GIEC sources). New regulations were thus established to tackle this phenomenon. European law requires that the new registered cars do not emit more than an average of 95 grams of CO₂ per kilometer (gCO₂.km⁻¹) by 2021 (GIEC sources). Increasing energy efficiency has thus become essential and led car manufacturers and oil manufacturers to develop new technologies and new products.

The International Energy Agency have evaluated the different key technologies for reduction of CO₂ emissions, in order to limit the global warming to 2 °C above pre-industrial levels by 2050 [29]. In Figure 1, the end-use energy efficiency is expected to present the largest impact (38%). The tribology field could then offer new technical solutions, including coatings, new engines less fuel consuming and new fuel-economy lubricants to reduce the fuel consumption by limiting friction losses. The present work focuses on this last point and how to reduce friction in car engine, while maintaining or improving engines efficiency.

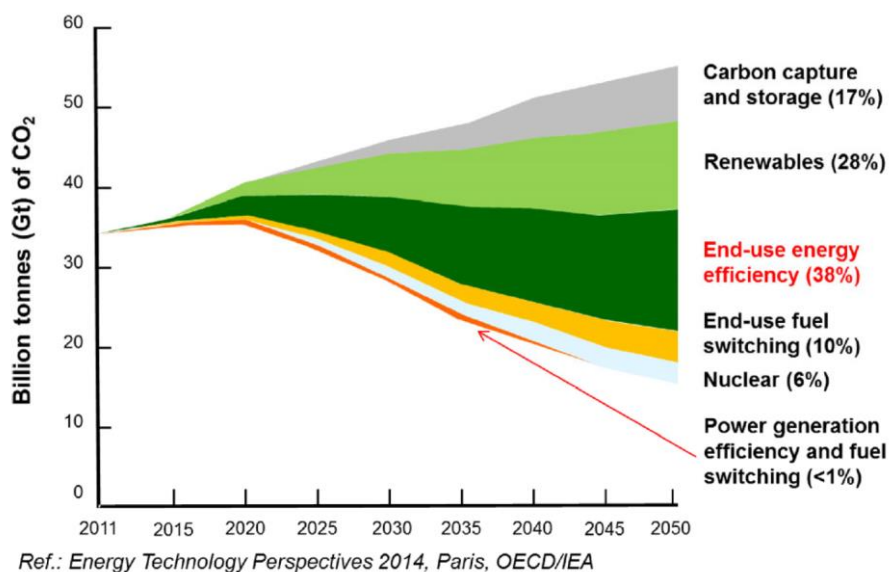


Figure 1: Key technologies for reduction of CO₂ emissions [29]

Over the last decades, several studies have been conducted on the fuel consumption and role of friction in passenger car. Holmberg *et al.* evaluated the global energy consumption due to friction and potential savings in passenger cars [1][2]. In a standard vehicle, only 38% of the fuel energy is actually converted into mechanical power, to overcome air drag (5%) and friction losses (33%). The latter are subdivided into several groups, friction in the engine (11.5%), the transmission system (5%), the tire-road contact (11.5%) and the brakes (5%), (see Figure 2). In total, only 21.5% of the fuel energy is used to move the car. In 2017 [2], Holmberg *et al.* also established that reducing friction and wear in transportation can reduce the global CO₂ emissions by as much as 620 MtCO₂ and result in 180,000 million Euros cost savings in the short term (8 years). In the longer term (15 years), the reduction can reach 1 364 MtCO₂

and the cost savings 400,000 million Euros. The development of high-performance lubricants is thus of main interest to achieve friction reduction in car engines, by maintaining a thin film of lubricant between the surfaces in motion.

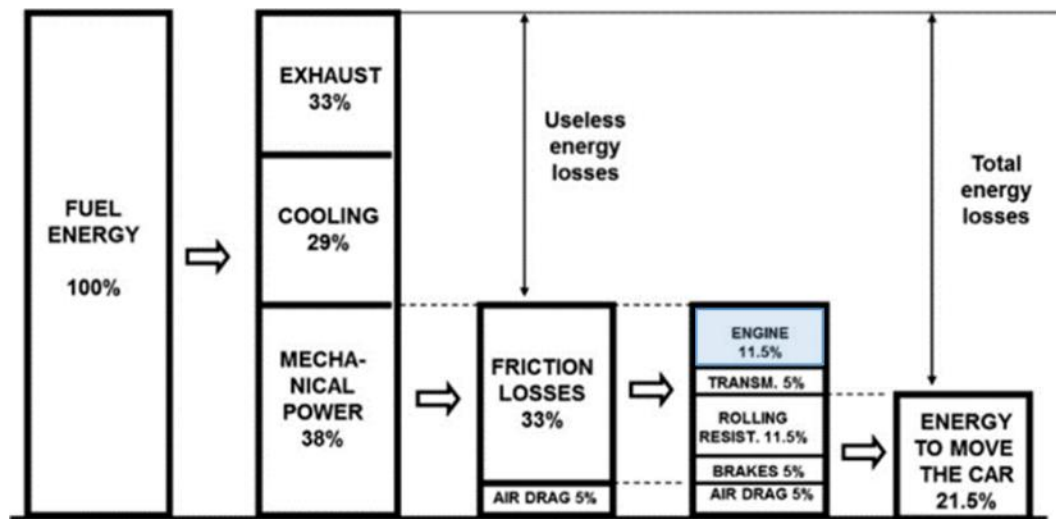


Figure 2: Energy losses in a passenger car, according to Holmberg et al. [1]

Lubricants are complex products composed of base oils and various mix of additives. Refined petroleum base oils have indeed a limited window of ideal conditions which afford optimal lubricity and require thus performance enhancing additives. Moreover, lubricants must be multifunctional as different conditions of temperature, pressure and shear stress are encountered in the diverse mechanical elements of an engine. For instance, temperatures up to 290 °C are reached in the piston-linear segment, whereas really low temperatures are attained under cold weather conditions. Understanding and controlling the lubricant response in realistic engine conditions is thus crucial to design a value-added product.

Lubrication properties are determined relatively by the viscosity of the lubricant, more generally its rheological behavior. The viscosity of a fluid is a measure of its resistance to motion and depends on temperature, pressure and shear stress. Typically, a high viscous media leads to the formation of a thick film between the contact surfaces and support greater loads. However, this film should not be too large to minimize the friction increase and heat dissipation. The viscosity must be thus controlled to meet engine specifications. It may be adjusted by the addition of viscosity index improvers (VIIs), which are high molecular weight polymers. Their function is to reduce the dependency of the lubricant's viscosity on temperature, in order to achieve an acceptable lubrication at high temperature, without experiencing excessive frictional losses at low one. The VIIs impact on the solution rheology is thus of primary interest to control the lubricant properties.

The high temperature, high pressure, high shear stress encountered in engine parts may lead to the elastohydrodynamic lubrication (EHL), a regime that has a strong impact on the lubricant response. This lubrication regime has been widely studied for more than 60 years [3][4]. Progress in quantitative EHL are the results of accurate measurements and predictions of the physical and rheological lubricant properties [5][6], as well as of the successful comparisons [6][7] between predicted and measured film thickness and friction. Therefore, establishing truthful rheological models for polymer-base oil solutions is of main importance to foresee their viscosity in engine conditions. These models can also be included

in elastohydrodynamic (EHD) simulations to predict film thickness without using a full-scale bench test [8] and without having to make measurements in places that are often almost inaccessible. This approach is time and cost saving for oil manufacturers and the present work follows the same approach.

The industrial objective for TOTAL is to obtain tools, such as those presented above, to choose the optimal VII that comply with car manufacturer's requirements. In this context, the scientific objective of this work is to link the molecular scale – impact of the VII structure and chemistry on the lubricant characteristics – to the laboratory scale, by looking at three different research directions:

- A complete rheological study in realistic conditions of temperature, pressure and shear stress for polymer-base oil solutions formulated without other additives. Indeed, it is of main interest to predict the viscosity of a lubricant under specific operating conditions so as to evaluate if the film thickness in the contact meets the required value to avoid direct contact and wear between the rubbing surfaces.
- A physico-chemistry approach to establish the relationship between the molecular properties of the polymer and the rheological response of the modeled lubricant.
- Tribological explorations to establish how rheology, and therefore the molecular structure, impacts the film thickness.

Figure 3 shows the different steps of the scientific approach followed in this work.

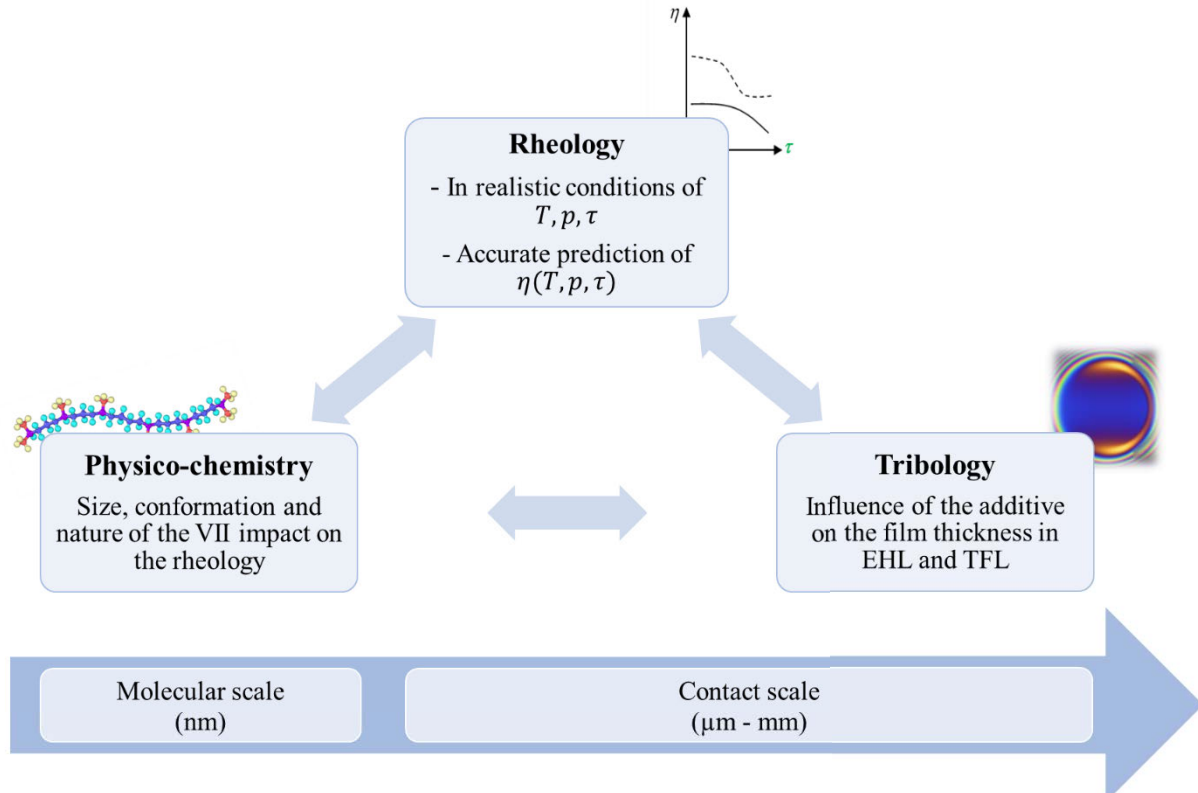


Figure 3: Approach of the study at different scales

Introduction and objectives

Four chapters constitute this thesis. The first one introduces the role and action of Viscosity Index Improvers. The necessary basis on lubrication, lubricants rheology and physico-chemistry of polymer solutions are provided to help readers with limited backgrounds in any of those fields.

The second and third chapter provide the complete pressure rheological study of the simplified lubricants in realistic engine conditions and link their behavior to their molecular structure. The second chapter focuses on the influence of the temperature and pressure on the solution properties at low shear stress and draws the relationship between the polymer chemistry and its rheology.

In chapter III, the shear stress impact on viscosity is investigated and again linked to the molecular structure of the polymers. However, the strong assumptions behind the Carreau-Yasuda model lead us to propose a more appropriate relationship which takes into account the viscoelastic properties of the lubricants.

The final chapter presents the relationship between rheology, physico-chemistry and tribology. Film thickness measurements are carried out in the elastohydrodynamic and thin film regimes. Experimental results are compared with analytical predictions based on the rheological models determined in chapters II and III. A good agreement between predictions and measured film thicknesses in the EHD regime is observed. However, at lower thickness, i.e. in the thin film regime, some polymers show a critical thickness from which it significantly departs from the predictions. Several explanations are considered, among them the non-Newtonian behavior of the lubricants and the adsorption of polymers on the solid bodies.

Lastly, a general conclusion summarizes the results obtained in this work and ends with the prospects for future research.

Chapter I – Literature overview on engine lubrication, polymer solutions and rheology

I.1	Engine lubrication	19
I.1.1	Friction and role of engine lubricants.....	19
I.1.2	Lubrication regimes.....	21
I.2	Nature and composition of engine lubricants	26
I.2.1	Base oils	26
I.2.1.a	<i>Mineral base oils</i>	26
I.2.1.b	<i>Synthetic base oils</i>	29
I.2.2	Additives	30
I.2.3	Viscosity index improvers (VIIs).....	31
I.2.3.a	<i>Mechanism of action and properties affecting VII</i>	31
I.2.3.b	<i>Polymers families and synthesis</i>	32
I.2.4	Distinction between VIIs and thickeners.....	34
I.3	Polymers and polymer solutions	36
I.3.1	Generalities.....	36
I.3.2	Conformation and sizes	36
I.3.2.a	<i>Molecular architecture</i>	36
I.3.2.b	<i>Solvency regimes</i>	38
I.3.2.c	<i>Characteristics sizes</i>	38
I.3.3	Concentration regimes.....	40
I.3.3.a	<i>Critical concentration</i>	40
I.3.3.b	<i>Einstein's law</i>	41
I.4	Rheology of lubricants	42
I.4.1	Generalities and definitions.....	42
I.4.2	Non-Newtonian rheological behavior	43
I.4.3	Rheological models for lubricants.....	45
I.4.3.a	<i>Temperature dependence</i>	45
I.4.3.b	<i>Pressure dependence</i>	46
I.4.3.c	<i>Combined temperature and pressure dependences</i>	47
I.4.3.d	<i>Shear stress dependence</i>	47
I.5	Simplified lubricants	50
I.6	Conclusion.....	52

In the previous introduction, the industrial and scientific contexts were set, as well as the objectives of the thesis. The following chapter aims at providing the necessary technical and scientific background to understand the role and action of polymers on engine lubricant, and to predict their behavior in realistic engine conditions. Basics on engine lubrication, lubricants, physico-chemistry of polymer solutions and rheological models used in this area are thus recalled.

I.1 Engine Lubrication

Lubricants have to ensure the required minimum separation of surfaces in relative motion in order to prevent and limit wear in mechanical systems. A lubricant is generally designed for a given application, hence a wide diversity of lubricants exists to fully perform on all mechanical devices and different operating conditions. The lubricant can be solid (graphite, salt), pasty (grease, wax), gaseous (air) or liquid (mineral and synthetic base oils), as for car engines application.

I.1.1 Friction and role of engine lubricants

Basically, employing a lubricant aims at reducing friction in an engine and extending the lifetime of all its lubricated mechanical parts. This is a complex task as a broad variety of mechanical elements composes car engines, as presented in Figure 4.

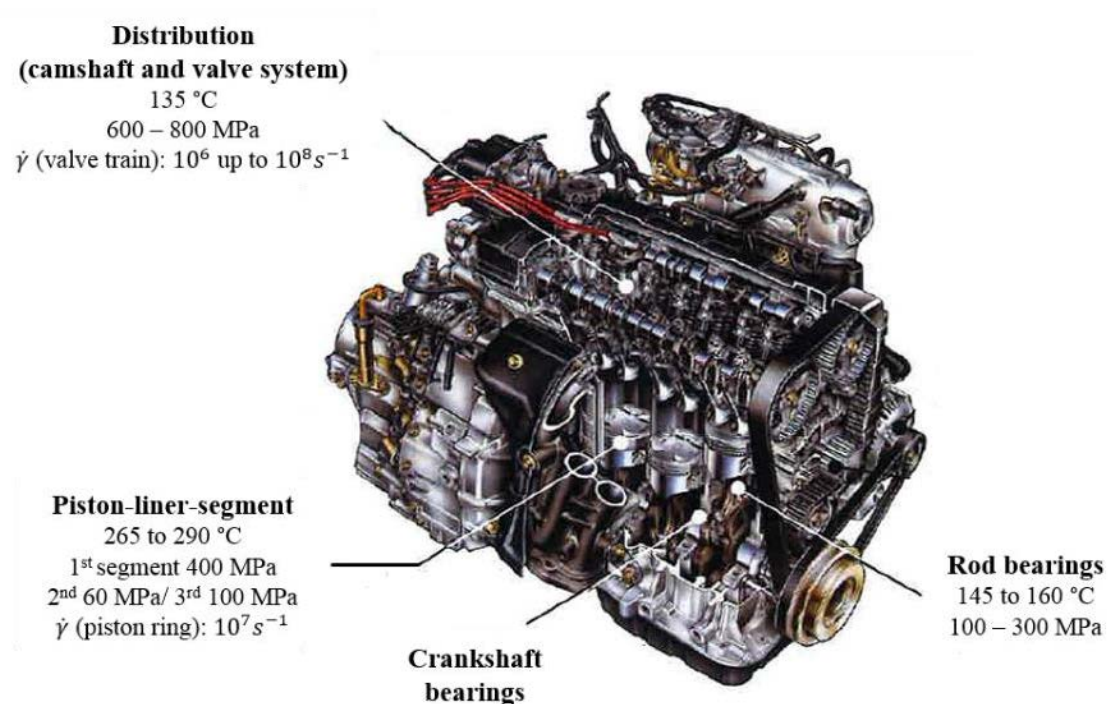


Figure 4: Severe conditions of temperature and pressure in a combustion engine [30]

This highlights the intricacy of a lubricant formulation as the path it follows in the engine is complex which involves a large panel of severe mechanical and thermal stresses. Indeed, the lubrication system provides clean oil at the appropriate temperature and pressure to each part of the engine. The oil is then pumped out from the oil pan thanks to a volumetric pump. The latter adjusts the oil pressure upon the engine rotational speed and the oil viscosity. The lubricant is filtered to avoid any malfunctions, before being dispensed between the different mechanical parts. The excess oil then drains back to the sump, where the heat is being transferred to the surrounding air (see Figure 5).

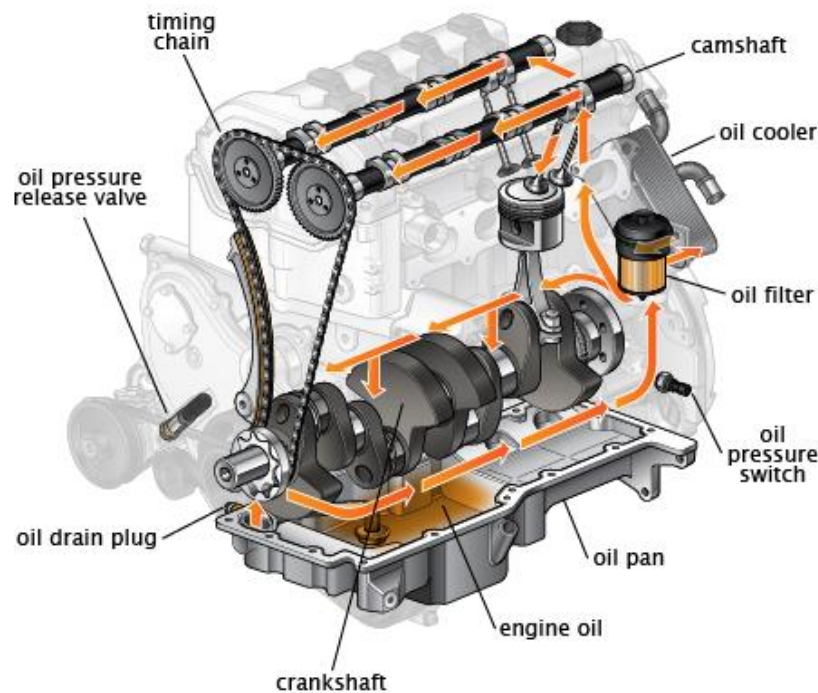


Figure 5: Description of the lubrication system in a combustion engine [31]

Severe conditions of temperature, pressure and shear rate are encountered in these components. For instance, the temperature in the cylinder can reach 290 °C due to the fuel combustion, whereas the pressure can be up to 800 MPa in the camshaft and valve system. In general, a shear strain rate $\dot{\gamma}$ of 10^6 s^{-1} is usually considered in engines. However, much higher shear rates can occur under the piston rings and in the valve train contacts of the engine, where it can reach a maximum of 10^8 s^{-1} [32]. The lubricant properties – especially its viscosity – are thus affected by important variations of temperature, load and shear strain rate.

All along this complex path, the presence of lubricant fulfills several functions.

First, it enables to reduce energy losses due to friction between the contacting surfaces by separating them with a thin film.

Second, it protects the mechanical elements against any kind of degradation (wear and fretting corrosion) by several mechanisms. Indeed, the lubricant cleans surfaces and remove contaminating compounds, including for instance metal debris from wear, impurities from corrosion, dust and soot. In addition, motor oils protect the surfaces against corrosion by neutralizing the unwanted products, such as water.

Third, the lubricant helps to maintain an appropriate temperature in the engine. Indeed, thermal equilibrium of engines is a crucial function of motor oils. The excess heating generated by viscous forces or mechanical frictions between the mechanical parts are evacuated through the oil to the heat exchangers.

Fourth, in some applications, such as piston engines, the oil film between the piston and the cylinder wall must also seal the combustion chamber, avoiding the escape of combustion gases into the crankcase zone. Finally, lubricants may facilitate the engine start-up at any temperature.

Due to the large panel of complex mechanical and thermal stresses involved in an engine, the lubricant experiences the several well-known regimes of lubrication whose main characteristics are briefly described in the next section.

I.1.2 Lubrication regimes

The variety of lubrication regimes found in an engine reveals the challenges that faces the lubricant, as well as the difficulty to optimize its formulation to fulfill all its dedicated roles.

Four distinct situations are observed with respect to the mode of lubrication, also called regimes of lubrication. These regimes are defined according to their range of friction coefficients μ – ratio of the tangential force to the normal force – in function of the variation of a Sommerfeld grouping– the ratio of the viscosity times the speed by the load (Stribeck curve, Figure 6): **boundary**, **mixed**, **elastohydrodynamic (EHD)**, **hydrodynamic (HD)**.

The regimes of lubrication are identified by the mechanism of film formation. At constant load, the film thickness formation is driven by the entrainment velocity. At low speed, the film is insufficiently thick and direct contacts between surface asperities occur. Such contacts are the cause of the high friction characterizing **the boundary regime**. As the speed increases, a thin film of lubricant starts to partially separate the surfaces, leading to the reduction of the friction coefficient. This regime is called **mixed lubrication**. The transition to **elastohydrodynamic lubrication** results in the full separation of the sliding surfaces thanks to the formation of a continuous thin film. The friction coefficient μ reaches there its minimum value. A further speed increase allows the transition in **the hydrodynamic regime**, where both film thickness and friction increase. In full film conditions, the load is fully supported by the lubricant and any solid–solid contact is avoided. In the following sections, each lubrication regime is detailed.

Boundary lubrication is the regime with the most severe contacts in which the load is carried by the surface asperities rather than by the lubricant. The lubricant film is nearly nonexistent, whose thickness is close to or lower than molecular size. Its role under these conditions is limited to introduce additives into the contact.

Mixed lubrication is in between the full film elastohydrodynamic and boundary lubrication regimes [33]. The generated lubricant film is not thick enough to fully separate the contacting bodies, though hydrodynamic effects are significant. Both the lubricant film and direct contacts between asperities support here the load. Therefore, anti-wear and friction improvers are essential to prevent wear and limit the increase in friction.

In the **elastohydrodynamic lubrication (EHL)**, the lubricant film completely separates the surfaces. This regime occurs when the pressure generated in the oil film is sufficiently high to elastically deform the sliding surfaces, typically over 300 MPa. Note that the amplitude of the elastic deformations are here much larger than the film thickness and they strongly impact the geometry of the lubricant film. This regime mostly concerns non-conformal contacts that can be encountered in piston rings, valve train, or rolling-element bearings [5][32]. The maximal pressure encountered in current mechanisms exceeds 1 GPa and can even reach 3 to 4 GPa.

Hydrodynamic lubrication regime (HL) takes place when the generated pressure is relatively low and does not significantly elastically deform the sliding surfaces. This is typically the case of conformal contacts, with pressures of about 1 to 100 MPa. The film thickness is here much larger than the elastic deformations and the average roughness of the contacting surfaces. In car engines, journal bearings are representative of hydrodynamic lubrication, as they present surfaces with low roughness and exhibit conformal contacts [34].

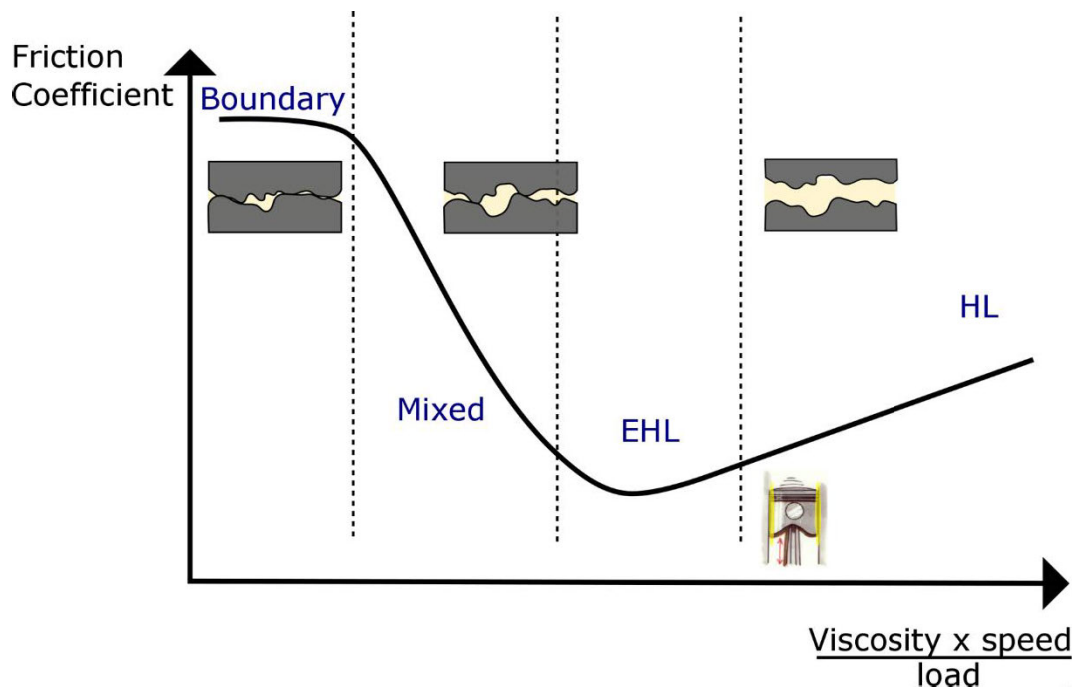


Figure 6: Stribeck curve associated with automotive engine parts

The operation of engine components relies on different lubrication regimes to achieve satisfying performance. Different modes of lubrication can be experienced during a cycle. Piston rings perform from the mixed lubrication to the HD regime, whereas engine bearings operate from EHD to HD regime [39]. Boundary lubrication is conventionally associated in engines with the distribution, mainly composed of camshafts and cam-tappet parts.

Figure 7 depicts the profile of a typical EHD contact, between a couple of solids (1 and 2), whose velocities are respectively U_1 and U_2 . The film thickness in the central zone is called h_c . At the contact inlet, the pressure stays low before rising up to a pressure close to the maximum Hertzian pressure p_H in the central zone, to finally decrease down to atmospheric pressure at the contact outlet [35]. It has been showed that the lubricant flow and the film thickness formation are highly determined by the hydrodynamics phenomena occurring at the contact inlet. The moving surfaces entrain the fluid in the contact, where the gap is drastically reduced due to the applied load. Consequently, a severe compression of the lubricant occurs, leading to an almost exponential increase of the oil viscosity. The piezoviscous fluid can then separate the sliding surfaces, which eliminates wear and reduces friction.

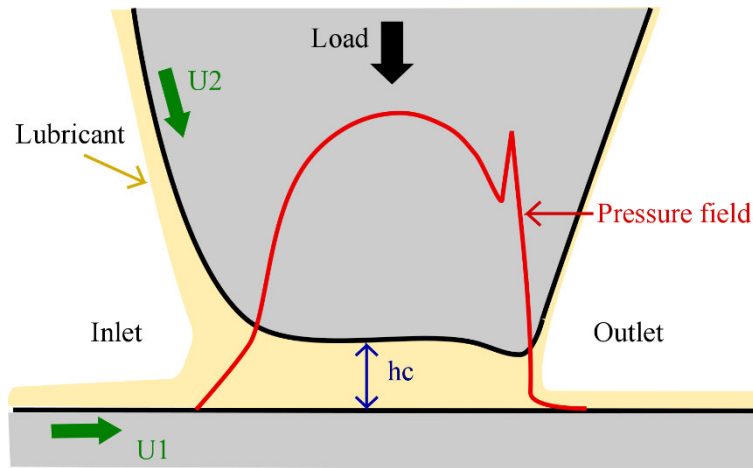


Figure 7: Film thickness and pressure profiles in an EHD contact

In EHL, the accurate measurement of the film thickness h is essential since h controls the separation of the surfaces in relative motion, and consequently the friction. One of the most effective techniques for measuring lubricant film thickness is based on differential colorimetric interferometry (DCI) [24][36][37]. The lubricant film is formed by loading and rolling a steel ball against a glass disc covered by specific layer. Then the lubricant film thickness can be determined by matching the measured light intensity of dynamic interferograms to a calibration curve. Details on this measurement principle are provided in IV.1.1 (p. 99).

Many analytical solutions have been developed to model EHD contacts. The central film thickness of such contacts can be calculated using the Chittenden formula [25][38], which takes into account the geometry, the materials properties, the entrainment velocity and the normal load. This equation is as followed:

$$h_c \propto \eta_0^{0.67} \alpha^{*0.49} W^{-0.073} U_e^{0.67} \quad \text{Eq. (1)}$$

where η_0 is the low shear viscosity at atmospheric pressure, α^* reciprocal asymptotic isoviscous pressure coefficient, U_e is the entrainment speed and W is the applied normal load.

It appears from Eq. (1) that both the viscosity η_0 and the piezoviscous coefficient α^* play a major role as their power exponents are among the highest. The film thickness in the central zone is thus really sensitive to the lubricant rheological properties.

The film thickness ratio λ is a valuable tool which allows the distinction between these different regimes. λ is defined as the ratio of the minimum film thickness h_{min} to σ , the equivalent RMS (root mean square) roughness of the couple of solids (1 and 2) in contact, whose RMS roughness are Rq_1 and Rq_2 respectively [40].

$$\lambda = \frac{h_{min}}{\sigma}$$

Eq. (2)

Where $\sigma = \sqrt{(Rq_1^2 + Rq_2^2)}$

Different lubrication regimes are explored regarding the film thickness ratio (see Table 1). The latter also proved to be a beneficial design concept, as it has helped to evaluate the occurrence of surface interaction in engine elements [32].

$2.5 \leq \lambda$	Full separation in EHD regime
$1.2 \leq \lambda \leq 2.5$	Mixed regime with a thick film trend
$0.6 \leq \lambda \leq 1.2$	Mixed regime
$0.35 \leq \lambda \leq 0.6$	Mixed regime with a boundary trend
$\lambda \leq 0.35$	Boundary or limit lubrication

Table 1: Lubrication regimes in function of the film thickness ratio λ [23]

However, this standard evaluation of the lubrication regime cannot be used to describe the lubrication conditions when the contacting bodies present smooth surfaces [36]. Indeed, considering film thickness of about 5 nm and RMS roughness σ equal to 1 nm would induce a λ of 50. A hydrodynamic lubrication regime would be assumed instead of the correct boundary conditions. Luo and Wen [41] proposed a lubrication map (Figure 8) to precisely differentiate the lubrication regimes, while considering the ratios h/R_a (similar to λ) and h/R_g . The gyration radius R_g is described later in this chapter (I.3.2.c, p. 38) and defines the size of the polymer. The Luo map involves not only the film thickness and surface roughness but also the molecular size. Molecular considerations have indeed been highlighted as essential to understand the phenomenon at low film thickness and the transition between EHL and boundary lubrication, also identified as the **thin film lubrication** regime (TFL).

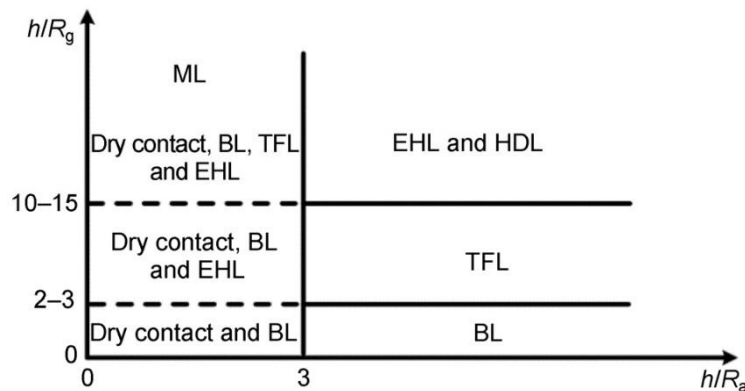


Figure 8: Lubrication map proposed by Luo et al [36]

The tribological properties in TFL are different from those in both the EHL and boundary lubrication regimes. The TFL regime has been indicated to be influenced by both hydrodynamic (including the viscosity) and molecular factors and deviates from classical EHL predictions [42]. TFL models explain these deviations by the presence of adsorbed molecules on the contacting bodies [23][42], which could reduce friction and wear of the sliding surfaces [43]. Transitions between different lubrication regimes at the molecular scale have been investigated by both experimental and theoretical approaches [44][45]. Those studies have verified the assertion that the lubrication regime is dominated by molecular behaviors when the lubricating film is relatively thin. Details on this lubrication regime are provided in *IV.3* (p. 111).

I.2 Nature and composition of engine lubricants

I.2.1 Base oils

Typical automotive lubricants are formulated from about 70 to 80 % of base oil and 20 to 30 % of chemical additives. Most functions of the lubricant are guaranteed by the base oil which creates a film between the contacting surfaces to avoid wear and lower friction. Its rheological properties and pour point value must be close to those wanted for the formulated lubricant. The base oil must also help to solubilize additives and maintain them in solution. These additives are employed to improve the base oil properties. Nowadays, one motor oil may be formulated with several base oils qualities (multi-grade oil) and up to fifteen different additives.

Base oils can be of mineral, synthetic or vegetable origins. Only the first two mentioned are currently used in engine lubricants. According to the American Petroleum Institute (API), base oils fall into five groups (see Table 2) [46]. This classification is based on the refining method and base oil's properties – its viscosity index (whose definition is given later in this section), its content of saturates and its sulfur proportion. Saturates and sulfur stand respectively for saturated hydrocarbons and compounds containing sulfur. Groups from I to III are mineral base oils, while Group IV and V are synthetic ones.

Both mineral and synthetic oils are described in the two following sections.

	Base oil category	Saturates (% _{w/w})	Sulfur (% _{w/w})	Viscosity Index (VI)
Mineral	Group I (<i>solvent refined</i>)	< 90	> 0.03	$80 \leq VI < 120$
	Group II (<i>hydrotreated</i>)	≥ 90	≤ 0.03	$80 \leq VI < 120$
	Group III (<i>hydrocracked</i>)	≥ 90	≤ 0.03	$120 \leq VI$
Synthetic	Group IV	PAO (polyalphaolefin) synthetic lubricants		
	Group V	All other base oils (esters, polyalkylene glycol ...)		

Table 2: API classification of base oils [47]

I.2.1.a Mineral base oils

Mineral base oils result from refining treatments of distilled crude oils which consist of intricate mixtures of hydrocarbons, along with a small amount of other organic compounds like sulfur and oxygen [48]. The hydrocarbons in pure petroleum are mostly paraffins, naphthenes and various aromatic hydrocarbons.

Paraffins are either linear saturated hydrocarbons (n-paraffins) or branched alkanes (iso-paraffins). The viscosity of n-paraffins tends to be higher than the one of iso-paraffins of similar molecular weight. Their length can be as high as 60 carbons, even though it is more likely to be between 15 and 40 carbons in current oils [48].

Naphthenes are saturated cyclic hydrocarbon of 5 carbons per cycle (cyclopentane) and of 6 carbons per cycle (cyclohexane), and are usually branched. Cyclopentane offers a better viscosity index/pour point compromise rather than the cyclohexane [48].

Aromatics are cyclic, stable, planar molecules with conjugated double bonds. They mainly derive from benzene ring (1 cycle of 6 carbons) and other polyacene (linearly fused benzene rings). Aromatics present poor properties for lubrication purpose and are strongly toxic and mutagenic. Hence they are not welcome in base oils, even though their solvency power is high.

Due to the predominance of base oils in lubricants, several critical properties are thus monitored and are directly influenced by the hydrocarbons present in crude oil (see Table 3).

The **pour point** of a base oil is the temperature at which the lubricant becomes semi solid and loses its flowing capacity. The lowest pour point is desired for lubricant applications since the viscosity increases very sharply below such temperature due to the crystallization of paraffins, resulting in a laborious pumpability of the lubricant at colder temperatures.

The **oxidation stability** is the property of a chemical to resist to oxygen action at high temperature. The highest stability is sought since oxidation alters the original properties of base oils.

The **solvency power** evaluates the oil capacity to dissolve chemicals. High solvency power are desired for the lubricant formulation to dissolve lubricant additives and contaminants, such as wear impurities, for ensuring cleanliness of the lubricant.

The **compatibility with elastomers** is also required in order to avoid any damage of elastomeric seals.

Another essential property is **the viscosity index (VI)**, a standard value quantifying the viscosity variations upon temperature, whose formula is found below [49].

$$VI = 100 \frac{L - U}{L - H} \quad \text{Eq. (3)}$$

where U is the kinematic viscosity at 40°C of the oil whose VI is to be calculated, L and H are the kinematic viscosities at 40°C of two reference oils chosen to have the same kinematic viscosity at 100°C as the oil under study, and have VIs respectively equal to 0 and 100 (see Figure 9).

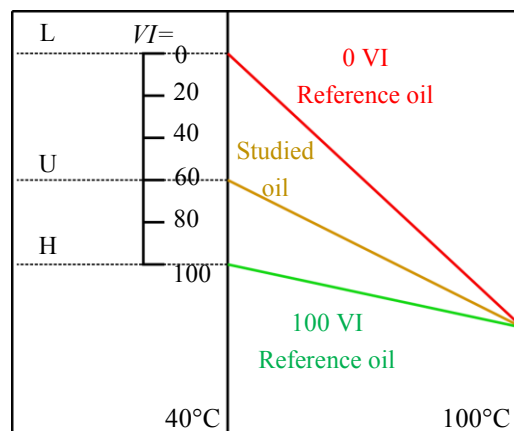


Figure 9: Viscosity Index determination [10]

The VI is a standard tool using reference oils different from the studied base oil. The lower the VI, the higher the viscosity variation upon temperature. Within the framework of automotive lubricant applications, high VI fluids are sought as smaller viscosity variations are required to the good efficiency of the lubricant across a wide range of temperatures. Deterioration of engine parts are thus avoided during cold start while the viscosity at high temperature still enables to separate the solid surfaces in contact.

Refining treatments set apart the desired components from others to obtain a base oil of a preferential API group [48]. The simplified steps for each group are detailed in Figure 10 below. Group III base oil presents the highest grade of these refining treatments, since oils from this group are fully produced by hydrocracking, which makes them purer. These chemical processes, along with the crude oil origins, affect the base oils properties. To begin with, the level of paraffin or naphthenes may vary. Base oils may then be either “paraffinic like base oil” or “naphthenic like base oil” [50]. The first category presents higher level of paraffins (60 to 70 %), less naphthenes (25 to 30 %) and aromatics (5 to 9 %). The second category is typically composed of 50 to 60 % of paraffins, 28 to 36 % of naphthenes, and 7 to 14 % of aromatics. “Paraffinic like base oils” prevail in motor oils, as they are less expensive, less toxic and present a more appropriate behavior at high temperature [50].

In addition, the viscosity index (VI) is also impacted. The solvent extraction removes aromatics, leaving the oil with a high rate of saturated hydrocarbons, which highly raises the VI. Hence, group III base oils exhibit higher VI than other mineral base oils as they contain less aromatics.

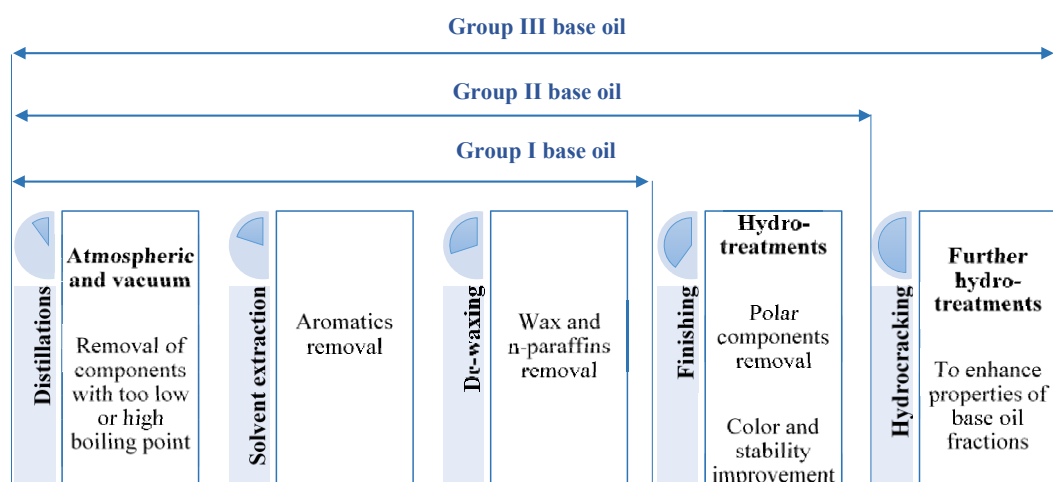


Figure 10: Simplified refining process of mineral base oils

Other properties are also affected by the refining process. The pour point of a base oil is directly related to the hydrocarbon structure and dewaxing step, since the paraffins removal improve the low-temperature properties of base oil (see Table 3). The proportion of the different types of hydrocarbons is also a crucial factor for the oxidation stability. Paraffins and naphthenes present excellent oxidation stability whether they are alongside antioxidants. Solvent extractions and hydrotreatments are thus decisive for base oils from group I and II.

I.2.1.b Synthetic base oils

Synthetic base oils result from a series of chemical reactions and are parts of API groups IV and V. The most common synthesis processes include polymerization, polycondensation and esterification.

Many synthetic oils are available and may be divided into three groups:

- **Hydrocarbons** including polyalphaolefin (PAO), polybutene, alkylated aromatics (dialkylbenzene DAB),
- **Oxygenated like esters** such as diesters, polyol esters, polyesters,
- **Others synthetic oils**, for instance silicones, polyglycols, borate ester, perfluoroethers...

Their composition is close to the one of mineral base oils. However, synthetic base oils are composed of identical molecules whose molecular structures and weights are controlled, while compounds of mineral base oils are not. Physical and chemical properties of synthetic base oils are thus more uniform, predictable and usually more interesting than those of mineral base oils. Indeed, synthetic oils have an elevated VI and a high oxidation stability, even though they are generally more expensive. Polyalphaolefins (PAO) are employed for the same applications as mineral base oils and are among the most used synthetic hydrocarbons. These products are made of iso-paraffins only, without any impurities or aromatics. Their nonpolar nature is the reason of their poor solvency power, a crucial drawback then for solubilizing additives. However, their superior functional properties (see Table 3) still make them a top choice for lubricants in engine applications.

	Paraffins		Naphthenes	Aromatics	PAO
	n-paraffin	iso-paraffin			
Chemical structure					-
Pour point (°C)	-19 to -8		-45 to -20	variable	-73 to -20
Viscosity index (VI)	high ~100		low $0 \leq VI < 60$	variable	very high $120 \leq VI$
Oxydation stability	high		intermediate	low	high
Solvency power	low		high	very high	low
Compatibility with elastomers	high		intermediate	low	low

Table 3: Chemical and physical properties of mineral and synthetic (PAO) oils components

The choice of a base oil influences the inherent properties of a lubricant, as well as the additives action. The additives selection is thus closely related to the base oil they are mixed with.

I.2.2 Additives

Additives are chemical compounds (organic, mineral or organometallic) introduced in the formulation of engine lubricants, as required by specifications given by automotive manufacturer. They enhance the base oil properties and even add specific ones, or annihilate unwelcome effects of additives or the base oil itself. Additives are usually supplied as a package in which several families of chemicals are distinguished [50]. They may form up to 20 % in volume of an engine lubricants. The different additives encountered in motor oils are briefly depicted in this section.

One of the major challenges of engine lubricant is to ensure the cleanliness of surfaces and lubrication circuit by getting rid of undesirable compounds, such as soots, sludges or particles from oxidation reactions. Additives called “stabilizers” and “deposit control agents” are thus needed [51][52].

Detergents are added to clean the warmest parts of an engine (pistons, turbine bearings) by preventing the adhesion of unwanted materials on hot surfaces. Typical detergents are calcium or magnesium salts, whose pH is basic or neutral to neutralize acid waste from the combustion or lubricant decomposition.

Dispersants ensure the protection of engine cold parts by solubilizing and keeping impurities in suspension to prevent agglomeration. These ashless dispersants are amphiphilic chemicals, in other words chemical compounds possessing both hydrophilic (water-loving, polar) and hydrophobic (fat-loving) properties. Physical bonds are created between the impurity and the polar head of the dispersant, while the lipophilic chain insures the solubility. The main dispersants are succinimides and succinic esters.

Anti-oxidants enhance the oxidation stability of the lubricant, and thus extend the engine lifetime. They perform differently according to their chemical structure. Phenols and aromatic amines are free-radical inhibitors, which prevent the oxidation initiation, while zinc dialkyldithiophosphates, ZDDP, degrade products like peroxides.

Anti-rust and **anti-corrosion** must protect respectively ferrous metal parts from the attack of water and oxygen, and non-ferrous metals against acid corrosion coming from combustion gases. These polar additives adsorb on the surfaces in order to prevent oxygen to access the metal beneath and also neutralize acids. These additives have usually other functions, like detergent or dispersant. Organometallic detergents, long chain carboxylic acids and fatty amines are prime candidates.

Anti-foam additives are added to prevent the foaming tendency, due in particular to the presence of detergents and dispersants in formulated motor oils. These additives are mostly silicones derivatives with high molecular weight and surface tension lower than the base oil one. They reduce foaming by decreasing the surface tension at the liquid/air interface, hence avoid the coalescence of air bubbles that form stable foam. Since they are not soluble in the lubricant, their concentration is about a few ppm.

The variety of contacts and operating conditions in engines lead to the different regimes described in section 1.1.2, p.21. The two most severe regimes, namely mixed and boundary lubrication regimes, induce direct contacts between the asperities of the sliding surfaces, resulting in an increased friction and surface damage. **Anti-wear**, **extreme pressure (EP)** additives and **friction modifiers** are thus added to counter these problems [51][52].

Anti-wear additives form a soft protection layer on the contacting surfaces under normal operating conditions [53]. These additives are mostly synthesized from an alcohol with a pentasulfur

phosphorus which leads to zinc salts like ZDDP, zinc dialkyldithiophosphate. Their concentration may vary in the range of 0.5 to 2 %.

The mechanism of action of **extreme pressure (EP)** additives is close to the anti-wear one. However, they are expected to react with a surface when temperature and pressure are so high that anti-wear additives become ineffective. Typical EP molecules are organosulfur or organochloride, which react quickly with bare surfaces. Their concentration is only about a few percent.

Friction modifiers are added to complete the role of previous additives. They reduce friction in mixed and boundary lubrication regimes, thanks to polar compounds which adsorb on the sliding surfaces to form a film whose shear-resistance depends upon its nature. The most efficient products are molybdenum dithiophosphate or dithiocarbamate, potassium triborate, fatty alcohol phosphate, natural fatty acid or solid lubricant (graphite, molybdenum disulfide) [51][52].

Finally, polymeric additives are added to enhance the rheological properties of the base oil. They may either ease the engine start at low temperature (**pour point depressants**) or improve the lubricant's properties at high temperature (**viscosity index improvers**).

Pour point depressants (PPD) slow down the crystallization of n-paraffins present in mineral base oils. PPD adsorb on the growing crystals, preventing then their proliferation. The pour point decreases thus by several tens of Celsius degrees below zero, enabling the lubricant to flow more easily at low temperature. Chosen chemicals are polymethacrylates of low molecular weight.

As their name suggests, **viscosity index improvers (VII)** are added to improve the viscosity index (VI) of the base oil. These additives are the main topic of this thesis and are detailed in the following section.

I.2.3 Viscosity index improvers (VIIs)

As the need grows to have lubricants working under more severe operating conditions, the challenge persists to develop a product providing excellent performance over a large range of temperatures and a long operating time. Viscosity index improvers (VIIs) are more and more added to lubricants to meet the current and future needs of industrial applications. These additives are polymers used to diminish the dependency of the lubricant's viscosity on temperature. Basically, VIIs enable lubricant formulators to widen the temperature operating range of their products. However, the addition of polymers to a base oil can affect its rheological behavior. Two key properties of VIIs need to be balanced for a specific lubricant application: the shear stability and the thickening efficiency. Furthermore, the selection of the proper VII is essential as it may lead to both higher fuel efficiency and longer durability [54].

I.2.3.a Mechanism of action and properties affecting VII

Ideally, engine lubricating oils must have a viscosity low enough at low temperatures to facilitate cold starting and a high enough viscosity at high temperature to ensure its load-bearing capability. The viscosity-temperature dependence must be as low as possible and may be adjusted by the addition of polymers. The usually accepted mechanism of action of a VII is that the polymer coils size increases as the temperature rises to counterbalance the decrease in base oil viscosity [9]. Indeed, a single polymer molecule (VII) in a dilute solution (base oil) is subjected to the interactions of the surrounding solvent. When the solvent quality improves with temperature, the polymeric additive (VII) expands to a larger

size than it would assume at low temperature [55]. This phenomenon is observed at high temperature thanks to a better solubility. Polymer coils swell, which increases the fluid flow resistance and the raise of viscosity. At lower temperatures, the polymer molecules contracts and look like globules. Thus, the viscosity is low as polymer chains interact much less with the solvent. The viscosity response to temperature changes of a VII solution is both nonlinear and reversible. Figure 11 illustrates the coil expansion, which has been extensively studied over the years [19][56][57].

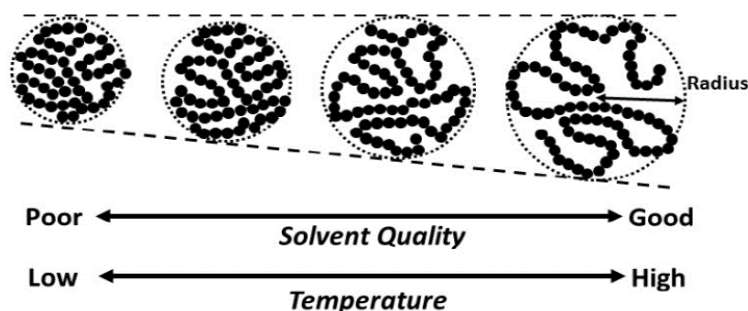


Figure 11: Schematic coil expansion model to explain viscosity index improvement by polymers [19]

This thickening effect is affected by the diverse conditions encountered by lubricants in engines: oxidation, temperature or mechanical stress are among the more important. It has to be noted that VIIs, made from fully saturated hydrocarbon polymers, exhibit only minimal oxidation during use and thus fulfill the oxidation stability required for efficient lubrication performances [54]. As for mechanical stress on VII, shear stability is an important criterion that determines the VII suitability in a lubricant formulation. After a long duration in operation, the viscosity drops and causes surfaces contacts. More shear-stable lubricants with the lowest molecular weight are targeted. However, for a given type of VII, the thickening effect described on Figure 11 increases with the molecular weight. An effective compromise between thickening efficiency and shear stability can be achieved by using VIIs with narrow molecular weight distributions [54].

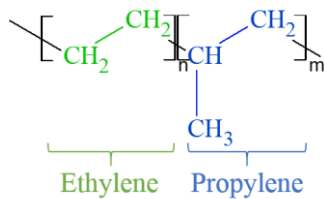
VIIs find major use in multigrade engine oils and transmission fluids [55]. Lubricants called “multigrade” are defined with both “a low temperature grade” and “a high temperature grade”. A grade is a number corresponding to a range of viscosities, determined according to standards. This enables one type of oil to be used throughout the year. The SAE (Society of Automotive Engineers) designation for multi-grade oils includes two viscosity grades. For instance, in the denomination “0W-20”, W” is used for “winter” and the number “0” stands for the cold viscosity grade, while “20” represents the hot viscosity grade. Multigrade oils formulated with VIIs maintain the viscosity above a critical value under high engine shear at high temperatures, while allowing oil pumpability at low temperatures [58].

I.2.3.b Polymers families and synthesis

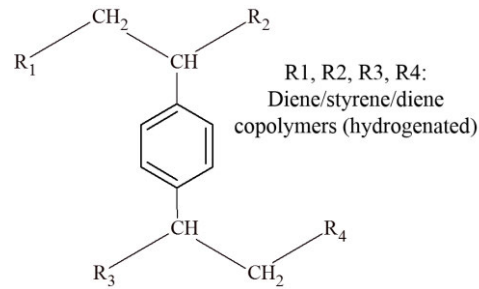
Viscosity index improvers (VIIs) belong to several families of polymers [59], whose structures are described in Figure 12 for the polymers used in this work.

The first family of polymers is composed of hydrocarbon polymers, including polyisobutenes (PIB), **olefin copolymers (OCP)** and **hydrogenated diene-styrene copolymers**, which can include either **butadiene (PBSH)** or **isoprene (PISH)** as the diene. OCPs are of the most popular type, followed by PISHs. PIBs were among the first VIIs used in engine lubricants, which is no longer true due to their high thickening effect at low temperatures.

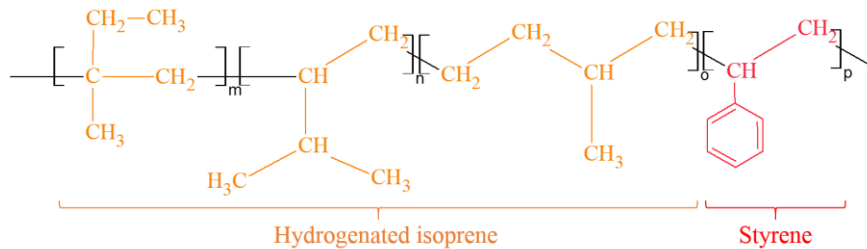
Olefin copolymers (OCPs) are mostly obtained by the copolymerization of ethylene and propylene, using homogenous Ziegler-Natta catalysts. These latter are usually based on complexes of titanium or vanadium, in combination with a different organoaluminium cocatalyst. The most common catalyst is composed of an aluminium alkyl halide with a soluble vanadium component [60]. Their molecular weight M_w can be in the range from 50 000 to 200 000 g/mol, with a low polydispersity. Furthermore, the ratio of ethylene/propylene is a crucial criterion for OCP. Indeed, high ethylene content OCPs provide better thickening efficiency but because of the inherent crystallinity of the polymer, it can make low-temperature pumpability difficult. A compromise must be found to comply with the given lubricant application [54].



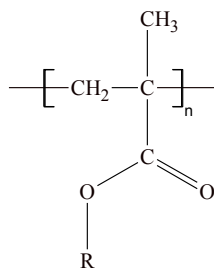
Olefin copolymers (OCP)



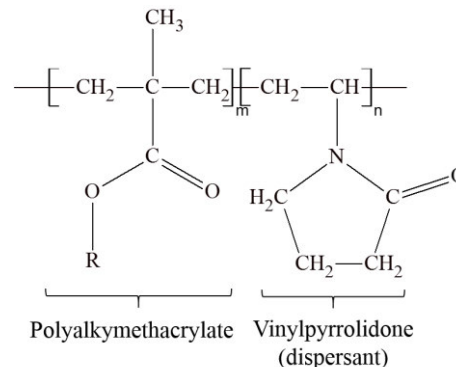
Star copolymers



Polyisoprene-styrene hydrogenated (PISH)



Polyalkylmethacrylate (PAMA)



PAMA with a dispersant function

Figure 12: Chemical structures of viscosity index improvers

Poly-hydrogenated isoprene-styrene copolymers (PISHs) are synthesized by anionic polymerization. This mechanism involves the polymerization of vinyl monomers with strong electronegative groups, such as styrene and isoprene, and is conducted through a carbanion active species. Like all chain-growth polymerizations, it takes place in three steps: chain initiation, chain propagation, and chain termination. Linear block polymers are obtained from an anionic copolymerization of an isoprene (2-methyl-1,3-butadiene) with styrene (vinyl benzene), followed by a hydrogenation. Their molecular weight ranges between 75 000 and 200 000 g/mol. Star polymers are bigger molecules and are also obtained by an anionic reaction between a block copolymer isoprene/styrene/isoprene and divinylbenzene, followed again by a hydrogenation. Their molecular weights lies between 300 000 and 700 000 g/mol [61].

The second family of polymers is composed of polyesters like polyalkylacrylates and **polyalkylmethacrylates (PAMAs)**. Their alkyl chains are rather short, between 1 to 22 carbons atoms, with an average of 12, randomly distributed along the main chain. PAMAs typically used have a low molecular weight, between 70 000 and 150 000 g/mol. However, PAMAs with higher molecular weight (300 000 up to 650 000 g/mol) are present in engine lubricants due to their specific properties at low temperatures. Most polyalkylmethacrylates are obtained by free-radical initiation with peroxides on alkyl methacrylate monomers in mineral base oils [55]. Although this method is important for producing PAMAs in large scale, it is difficult to control the final structure of the polymer, its molecular weight and its distribution. Other methods exist and involve controlled radical polymerization, in particular atom transfer radical polymerization (ATRP). These polymers offer a variety of molecular structures, using different processes and monomers combinations. PAMAs with comb architecture can be obtained by copolymerization of OCP macromonomers and methacrylic ester monomers [62]. PAMAs may also be synthesized with a dispersant function (a nitrogenous polar compound for instance, see Figure 12) to neutralize the black-sludge present in engine [51].

As previously mentioned, the chemistry and structure of the polymer determine the viscosity index improvers properties. The choice of monomers and polymerization techniques provides different types of polymer architectures such as linear, branched, star or comb polymers. By optimizing the molecular weight, the branching length and the crystallization behavior of the polymer, a shear stable and performant viscosity index improvers may be obtained. VIIs are mostly sold diluted in a mineral oil. Their concentration may vary between 40 to 60 % for PAMA, 10 to 15 % for OCP and 5 to 15% for hydrocarbons polymers [51]. Some of these polymers are also available in powder or granular form.

Viscosity index improvers are of main interest for extending the operating temperature domain and for friction reduction in lubricated contact. To understand the operating mode of these different macromolecules, the polymers behavior in solution should be first apprehended.

I.2.4 Distinction between VIIs and thickeners

The desired effect of a viscosity index improver (VII) is to enhance the viscosity index (VI) of the base oil and thus to display variations upon temperature of its thickening power, which must increase at high temperature due to the expansion of the polymer coils. This results in a decrease of the viscosity vs. temperature slope at high temperatures in comparison with the base oil. Other variations of the thickening power specify a thickener (see Figure 13).

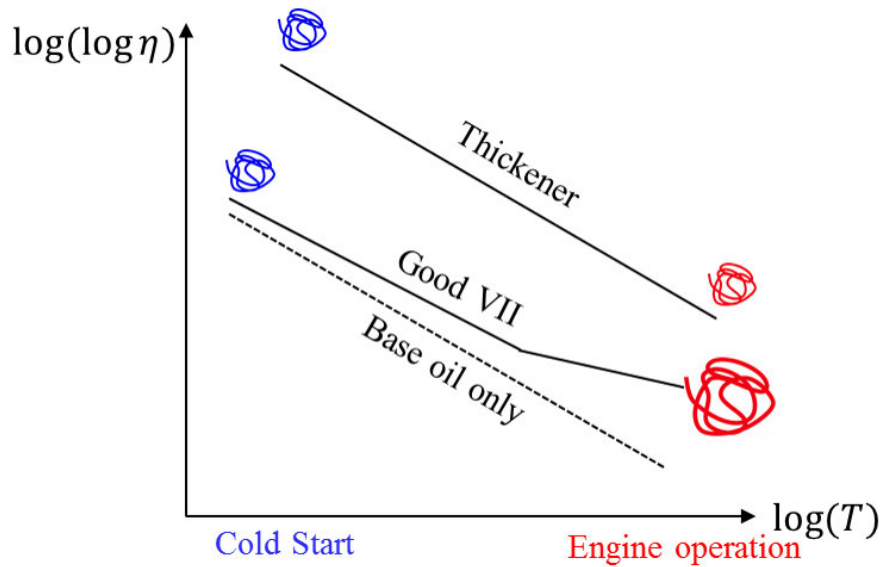


Figure 13: Schematic distinction between a viscosity index improver and a thickener

Although viscosity index (see equation Eq. (3)) is a practical and useful metric for industrial lubricating oils, it does not express the polymer temperature sensitivity and by thus is not the adequate parameter to distinguish VIIs from thickeners. To address this issue, another factor, called the thickening factor Q and shown in equation Eq. (4) may also be considered [9]. This factor quantifies the variations of the polymer thickening power between 40 °C and 100 °C in the base oil and it may be used at different pressures. Indeed, even though information at ambient pressure is imperative, engine lubricants encounter severe conditions in the contacts. It is then of primary interest to know how pressure affects both the VII and thickener properties to properly select lubricants.

$$Q = \frac{\eta_{sp}(100\text{ }^{\circ}\text{C}, p)}{\eta_{sp}(40\text{ }^{\circ}\text{C}, p)} \quad \text{Eq. (4)}$$

Where η_{sp} is the specific viscosity of the polymer solution (defined later on this chapter).

When $Q = 1$, the thickening power of the additive is constant over temperature (within the 40 – 100°C range) at the considered pressure. A thickening factor greater than 1 means that the thickening power is more important at high temperature, which is the desired effect of a VII. When $0 < Q < 1$, the thickening power is less significant at high temperature, which corresponds to the given definition of a thickener here. This factor Q appears thus to be a relevant indicator to quantify the actual performance of the so-called viscosity index improvers. Indeed, no correlation between the viscosity index and the thickening factor Q has been reported, as a VI exceeding 100 may be obtained for a product with a $Q < 1$ [56].

I.3 Polymers and polymer solutions

I.3.1 Generalities

A polymer is a large molecule, also called macromolecule in this manuscript, made of many repeated subunits. Polymers can be either natural, such as DNA, or synthetic, such as the VIIs studied here. Some definitions must be first given to evaluate the polymer properties. One of the most important characteristics of polymer is the molecular weight. The latter can be described in two ways: the number average molar mass M_n , or the weight average molar mass M_w [63][64].

$$M_n = \sum_i n_i M_i = \frac{\sum_i N_i M_i}{\sum_i N_i} \quad \text{Eq. (5)}$$

$$M_w = \sum_i w_i M_i = \frac{\sum_i N_i M_i^2}{\sum_i N_i M_i} \quad \text{Eq. (6)}$$

Where n_i and w_i are respectively the mole fraction and the weight fraction of macromolecule i , whose molecular weight is M_i . N_i is the number of macromolecules i .

Another important parameter is the degree of polymerization, a common means for expressing the length of a macromolecule chain. The latter corresponds to the number of repeated units in a polymer and it is also described either in number DP_n , or in weight N . Usually, increasing the degree of polymerization correlates with a higher melting temperature and a higher mechanical strength. With the molecular mass of one repeated unit of M_0 , the degrees of polymerization are equal to the ratio, in number $DP_n = M_n/M_0$ and in weight $N = M_w/M_0$ [65].

Polymer chains have roughly the same degree of polymerization and molar mass, and there is always a distribution around an average value. The polydispersity index (PDI) is the ratio between the two average molar weights (M_w/M_n) and is always greater or equal to one, as M_w is always superior or equal to M_n . It indicates the distribution of individual molecular masses of the macromolecules in a batch of polymers [66].

I.3.2 Conformation and sizes

The following section provides information on the polymer behavior in solution while being in the diluted regime. No interactions between the polymer molecules are thus considered, but only those between the latter and the solvent.

I.3.2.a Molecular architecture

The molecular architecture of a polymer is an important microstructural feature. Many different architectures can be synthesized (see Figure 14). A linear polymer presents no branches and each monomer is only bonded to two others. A branched polymer is composed of one or more side chains branched randomly or not (i.e. by block) along its main chain. Types of branched polymers include star

polymers, comb polymers, brush polymers, ladder polymers etc. Long branched polymers may connect one to another to create a three-dimensional network, like gels. Star polymers are made of at least three long chains connected at one point, which can be made of one or more molecules making the “core” of the polymer [67]. Other structures of polymers also exist.

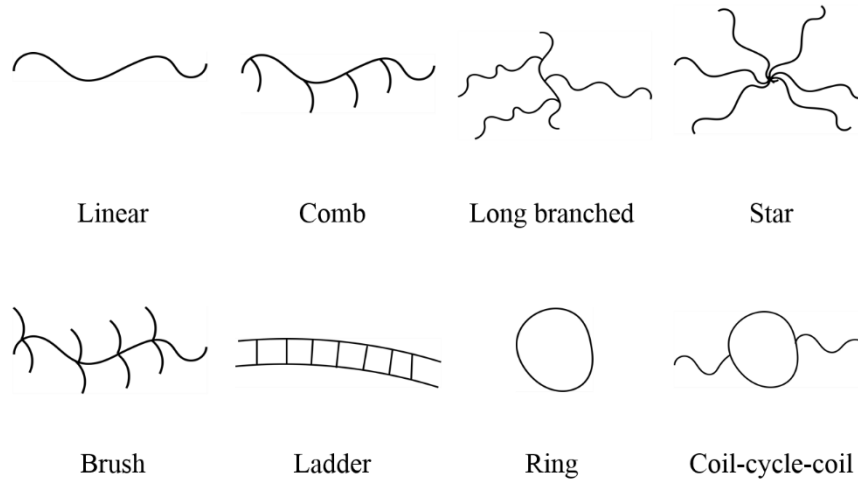


Figure 14: Various polymer architectures

Typical comb polymers are composed of short branches. However, this does not apply to “PAMA comb”. This comb structure combines the chemistry of linear polyolefin and linear PAMA (see Figure 15) [55]. PAMA comb presents then fewer but longer branches of OCP, which significantly improved their viscosity/temperature performance.

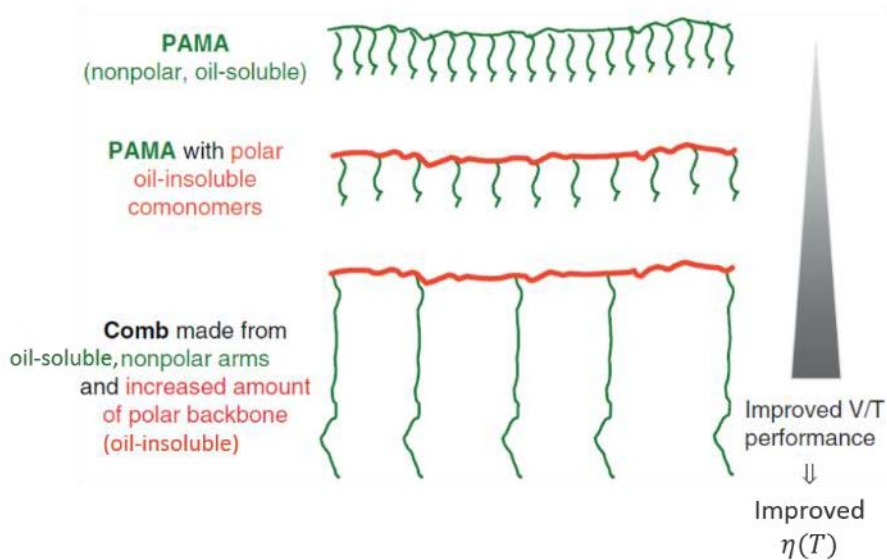


Figure 15: Comb polymer, a combination of PAMA and polyolefin chemistries [55]

Star shape structure may also be achieved by physical auto-associations rather than covalent bonds. This phenomenon is observed for amphiphilic copolymers, having then nonpolar blocks branched to polar ones, which are called micelles. Above the critical micelle concentration (cmc), blocks with no affinity with the solvent tend to interact with each other, in order to optimize their surface tension. Micelles of

various geometries (spherical in most cases) are thus formed and may be associated to star structures with long side chains (see Figure 16).

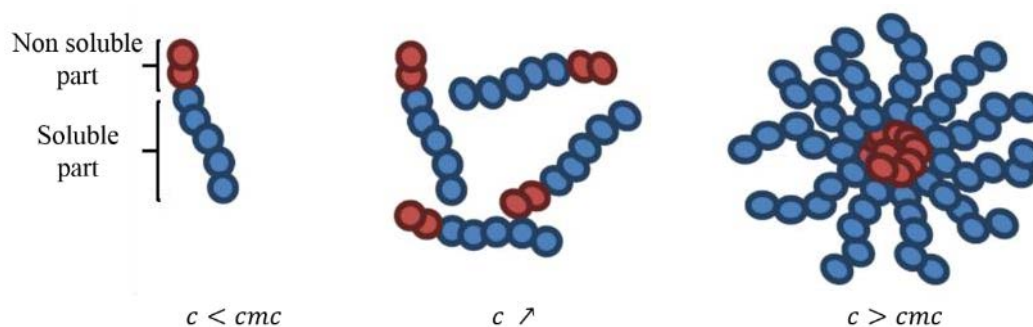


Figure 16: Micelle formation of amphiphilic copolymer [20]

Molecular architecture affects thus many of the polymer physical properties including solution viscosity, solubility in various solvents, glass transition temperature and the size of individual polymer coils in solution.

However, polymers conformation defines their properties in solution rather than their intrinsic structures. Their interaction with the solvent is of primary importance and the solvency capability often called solvent quality is thus defined in the section below.

I.3.2.b Solvency regimes

According to the nature of the interactions between the solvent and the polymer itself, three different regimes often referred as “solvent quality” may be encountered [68].

First, there is the “good solvent” regime, in which intermolecular interactions between the solvent and the polymer are greater than the intramolecular interactions within the polymer chains. The solvent molecules can easily enter within the macromolecules, inducing the swelling of polymer coils.

In the “theta solvent” state, intermolecular and intramolecular interactions are comparable. At the “theta temperature”, polymer coils act like ideal chains, assuming exactly their random walk coil dimensions. The macromolecules are in an unperturbed state. Their size is only sensitive to short range interactions that induce a contraction of the coils [64].

A “bad solvent” is a solvent in which intermolecular interactions between the solvent and the polymer are insignificant compared to the intramolecular ones within the macromolecules. Polymer coils tend then to collapse and are immiscible with the solvent.

I.3.2.c Characteristics sizes

A common way to describe the size of a polymer is the gyration radius R_g . This geometrical definition corresponds to the root mean square distance of the polymer parts from the center of mass of the macromolecule and refers to the distribution of the components of an object around an axis [63].

$$\langle R_g^2 \rangle = \frac{\langle \sum_i m_i r_i^2 \rangle}{\sum_i m_i} \quad \text{Eq. (7)}$$

where i repeated units of mass m_i are located at distances r_i from the center of mass of the molecule.

The radius of gyration offers many advantages. It can be determined experimentally using small angle neutron or static light scattering. Moreover, this radius provides the dimension of polymers of various architectures, such as branched or cyclic polymers.

Another way to calculate the radius of gyration R_g is proposed by Flory [68]. His formula takes into account the quality of the solvent through an exponent ξ , the number of monomers N and the mean monomer size l . The generic equation is written below, whereas details on each solvency conditions are given in Table 4.

$$R_g \propto N^\xi l \quad \text{Eq. (8)}$$

Flory equations must be taken cautiously as they have been established for linear polymers and they only give an estimation of the radius of gyration for branched polymers. The calculated radius should afterwards be multiplied by the characteristic Flory ratio C_∞ , which takes into account the valence angles imposed by the chemical structure.

Isolated macromolecules may be represented as hard spheres of equivalent radius. From geometric considerations, this radius is associated to the gyration radius R_g . The coil volume V_{coil} is thus written as:

$$V_{coil} = \frac{4}{3}\pi R_g^3 \quad \text{Eq. (9)}$$

Another radius exists to describe the size of macromolecules. The effective hydrodynamic radius R_h is defined as the radius of an equivalent hard sphere diffusing at the same rate as the molecule under observation. It actually represents the effective size of the polymer coils within their environment and varies with temperature, pressure and the solvent quality. It can be measured with Dynamic Light Scattering (DLS). Furthermore, the solvent quality can be evaluated by the ratio $\rho_f = R_g/R_h$ called the "form factor", which represents the polymer disposition in the solvent (details in Table 4) [69].

	Good solvent	Theta solvent	Poor solvent
Exponent ξ	0.6	0.5	0.33
R_g	$\propto \frac{1}{\sqrt{6}} N^{0.6} l$	$\propto \frac{1}{\sqrt{7}} N^{0.5} l$	$\propto N^{0.33} l$
ρ_f	1.56	1.24	0.77
Interaction	repulsive	ideal chains	sphere

Table 4: Flory exponent, gyration radius, form factor and nature of the interaction of polymers as a function of the solvent quality

I.3.3 Concentration regimes

Properties of polymer solutions also strongly depend on the concentration of the polymer which has a major impact on the physical phenomena occurring in the solution, and thus on its rheology. Several concentrations regimes exist according to the polymer concentration.

I.3.3.a Critical concentration

A fundamental distinction exists between dilute polymer solutions, where polymer coils are separated and no interactions between them occur, and more concentrated or semi-dilute solutions, where coils start to overlap and interact (see Figure 17). The critical concentration c^* is the concentration at which the coils begin to be densely packed. This threshold is not sharp but more properly defined as a region of crossover between the dilute and semi-dilute regimes [11].

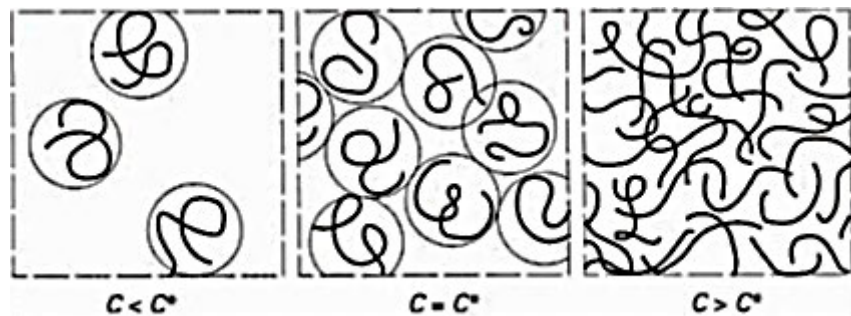


Figure 17: Crossover between dilute and semi-dilute solutions (from left to right: dilute, onset of interact and semi-dilute) [11]

The polymer contribution to the solution rheology depends on the concentration regime. The determination of c^* is thus of primary importance to evaluate the viscosity index improves performance. Several ways exist to determine this critical concentration. It can be derived experimentally from the low shear viscosity of solutions measured at different concentrations. As soon as the regime transition triggers, the specific viscosity exhibits a significant modification of slope upon concentration (see Figure 18). This technique is time consuming as many different solutions have to be prepared and characterized in order to determine accurately c^* .

Another possibility would be to calculate the critical concentration from geometric considerations [70].

$$c^* = \frac{M}{V_{coil}} = \frac{M}{\frac{4}{3}\pi(R_g)^3} \quad \text{Eq. (10)}$$

Where $M = M_w/N_a$ is the molecular mass of one molecule, with N_a the Avogadro constant. V_{coil} is the sphere volume previously described. The critical concentration is calculated for two concentration regimes leading to two solvent qualities (“good solvent” and “theta solvent”), as it affects the gyration radii (see equation Eq. (8) and Table 4, p. 39).

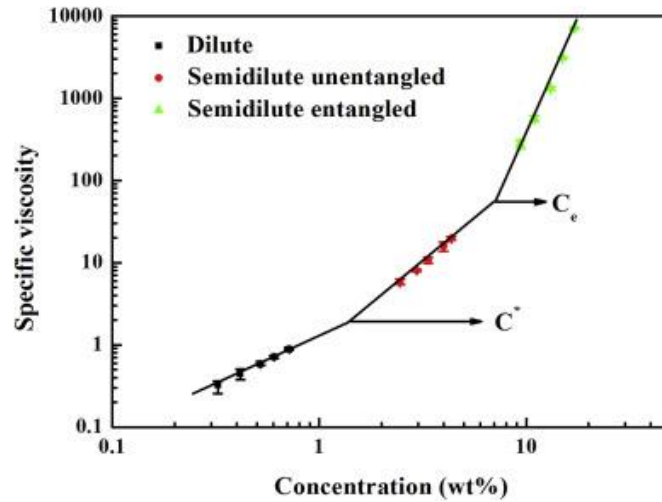


Figure 18: Scaling relationship between specific viscosity and concentration for 6FDA- TFDB PI/DMF solutions at 20 °C [71].

I.3.3.b Einstein's law

The polymer properties quoted through the former sections are essential to apprehend the relationship between the physico-chemistry of polymer solutions and their rheology. However, this link is difficult to establish due to the very different observations scales. Physico-chemistry considerations takes place at the molecular scale and involve elemental analysis, while rheology considerations are at laboratory scale and involve measurements on macroscopic volumes of fluid. From the Kirkwood approximation, it was established that a dilute solution of polymer behaves hydrodynamically like a group of hard spheres of radius R_{coil} [10][11][22]. This allowed ones to directly apply the viscosity law of suspensions established by Einstein which links the viscosity of a suspension of hard spheres to their volume fraction:

$$\eta_{solution} = \eta_{solvent} (1 + 2.5\phi)$$

$$\phi = \frac{c}{M} \frac{4}{3} \pi R_{coil}^3 \quad \text{Eq. (11)}$$

Where $\eta_{solution}$ and $\eta_{solvent}$ are the polymer solution and base oil viscosities, respectively. Here, ϕ is the volume fraction of the hard spheres. The coil radius is considered as the hydrodynamic radius R_h a more effective measure of the size of polymer coils in their environment.

This equation is assumed to be valid at atmospheric pressure. However, Mary *et al.* successfully applied this expression to high pressure in [22]. They validated the rheological approach of Einstein applied on microscopic structures of polymers in solution by combining direct measurements of R_h and calculations derived from Flory's equation.

Rheology appears to be the key to approach the molecular scale properties of lubricants to the oil performance within a contact. The following part presents the main models provided by the literature which have described, over the years, the rheological behavior of lubricants relatively to their main influencing parameters.

I.4 Rheology of lubricants

I.4.1 Generalities and definitions

Viscosity is a major property of a lubricant, closely linked to its ability to reduce friction and a key parameter to explain the generation of film thickness. It is thus of main interest to study the rheological behavior of lubricants.

Rheology is the study of the flow of materials, mostly in the liquid state, to gradual deformation by shear stress that cannot be described by classical fluid mechanics or elasticity equations. It applies to products which present complex microstructures, such as polymers and polymers solutions, as well as other substances for instance gas, suspensions of solid particles and semi-solids displaying a yield stress. Moreover, the rheology of lubricants explores the relationship between the viscosity and the combined influences of shear rate or shear stress, temperature and pressure. Only laminar simple shear flow cases are depicted here.

The dynamic viscosity of a fluid can be defined through the simple shear flow configuration, where a fluid is trapped between two horizontal surfaces, one fixed and one moving at a constant speed u (see Figure 19). If the speed of the top plate is low enough, the fluid particles will move parallel to it, and their speed will vary linearly from zero at the bottom to u at the top, considering that the no-slip condition applies at the boundaries. Each layer of fluid moves parallel to each other, and friction between them will give rise to a force resisting to their relative motion. An external force F_{ext} is therefore required in order to keep the top plate moving at constant speed.

$$F_{ext} = \eta S \frac{u}{y} \quad \text{Eq. (12)}$$

where S is the surface of each plate, u/y the rate of shear deformation, η the dynamic viscosity.

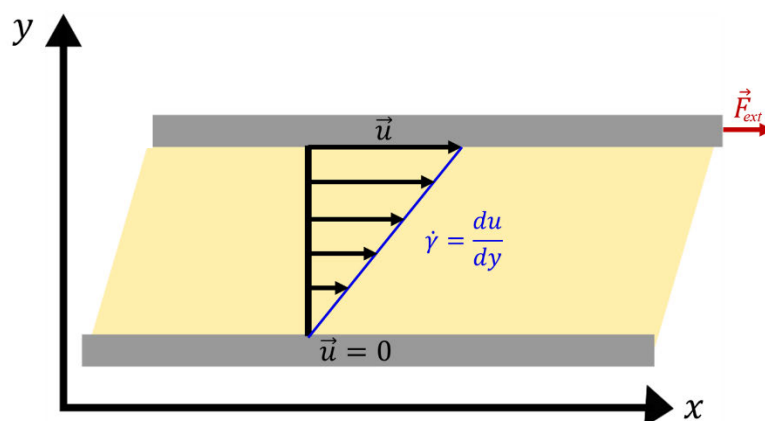


Figure 19: Description of simple shear flow

Newton expressed the viscous forces by the differential equation:

$$\tau = \eta \frac{du}{dy} = \eta \dot{\gamma} \quad \text{Eq. (13)}$$

where $\tau (= F/S)$ is the shear stress, $\dot{\gamma} (= du/dy)$ is the shear strain rate. Main assumptions for this formula are that the flow is moving along parallel lines to x-axis and that the y-axis is in the direction of maximum shear velocity. This equation is general and can be applied whatever the dependence of the velocity with y, for η the apparent viscosity of the flow.

Once the dynamic viscosity has been defined, other viscosity expressions can be used to describe the behavior of polymer in solution. Important formula are listed below:

$$\nu = \frac{\eta}{\rho} \quad \text{Eq. (14)}$$

$$\eta_r = \frac{\eta_{\text{solution}}}{\eta_{\text{solvent}}} \quad \text{Eq. (15)}$$

$$\eta_{sp} = \frac{\eta_{\text{solution}} - \eta_{\text{solvent}}}{\eta_{\text{solvent}}} \quad \text{Eq. (16)}$$

$$\eta_{red} = \frac{\eta_{sp}}{c} = \frac{1}{c} \frac{\eta_{\text{solution}} - \eta_{\text{solvent}}}{\eta_{\text{solvent}}} \quad \text{Eq. (17)}$$

$$[\eta] = \lim_{c \rightarrow 0} \eta_{red} \quad \text{Eq. (18)}$$

where $\nu, \eta_r, \eta_{sp}, \eta_{red}, [\eta], \eta_{\text{solution}}, \eta_{\text{solvent}}$ and c stands respectively for the kinematic viscosity, the relative viscosity, the specific viscosity, the reduced viscosity, the intrinsic viscosity, the solution (polymer and base oil) viscosity, the solvent (base oil) viscosity and the concentration in weight of the polymer.

The intrinsic viscosity represents the volume that one gram of polymer would occupy at infinite dilution, meaning if it was totally isolated from the other polymer coils [72]. This quantity is thus linked to the hydrodynamic radius of a polymer and may be evaluated from the following formula [73].

$$\text{Huggins} \quad \eta_{red} = [\eta] + k_H [\eta]^2 c \quad \text{Eq. (19)}$$

$$\text{Kraemer} \quad \ln(\eta_r) = c[\eta] - k_K [\eta]^2 c^2 \quad \text{Eq. (20)}$$

Here, k_H and k_K stand for the Huggins and Kraemer constants respectively. Even though the intrinsic viscosity is an interesting parameter, it will not be considered further. Indeed, a concentration study would have to be carried out to have direct access to the intrinsic viscosity, which is highly time consuming and was not possible in this work

I.4.2 Non-Newtonian rheological behavior

The Newton's law of viscosity is a constitutive equation and a fundamental law for ideal fluids. It is also an acceptable approximation for most common materials but it can fail with others. A fluid is known to be Newtonian if its viscosity is independent of the applied stress. Typical base oils used in lubricants

formulation belong to this category. However, the polymer addition increases the base oil sensitivity to shear stress, and the fluid can no longer be considered as a Newtonian liquid but as a viscoelastic and/or a shear-thinning material. Viscoelastic materials - such as amorphous polymers, semicrystalline polymers, blood, ligaments - present both viscous and elastic characteristics when enduring deformation or flow. Viscosity is the result of the diffusion of atoms or molecules inside an amorphous product, whereas elasticity is usually the result of bond stretching in an ordered material [74]. A simple model was proposed by Maxwell to describe the behavior of viscoelastic products [75]: it is a mechanical model in which a purely viscous damper and a purely elastic spring are connected in series and give an equivalent viscosity (see Figure 20).

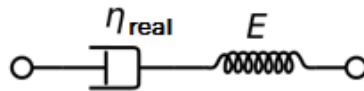


Figure 20: Maxwell model – where η_{real} is the real viscosity and E is the elastic modulus

Formulated lubricants are known to be shear-thinning fluids [76]. While engine oil viscosity is controlled primarily by the viscosity of the base oil, it is however considerably modified by the addition of viscosity index improvers (VIIs). The main molecular chain of these polymers is generally rather flexible: these materials are therefore shear sensitive. Different rheological responses regarding the temperature, pressure and shear stress influences are then expected, according to the VII's structure and conformation and their variations with the above-mentioned parameters [77][78].

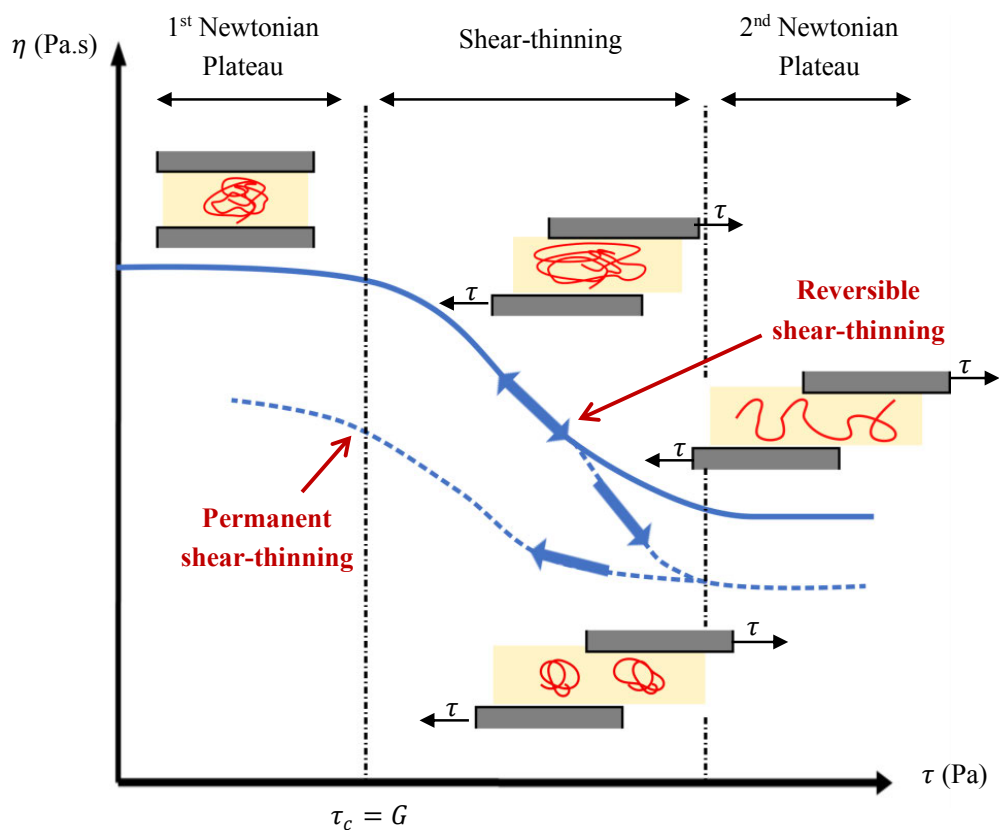


Figure 21: Shear-thinning behavior of lubricants

Flow curves of engine lubricants usually exhibit two Newtonian plateaus – one at low shear stress, the other one at high shear stresses – with the shear-thinning area between these two domains (see Figure 21). The “first Newtonian plateau” is characterized at very low (if no) shear stress solicitation. The polymer coils remain in a steady state and the low shear viscosity η_0 remains constant. Above a critical stress, corresponding to the shear modulus of the fluid, the lubricant’s behavior is no longer Newtonian. The stretching occurring in-between the fluid layers induces distortion and alignment of the macromolecules, which result in a viscosity drop. The macromolecules are aligned in the flow direction at very high shear stress and are eventually fully stretched. The “second plateau” is thus reached and the viscosity is once more stable. This shear-thinning behavior may either be reversible (temporary), or irreversible, if the molecular chains are damaged. In this last case, the viscosity does not recover its initial value at low shear stress.

I.4.3 Rheological models for lubricants

If the rheological characterization of a lubricant is to be useful, it is also of main importance to model the viscosity changes for any arbitrary temperature, pressure and shear stress variations, in conditions close to the engine ones. Hence, these equations must accurately describe the lubricant rheology, with a minimum number of parameters. The latter must preferably have a physical meaning and possibly be determined by independent measurements from the application. Many accurate models exist, still only over a limited range of state variables. In this section, typical rheological equations used for lubrication are depicted, for temperatures between -20 and 150 °C, pressures up to 800 MPa and shear stresses up to 1.5 MPa.

I.4.3.a Temperature dependence

Early developments on the temperature dependence of viscosity came from Andrade [79] and Eyring [80] who applied the Arrhenius equation, based on the thermal activation theory for describing the transition from static molecules to transport properties, leading to the viscosity of liquids:

$$\text{Andrade} \quad \eta_0(T) = \eta_\infty \exp\left(\frac{E_a}{RT}\right) \quad \text{Eq. (21)}$$

Where η_0 is the low shear stress viscosity, η_∞ the viscosity extrapolated to infinite temperature, E_a the thermal activation energy, R the ideal gas constant, and T the temperature. Liquids present an Arrhenius behavior at temperatures near the boiling point and far from the glass transition, where a viscous liquid changes continuously into an amorphous solid with a temperature decrease [81]. This model is thus only relevant for temperature above 100 °C for lubricants, according to [5].

The Vogel, Tamman and Fulcher (VTF) model [12] introduces another constant, more suitable for base oil and lubricant applications [19][82]. The relevance of the VTF model over Arrhenius, for the temperature range studied in this thesis (-20 °C to 150 °C), was shown in [5] for a polyphenyl ether and in [10] for polymer solutions.

$$\text{VTF} \quad \eta_0(T) = \eta_\infty \exp\left(\frac{D_F T_\infty}{T - T_\infty}\right) \quad \text{Eq. (22)}$$

Here, D_F is the fragility parameter and T_∞ the temperature at which the viscosity diverges. D_F quantifies the fragility of the material, the lowest the parameter ($D_F < 20$) the fastest the changes in viscosity with temperature near the glass transition.

An alternative to the VTF equation is the Williams, Landel, Ferry (WLF) formula [83]

$$\text{WLF} \quad \eta_0(T) = \eta_g \exp\left[\ln(10) \frac{-C_1(T - T_g(0))}{C_2 + (T - T_g(0))}\right] \quad \text{Eq. (23)}$$

Where $T_g(0)$ is the glass transition temperature at atmospheric pressure, η_g the viscosity at the glass transition temperature, C_1 and C_2 are the universal WLF parameters. Williams *et al.* advise to limit the application of this model to temperatures between T_g and $T_g + 100^\circ\text{C}$ [83].

I.4.3.b Pressure dependence

As mentioned in *I.1.2*, (p. 21), the pressure rises drastically within the EHD contact and strongly impacts the lubricant viscosity. This pressure-viscosity relationship is thus of main interest since the calculation of film thickness is determined by the viscosity in the inlet zone. Many models have been proposed to depict the lubricants pressure sensitivity and are based on exponential equations (Sargent, 1983; Winer, 1984), parabolic formula (Hersey and Lowdenslager, 1950), or power laws, (McEwen, 1952) [3][65]. One of the most known equation in the lubrication field for the viscosity-pressure relationship is the empirical Barus equation:

$$\text{Barus} \quad \eta_0(p) = \eta_{0,(p=0)} \exp(\alpha p) \quad \text{Eq. (24)}$$

Here, α is the pressure-viscosity coefficient. This exponential expression is rather simple and often provides an analytical solution to theoretical problems. However, since the first tests performed at high pressure on lubricants, important discrepancies have been observed. Indeed, Bridgman reported that the plot of the viscosity logarithm against pressure is concave at moderate pressure, whereas the curve becomes convex at higher values [84][85]. Moreover, this equation considers the pressure-viscosity coefficient α constant with temperature, whereas it has been experimentally proven that it is not [5].

There are several definitions for α , which may depend on the viscosity model chosen. The reciprocal asymptotic isoviscous pressure coefficient α^* was proposed by Block [86]:

$$\alpha^* = \left[\int_0^\infty \frac{\eta_{0,(p=0)}}{\eta_0(p)} dp \right]^{-1} \quad \text{Eq. (25)}$$

This parameter is used to solve EHD problems, such as the Chittenden analytical equation (Eq. (1), p.23). The α^* coefficient can be either calculated with viscosity-pressure models or acquired directly from experimental data.

It was shown that none of the previous viscosity-pressure models are reliable enough for film thickness predictions [87] and cannot be applied over the entire range of temperature and pressure of interest. Moreover, the pressure and temperature dependence of the low shear viscosity η_0 is coupled and must not be treated independently.

I.4.3.c Combined temperature and pressure dependences

The pressure dependence of viscosity cannot be accurately described by any empirical equations. Several models based on the free volume theory provide a fairly correct approach to the natural description of the viscosity dependencies with temperature and pressure. Furthermore, some of their parameters are physically meaningful, outside of the application to viscosity, and can be independently acquired. This section presents the model used in this work and complementary models are described in [5].

The WLF equation modified by Yasutomi *et al.* [13] model the viscosity dependence on both temperature and pressure. This equation was latter modified by Bair *et al.* [14] to improve the prediction of the pressure-viscosity relationship for fluids with high inflection pressures. The new equation provides a more reliable representation of the viscosity-pressure dependency, which also improves the α^* determination [10][14]:

$$\begin{aligned} \text{Modified WLF-} & \quad \eta_0(T, p) = \eta_g \exp \left[\ln 10 \frac{-C_1 (T - T_g(p)) F(p)}{C_2 + (T - T_g(p)) F(p)} \right] \\ \text{Yasutomi} & \quad T_g(p) = T_g(0) + A_1 \ln(1 + A_2 p) \\ & \quad F(p) = (1 + B_1 p)^{B_2} \end{aligned} \quad \text{Eq. (26)}$$

Here, $T_g(p)$ stands for the glass transition temperature at pressure p , η_g is the viscosity at the glass transition, $F(p)$ the dimensionless relative thermal expansion of the free volume. $A_1, A_2, B_1, B_2, C_1, C_2$ are the WLF constants determined by least mean squares regression.

This model may be applied to temperatures up to $T_g + 300$ °C [13]. However, it cannot be applied to fluid undergoing physical transition at very high pressure. This model offers an interesting alternative for EHD applications, since it does not require an equation of state and includes parameters with physical meaning.

I.4.3.d Shear stress dependence

Lubricants are shear sensitive materials which is clearly important for lubrication, as this effect contributes to friction reduction through a shear thinning mechanism at the high shear rates experienced in engine elements.

A power law is commonly used to evaluate the viscosity variations against, either shear rate or shear stress [5].

$$\text{Power law} \quad \eta(\dot{\gamma}) = \eta_0 (\lambda_r \dot{\gamma})^{n-1} \quad \text{Eq. (27)}$$

$$\eta(\tau) = \eta_0 \left(\frac{\tau}{\tau_c} \right)^{1-\frac{1}{n}} \quad \text{Eq. (28)}$$

Here, $\dot{\gamma}$ corresponds to the shear strain rate, τ is the shear stress, $\eta_0(T, p)$ the low shear viscosity, n the power law exponent. λ_r stands for a characteristic time which can be associated to the relaxation time of the fluid, i.e. “a measure of the time scale for reorientation of the molecules or, in the case of polymers, correlated conformational transitions of a couple of backbone bonds (local segmental dynamics)” [88]. It characterizes the time taken by a polymer coil to recover its initial state by releasing its stored energy after being stressed. Here, τ_c is a characteristic stress, which can be associated to the shear modulus G .

Many equations exist to describe the dependence of viscosity upon shear rate or shear stress (Cross [89], Ellis [90]). Among them, the Carreau model [91] is widely used in lubrication, with η_2 standing for the viscosity of the second Newtonian plateau.

$$\text{Carreau} \quad \eta(\dot{\gamma}) = \eta_2 + \frac{\eta_0 - \eta_2}{(1 + (\lambda_r \dot{\gamma})^2)^{\frac{1-n}{2}}} \quad \text{Eq. (29)}$$

This model has been improved many times over the years. In 1981, Yasuda modified the Carreau expression to provide a better determination of the transition from the Newtonian to the power-law regimes by introducing the parameter a [15].

$$\text{Carreau-Yasuda} \quad \eta(\dot{\gamma}) = \eta_2 + \frac{\eta_0 - \eta_2}{(1 + (\lambda_r \dot{\gamma})^a)^{\frac{1-n}{a}}} \quad \text{Eq. (30)}$$

In 2004, Bair proposed the generalized Carreau-Yasuda formula, with a shear stress τ dependence of the viscosity [16]. Presenting the viscosity as a function of shear stress enables to normalize the data and obtain master curves [5].

$$\text{Carreau-Yasuda modified by Bair} \quad \eta(\tau) = \eta_2 + \frac{\eta_0 - \eta_2}{\left(1 + \left(\frac{\tau}{G}\right)^a\right)^{\frac{1-n}{a}}} \quad \text{Eq. (31)}$$

The previous equations can be used with η_2 equals to zero. The Newtonian viscosity at low shear rate η_0 can be determined from the combined temperature-pressure expressions described in 1.4.3.c (p.47) and then, inserted in shear-thinning formula.

In a recent paper [17], Zhang proposed a new approach to describe the shear rate influence on viscosity based on a Maxwell viscoelastic-like response. All existing models consider that only the real part of the complex viscosity– as defined in [17] and which corresponds to viscosity of the first Newtonian

plateau η_0 - changes under the shear stress influence without taking into account that the elastic parameter – thus the elastic shear modulus G – may also change. Zhang [17] explained that the measured viscosity η deviates from the prediction of the linear Maxwell model because of the variations of the elastic parameter and not the variations of viscosity. A linear dependence of the elastic modulus on the shear strain rate, pressure and temperature is thus proposed. The resulting expression is adapted to T , p and $\dot{\gamma}$ influences as shown below:

$$\begin{aligned} \eta(\dot{\gamma}) &= \frac{\eta_0}{\left(1 + \left[\frac{\eta_0 \dot{\gamma}}{2 \cdot G(T, p, \dot{\gamma})}\right]^2\right)} \\ G(T, p, \dot{\gamma}) &= G_0 + \beta \eta_0(T, p) \dot{\gamma} \end{aligned} \quad \text{Eq. (32)}$$

Here, $\dot{\gamma}$ is the shear strain rate, G corresponds to the equivalent shear modulus, G_0 is the equivalent shear modulus at low shear rate and β a dimensionless constant.

Taking into account the variations of the shear modulus is an interesting approach because it induces, without introducing any supplementary parameter, a second plateau which is known to be difficult to achieve in experiments. The linear dependence of G was chosen here because it is the first order of approximation [17]. The maximum elastic deformation is dependent only on the parameter β . The Zhang model only applies though to solutions which show a strong elastic deformation, meaning with an important shear-thinning response. According to the author, parameter β latter should be less than 0.5 to represent a significant viscoelastic behavior.

I.5 Simplified Lubricants

As previously mentioned in I.2.3 (p. 31), VIIs are polymers used to improve the base oil properties and reduce the temperature dependency of the lubricant viscosity, in order to maintain an acceptable lubrication regime at high temperatures, without experiencing excessive friction at low ones.

In this work, binary mixtures of base oil and polymers were considered as model automotive lubricants. All materials were provided by TOTAL and were property of TOTAL. The base oil studied, Yubase 4+, is a hydrocracked mineral base oil from group III (according to API classification), with no aromatics compounds. Six polymers with different chemistry - PAMA (polyalkylmethacrylate), PISH (polyisoprene styrene hydrogenated), OCP (olefin copolymer) - and conformations - comb, star, linear (noted -C, -S and -L) - were studied and details can be found in Table 5. OCPs have different annotations, where OCP-HE and OCP-LE stands respectively for high ethylene content OCP and low ethylene content OCP. The mass average molar mass M_w and polydispersity index were obtained through quadruple detection size exclusion chromatography (SEC) (see Table 5).

Commercial liquid version products were used, meaning that all polymers were previously mixed with an extender oil, with the exception of OCP-HE, only sold as a dry product. Extenders oils have chemical properties close to that of the mineral base oil, apart from the PAMA whose extender oils are a mix of group I and group III base oils. However, their influence on the polymer solutions is not considered. This selection of raw materials allows the comparison between the different structures while providing base oil-polymer solutions close to commercial formulations.

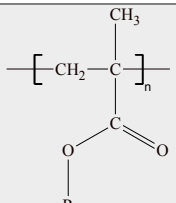
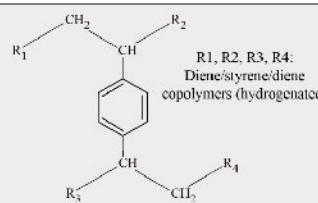
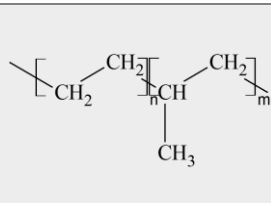
Polymer	PAMA		PISH		OCP	
Chemical Formula						
Name	PAMA-C	PAMA-L	PISH-S	PISH-L	OCP-HE	OCP-LE
Molecular structure	Comb	Linear	Star	Linear	Linear	Linear
M_w (g.mol⁻¹)	678 800	332 000	689 600	113 000	86 700	87 300
Polydispersity	3.2	2.3	2.2	1.6	1.1	1.1
Concentration of active ingredient (%_{w/w})	3.36	4.67	1.18	1.49	1.19	1.28

Table 5: Main characteristics of the polymers studied in this work

The PAMA-L is considered as a linear polymer, even though it presents side chains made of C₁₂, C₁₈, C₁₆ and C₁₄ in decreasing percentage of the total side chain. This polymer also includes a polar dispersant function. The PAMA-C matches the definition given in *I.3.2.a* (p. 36) and presents long olefin copolymer chains. The star-shaped PISH displays a rich styrene core, whereas the linear PISH is a block co-polymer made of 30% in weight of styrene and the rest of isoprene and butadiene. Moreover, the PISH-L is known to form micelles within the solution at the considered concentrations [20]. Both OCPs are considered as linear polymers. The OCP-HE, high ethylene content is formed of 70% in weight of ethylene and 30% in weight of propylene, whereas the low ethylene content OCP, OCP-LE, is equally made in weight of ethylene and propylene.

Precedent studies were carried out with similar products (see C. Mary's thesis [10]), where the final polymer concentration in the mineral base oil was 1.2 %_{w/w} of active ingredient. However in engine lubricants, higher amount of PAMAs have to be introduced in order to obtain sufficiently high viscosities at high temperatures. Hence in this study, all solutions were formulated in such a way as to comply with a HTHS (High Temperature High Shear) viscosity value of 2.6 mPa.s. The HTHS test consists to measure the dynamic viscosity at 150 °C, elevated shear rate (10⁶ s⁻¹) and at atmospheric pressure, according to the ASTM standard D4741 [92]. These specifications are representative of the engine conditions met by the lubricant and help in determining whether the prediction of film thickness gives an acceptable value. All solutions have thus different polymer concentrations, given in Table 5. Both PISHs and OCPs solutions are formulated at similar concentrations, whereas the PAMAs are introduced in larger quantity. Concentration regimes of each solution are detailed further in the manuscript.

The atmospheric pressure and high pressure rheometers used to obtain the rheological behavior of the lubricants studied are depicted in Appendix 1 to Appendix 4.

I.6 Conclusion

Lubricants play an essential role in fuel efficiency and in preventing wear in engines. The lubricants viscosity, and more generally their rheological behavior, appear to have an essential role in the film thickness formation within lubricated contacts and on friction. Throughout this chapter, one kind of additives was highlighted to strongly impact the lubricant rheology: the viscosity index improvers. In order to optimize the formulation process, it is thus of primary importance to accurately predict their behavior in EHD contacts. However, the film thickness can be as low as a few nanometers, which made EHD contacts more sensitive to their environment (surface, roughness, additives) or to thermal effects that may result from large friction. The prediction of film thickness or friction is thus a crucial issue, but nevertheless possible thanks to the consideration of relevant rheological models [71]. These models can be derived from measurements conducted on specific and independent experimental devices.

The second and third chapter provide the complete rheological study of the simplified lubricants in realistic engine conditions and link their behavior to their molecular structure. Chapter II focuses on the influence of temperature and pressure on the solutions properties at low shear stress, from atmospheric pressure up to 800 MPa. Tools, such as the viscosity index and the thickening factor are then used to evaluate the viscosity index improvers performance and distinguish them from thickeners. The structure-properties relationship is finally highlighted thanks to hydrodynamic radii considerations.

In chapter III, the shear stress impact on the viscosity of the simplified lubricants is investigated and again linked to the molecular structure of the polymers. Interestingly, the results underlined some limitations of the Carreau-Yasuda equation. An alternative, the Zhang model, is then proposed.

The last chapter establishes the relationship between the rheology and physico-chemistry of the polymer solutions to their tribological response in EHL and TFL. Film thickness measurements are carried out in EHD conditions and compared with analytical predictions. Combining results from the high pressure rheology and classical EHL analytical equations allowed thus a good evaluation of the film thickness of non-Newtonian solutions but could not explain their behaviors at low film thickness. The TFL regime briefly described in this chapter is finally discussed.

Lastly, a general conclusion summarizes the results discussed in this work and ends with some prospects for future research.

Chapter II - Low-stress rheology of polymer solutions: effect of pressure and temperature

II.1	VII_s against thickeners at atmospheric pressure	55
II.2	Behavior at high pressure.....	58
II.2.1	Temperature and pressure dependence at low shear stress.....	58
II.2.2	Pressure-viscosity coefficients variations against temperature	62
II.3	Pressure influence on the VII properties	63
II.3.1	Comparative study using the reduced viscosity η_{red}	63
II.3.2	Distinction between VII _s and thickeners at high pressure.....	65
II.4	Impact of the molecular structure on the pressure-viscosity dependence	67
II.4.1	Concentration regime and determination of R_h at atmospheric pressure.....	67
II.4.2	Determination of R_h at high pressure using the Einstein's law	69
	<i>II.4.2.a Temperature variations at constant pressure.....</i>	<i>72</i>
	<i>II.4.2.b Pressure variations at constant temperature</i>	<i>74</i>
II.5	Conclusion.....	76

As mentioned in the previous chapter, establishing accurate rheological profiles for simplified lubricants is of main importance to correctly predict film thickness and friction in order to eventually help oil manufacturer in the selection of the optimal viscosity index improvers (VII) to match the engine specifications and enhance performance. The original aspect of this work is to employ two non-commercial high pressure rheometers to study the rheology of polymer solutions at higher pressure than those reached with commercial devices. The effect of temperature, pressure and shear stress on the lubricant viscosity is thus investigated over a broad experimental range, close to real automotive conditions. This chapter focuses on the temperature and high pressure influence on the response of simplified lubricants by providing both experimental measurements and modeling of their rheological behavior. These results added to the considerations of the size variations of polymer in solutions, help to distinguish VIIs from thickeners. Many results detailed in this chapter were published in [93].

II.1 VIIs against thickeners at atmospheric pressure

The temperature dependence at atmospheric pressure of the low shear viscosity η_0 was obtained from measurements carried out on a Physica MCR 301 rheometer (Appendix 1). The temperature was varied from -20 to 150 °C and the shear rate from 0.3 to 3000 s⁻¹ (equivalent to shear stress of about 10⁻² to 10² Pa), where the fluid behavior is Newtonian. Experimental data η_0 are obtained by averaging the viscosity on the first Newtonian plateau. They are fitted to the Vogel-Tamman and Fulcher model (VTF model in the following, reminded below (Eq. (22), p. 46) [12] by the least mean squares method.

$$\text{VTF} \quad \eta_0(T) = \eta_\infty \exp\left(\frac{D_F T_\infty}{T - T_\infty}\right) \quad \text{Eq. (22)}$$

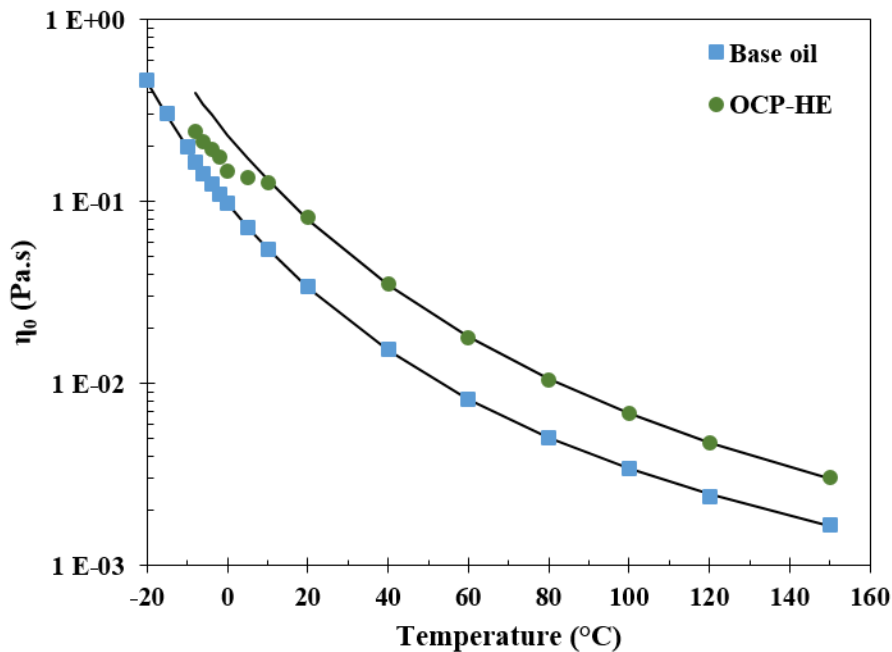


Figure 22: Viscosity of the base oil and the OCP-HE solution at different temperatures and fitted by the VTF equation (plotted as the black line).

The viscosity variation against temperature is plotted in Figure 22 for the base oil and the OCP-HE solution only. The polymer addition clearly thickens the solution and the VTF equation fits the experimental data well for both fluids above 10 °C. A change of state is however noticed for the OCP-HE below this temperature, which is reflected by the experimental viscosity being lower than its predicted value. Among all solutions studied in this work, this phenomenon is only observed for the OCP-HE. It has been shown in [20] that OCPs with high ethylene content (above 57% weight), such as the OCP-HE, undergo crystallization at rather high temperature (about 10 °C). The long ethylene sections are sensitive to the decrease of the solvent quality during cooling. The ethylene chains tend then to order themselves and can co-crystallize with the n-paraffins present in the base oil. This co-crystallization affects the physical properties of the OCP-HE solution, by reducing the viscosity at low temperature [20].

Another representation of the data enables the distinction between VIIs and thickeners, as explained in *I.2.4* (p. 34). For the sake of clarity, results for the base oil and one polymer solution of each family, PAMA-C, PISH-S and OCP-LE, are presented in Figure 23. Again, the thickening effect on the base oil is noticed for each polymer solution. However, their thickening contribution on the considered temperature domain is not the same. The desired effect of a true VII is to present variation of its thickening power (i.e. a viscosity rise relatively to the base oil one), which must increase at high temperature and be visible through a slope change. Figure 23 - a) and b) - brings out the different properties of each polymer family.

The strongest VII effect is noticed for the PAMA-C solution, whose low shear viscosity is close to the base oil's one at low temperature (+ 20 % at 20 °C due to the PAMA-C addition) and greatly rises at high temperature (+112% at 150 °C). This effect is less noticed for the PISH-S solution (rise of 95 % at 20°C and 106 % at 150 °C), even though the latter can still be reckoned as a VII. By contrast, the OCP-LE solution exhibits a typical thickener's behavior, with no significant variation of its thickening power regarding temperature.

The viscosities calculated with the VTF equation are in good agreement with the experimental data, apart from the PAMA-C above 60 °C and the PISH-S above 80 °C. The swelling of the polymer coils leads to an additional increase of the solution viscosity [19] which may explain the reduced slope observed above this temperature. The zoom between 60 °C and 120 °C in Figure 23 b) helps to clearly see this phenomenon. This latter is also slightly noticed for the PISH-S above 80 °C. Other products are not presented here. PISH-L and OCP-HE did not exhibit variations of their thickening power with temperature and are both considered as simple thickeners. The PAMA-L thickens more the solution at high temperature than at low ones, even though no slope change (as those highlighted for the PAMA-C and PISH-S) was observed. This product is thus considered as a weak VII. These results are confirmed by viscosity index (VI) calculations (see Table 6) since the PAMA-C presents the highest VI, whereas the OCPs exhibit the lowest one but still improves the base oil VI.

The VTF model is also applied to determine the glass temperature transition $T_g(0)$ at atmospheric pressure. Typical viscosity for lubricants at the glass transition η_g is presumed to be arbitrarily equal to 10^{12} Pa.s [18]. The regression to the VTF equation was done on a smaller temperature range, below the swelling temperature, for polymer solutions exhibiting a true VII behavior in order to improve the

$T_g(0)$ calculation without being impacted by the properties change at high temperature. The PAMA-C and PISH-S solutions are thus both concerned and the regression was done below 80 °C and 100 °C respectively. Similarly, the VTF regression was done between 10 °C and 150 °C for the OCP-HE solution, due to the solidification observed below 10 °C. Values below this solidification temperature were not considered as the calculated $T_g(0)$ would have been equal to -107.4 °C and thus less pertinent compared to DSC results. All glass transitions temperatures can be found in Table 6.

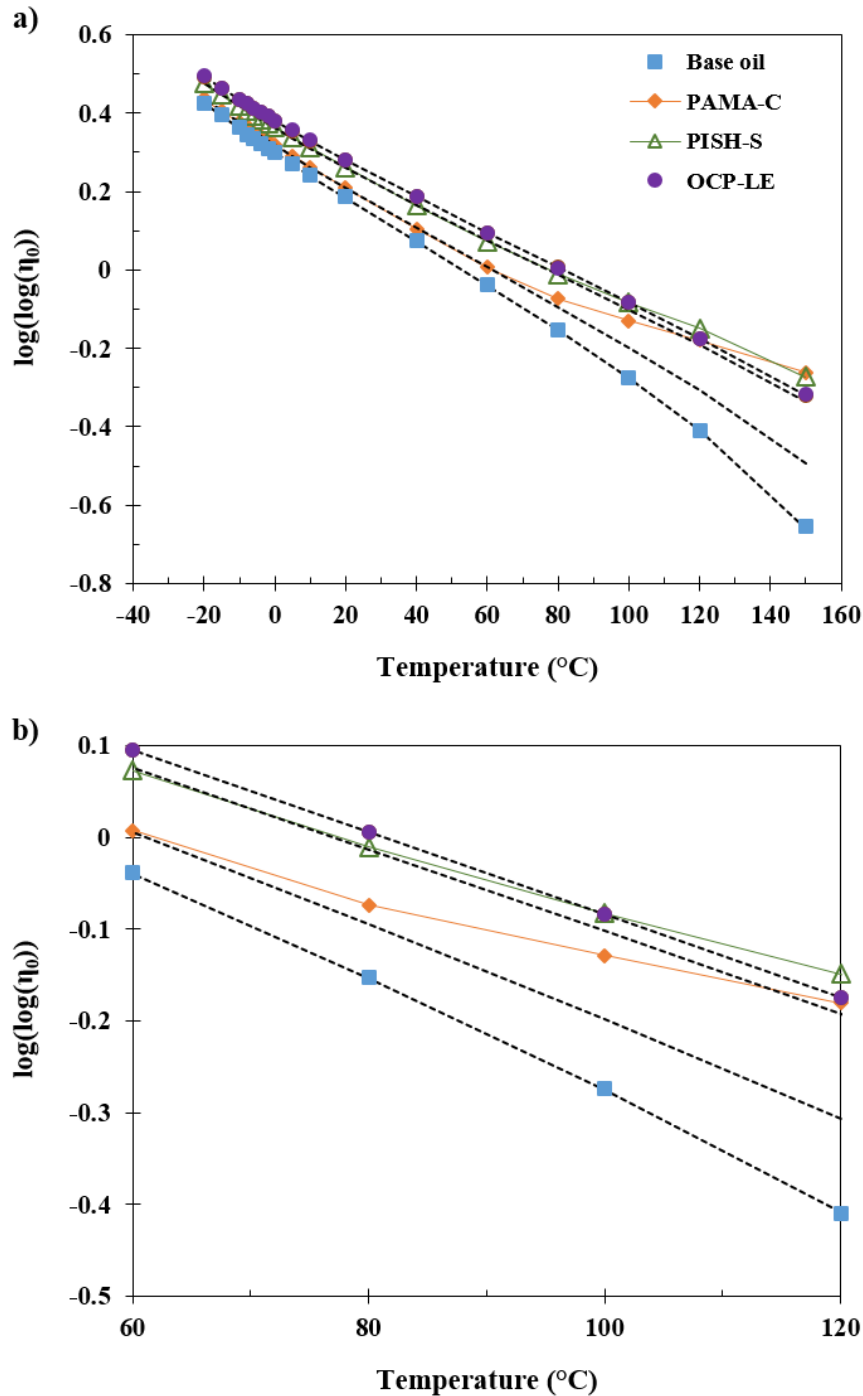


Figure 23: Low shear viscosity, expressed as $\text{Log}(\text{Log}(\eta_0))$ of the base oil, PAMA-C, PISH-S and OCP-LE solutions versus temperature and fitted by the VTF expression plotted as the dotted black line, between - a) 40°C and 160°C and b) zoomed between 60 and 120°C to highlight the slope change of PAMA-C and PISH-S.

Direct measurements using differential scanning calorimetry (DSC, see Appendix 5) analyses were performed and provided by TOTAL on all simplified lubricants and are listed in Table 6, as well as the VI of the solutions. Measured glass transition temperatures of the studied products are close to the ones derived from the VTF model, apart from the OCP-HE solution. The extrapolation to the glass transition of this OCP is thus impacted and must be considered with caution.

Notwithstanding this specific case, the method of calculation of $T_g(0)$ appears to be acceptable for all other solutions. Furthermore, all the $T_g(0)$ of the polymer-thickened base oil solutions are close to the base oil value, regardless the determination process used. This result could have been expected as all solutions contain a small amount of polymers (see concentrations in Table 5 p.50). Moreover, the $T_g(0)$ values found here are similar to those reported for mineral base oils at atmospheric pressure in [13] (about -85 °C).

$T_g(0)$ (°C)	Base oil	PAMA-C	PAMA-L	PISH-S	PISH-L	OCP-HE	OCP-LE
VTF	-90.5	-92.4	-91.5	-91.9	-90.2	-103.2	-92.7
DSC	-95.6	-95.7	-95.0	-95.3	-94.8	-94.6	-94.3
VI	148	306	257	235	200	190	187

Table 6: Extrapolated (from the VTF model) and measured (from DSC) glass transition temperatures at atmospheric pressure with the Viscosity index (VI, see Figure 9) of all solutions

The rheological study at atmospheric pressure is the first step to assess the VIIs efficiency. However, the rheological investigation under representative conditions of pressure is necessary to fully understand how these additives behave in realistic conditions.

II.2 Behavior at high pressure

II.2.1 Temperature and pressure dependence at low shear stress

Series of tests were carried out on the high pressure viscometer (depicted in Appendix 3) to measure the pressure-viscosity dependence of simplified lubricants over a wide range of pressure up to 800 MPa. Temperatures was varied from 40 to 120 °C and shear stresses measured between 1.5 and 70 Pa. The low shear viscosity η_0 of the base oil is plotted against pressure in semi-log scales in Figure 24. The base oil viscosity appears to highly increase, by three orders of magnitude from ambient pressure up to 800 MPa. The compressibility indeed reduces the free volume within the base oil, leading then to higher friction between the laminar layers of fluid, which explains the rise of viscosity. Similar temperature-pressure-viscosity dependence are observed for all solutions, as can be seen in Appendix 6 and Table 7.

Experimental data were fitted by the modified WLF-Yasutomi [13](WLF model in the following), Eq. (26) previously described in *I.4.3.c* (p. 47). This equation, whose expression is reminded below, is considered for the calculations of viscosity, pressure-viscosity coefficients and hydrodynamic radii. The latter are impacted by the model uncertainty but still give accurate tendencies.

$$\begin{aligned}
 \text{Modified WLF-} & \quad \eta_0(T, p) = \eta_g \exp \left[\ln 10 \frac{-C_1 (T - T_g(p)) F(p)}{C_2 + (T - T_g(p)) F(p)} \right] \\
 \text{Yasutomi} & \quad T_g(p) = T_g(0) + A_1 \ln(1 + A_2 p) \\
 & \quad F(p) = (1 + B_1 p)^{B_2}
 \end{aligned}
 \tag{Eq. (26)}$$

The model fitting to the experimental data is evaluated by the relative root mean square deviation (*rms*), whose formula is presented below.

$$rms = \sqrt{\frac{\sum \left(1 - \frac{\eta_{model}}{\eta_{experiment}}\right)^2}{N_{experiment} - N_{parameters}}}
 \tag{Eq. (33)}$$

Here, η_{model} stands for the viscosity calculated from the model, while $\eta_{experiments}$ stands for the measured viscosity. $N_{experiment}$ and $N_{parameters}$ are the number of studied temperature, pressure and shear stress conditions, and the number of parameters in the model, respectively. The WLF model presents a fairly good fitting of the raw data, as its *rms* is below 6% (mean value of 3.7%) and can be found in Table 7.

The application of the WLF formula is performed using the values of $T_g(0)$ previously determined by extrapolation with the VTF expression. The latter values can be relied on as other calculations highlighted that an uncertainty of 5 °C on $T_g(0)$ implies a maximum variation in viscosity of 2%. Moreover, realistic initial data were used as initial parameters for the least mean squares regressions of the experimental data. WLF parameter values, low shear viscosity at atmospheric pressure and pressure-viscosity coefficients at 40 °C and 100 °C can be found in Table 7 for all polymer solutions and the base oil.

Viscosities measured at ambient pressure on the high pressure viscometer are also compared to those obtained on the Physica-MCR-301 rheometer to assess their validity. A good continuity between the devices is highlighted, with a relative difference of 10 % maximum for all solutions. Note that in Figure 24, a discrepancy between the measured and calculated values can be seen at 40 °C and 400 MPa. Indeed, solidification of the base oil occurred at these conditions and the measured viscosity was not taken into account for the curve fitting [94]. The addition of polymers has an impact on the state diagram of the solutions and solidification can occur at lower or higher pressures than that of the base oil. For instance at 40°C, solidification starts at 200 MPa for the OCP-HE, or even at higher pressure, at 500 MPa in the case of the PAMA-L solution (see Appendix 6 for the pressure-viscosity dependence of polymer solutions)

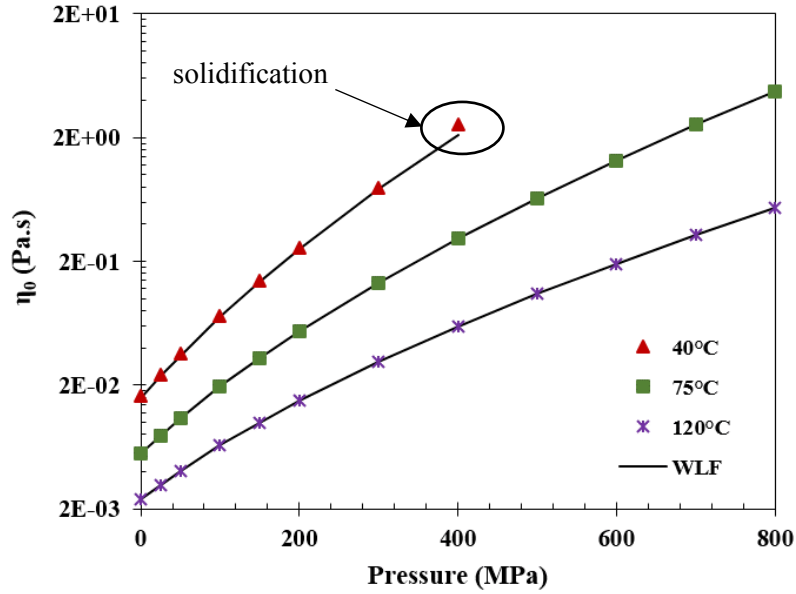


Figure 24: Viscosity-pressure dependence of the base oil (experimental data as colored dots) at different temperatures and regressed to the WLF expression (black line)

Material	Base oil	PAMA-C	PAMA-L	PISH-S	PISH-L	OCP-HE	OCP-LE
A_1 (°C)	61.09	55.46	113.22	106.67	100.81	140.85	161.31
A_2 (GPa ⁻¹)	0.978	0.866	0.356	0.498	0.316	0.551	0.320
B_1 (GPa ⁻¹)	6.49	7.72	6.14	7.34	6.65	5.56	6.15
B_2	-0.499	-0.550	-0.555	-0.515	-0.551	-0.429	-0.487
C_1	16.18	15.54	15.84	15.72	15.98	16.30	16.11
C_2 (°C)	22.57	17.99	22.74	21.04	24.15	30.40	26.02
η_g (Pa.s)	10 ¹²						
$T_g(0)$ (°C)	-90.5	-92.4	-91.5	-91.9	-90.2	-103.2	-92.7
rms (%)	3.47	4.19	4.08	3.82	2.14	5.32	2.83
$\alpha_{40^\circ C}^*$ (GPa ⁻¹)	14.7	14.4	14.5	15.1	15.9	13.9	14.7
$\alpha_{100^\circ C}^*$ (GPa ⁻¹)	10.1	9.9	10.2	10.4	11.3	9.7	10.3
$\eta_0(40^\circ C, p_{atm})$ (mPa.s)	16.36	21.28	32.91	30.33	34.19	35.78	34.87
$\eta_0(100^\circ C, p_{atm})$ (mPa.s)	3.33	6.11	6.99	6.88	6.68	6.66	6.42
VI	148	306	257	235	200	190	187

Table 7: Parameters of the WLF, reciprocal asymptotic isoviscous pressure coefficients computed from the WLF model and VI, for the base oil and all polymer solutions.

The principle of viscosity-temperature-pressure equivalence suggested by Yasutomi *et al.* [13] is now applied to all solutions. Isothermal curves of viscosity over pressure, such as the ones of Figure 24, are plotted as the viscosity over $(T - T_g(p))F(p)$. All the results overlap on a unique curve, simplifying the comparison between the solutions (see Figure 25). On this diagram, high values of the abscissa correspond to a system subjected to high temperature or low pressure, whereas the low values stand for the low temperature or high pressure conditions. It is thus possible to evaluate the VII efficiency of the studied polymers with pressure. The viscosity of the solution should then be close to the one of the base oil at low abscissa values and larger at higher ones. This effect is especially well observed for the PAMA-C and the PISH-S solutions. It is also visible, but to a lesser extent, for both the PAMA-L and PISH-L solutions, which present thus a similar temperature-pressure-viscosity dependence. Both OCPs behave definitely as thickeners, with the same contribution to the viscosity all along the temperature and pressure range. These observations are further explained in this chapter.

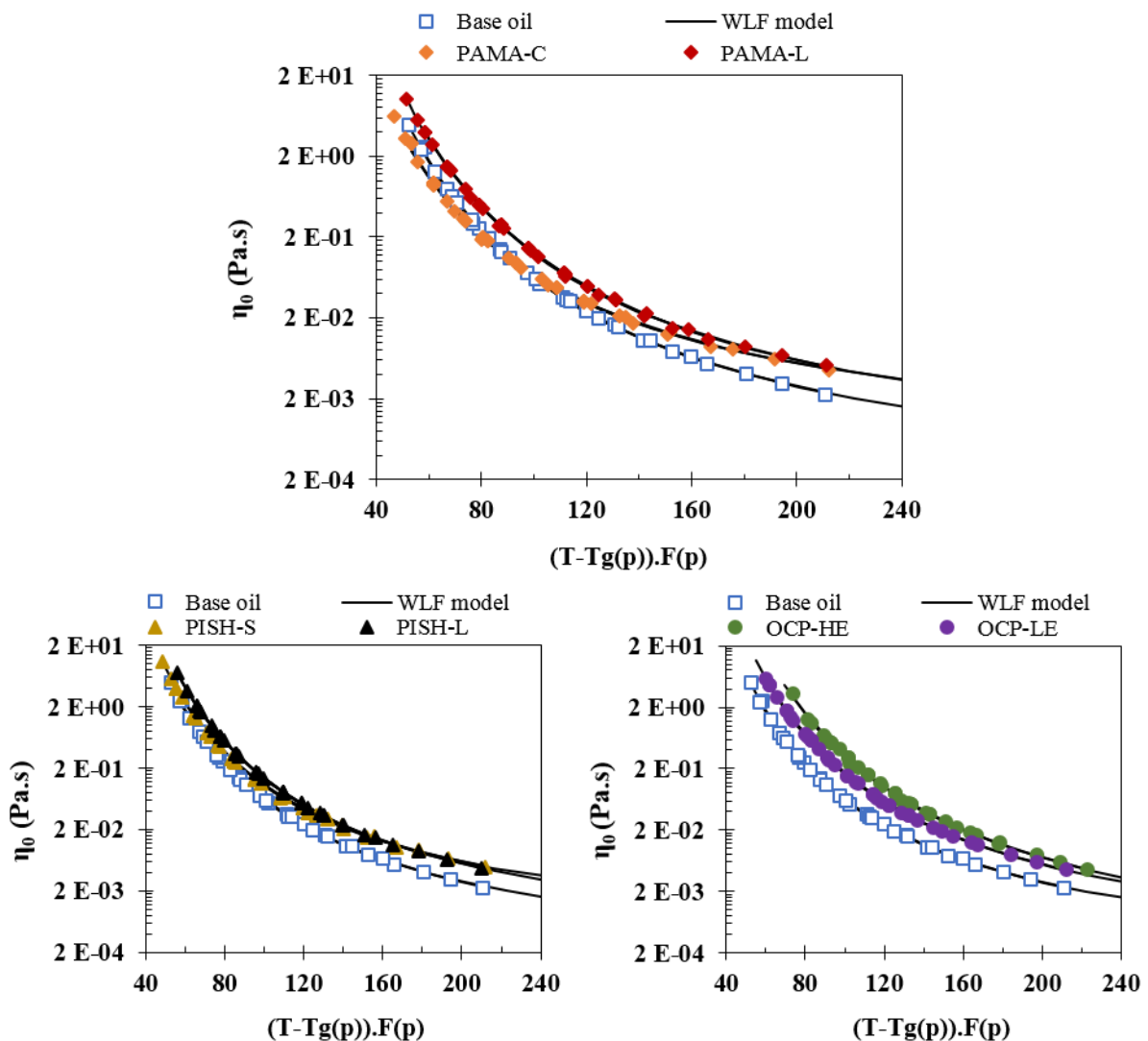


Figure 25: Master curves of the base oil and the polymer solutions – Top) PAMA solutions, Bottom left) PISH solutions, Bottom right) OCP solutions

II.2.2 Pressure-viscosity coefficients variations against temperature

The reciprocal asymptotic isoviscous pressure coefficient α^* is used to estimate the viscosity-pressure dependence at constant temperature (Eq. (25), p. 46) [86]. This parameter is of primary importance as it strongly impacts the central film thickness of any lubricant in an EHD contact (Eq. (1) p. 23). Figure 26 depicts the variations of α^* against temperature for each family of polymers and for the base oil. The coefficients are computed from the modified WLF expression for values obtained at 40 °C ($\alpha_{40\text{ }^\circ\text{C}}^*$) and 100 °C ($\alpha_{100\text{ }^\circ\text{C}}^*$) (see Table 7 p. 60).

The pressure-viscosity coefficients decrease with temperature for all products. The values for the polymer solutions are close to the one of the base oil and it is difficult to tell them apart. However, a slight variation on α^* may lead to a significant variations on the viscosity at moderate to high pressure. This parameter should thus be define as exactly as possible. The PAMAs α^* are lower than the base oil ones at low temperature and get slightly higher at high temperature. However, the variations of α^* for PAMAs should be regarded as similar to those of the base oil, considering the measurement and fitting uncertainties. Same comments apply to PISH-S and OCP-LE mixtures. It is interesting to notice that the PISH-L solution is the most sensitive one to pressure, with the highest pressure-viscosity coefficient all along the temperature range. The difference between the base oil and the OCP-HE is difficult to explain but considered not necessarily meaningful, as the model rms for this solution is the highest (see Table 7, p. 60) and might impact thus the α^* calculations.

All solutions present then similar pressure dependence at any considered temperatures, apart from the PISH-L solution. This specific pressure response will be analyzed further in the following section, while considering the reduced viscosity and thickening factor Q (Eq. (4), p. 35) of all solutions. The latter allow to emphasize the contribution of the polymer itself to the base oil properties and enable the distinction between VIIs and thickeners at high pressure.

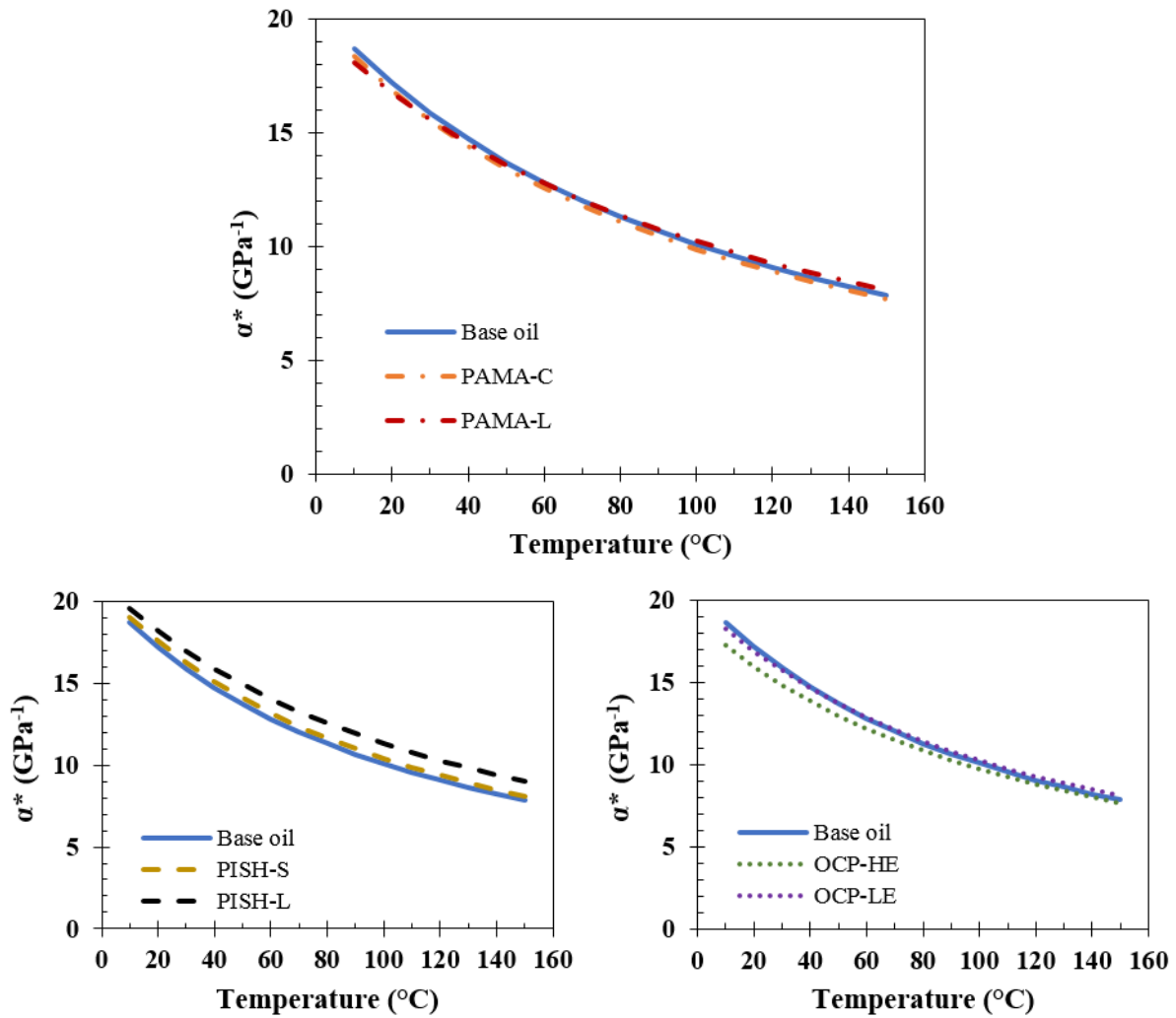


Figure 26: Pressure viscosity coefficient α^* variations against temperature for the base oil and each polymer family – Top) PAMA, Bottom left) PISH, Bottom right) OCP

II.3 Pressure influence on the VII properties

II.3.1 Comparative study using the reduced viscosity η_{red}

The reduced viscosity η_{red} , Eq. (16) p. 43, is the relative difference between the viscosity of the polymer solutions and the viscosity of the base oil, divided by the polymer concentration. It illustrates the actual contribution of the polymer to the lubricant rheology. The reduced viscosity, calculated from the WLF model, is thus plotted against temperature at atmospheric pressure and 600 MPa (see Figure 27), and against pressure at 40 °C and 120 °C (see Figure 28) for all solutions.

Clearly, both PAMAs present lower reduced viscosities and thus thicken less the base oil than PISH and OCP polymers, at any conditions of temperature and pressure. Indeed, PAMAs are introduced in bigger quantities to assume the same viscosity at high temperature and high shear rate, as their thickening effect per unit of mass is less important. However, the actual value of the reduced viscosity is not of main interest here, but rather its variations against temperature and pressure.

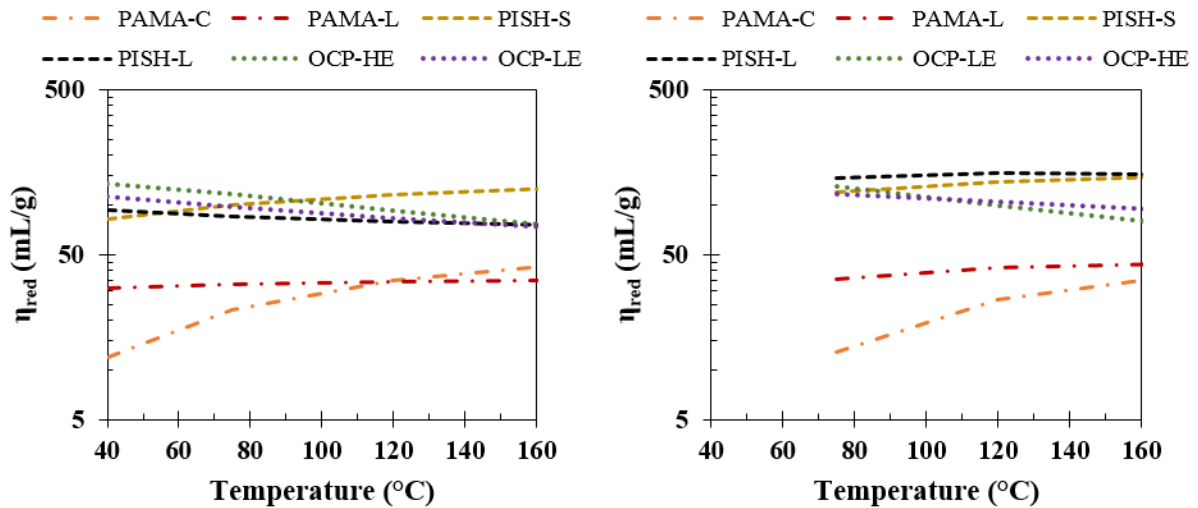


Figure 27: Reduced viscosity η_{red} calculated from the modified WLF equation plotted against temperature for all solutions at left) atmospheric pressure, right) 600 MPa

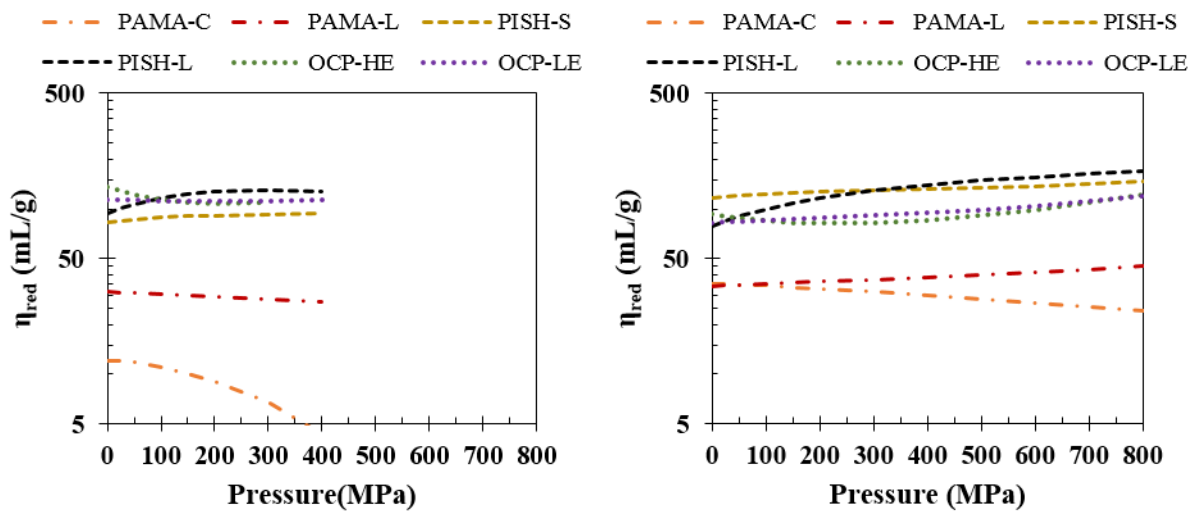


Figure 28: Reduced viscosity η_{red} calculated from the modified WLF equation plotted against pressure for all solutions at left) 40 °C, right) 120 °C.

At constant pressure, the reduced viscosities of the PAMA-C and the PISH-S solutions increase with temperature. This reflects the larger contribution of the polymer at high temperatures rather than at low ones, which is the desired effect of viscosity index improvers. This effect is also seen for the PAMA-L at high pressure, while its reduced viscosity remains almost steady at ambient pressure. η_{red} for both OCPs solutions decreases with temperature, whereas the PISH-L solution presents a peculiar behavior (see Figure 27). Indeed, the latter displays a decrease of its reduced viscosity with temperature at atmospheric pressure (Figure 27 left), whereas it weakly rises with temperature at high pressure (600 MPa, Figure 27 right). This polymer contribution to the lubricant viscosity is then enhanced above a certain pressure, from which the PISH-L behaves like a VII and no longer as a thickener. As mentioned in *I.5 p. 50*, this polymer has the particularity to form spherical micelles while being in solution. Pressure increase may impact the micelles formation and thus the polymer properties. This effect is detailed later in this chapter.

At constant temperature, the behavior of the PAMA-C mixture differs from the other solutions. Indeed, its reduced viscosity decreases with pressure, whereas it slightly increases for the PISH-S and both OCPs and more significantly in the case of the PISH-L solution (see Figure 28). The PAMA-L behavior is here atypical, its reduced viscosity decreases with pressure at 40 °C but increases at 120 °C. From the application point of view, the behavior of the PAMA-C is again the most interesting since it thickens less the solution in the hardest conditions (i.e. at high pressure). This may contribute to limit friction in EHD contacts where the pressure increases drastically.

The coupled influence of temperature and pressure must be meticulously analyzed for each polymer solution and they will be explained further in this chapter thanks to molecular scale considerations. The variations of both experimental and calculated reduced viscosity of each solution are detailed in Appendix 7. Table 8 presents the variations of η_{red} and thus the actual contribution of the polymer addition to the base oil viscosity at low shear stress. Three polymers - PAMA-C, PAMA-L, PISH-S - present the expected effect of a VII, with an increase of their contribution at high temperature, while both OCPs act as thickeners. In these conditions, the PAMA-C appears to be the most interesting product for the VII application. The PISH-L behavior is peculiar as it behaves as a VII only above a certain pressure, and in a rather weak manner.

	Pressure	PAMA-C	PAMA-L	PISH-S	PISH-L	OCP-HE	OCP-LE
From 40 to 150 °C	p_{atm}	+246 %	+10 %	+51 %	-19 %	-41 %	-34 %
From 75 to 150 °C	600 MPa	+168 %	+24 %	+21 %	+7 %	-35 %	-17 %

Table 8: Variations of the reduced viscosity η_{red} calculated by the WLF model between 40 to 150 °C at ambient pressure and between 75 to 150 °C at 600 MPa

II.3.2 Distinction between VIIs and thickeners at high pressure

The temperature dependence of the low shear viscosity η_0 at atmospheric pressure enlightened the interesting VII effect of the PAMA-C additive. It is also possible to evaluate the VIIs efficiency at ambient pressure by the viscosity index (VI) (see Table 7, Eq. (3))[49], which confirm our previous observations regarding the PAMA-C efficiency as this product presents the highest viscosity index. However, the consideration of the viscosity index parameter only does not enable the full evaluation of the variations of the polymer thickening power with temperature. Indeed, the viscosity index is a standard tool defined a long time ago and is calculated using reference oils, which are very different from the base oil studied here. This index is thus characteristic of the solution viscosity at 40 °C and 100 °C, and it is impossible to bring out the contribution of the polymer itself from it. VII and thickeners cannot be then clearly or quantitatively distinguished by only looking at the viscosity index.

The thickening factor Q mentioned in 1.2.4 (Eq. (4), p. 34) is another tool defined to quantify the variations of the thickening power of a polymeric additive between 40 °C and 100 °C in a base oil [9]. This factor is calculated here from ambient pressure up to 300 MPa using raw data, and at 400MPa using calculated viscosities by the WLF equation. Figure 29 shows the variations of Q against pressure for all

the polymer solutions. The threshold value ($Q = 1$) is highlighted as the red line below which the polymers are no longer considered as VII but as thickeners. The uncertainty is about 10 %.

Noticeably, the PAMA-C additive presents the highest thickening factor's values whatever the pressure and it is confirmed as the most efficient viscosity index improver studied in this work. The PAMA-L and PISH-S are identified as weak VIIs, even though the PISH-S performs better than the former. From Figure 29, it becomes clear that both OCPs have to be considered as thickeners: their thickening factors are below one all along the pressure range.

The PISH-L additive is the only polymer studied whose thickening factor is impacted by the pressure. Indeed, its factor Q is close to one and this additive can then be considered either as a VII or as a thickener. Here, its Q factor globally increases with pressure and even goes above one from approximately 250 MPa. The PISH-L properties are then those of a VII at high pressure, whereas it was identified as a thickener at atmospheric pressure. This is confirmed by previous comments made on the variations of its reduced viscosity (see Figure 27). Results above 300 MPa are necessary to confirm the value of this “activation” pressure, i.e. where the transition to a true VII behavior occurs. However, it is not possible to obtain experimentally the thickening factor at such pressure due to the solidification of the base oil above 300 MPa at 40 °C. The extrapolation at 400 MPa calculated by the WLF model (empty colored dots in Figure 29) must be then taken cautiously.

To conclude, the thickening factor Q appears as a relevant indicator to quantify the actual performance of the viscosity index improvers, at different pressures. In the following section, the results obtained here are discussed and linked to the molecular properties of the polymers. The consideration of their conformation, size and solubility in the base oil will eventually explain the different VIIs and thickeners responses.

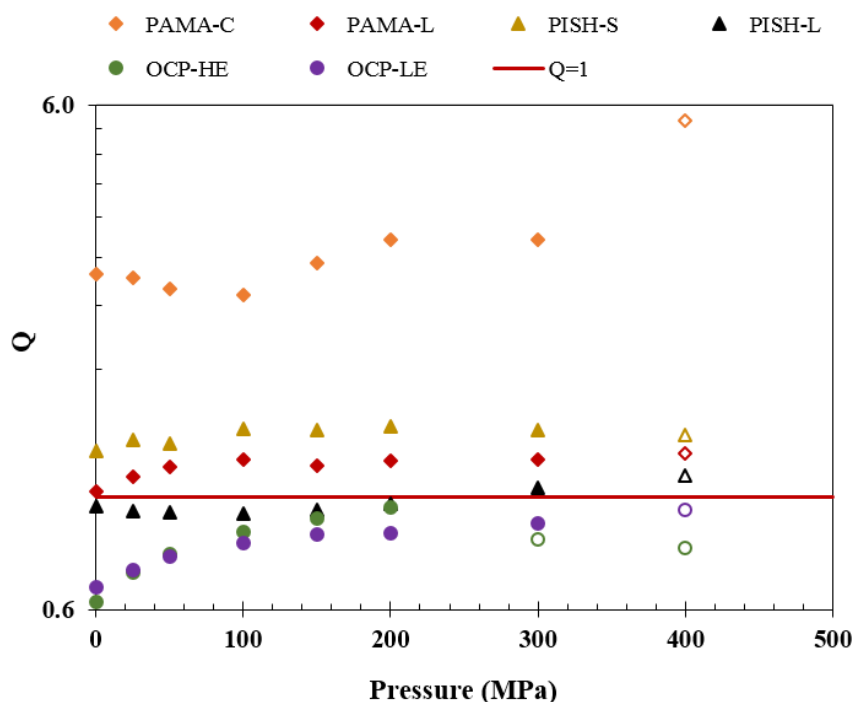


Figure 29: Thickening factor Q versus pressure for all polymer solutions – full colored dots for thickening factor from experimental data and empty colored dots for Q extrapolated at 400 MPa using the WLF model

II.4 Impact of the molecular structure on the pressure-viscosity dependence

The mechanisms occurring at the molecular scale are detailed in this section, in order to understand the temperature and high pressure responses of polymer solutions. All polymers present different conformations. Both OCPs are linear products with different ethylene content. Both PAMAs are made of a polar skeleton with non-polar side chains, the PAMA-C with long ones made of olefin copolymer, and the PAMA-L with short side chains. The PISH-S is a star polymer, whereas the PISH-L has a linear structure but forms spherical micelles leading to a star shape. All the results obtained so far may be explained by the polymers chemistry and conformation, especially the PAMA-C efficiency as a true VII and the peculiar response of the PISH-L additive. The hydrodynamic radius R_h is the key parameter to link the rheology to the physico-chemistry of macromolecules [10][22]. Its influence on the response of the polymer solutions is examined and the different determinations of its value – by the Flory equations, direct measurements or the Einstein's law applied at high pressure - are compared in this section.

II.4.1 Concentration regime and determination of R_h at atmospheric pressure

All polymer solutions are formulated at different concentrations, recalled in Table 9, due to the preparation at iso HTHS viscosity of 2.6 mPa.s at high temperature and high shear rate. The critical concentration c^* must be first determined to certify that all solutions are in diluted regime in order to apply the Einstein's law. It is thus approximated from Eq. (10) (p. 40), together with the radii of gyration determined with the Flory equations Eq. (8) (p. 39), at ambient temperature and pressure conditions and for theta and good solvent conditions. The calculation of the mean monomer size l is different according to each polymer conformation. For linear polymers such as OCP and PISH-L, it directly corresponds to the sum of the total bond lengths between the carbon atoms in the main polymer skeleton. As for PAMA and PISH-S, l is determined from their densities. The number of monomers N corresponds to the weight average degree of polymerization and is equal to the product of the number average degree of polymerization to the polydispersity index (PDI), i.e. $N = DP_n * PDI$ (see I.3.1 p. 36). The number of monomers N , the mean monomer size l , the hydrodynamic radius R_h , the critical concentration c^* and the concentration of polymer c are detailed in Table 9, for both theta and good solvent conditions.

	l (nm)	N	Theta solvent		Good solvent		
			R_h (nm)	c^* (%)	R_h (nm)	c^* (%)	c (%)
PAMA-C	0.65	3502	11.8	10.4	22.9	0.7	3.36
PAMA-L	0.70	1394	8.0	16.3	14.1	1.5	4.67
PISH-S	0.48	10 036	23.3	5.6	39.6	0.3	1.18
PISH-L	0.59	1886	7.9	5.7	14.4	0.5	1.49
OCP-HE	0.31	2723	4.9	18.6	9.3	1.4	1.19
OCP-LE	0.31	2510	4.7	21.2	8.8	1.6	1.28

Table 9: Hydrodynamic radii and critical concentrations of polymer solutions in theta and good solvent conditions using the Flory equations. Results at the chosen solvency regime are bolded. The polymers weight concentration in the solution is indicated in the extreme right side colusmn.

The concentration of polymers in this study is not systematically lower than the critical concentrations for all solutions regarding the solvent quality (see concentrations in Table 9). The determination of the concentration regime must then take into account the polymer and solvent interactions.

Both OCPs are supposed to be in good solvent conditions as these polymers are non-polar macromolecules dissolved in a non-polar solvent. They are both considered in the dilute regimes even though their concentrations are close to their critical values.

Both PAMAs are presumably in theta solvent conditions due to their main polar skeleton. This assumption is supported by SANS (small angle neutron scattering) direct measurements performed by Covitch *et al.* [19]. Measurements were carried out in D-squalane, which was selected because of its viscosity and solvency, similar to those of currently used paraffinic base oils. They highlighted that PAMAs polymer coils were not fully swelled in the solvent. The conditions were not identified as good but rather theta ones. Given their weight concentrations, both PAMAs solutions studied here are thus in the dilute regime.

The PISH-S solution is also assumed to be in theta conditions. Indeed, a rather low solubility between the PISH-S and the base oil was expected due to the steric hindrance induced by the long branches of the star skeleton and the high amount of styrene in this polymer (27 % in weight). Indeed, several studies have shown that styrene is in bad solvent conditions when mixed in non-polar solvents, such as heptane [95] or in Nexbase 3043 [20], a lubricant similar to the base oil studied here. The good solvent assumption is thus not appropriate. The theta condition is here considered as the isoprene chains improve the solubility of the styrene core. The PISH-S critical concentration is estimated at 5.6 % rather than 0.3% and this polymer solution is also in the dilute regime.

The case of the PISH-L solution is singular. This polymer is a linear copolymer made of 30 % in weight of styrene and 70 % in weight of butadiene and isoprene. The PISH-L was investigated in previous studies [20]: it forms micelles above its critical micellar concentration (cmc), which is about 10^{-8} g.mol⁻¹ and below the PISH-L concentration of this study [20][95]. The turbid aspect of the PISH-L solution is thus explained by aggregates formed within the product. The spherical micelles formation was revealed at 20 °C thanks to direct measurements using dynamic light scattering (DLS) and size exclusion chromatography (SEC) results in n-heptane. Even though, the solvent employed in [20] was different from the Yubase 4, the measured radii of gyration were about 30 nm and do not comply with those determined in Table 9: hence, the Flory equations may not be applied to this polymer. Nonetheless, the solvent quality is supposed to be in theta conditions and the solution is considered in the dilute regime.

To conclude, the concentrations of all polymer solutions are below the calculated critical concentrations and this work concerns the dilute regime. The Flory equations can also give access to size considerations through the hydrodynamic radius R_h which is here the relevant notion to explain how the polymer chemistry, conformation and solubility can affect the rheological behaviors. The Flory R_h are compared at atmospheric pressure to hydrodynamic radii obtained by other methodologies in Table 10 and will be discussed further. It is however interesting to notice that at a given temperature the polymers size depends on specific atomic-scale features, including molecular weight and conformation. Direct measurements were also performed at atmospheric pressure to confirm the values of the hydrodynamic

radii. The IMMM laboratory (Université du Maine, France) supplied quadruple detection size exclusion chromatography (SEC) results of the average hydrodynamic radii of all polymer solutions in THF (Appendix 5). Table 10 recaps all the different determinations of the hydrodynamic radii at atmospheric pressure and for all polymer solutions.

R_h (nm)		PAMA-C	PAMA-L	PISH-S	PISH-L	OCP-HE	OCP-LE	
Deduced	Einstein's law (25 °C, at p_{atm})	8.9	11.6	20.0	12.0	12.5	13.0	
	Flory equations (25 °C, p_{atm})	Theta solvent	11.8	8.0	23.3	7.9	4.9	4.7
		Good solvent	22.9	14.1	39.6	14.4	9.3	8.8
Measured	Quadruple detection SEC (in THF) 20 °C	32.2	20.2	23.3	13.7	10.6	13.8	

Table 10: hydrodynamic radii from different methodologies at atmospheric pressure – in bold the solvent quality chosen for the Flory equations

II.4.2 Determination of R_h at high pressure using the Einstein's law

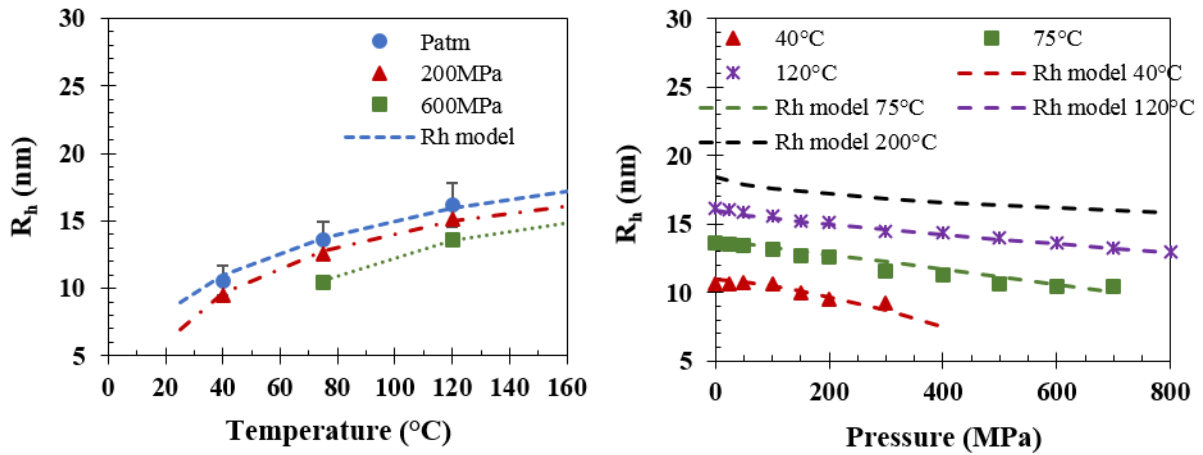
Previous considerations on the hydrodynamic radii were only done at atmospheric pressure. It is thus proposed to calculate R_h by applying the Einstein's law at high pressure (Eq. (11)) [11][22], which directly links the viscosity to the hydrodynamic radius.

$$\eta_{solution} = \eta_{solvent}(1 + 2.5\phi)$$

$$\phi = \frac{c}{M} \frac{4}{3} \pi R_{coil}^3$$
Eq. (11)

Assumptions for the calculations are considering the polymer coils as rigid spheres and working with diluted solutions. Moreover, the notion of hydrodynamic volume is still considered valid at high pressure. The hydrodynamic radius R_h is a key parameter to explain how the structure of a polymer affects its macroscopic properties. R_h for all polymer solutions is determined from the high pressure viscometer measurements and by the Einstein's law, and is plotted upon temperature and pressure in Figure 30, Figure 31 and Figure 32. The viscosity values come either from high pressure viscometer measurements (colored dots) or are calculated by the WLF model (dotted lines). The uncertainty is equal to 10 %. For the sake of clarity, the error bars are plotted at atmospheric pressure only.

PAMA-C



PAMA-L

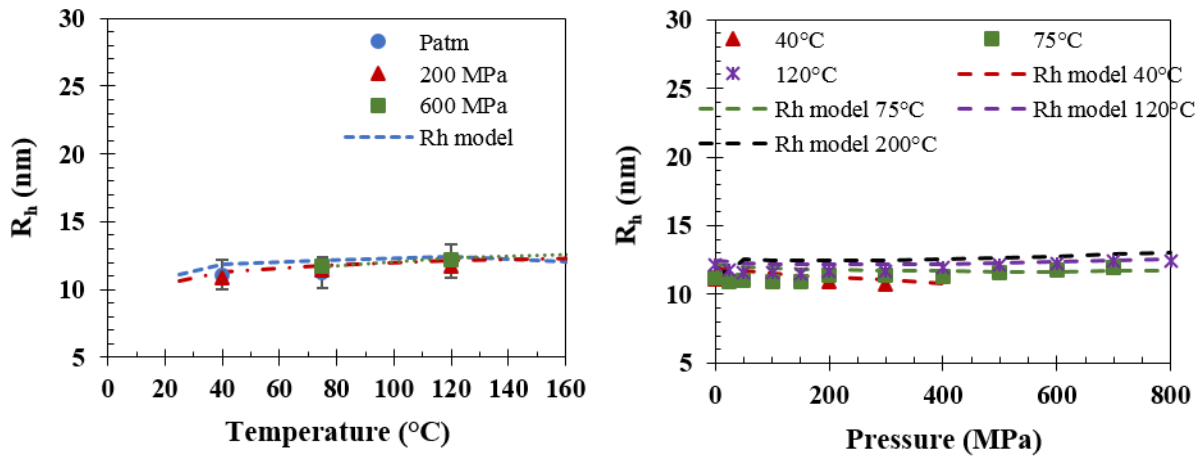
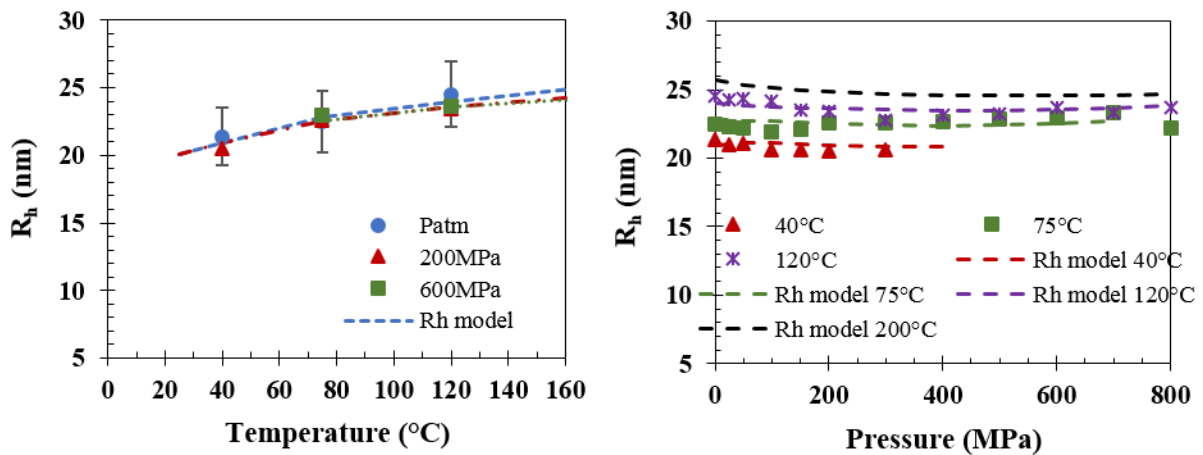


Figure 30: Hydrodynamic radius variations versus temperature (left) and pressure (right) for PAMA-C (top) and PAMA-L (bottom) - R_h determined from experimental values plotted as color dots and R_h calculated by the WLF equation plotted as dotted lines.

PISH-S



PISH-L

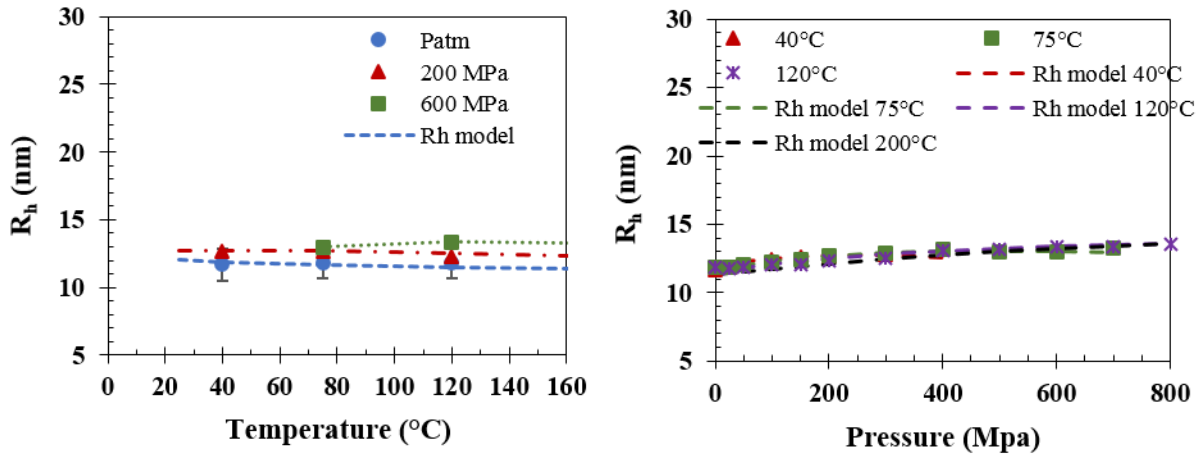
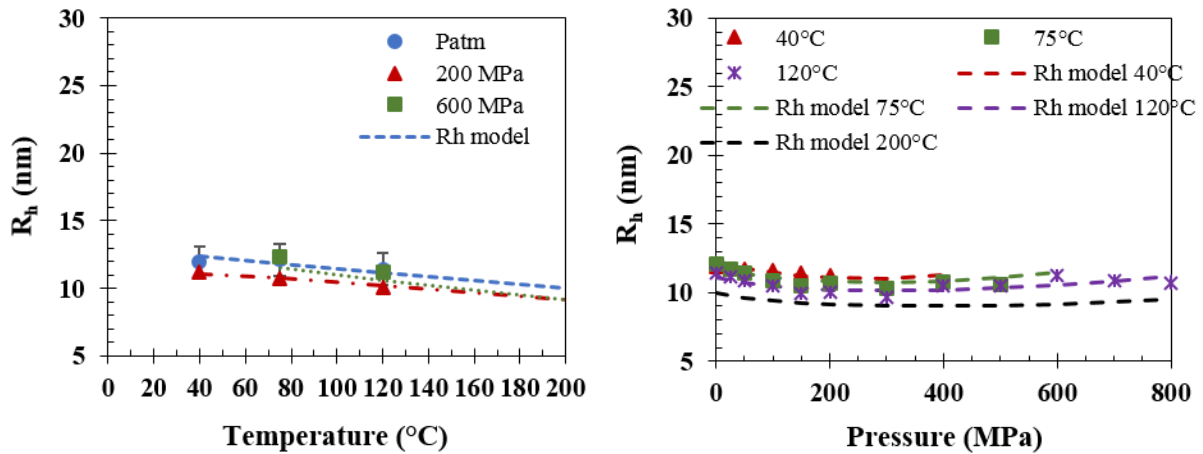


Figure 31: H Hydrodynamic radius variations versus temperature (left) and pressure (right) for PISH-S (top) and PISH-L (bottom) - R_h determined from experimental values plotted as color dots and R_h calculated by the WLF equation plotted as dotted lines.

OCP-HE



OCP-LE

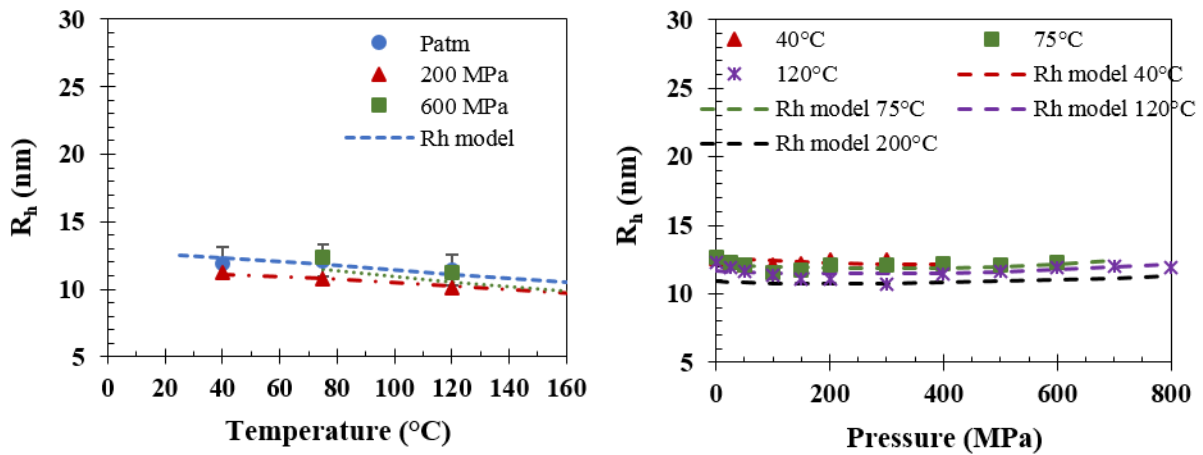


Figure 32: Hydrodynamic radius variations versus temperature (left) and pressure (right) for OCP-HE (top) and OCP-LE (bottom) - R_h determined from experimental values plotted as color dots and R_h calculated by the WLF equation plotted as dotted lines.

The hydrodynamic radii calculated with the Einstein's law are compared to theoretical Flory predictions and direct measurements to corroborate the assumptions on the solvency regimes (see Table 10). The Einstein's values and measured hydrodynamic radii are consistent for OCPs and PISHs. However, the PAMAs calculated values do not comply with SEC measurements. This discrepancy may be the result of the solvent (tetrahydrofurane, THF) employed, in which the interactions between the polymers and the solvent may be quite different from those encountered in the base oil. Since this polymer is the most sensitive to variations of solvency conditions, it may explain the gap between the different methods to determine its size. Direct measurements carried out on dynamic light scattering (DLS) in the actual base oil studied would be necessary for PAMAs to obtain accurate R_h .

Another methodology to determine the hydrodynamic radii is employed and already presented with the Flory equations. Again, the calculated values are close to those obtained by the other ways, while in the correct solvent conditions. The PAMA-C, PAMA-L and PISH-S are confirmed to be in theta conditions, whereas the OCPs are both in good solvent conditions (results highlighted in bold in Table 10). The dilute regime assumption, mandatory for the application of the Einstein's law, is thus verified. However, the PISH-L values from the Flory equations do not comply with the Einstein's values. Indeed, this polymer forms micelles in the solution, supporting then the theta solvent assumption and the polymer coils should be smaller. The Flory equations may not thus be applied to polymer with such singular molecular structure. Apart from this product, the hydrodynamic radii derived from all the different methods confirm the initial assumption of dilute regime in all the cases. Therefore, the Einstein's law can be applied.

II.4.2.a Temperature variations at constant pressure

The calculated radii are different from one polymer to another and various evolutions of the radii are observed. The PAMA-C hydrodynamic radius increases with temperature by 53 % at atmospheric pressure and by 59 % at 200 MPa, from 40 °C to 120 °C (raw data). The polymer coils swell between 40 °C and 75 °C at atmospheric pressure, confirming previous observations on the PAMA-C's efficiency (Figure 23, p. 57). The PISH-S polymer coils slightly rise with temperature (by 15 % at ambient pressure and 14 % at 200 MPa), which corroborates its low but real VII properties. The PISH-L differs from the others, with its hydrodynamic radius only increasing with pressure while remaining steady with temperature. At first view, the PAMA-L properties seem close to the PISH-S ones, its hydrodynamic radii increasing by 10 % at ambient pressure and by 7% at 200 MPa. However, these variations are low and within the uncertainty range. The PAMA-L behavior is thus considered closer to the PISH-L one, its radii remaining steady with the temperature. This tendency is also observed while considering the extrapolated values at higher temperature. Finally, both OCPs see their radii decreasing with temperature (by 3% at ambient pressure and 10 % at 200 MPa). As previously stated, these additives are in "good solvent" conditions, with their macromolecules fully swelled. This explains the tiny influence of temperature on their hydrodynamic radii. To conclude, the biggest polymer coils are the PISH-S ones, a result of its important molecular weight. The size of PAMA and OCP coils are rather similar, even though their molecular weights are not comparable (about 600 000 g/mol against 80 000 g/mol, respectively).

Although coil expansion is not required for viscosity index improvement, it has been suggested that polymers whose coils swell with temperature may contribute more to VI than those that do not [19].

Among all polymers usually employed as commercial viscosity index improvers, the positive variation of the polymers radii is supposedly observed for the methacrylates only [56][22][96]. Molecular dynamics simulation ran by Ramasamy *et al.* also support these observations. In [97], the trends in polymers coil size were investigated for model polymers of PAMA and OCP. In a non-polar solvent, the oxygen content of the polymers appears to be the determinant factor on the molecules expansion, as it affects the polymer solubility and its interactions with the solvent.

This explains then the PAMAs behaviors. Nonpolar solvent such as the base oil used here dissolves more easily nonpolar additives. The solubility is high, interactions between the solvent and the polymer segments are greater than intramolecular ones. The nonpolar additive can be then considered in “good solvent conditions”, where the polymer coils are already fully swelled [22]. Conversely, if the solubility is low, the attraction between polymer segments themselves is preferred. The polymer is thus in “theta solvent” conditions, where the polymer chains tend to collapse and take a globule conformation. This is the case for both PAMAs at low temperature and is confirmed by hydrodynamic radius calculations using Flory equations in a theta solvent conditions (see Table 10) at ambient temperature and pressure. As the temperature increases, the thermal agitation of the molecules increases: it is easier for the polymer to be surrounded by solvent molecules and the solubility of the polymer in the base oil is improved. Thus, the Van der Waals interactions between the polymer coils and the solvent are enhanced. The PAMA-C peculiarity lies in its amphiphilic nature, having nonpolar long carbonyls chains branched to a polar skeleton. Compared to the PAMA-L, this additive is thus more sensitive to solvency change, which leads to fully swell polymer chains as the PAMA-C is in “good solvent” conditions at high temperature [19].

However, the PISH-S is also considered as an interesting viscosity index improvers, whose molecules size slightly rises with temperature. Its interesting behavior complies with the same solvency considerations. Indeed, the PISH-S studied in this thesis was also investigated at atmospheric pressure only, by Chaveroux in [20], through intrinsic viscosity measurement $[\eta]$ (Eq. (18), p. 43), which is another mean to reach the hydrodynamic radius. An increase of $[\eta]$ is thus desired to depict the coil expansion: in [20], this response was observed for the PISH-S only, which presents the highest styrene content. As mentioned previously, the PISH-S solution is in theta conditions due to the steric hindrance induced by the star conformation and its styrene core, hardly dissolved in mineral base oils. No change of solvent quality was observed for this product [19][20]. The solvation of the styrene block is improved by heating, leading to a slight polymer expansion (Figure 33). Chaveroux also highlighted that the aromatic content of the base oil affects the swelling temperature of the polymer coils, the higher the content the lower the temperature at which the solvation of the styrene core is improved.

Conversely, the PISH-L solution is not affected by heating. Considering that this polymer presents the same styrene content as the PISH-S and is in ‘theta solvent’ condition, a slight increase of its hydrodynamic radii would have been expected. However, this polymer is singular since it forms micelles within the solution, whose development mechanism is highly impacted by the thermal agitation of molecules [21]. Micelles are characterized by a number of aggregates and a number of “chains”. It is proposed for the PISH-L that heating induces a modification of the micelles profile (Figure 33). The swelling of its styrene section may lead to the formation of more micelles with less chains. The volume

of the spherical micelles remains steady, the reduction of the chains number being counteracted by the swelling of the styrene core [20].

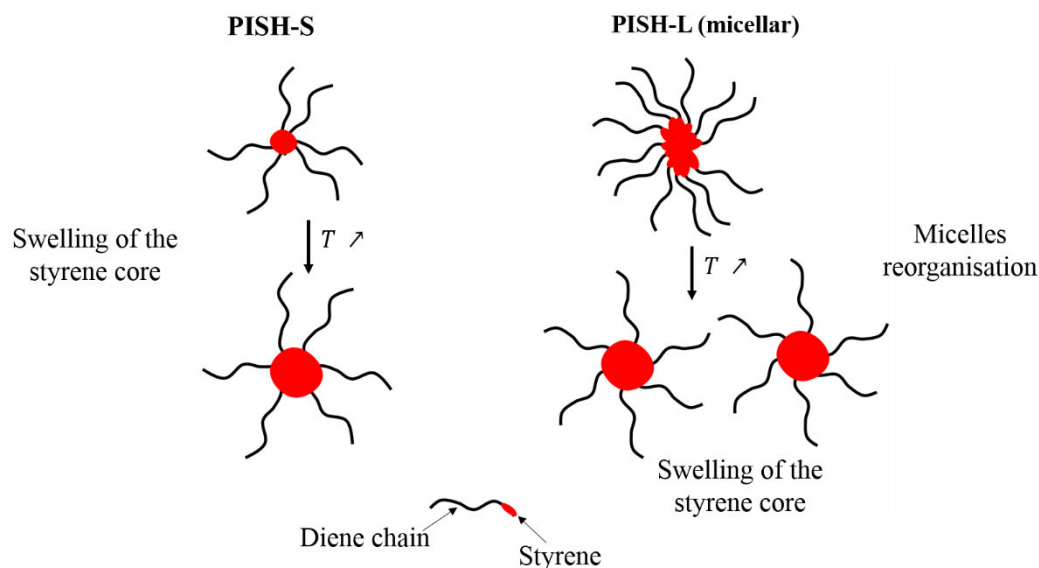


Figure 33: Molecular behavior of PISH according to their structure, star-shape or micellar shape [20]

II.4.2.b Pressure variations at constant temperature

When it comes to pressure, three different behaviors are observed (Figure 30 to Figure 32). The hydrodynamic radius R_h of the PAMA-C decreases by 20% at each temperature, whereas it remains almost constant for both OCPs, PAMA-L and PISH-S. Finally, the size of the PISH-L macromolecules increases with pressure (by 10 % at 40 °C and 15 % at 120 °C).

The raise of pressure involves an increase of the density of the solvent, thus it is more difficult for the solute to be surrounded by solvent molecules. Polymers in theta conditions, such as the PAMA-C, would make less interactions with the base oil and would shrink. However, polymers in good solvent conditions, such as the OCPs, would not be impacted by the pressure rise since intermolecular interactions with the solvent are preferred.

Both the PISH-S and the PAMA-L solutions are in theta conditions but does not present significant variations of their radius with the pressure. These two additives, identified as weak VIIs, are not assumed to undergo a solvent quality change, contrary to the PAMA-C. They also appear less sensitive to temperature changes and pressure variations than the PAMA-C. These different solvent affinity may explain why pressure doesn't impact their properties.

Regarding the PISH-L, it is difficult to explain the moderate but visible R_h rise with pressure, even though it was previously shown that pressure influences its properties (Figure 27 at p. 64, Figure 29 at p. 66). It is assumed that the micelle dynamics with temperature (see Figure 33) is reduced by the pressure increase. The various associations may not take place, leading to a global increase of the macromolecules due to the styrene swelling.

Figure 34 summarizes the relationship between the polymer VII properties and its size variations with temperature or pressure.

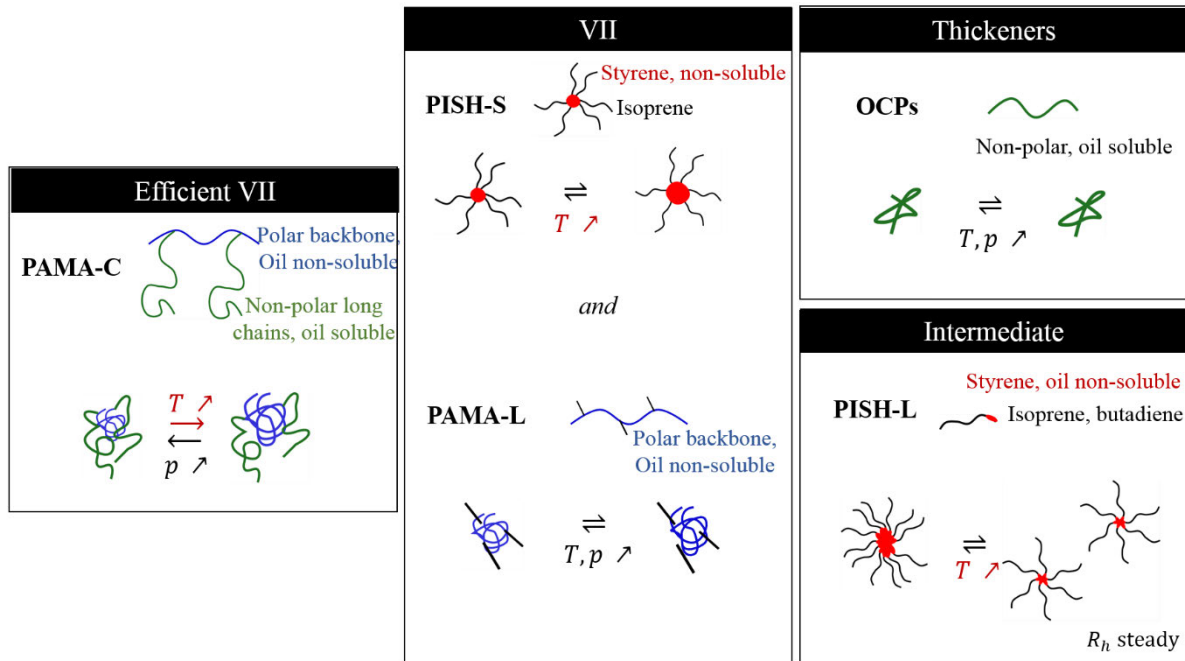


Figure 34: Summary on the relationship between the VII/thickeners and their molecular properties, at low shear stress.

II.5 Conclusion

In this chapter, the temperature and high pressure rheological responses of simplified lubricants were first accurately characterized. True viscosity index modifiers (VIIs) could be distinguished from thickeners in realistic engine conditions, at high temperature and pressure, by considering variations of their reduced viscosity η_{red} and their thickening factor Q , rather than the single calculation of their viscosity index. The PAMAs and PISH-S polymers were confirmed as VIIs, the PAMA-C being the most efficient one studied in this work. Both OCPs were considered as thickeners only, whereas the PISH-L polymer has the singularity to present the typical properties of a thickener at low pressure and the VII ones at high pressure.

The hydrodynamic radius approach has been proposed to explain the different responses. Various methods were used and detailed to determine this parameter. The Einstein's law was successfully applied at any temperature and pressure. These calculated values showed good agreement with hydrodynamic radii determined through the Flory equations and by direct measurements carried out by SEC. Several tendencies have emerged. For PAMA-C, R_h rose with temperature and decreased with pressure. Both PAMA-L and PISH-S presented the same temperature and pressure responses, a slight increase of R_h with temperature and no visible effect of the pressure. However, the R_h rise of the PAMA-L molecules was within the uncertainty range and could not be attributed to a significant swelling of its molecules. The latter also had no impact on the OCP polymer size, whereas their R_h decreased with temperature. The PISH-L was the only polymer whose hydrodynamic radii increased with pressure.

These different behaviors were explained while considering the nature of the solvent and polymer interactions. The PAMA-C's efficiency was the result of its amphiphilic nature induced by its comb structure. The PISH-S is considered as a weaker VII. It is once again the solvency considerations that explained its behavior, due to its high styrene content. Both PAMA-L and PISH-L had similar properties, even though their chemistry and macrostructure were really different. The PISH-L singularity was linked to its ability to form micelles when solvated

This chapter showed how the high pressure and temperature responses of simplified lubricants, important to the automotive industry, could be explained on the consideration of hydrodynamic size and composition of polymers. However, these observations were only made at low shear stress. The following chapter aims to understand how the rheological response is linked to the structure of polymer and how the VII efficiency is affected at higher shear stress.

Chapter III - High shear stress response of polymer solution

III.1 Rheological response at high shear stress	79
III.1.1 Thixotropy of the OCP-HE solution.....	79
III.1.2 Shear-thinning response of all solutions.....	80
III.2 Relationship between the additive’s structures and their rheological responses ...	86
III.2.1 Mass average molecular weight effects.....	87
III.2.2 Conformation effect	87
III.2.3 Size effect	88
III.2.4 Limits of the Carreau model.....	89
III.3 Zhang model for low viscoelastic solutions	91
III.3.1 Model and experiments	91
III.3.2 Comparison to Carreau predictions	92
III.4 Conclusion.....	95

Polymers performance was evaluated at high pressure and temperature in the previous chapter. Although the PAMA-C appeared to be the most interesting product, these observations were only done at low shear stress which does not reflect actual engine conditions. This chapter focuses then on the high shear stress influence on the behavior of polymer solutions. It aims to understand how their rheological response is linked to the structure of the polymers and how the viscosity index improver (VII) function is affected. These considerations will also help to highlight some limitations of the widely used Carreau-Yasuda model in the case of VIIs and propose an alternative, the Zhang model.

III.1 Rheological response at high shear stress

Series of tests were carried out on a high pressure Couette rheometer, depicted in Appendix 4 [98]. Temperatures and pressures ranged respectively from 30 to 60 °C and from 200 up to 400 MPa. Three cylinders sets – “low shear”, “middle shear”, “high shear” - were used here to cover a large range of shear stresses from 0.5 up to 1000 kPa. The cylinders sets have allowed to carry out several series of experiments: the experimental results used hereafter were obtained from the mean values between these different sets. Moreover, no heating by viscous friction is supposed to alter the experimental data, as the Nahme-Griffith number (described in Appendix 4) was low and below 0.3 [5].

III.1.1 Thixotropy of the OCP-HE solution

Shear-thinning behavior is expected to occur for polymer solutions [76]. However, it may not be the only type of non-Newtonian response observed in lubricants. Indeed, thixotropy may also be present, in our case for the OCP-HE solution (Figure 35 below) [94].

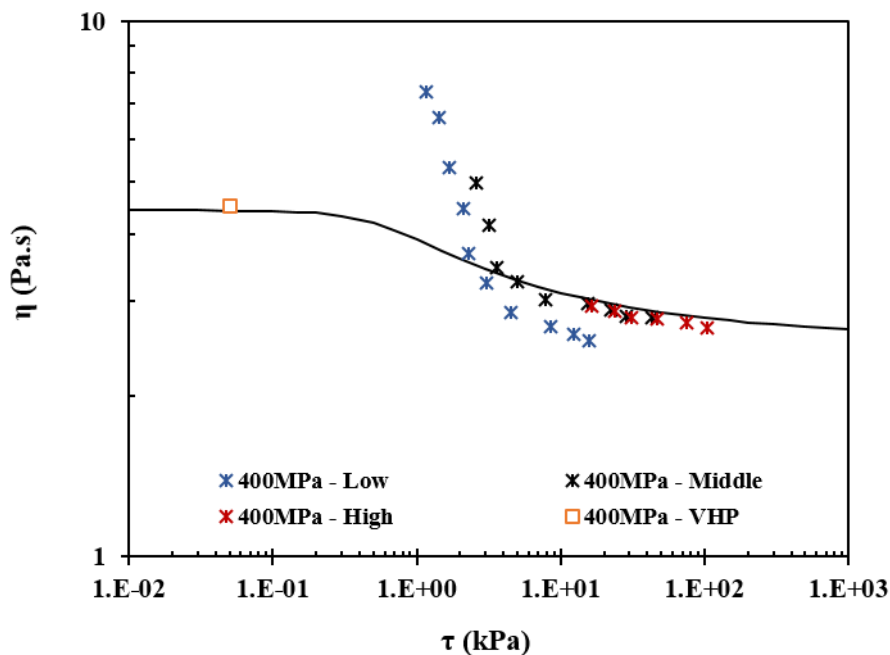


Figure 35: Raw data of the OCP-HE solution acquired from the different cylinders sets of the high pressure Couette rheometer at 40 °C and 400 MPa and showing thixotropy at low shear stress. The Carreau-Yasuda model is fitted to the experimental data (black line).

At high pressure or low temperature, a solid-like behavior of the solution occurs, as previously highlighted in *II.1* (p.55). At 40 °C and 400 MPa, the OCP-HE viscosity is shear dependent and time dependent for shear stresses below 10 kPa, as can be seen in Figure 35. The viscosity increases with time due to the solidification of some of the solution components and it may decrease with the shear stress as the solid phase is fragmented. As experiments below 10 kPa take more time, the solution is thus more sensitive to solidification and the measured viscosities do not comply at all with the first Newtonian plateau calculated by the modified WLF-Yasutomi equation [14](WLF equation in the following, empty colored square in Figure 35). Moreover, the second Newtonian plateau may also be affected by the solid structure formed within the solution [94]. This thixotropic response is thus unwanted and impacts the extrapolation of viscosity at high shear stress. The results obtained with the OCP-HE solution will not be presented in this section for this reason.

III.1.2 Shear-thinning response of all solutions

For all other solutions, the dynamic viscosity η is plotted against shear stress τ (Figure 36 to Figure 39) at different pressures for the base oil and simplified lubricants. For the sake of clarity, only the results acquired at 40 °C are shown. However, the general behavior is the same regardless the temperatures studied here, while remaining within the range of experimental conditions i.e. below 60 °C. The Carreau-Yasuda equation modified by Bair (Carreau-Yasuda equation in the following) is the model chosen to fit to the experimental data [16]. Its expression is described in *I.4.3.d* and is reminded below:

$$\begin{array}{l} \text{Carreau-Yasuda modified by} \\ \text{Bair} \end{array} \quad \eta(\tau) = \eta_2 + \frac{\eta_0 - \eta_2}{\left(1 + \left(\frac{\tau}{G}\right)^a\right)^{\frac{1-n}{a}}} \quad \text{Eq. (31)}$$

This expression is applied with either a second Newtonian plateau viscosity ($\eta_2 \neq 0$) or not ($\eta_2 = 0$), depending on the presence or not of the onset of a second Newtonian plateau while looking at the experimental data. The calculated viscosities are plotted with black lines in Figure 36 to Figure 39, for shear stresses varying from 0.01 to 1000 kPa. Rheological parameters described by the Carreau-Yasuda model (the low shear modulus G , the numerical parameters a and n , the ratio between the second and first Newtonian plateau η_2/η_0) are detailed in Table 11. Both G and η_2/η_0 are here kept constant with temperature and pressure. However, these assumptions will be questioned later in this chapter, in *III.2.4*. Moreover, the low shear stress viscosities η_0 are also set as variable parameters, whose initial values are determined through the WLF equation adjusted on the high pressure viscometer data, as described in *II.2.1* (p. 58). The experimental data from the high pressure viscometer are thus plotted on Figure 36 to Figure 39 (empty colored symbols) to assess the consistency between the results obtained from the two devices.

The values of the parameters of the Carreau-Yasuda model, with or without a second Newtonian plateau are listed in the table below for all fluids. The viscosities computed with this model are in good agreement with experimental data, as confirmed by all *rms* values being below 4 %.

		<i>G</i> (kPa)	<i>a</i>	<i>n</i>	η_2/η_0	<i>rms</i> (%)
Base oil	$\eta_2 = 0$	515.6	0.002	1.000	-	1.6
OCP-LE	$\eta_2 = 0$	5.0	0.956	0.881	-	3.2
PISH-S	$\eta_2 \neq 0$	2.7	1.823	0.751	0.51	2.7
PISH-L	$\eta_2 \neq 0$	2.9	1.393	0.756	0.48	3.8
PAMA-C	$\eta_2 = 0$	8.3	0.988	0.975	-	2.0
PAMA-L	$\eta_2 = 0$	1.2	2.927	0.951	-	2.2

Table 11: Parameters of the Carreau-Yasuda model with ($\eta_2 \neq 0$) or without ($\eta_2 = 0$) a second Newtonian plateau

Different rheological responses were observed for each solution. First, in Figure 36, the experimental viscosity for the base oil does not vary with the applied shear stress. The lubricant will be thus considered as a Newtonian fluid, all along the explored experimental conditions: the Carreau-Yasuda model is here applied without a second Newtonian plateau ($\eta_2 = 0$). Experimental results from both high pressure devices are in good agreement on the plateau value of the base oil.

Conversely, the OCP-LE solution exhibits a large shear-thinning response within the range of experimental conditions. The low shear stress viscosity η_0 derived here from the Carreau-Yasuda fit should match the value previously determined from the WLF fit as the low shear stress values should not influence the solution response on the first Newtonian plateau. However, a difference of about 15 % appears between the viscosities from the two high pressure devices. This mismatch results from experimental uncertainties and approximations from the WLF calculation, even though it does not strongly impact the shear-thinning modeling. The latter is made without a second Newtonian plateau ($\eta_2 = 0$).

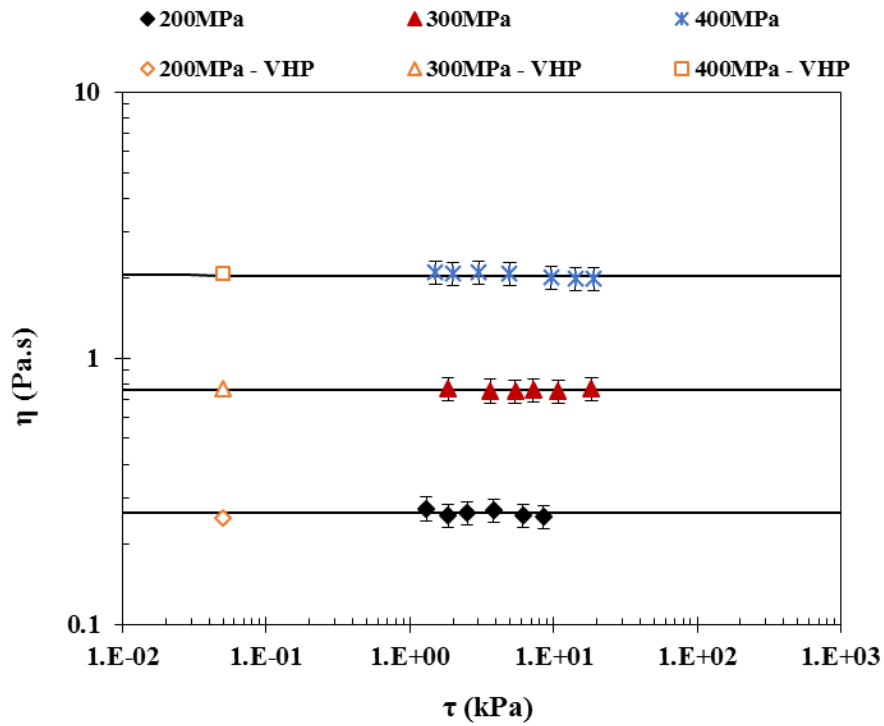


Figure 36: Viscosity of the base oil versus shear stress at 40 °C, from 200 MPa to 400 MPa and fitted by the Carreau-Yasuda model (black line)

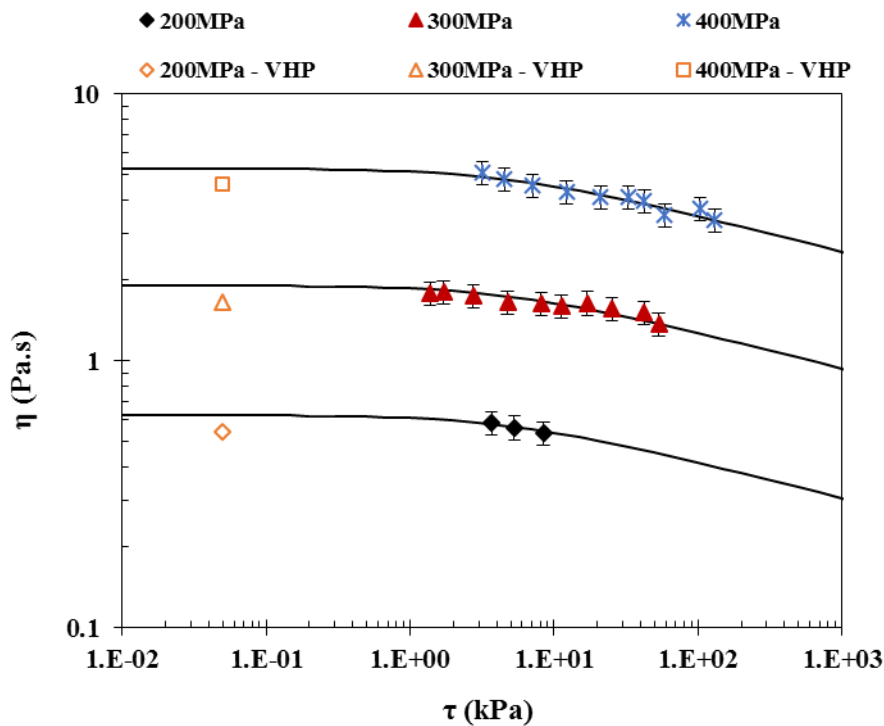


Figure 37: Viscosity of the OCP-LE solution versus shear stress at 40 °C, from 200 MPa to 400 MPa and fitted by the Carreau-Yasuda model (black line)

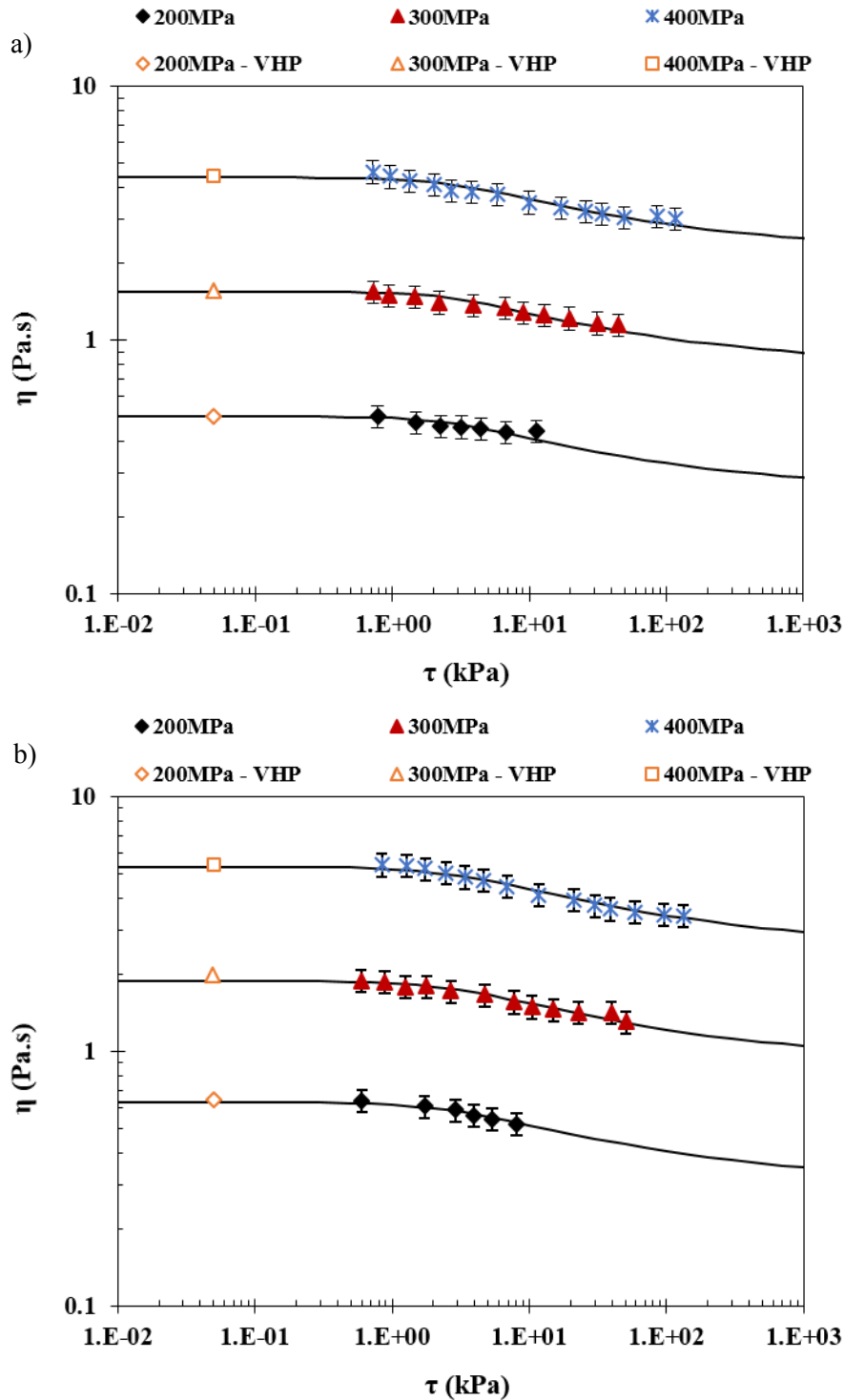


Figure 38: Viscosity of the PISHs solutions versus shear stress at 40 °C, from 200 MPa to 400 MPa and fitted by the Carreau-Yasuda model (black lines) – a) PISH-S, b) PISH-L

In Figure 38, both PISH solutions display a large shear-thinning behavior and the onset of a second plateau is present. The Carreau-Yasuda model was thus applied with $\eta_2 \neq 0$. Again, the calculated viscosities by the WLF model comply with the prediction of the first Newtonian plateau for both PISH solutions.

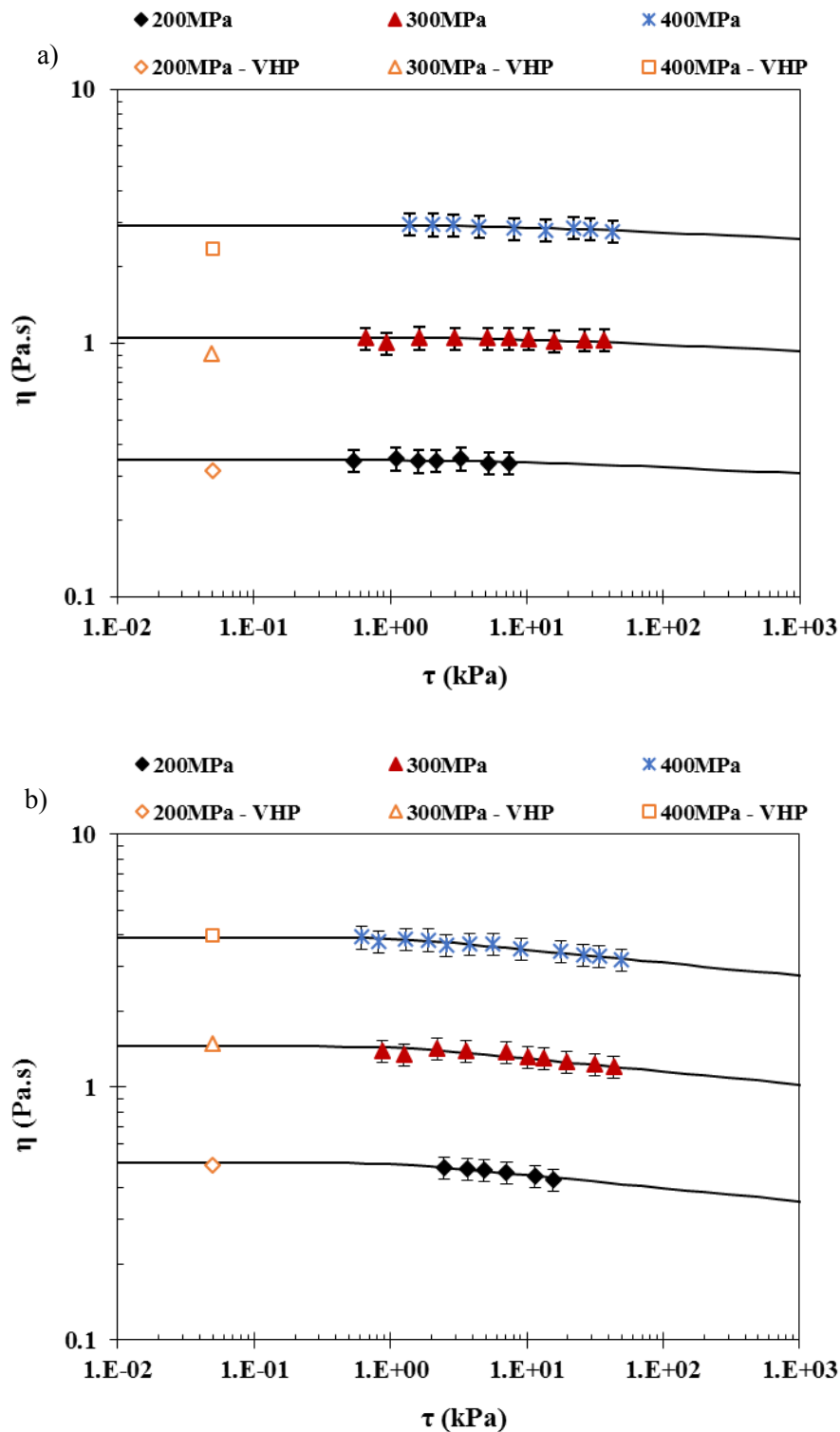


Figure 39: Viscosity of the PAMAs solutions versus shear stress at 40 °C, from 200 MPa to 400 MPa and fitted by the Carreau-Yasuda model (black lines) – a) PAMA-C, b) PAMA-L

Figure 39 a) highlights the almost Newtonian behavior of the PAMA-C solution, whereas in Figure 39b) the PAMA-L solution exhibits a weak shear-thinning tendency. The PAMA-C behavior is surprising as all polymers solutions are expected to shear-thin as described in 1.4.2 (p. 43). Likewise the OCP-LE solution, a deviation of about 20% is observed for the PAMA-C between the η_0 values derived from both WLF and Carreau-Yasuda models. However, shear-thinning extrapolations are not strongly affected by this mismatch. Flow curves of both solutions are fitted by the Carreau-Yasuda model without a second Newtonian plateau ($\eta_2 = 0$).

Noticeably, the rheological response depends on the polymer choice. The shear dependency of the solutions at 40 °C and 400 MPa is gathered on Figure 40 for all solutions. Clearly, shear-thinning is here much more important for the two PISH and the OCP-LE solutions than for the two PAMA ones. While considering the calculated viscosities, the latter decreases by 45 % for both PISH and by 55 % for the OCP-LE, whereas it only declines by 30 % and 10% for the PAMA-L and the PAMA-C respectively. In order to understand the origin of these discrepancies, it is necessary to consider the molecular structure of the polymer-base oil solution. Thus, the next section identifies the main parameters characterizing the solutions microscale and potentially influencing larger scales.

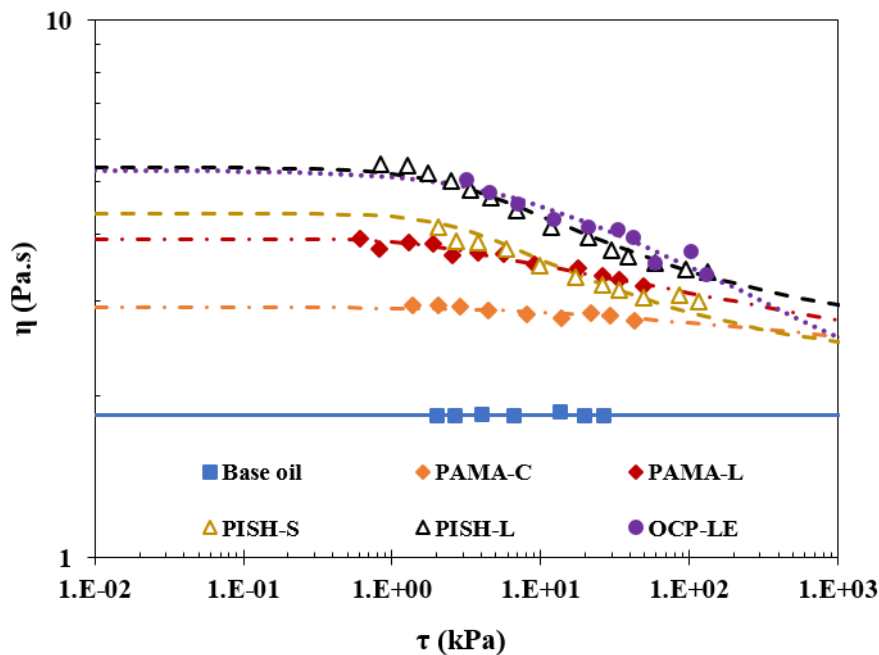


Figure 40: Comparison of the rheological response of the base oil and polymer solutions at 40 °C and 400 MPa – experimental data as colored dots and predicted viscosities as colored lines.

The different rheological responses of the base oil and polymer solutions are summarized in Figure 41.

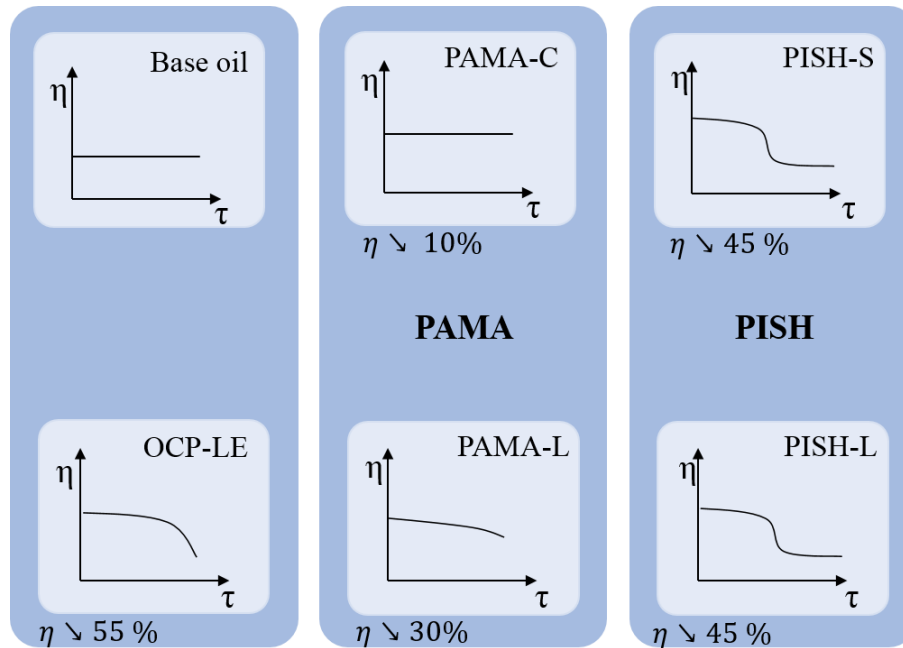


Figure 41: Summary of the rheological behaviors of the base oil and polymer solutions.

III.2 Relationship between the additive's structures and their rheological responses

In the previous section, different shear dependencies have been highlighted for all polymer-base oil solutions. The origin of these discrepancies can be apprehended by considering the solution microstructure, which is characterized by i) polymer geometrical considerations, ii) affinity between polymers and the base oil, iii) interactions between the macromolecules in solution.

In II.4.1 (p.67), all polymers solutions have been shown to belong to the diluted regime, where no interactions between the polymers occur and do not affect the macroscopic behavior of the solution. Only contributions i) and ii) will be thus detailed here. Several properties of polymer in solutions are considered: the polymers structure, the average molar mass and the hydrodynamic radius representative of the polymer conformation. These values are reminded in Table 12 below for each polymer solution.

	PAMA-C	PAMA-L	PISH-S	PISH-L	OCP-LE
R_h (nm) Einstein's law	8.9;	11.6;	20.0;	12.0;	13.0;
(25; 120 °C at p_{atm})	16.0	12.5	24.0	11.5	11.5
M_w (g.mol⁻¹)	678 800	332 000	689 600	113 000	87 300
Decrease of η (%)	10	30	45	45	55

Table 12: Characteristics of the polymers to apprehend the relationship between the VII structure and its rheological response - Hydrodynamic radii calculated from 25 to 120 °C at atmospheric pressure using the Einstein's law, the mass average molar mass of each VII and the viscosity decrease calculated between shear stresses from 10⁻² and 10³ kPa

III.2.1 Mass average molecular weight effects

The molecular average weight may be questioned to explain the different shear-thinning amplitudes, as higher molecular weight polymers are more susceptible to shear [54][99]. Moreover, several flow parameters (including the viscosities of the first and second Newtonian plateau) have been shown to be directly dependent on the molecular weight M_w [100]. Yet, the influence of M_w is only relevant while considering polymers of the same chemistry and structure [101]. Both OCP have similar molar average weight (about 87 000 g.mol⁻¹), however their shear-thinning behavior is different due to the occurrence of thixotropic effects in the OCP-HE mixture (see Figure 35). Conversely, both PISH display large shear-thinning behaviors, whereas their molecular weights are not similar (689 600 g.mol⁻¹ for the PISH-S and 113 000 g.mol⁻¹ for the PISH-L). The micelles formation of the PISH-L, described in *II.4* (p. 67), may explain its broad shear-thinning amplitude, as the polymer forms larger and star-shape alike coils comparable to those of the PISH-S. It is thus the polymer apparent structure in solution that explains its rheological behavior rather than its intrinsic properties.

It is known that the molecular weight M_w have an influence on the polymer viscosity. However, the different shear stress dependencies observed here cannot be directly linked to M_w as the polymers are too disparate. Polymers of same chemistry, conformations and behaviors in solution should be studied to highlight the molar mass influence. It may be then more relevant to look at the polymer behavior in solution, its size and conformation, to explain the various rheological responses

III.2.2 Conformation effect

In their paper [22], Mary et al. distinguish conformation effect and size effect to explain the rheological response of each polymer. When it comes to molecules with comparable sizes, the conformation effect (the impact of the molecule shape) can be investigated to explain the different behaviors. As a reminder, the OCP-LE is a linear polymer, the PAMA-L a linear polymer with short ramifications and the PAMA-C a comb polymer with long side chains. Although they have different molecular weights, PAMA-C, PAMA-L and OCP-LE have comparable hydrodynamic radii at 25 °C and p_{atm} (about 10 nm, Table 12), and all along the experimental range investigated with the high pressure rheometer. However, the OCP-LE solution exhibits a strong shear-thinning response, the PAMA-L an intermediate one, whereas the PAMA-C solution is almost Newtonian. The main difference between these polymers is linked to the various steric hindrance encountered and the polarity of the PAMA backbone (see Figure 42). Steric hindrance occurs when the congestion of the macromolecule due to its conformation prevents intermolecular reactions with the base oil that are observed in more flexible polymers, such as linear polymers. This effect, combined with the intramolecular interactions due to the PAMA-C amphiphilic nature, explain why the PAMA-C presents much less flexible macromolecules than the OCP-LE ones. This could explain the PAMA-C solution lower shear sensitivity, and its almost Newtonian behavior. The PAMA-L behaves between these two extremes, with rather flexible chains and weaker intramolecular interactions compared to the PAMA-C (Figure 42).

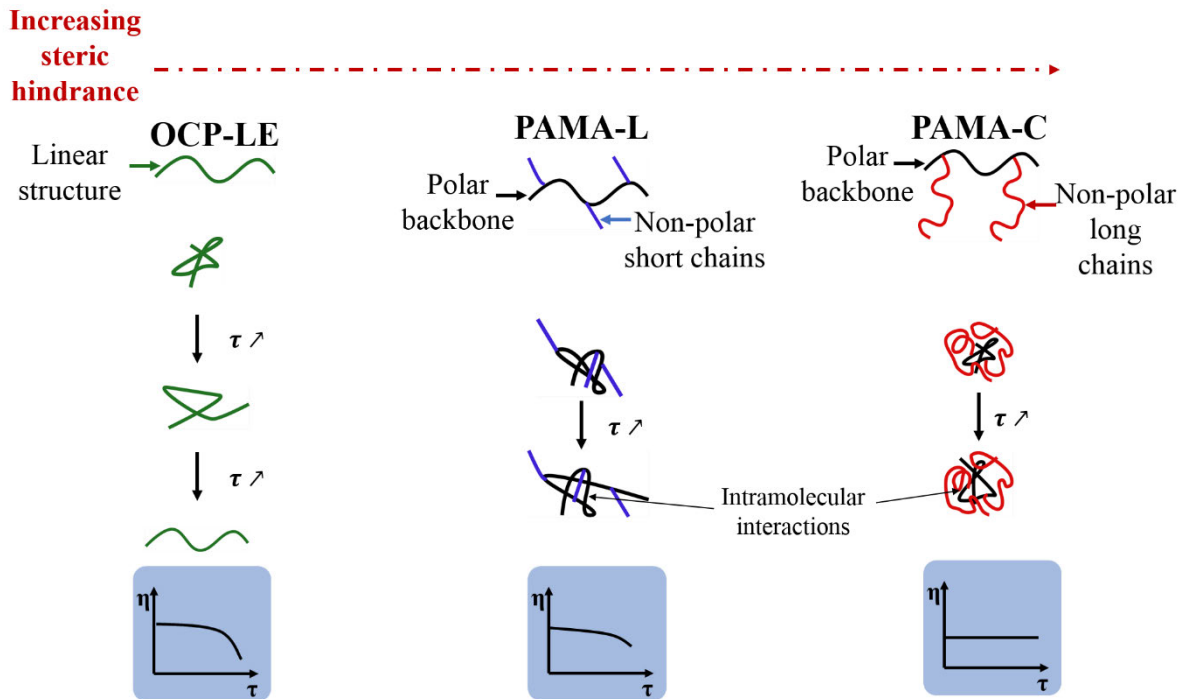


Figure 42: Schematic representation of the polymers responses with respect to the steric hindrance of their macromolecules and the intramolecular interactions

III.2.3 Size effect

Conformations considerations could explain the origin of the different shear dependencies observed for the PAMA and the OCP-LE. On the other hand, both PAMA-C and PISH-S additives have conformation implying strong steric hindrance and they present very different rheological responses. However, these two polymers present rather different sizes while in solutions, as detailed in II.4 (p. 67). Indeed, the calculated PISH-S hydrodynamic radii are larger than the PAMA-C ones at each temperature (about 25 nm against 10 nm) and both solutions are in similar conditions of solvation (theta solvent). According to [78], shearing implies a drop of viscosity for larger molecules of comparable intramolecular bonds, which explains then these different behaviors.

It is also interesting to mention that the PAMA-C was identified as the most efficient VII while considering its properties at low shear stress only. However, its viscosity appears to be almost independent from the shear stress, within the domain investigated in this work. The PISH-S could be an appealing compromise, by providing a mild VII effect and an important shear-thinning response in order to provide an energy-efficient lubricant to reduce wear between two surfaces exposed to a high shear condition. Even though the normal stress is not studied in this work, it should be mentioned that shear thinning induces a discrepancy between the normal stress in the flow direction and the cross-film direction. The load capability of a lubricant film may then rise without experiencing increasing frictional losses [102].

III.2.4 Limits of the Carreau model

In II.4 (p. 67), the swelling of polymer coils, as for the PAMA-C, was shown to enhance the VII properties. This behavior is difficult to replicate using the Carreau-Yasuda expression. Indeed, this model requires many parameters to be determined and relies on rather strong assumptions. In particular, the shear modulus G and the ratio between the first η_0 and second Newtonian plateau η_2 are both kept constant at any temperature and pressure. As previously mentioned, PAMA-C molecules are fully swelled at high temperature (above 80 °C): they should exhibit a higher shear sensitivity at temperature above the swelling one and a shear-thinning response may then be expected at high shear stress. Therefore, the ratio between the two plateaus values may be affected by temperature in the case of polymers showing effective VII's properties. Unfortunately, this hypothesis could not be tested as the swelling temperature of PAMA-C is above the device capabilities. Another PAMA comb was thus investigated, whose particularity is to start swelling at lower temperature (60 °C). To lighten the manuscript and avoid any confusion with other products, this study is given in Appendix 8. It should be however mentioned that this investigation did not provide any significant results, as the swelling temperature of this PAMA comb is too close of the device limitations. Moreover, no measurements above 30 kPa could be carried out at 60 °C, limiting the possibility to witness the onset of a shear-thinning response. Nonetheless, the possibility of a variable η_2/η_0 can also easily be evaluated with Ultra Shear Viscometer experiments carried out on the simplified lubricants.

Ultra Shear Viscometer (USV, depicted in Appendix 2) experiments were ran from 40 to 150 °C, at atmospheric pressure and from 10^6 to 9.10^7 s⁻¹. Figure 43 gathers for the PISH-S and PAMA-C solutions, the viscosity results against shear stress obtained through different devices at different temperatures and at ambient pressure. The first Newtonian plateau η_0 is plotted as a colored line at each temperature. The viscosity decrease (reported on the figures right side) is calculated as the ratio between the experimental viscosity at the highest shear rate and η_0 at each temperature. It must be noted that the second Newtonian plateau may not be reached here and that the shear-thinning amplitude may be more important. Nonetheless, it is interesting to notice that the viscosity loss of the PISH-S solution is almost constant, whereas it increases with increasing temperature for the PAMA-C solution. These observations confirms our concern about the previous assumption, *i.e.* the η_2/η_0 ratio may vary with temperature.

As PAMA and VII presenting swelling temperatures are more and more used in lubricants formulation, the Carreau-Yasuda rheological model might be not appropriate and therefore inaccurate, leading for instance to unsatisfactory film thickness predictions. An alternative approach should then be considered.

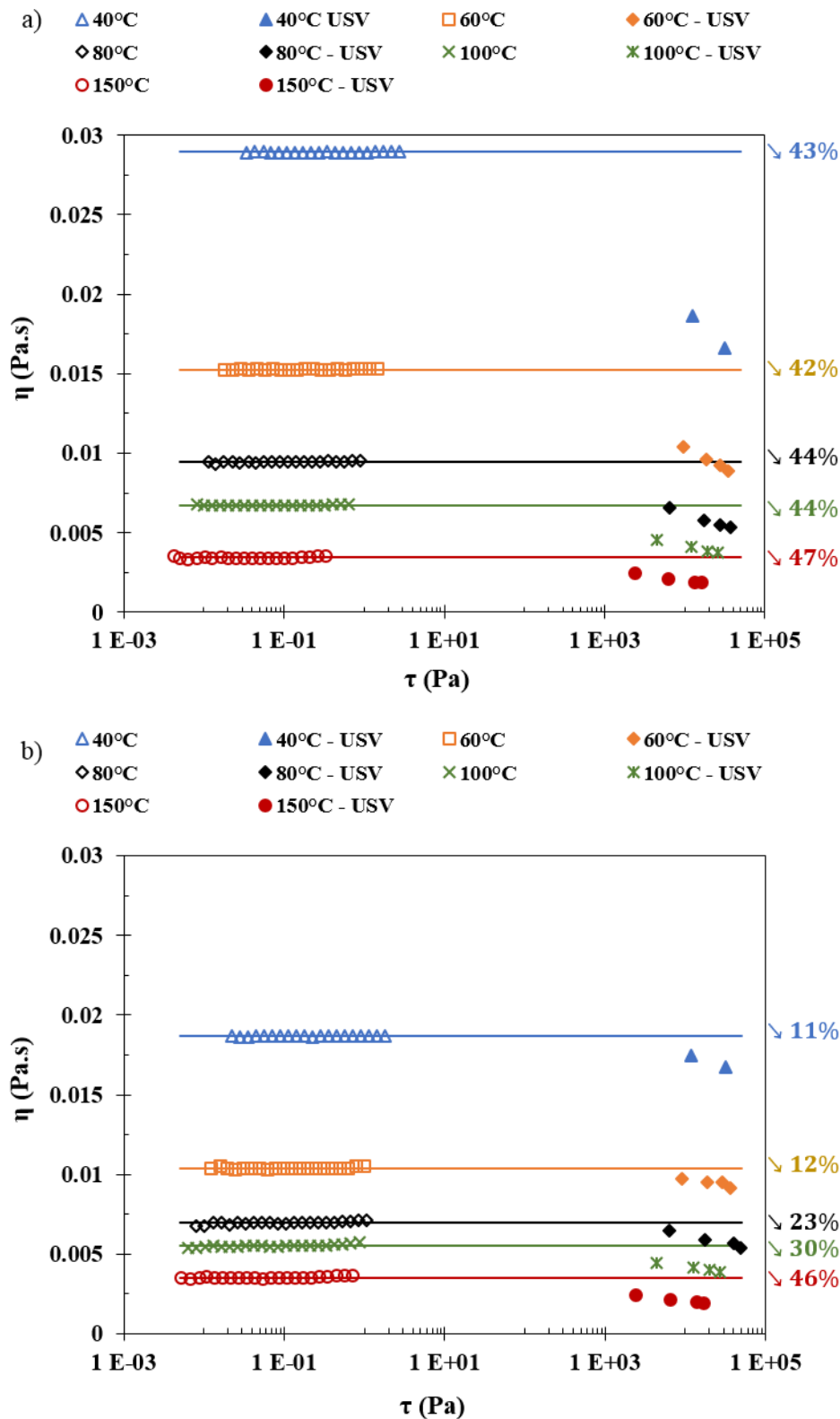


Figure 43: Experimental viscosity against shear strain rate from different devices – from the Physica MCR301 (empty colored dots), the USV (colored dots). Experiments were carried out from 40 °C up to 150 °C at atmospheric pressure. The colored lines stand for the first Newtonian plateau η_0 extrapolation in order to appreciate the viscosity decrease, which is calculated between η_0 and the highest shear-rate USV value – a) PISH-S, b) PAMA-C

III.3 Zhang model for low viscoelastic solutions

III.3.1 Model and experiments

The Zhang equation [17], detailed in *I.4.3.d* (p. 47) and reminded below, describes the shear rate influence on viscosity, based on the Maxwell model for fluids exhibiting strong viscoelastic behavior and takes into account the variations of the shear modulus G .

$$\begin{aligned} \eta(\dot{\gamma}) &= \frac{\eta_0}{\left(1 + \left[\frac{\eta_0 \dot{\gamma}}{2 \cdot G(T, p, \dot{\gamma})}\right]^2\right)} \\ G(T, p, \dot{\gamma}) &= G_0 + \beta \eta_0(T, p) \dot{\gamma} \end{aligned} \quad \text{Eq. (32)}$$

As previously mentioned, the shear-thinning amplitude depends only on the parameter β , which should be less than 0.5 according to the author [17]. This implies that the measured viscosity η should decrease about half compared to the viscosity of its first Newtonian plateau, which is not the case for most of the solutions studied here. The application to low-viscoelastic solutions such as the simplified lubricants studied considered in the present work needs to be verified. The Zhang model is first fitted to the experimental data. Then, all the values resulting from the Zhang model are compared to the Carreau-Yasuda expression in order to validate the application of the former to less viscoelastic products.

First of all, the experimental data and the viscosities calculated from the Zhang model are shown in Figure 44, only for the PISH-S solution. The comparisons for the other solutions can be found in Appendix 9. The dynamic viscosity η is here plotted against shear strain rate $\dot{\gamma}$ at 40 °C and from 200 to 400 MPa. The viscosity predicted by the Zhang expression is then calculated for shear strain rates varying from 10 to 1.10^6 s^{-1} . The values of the parameters of the Zhang equation are listed in Table 13 for all solutions. The initial shear modulus G_0 and the dimensionless parameter β were determined by curve fitting to rheological model. The shear-thinning amplitude is only linked to the parameter β , the lower the parameter the larger the shear-thinning.

	G_0 (kPa)	β	rms (%)
OCP-LE	8.0	0.66	5.75
PISH-S	4.56	0.68	3.05
PISH-L	5.28	0.68	3.86
PAMA-C	50.17	1.33	1.96
PAMA-L	4.78	1.03	2.06

Table 13: Parameters of the Zhang model

Even though the solutions studied don't exhibit the requested viscoelastic behavior characterized by the value $\beta > 5$, the calculated viscosities are in good agreement with the experimental data, with the rms value being below 6 %. The comparison to the Carreau-Yasuda predictions aims to validate the application of the Zhang expression to solutions that exhibit low shear-thinning response, such as those studied in this work.

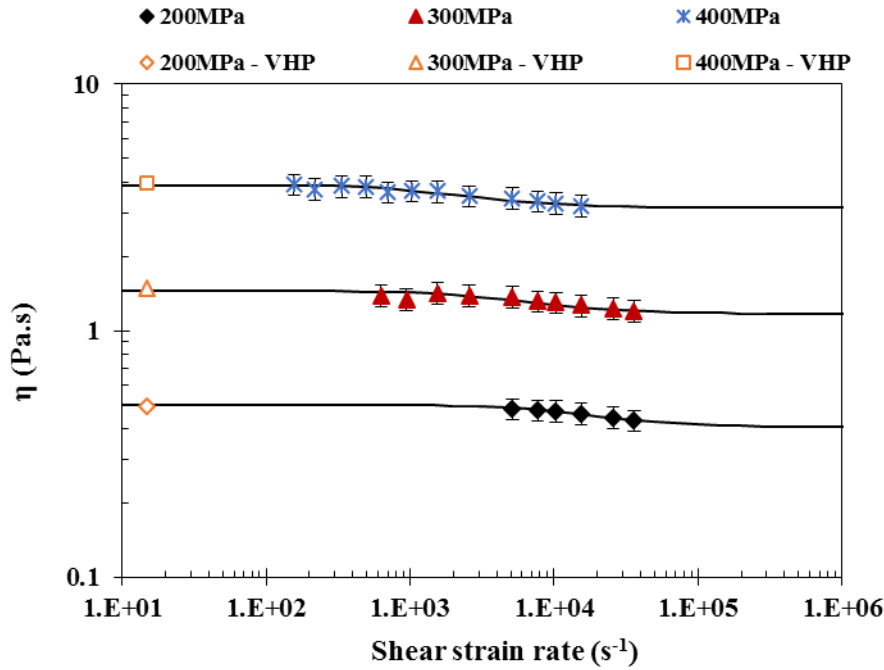


Figure 44: Viscosity of the PISH-S solution versus shear strain rate at 40 °C, from 200 MPa to 400 MPa and fitted by the Zhang model (black line)

III.3.2 Comparison to Carreau predictions

In this paragraph, the viscosities computed from Zhang's expression are compared to the Carreau-Yasuda predictions in order to validate their application to low-viscoelastic solutions. To easily compare both models, master curves are presented for the PAMA-C and OCP-LE solutions (Figure 45, Figure 46), where all the viscosities at each condition of temperature and pressure overlap on a single curve. These master curves are obtained by dividing the viscosity of the fluid by its viscosity at low shear stress. This normalized viscosity is then plotted against shear stress, as representing it against shear rate does not superimpose the data properly [5]. The advantages of the Zhang model and limits of the modeling are illustrated by these graphs.

As it can be seen in Figure 45, the viscosities calculated using the Zhang model are in good agreement with the Carreau-Yasuda predictions, which seems to be promising for VII application. The regression made with the Zhang equation gave results as good as those obtained using the Carreau-Yasuda one according to the *rms* values reported in Table 11 and Table 13. Moreover, no assumption was made on the value of the second Newtonian plateau η_2 , which is a significant advantage. The shear modulus G_0 prediction for the PAMA-C solution is five times larger than the G from the Carreau-Yasuda expression, although this result was expected as the Zhang model is here applied to an almost Newtonian solution. Unfortunately, it is not possible to say which G prediction is the most relevant, as the shear modulus can't be independently determined experimentally yet for the solutions studied. However, G_0 calculated from the Zhang expression is physically more coherent because its variations upon temperature, pressure and shear rate are explicitly taken into account. Finally, the Zhang model needs less parameters, whose physical significations are better defined. As the limitations of the Carreau-Yasuda model – i.e. keeping the shear modulus and the ratio between the two plateaus constants - mainly concerned VII which swell with temperature (such as the PAMA-C), these results are really promising for similar applications.

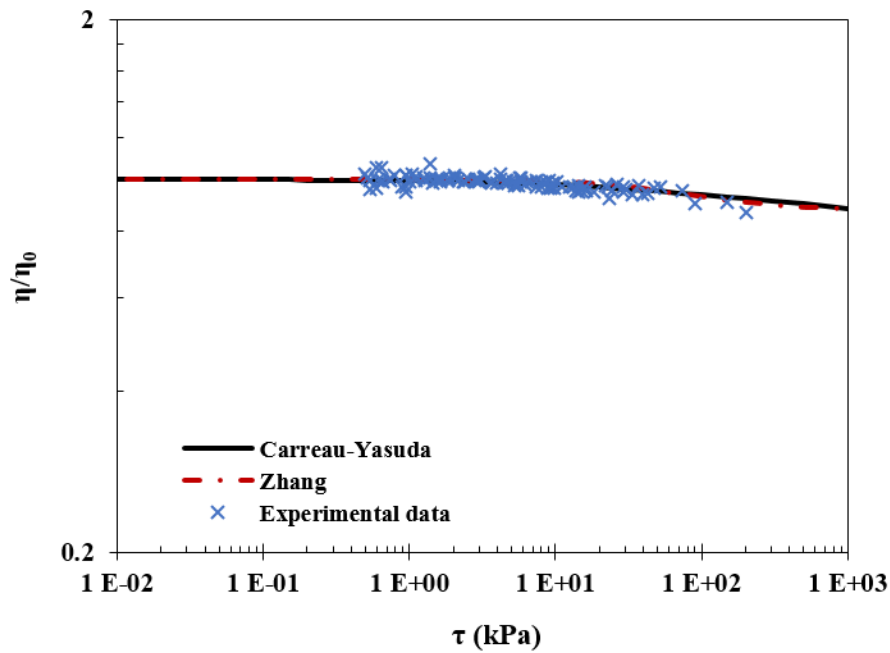


Figure 45: Comparison between the Carreau-Yasuda predictions, the Zhang's results and the master curve resulting from the experiments carried out at different temperatures and pressures for the PAMA-C solution.

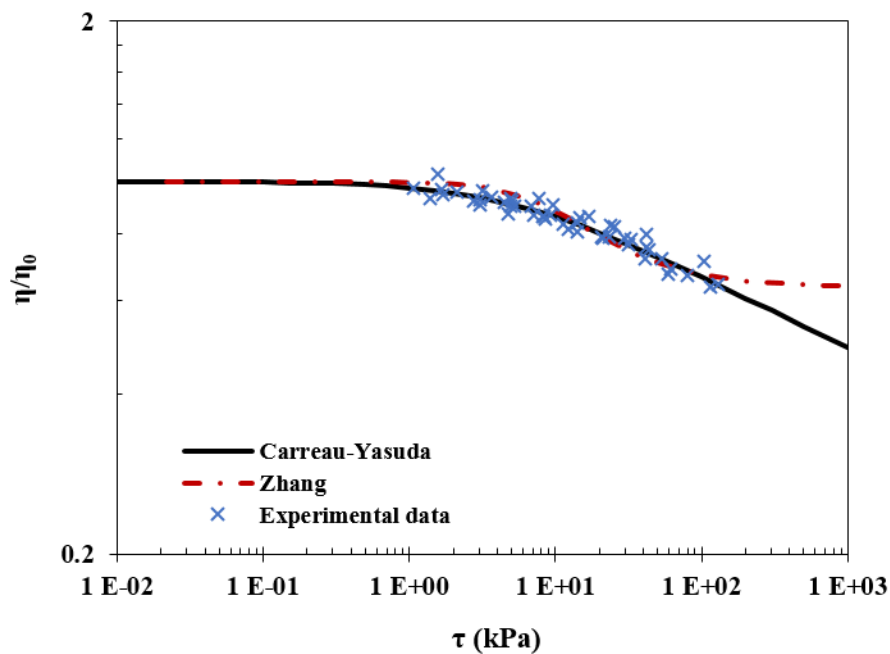


Figure 46: Comparison between the Carreau-Yasuda predictions, the Zhang's results and the master curve resulting from the experiments carried out at different temperatures and pressures for the PAMA-C solution.

Regarding the OCP-LE results (Figure 46), the experimental data fit well with both expressions though extrapolated viscosities are different above 100 kPa. The results show indeed different behaviors according to the chosen model. A second Newtonian plateau is always present when fitting data with the Zhang equation due to its construction whereas an important and continuous shear-thinning response is observed with Carreau-Yasuda predictions. This discrepancy highlights one of the limitations of this particular modeling due to experimental constraints. In most cases, a second plateau or its onset should be expected at very high shear stress, but it cannot be reached experimentally yet. It is thus not possible to say if the viscosity drop is over or underestimated here by either of the models. Same comment is made for all other solutions, PAMA-L, PISH-S and PISH-L, whose similar master curves can be found in Appendix 10.

The Zhang model could be a good alternative to the Carreau-Yasuda one for polymers which exhibit different shear-thinning behavior with temperature variations. Less parameters are necessary, no assumptions on the second Newtonian plateau are made and the shear modulus G is not kept constant. However, experimental characterization of the second Newtonian plateau would be necessary to improve the full viscosity extrapolation of both models studied here, as well as experiments at higher temperature to validate the assumption of the shear-thinning variations above the polymers swelling temperature.

III.4 Conclusion

Experiments carried out on the high pressure rheometer provided the rheological response of a base oil and polymer-base oil mixtures over a large range of shear stress at different temperatures and pressures. The dependence of the viscosity on shear stress was represented by different rheological models, with a reasonable agreement to the experimental data.

Different rheological responses were highlighted regarding each considered additive and are summarized in Figure 41. An almost Newtonian behavior was noticed for the PAMA-C solution, within the investigated range of experimental conditions. Size and conformations considerations at the molecular scale explained why this polymeric additive didn't show any shear-thinning response unlike the other VIIs studied. At comparable sizes, conformation effects prevailed and explained the different behaviors of both PAMAs and OCP-LE solutions. The linear molecule (OCP-LE) was more shear-sensitive than the comb polymer (PAMA-C) because of the latter strong steric hindrance and intramolecular bonding, whereas the PAMA-L with its short side chains was an intermediate case.

Moreover, both PISH-S and PAMA-C polymers were difficult to stretch because of their conformation at low temperatures. However, PISH-S's molecules were larger than PAMAs' ones: they were then more stretchable and affected by shear stress.

On the other hand, PAMA-C's macromolecules swelled at higher temperature than those studied and once fully swelled, they should be more shear-sensitive. A shear-thinning response may thus be expected above the swelling temperature of a VII. The ratio between the two plateaus, kept constant in the Carreau-Yasuda model should be affected by a temperature variation. USV results showed a confirmation of this assumption. The Zhang model was then applied to solutions with low viscoelastic behaviors. Results were promising and applying this model to solutions of viscosity index improvers could be a good alternative to the widely used Carreau-Yasuda equation, even though experimental data at higher shear stress and temperature would be required.

While the PAMA-C was identified in a previous chapter as the most interesting VII at low shear stress, the PISH-S appears to be a good compromise. This latter may be considered as a rather low VII but it exhibits a large shear-thinning behavior. Such product could also be interesting in function of the applications and specifications sought by car manufacturers. It may also be possible to extrapolate these models and observations to fluids with similar base oils and polymers, in order to guide oil manufacturer in the correct choice of base oil and polymers.

For each lubricant, it is now possible to accurately predict its rheological behavior in conditions representative of those found in a contact. This will be explored in the following chapter, through a complete tribological study.

Chapter IV – Tribological response of polymer solutions in elastohydrodynamic and thin film regimes

IV.1	Films thickness measurements method	99
IV.1.1	Differential colorimetric interferometry principle.....	99
IV.1.2	Description of the classical EHL analytical models.....	102
IV.1.3	Operating conditions	103
IV.2	Film thickness results.....	104
IV.2.1	Tribological response of the base oil.....	104
IV.2.2	Tribological behavior of polymer solutions	106
IV.3	Thin film lubrication regime	111
IV.3.1	Approach	111
IV.3.2	Discussion on the PAMA-L in TFL	112
IV.3.3	Discussion on the PAMA-C in TFL.....	115
IV.3.4	Discussion on the OCP-LE and parameters influencing the thin layer formation	118
IV.3.5	Discussion on the PISH-S limitations	120
IV.4	Conclusion.....	122

An automotive engine is a complex device composed of a broad variety of mechanical elements, in which the encountered physical and mechanical conditions are diverse and severe, leading to complex tribological behaviors. In elastohydrodynamic lubrication (EHL in the following), the two sliding surfaces are supported by a full film of lubricant, whose performance is closely linked to its rheology. It is thus of main interest to understand how the different rheological behaviors of polymers solutions highlighted in the previous chapters, affect their tribological responses in realistic engine conditions.

This last chapter provides film thickness measurements of the polymer solutions. It also aims to link their rheology response, as well as the additives physico-chemistry, to their tribological behaviors. Precedent studies were run by Mary [10] on similar products, for film thicknesses between 100 nm and 600 nm. No significant impact of the polymer addition on the base oil tribological response was however noticed. It was thus decided here to run experiments at lower film thicknesses, down to 15 nm, in conditions that simulate a lubricated contact in EHL and also in thin film regimes.

IV.1 Films thickness measurements method

This section describes the method employed for obtaining the film thickness results and the semi analytical models used for film thickness predictions.

IV.1.1 Differential colorimetric interferometry principle

The film thickness experiments were carried out on the Jerotrib test-rig, fully described in Appendix 11. The chosen configuration for this work is a ball-on-disc contact. The measurement principle developed by Molimard et al [23][24], called differential colorimetric interferometry (DCI), is based on white light optical interferometry, one of the most effective techniques for measuring lubricant film thickness [36].

The lubricated contact is formed by loading and rolling a mirror-polished steel ball against the surface of a coated glass disc. The monochromatic interferometry is introduced as it is here easier to explain the DCI technique. An incident light I_0 is shone through the transparent disc into the contact area, where it is successively distributed at the disc surface between a partially transmitted and a partially reflected beam, leading to light beams of various intensities I_1 to I_n . The retrieved light beams interfere constructively or destructively with each other, after traversing the film thickness. The basic principle of monochromatic interferometry is shown in Figure 47.

The values of intensities I_n can be neglected for a number of reflected and transmitted light beams superior to 2. The intensity I recovered on the detector is directly linked to the distance between the ball and the disc (i.e. the film thickness h) [103]. The intensity value I is given below for an incident wavelength λ_i and n_0 the lubricant refractive index:

$$I = I_1 + I_2 + 2\sqrt{I_1 I_2} \cos \left[2\pi \left(\frac{2n_0 h}{\lambda_i} + \varphi_1 \right) \right] \quad \text{Eq. (34)}$$

Where φ_1 is the phase shift due to reflection onto the steel spherical surface.

However, techniques based on monochromatic interferometry involve some inaccuracy mostly due to the periodicity in trigonometric functions, fringe order dependence and sensitivity defects. These limits can however be overcome by the differential colorimetric interferometry technique, in which a white light source generates the colored intensity beams and each component of the RGB intensities is analyzed [104][37]. Since no explicit optical law such as Eq. (34) exists for the full white light spectrum, the film thickness is obtained by color matching between interferograms (see Figure 48) and an experimental calibration curve based on an analytical formula of the deformed gap of a circular static contact [105]. This calibration curve establishes the dependence of the film thickness h upon the RGB intensity triplet (intensity of the Red, Green and Blue wavelengths respectively) when both ball and disc are stationary (see Appendix 11).

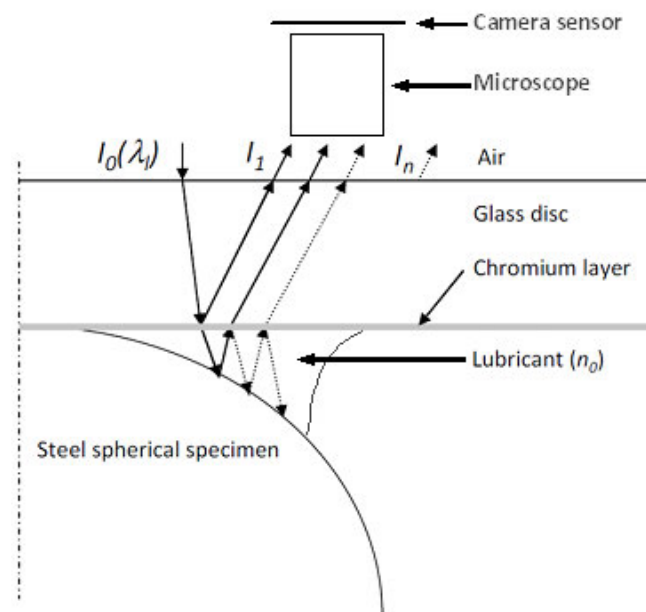


Figure 47: Basic principle of monochromatic optical interferometry [103]

To obtain reliable calibration curves, the disc is here coated with a metallic chromium layer in order to increase the reflection at the interface between the disc and the lubricant of the light beams and improve the contrast [106][107][108]. The chromium layer is homogenous over the disc surface, in contact with the lubricant and is about 17 nm thick. The layer thickness is close to the theoretical optimal of 20 nm, which corresponds to an optical transmittance of 30 % [108]. The calibration curve is obtained from an interferogram of a slightly loaded static contact between the ball and the chromium coated disc. However, the shape of this curve shows that no accurate film thickness measurements can be carried out below 60 nm, where all R, G and B intensities simultaneously reach their minimum and the resolution is zero.

Another disc, coated with both a chromium layer and a spacer layer, can be used to reach lower film thickness. The silicon dioxide SiO_2 “spacer layer” overlays the chromium thickness and is about 70 nm thick. The spacer layer covers the entire surface of the disc, except an external radial strip. The measurement method consists in the following steps [24]:

- First, the calibration curve is obtained on a static contact, which is located on the chromium layer only.
- Then, the spacer layer thickness area is loaded against the static steel ball.
- Interferograms of dynamic contacts are thus acquired to determine the combined silica plus lubricant film thickness.
- Finally, the silica layer is subtracted from previous evaluations to determine the lubricant film thickness at the center of the contact h_c and at the side lobes area, where it reaches its minimal value h_{min} .

The film thickness evaluation process is depicted in Figure 48.

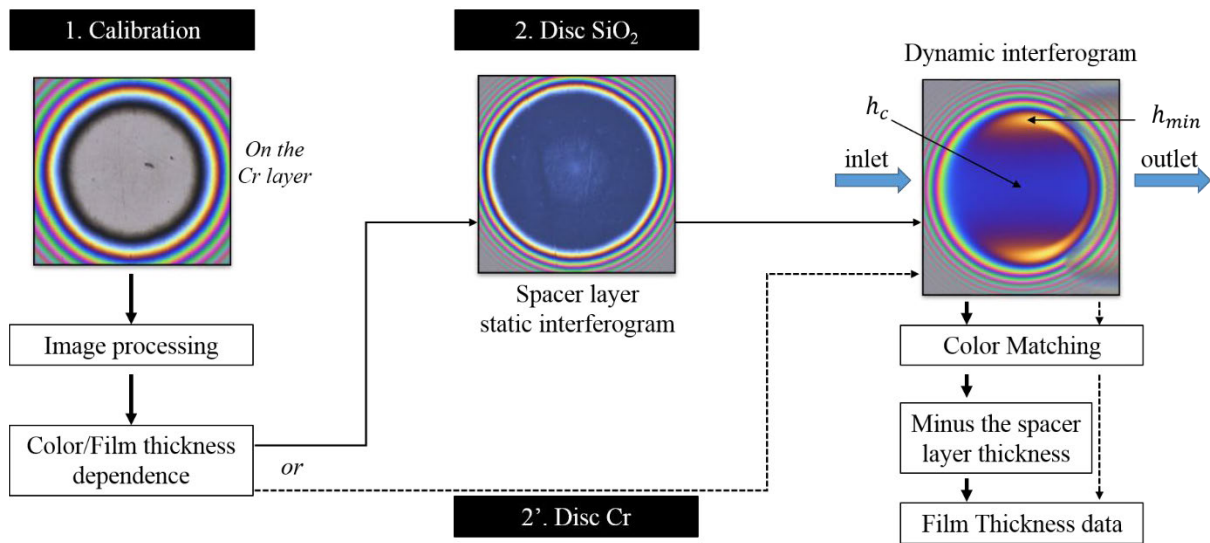


Figure 48: Block diagram of the film thickness evaluation process.

Both glass discs used in this work have a composite RMS roughness of about 3nm but are made of different materials. The chromium coated only disc (called “disc Cr” in the following) is a BK7 glass one, whereas the disc with a spacer layer (called “disc SiO₂” in the following) is made of S-BSL7. In this work, the lubricated contact is created between one of the disc mentioned above and a 12.7 mm radius, 100C6 steel ball, which was carefully polished leading to a RMS roughness R_q below 5 nm. A 3CDD high resolution color camera and an optical microscope are used to collect the reflected white light beams. The properties of the materials are reported in Table 14.

	Material	R_q (nm)	E' (GPa)	ν_p	ρ (kg/m ³)	c_p (J.kg ⁻¹ .K ⁻¹)	k (W.m ⁻¹ .K ⁻¹)
Disc Cr	BK7 +17 nm Cr layer	3	81	0.208	2510	858	1.114
Disc SiO₂	S-BSL7 + 17 nm Cr layer + 70 nm SiO ₂ “spacer layer”	3	80	0.205	2520	858	1.126
Steel ball	100C6	3 to 5	210	0.3	7850	470	46

Table 14: Material properties of the ball and discs used in Jerotrib [40]

IV.1.2 Description of the classical EHL analytical models

The experimental work of this project aims to provide and analyze the tribological behavior of the base oil and polymer solutions. Film thicknesses are thus compared to semi analytical predictions, using the viscosities and pressure-viscosity coefficients previously determined (II.2, p. 58).

Several semi analytical expressions have been proposed to predict film thicknesses in EHD contacts. Chittenden [25], Moes *et al* [26] and Chevalier [27] solved the EHD problem for circular contacts under pure rolling and isothermal conditions, lubricated by a Newtonian fluid.

The Chittenden equation [25](Eq. (37)) is here employed for the determination of central film thicknesses h_c . In [109][110], van Leeuwen stated that this expression was the most accurate for both moderately loaded and highly loaded circular EHD contacts. Wheeler *et al.* [38] confirmed the previous statement by comparing various analytical expressions to full EHD numerical model for 5 reference cases, in which the Chittenden expression was again in excellent agreement with numerical predictions (relative deviations within 3 %). The Chittenden equation [25] is a modification of the Hamrock and Dowson expression [111]. Three dimensionless parameters are defined by associating the operating and material parameters. This allows the complete description of a typical circular contact EHD problem. The dimensionless speed U_C , the load W_C and the material properties G_C are defined below:

$$U_C = \frac{\eta_0 U_e}{E_{eq} R_{ball}} \quad W_C = \frac{W}{E_{eq} R_{ball}^2} \quad G_C = \alpha^* E_{eq} \quad \text{Eq. (35)}$$

Where W is the load, E_{eq} the reduced Young modulus of the sliding surfaces (described in Appendix 12), R_{ball} the ball radius, α^* the pressure-viscosity coefficient (defined in I.4.3.b, p. 46) and η_0 the Newtonian viscosity at low shear stress and atmospheric pressure. Both α^* and η_0 are computed from the modified WLF-Yasutomi model (Eq. (27), p. 58, called WLF model in the following) [14]. The entrainment speed U_e is equal to the mean of the speeds of the ball U_{ball} and the disc U_{disc} .

The dimensionless film thickness H_C is given below, as well as the coefficient K for central film thickness calculation:

$$H_C = \frac{h_c}{R_{ball}} \quad K = 4.31(1 - e^{-1.23(R_y/R_x)^{2/3}}) \quad \text{Eq. (36)}$$

These equations are valid only when $R_x < R_y$.

The Chittenden equation for the central film thickness is thus written as follows:

$$H_C = K U_C^{0.68} W_C^{-0.073} G_C^{0.49} \quad \text{Eq. (37)}$$

Moes [26] proposed two analytical parameters, the dimensionless load M_{Moes} and material properties L_{Moes} , by combining the previous dimensionless Chittenden parameters to describe an EHD contact. The Moes parameters are detailed below, as well as the dimensionless Moes film thickness H_{Moes} :

$$M_{Moes} = \frac{W_C}{(U_C)^{3/4}} \quad L_{Moes} = G_C(U_C)^{1/4} \quad \text{Eq. (38)}$$

$$H_{Moes} = \frac{h}{R_{ball}\sqrt{U_C}} \quad \text{Eq. (39)}$$

The Moes equation for central film thickness is defined as follows:

$$H_{Moes}^{center} = \left[\left(\{1.70tM_{Moes}^{-1/9}L_{Moes}^{3/4}\}^r + \{1.96M_{Moes}^{-1/9}\}^r \right)^{s/r} + (47.3M_{Moes}^{-2})^s \right]^{1/s} \quad \text{Eq. (40)}$$

Where

$$\begin{aligned} r &= \exp[1 - 6/(L_{Moes} + 8)] \\ s &= 12 - 10\exp[-M_{Moes}^{-2}] \\ t &= 1 - \exp[-0.9M_{Moes}^{1/6}/L_{Moes}^{1/6}] \end{aligned}$$

The minimum film thickness h_{min} is here calculated from the Moes equation above (Eq. (40)) divided by a ratio deduced from the Chevalier table [27], as functions of the Moes parameters M_{Moes} and L_{Moes} [112]. These predictions are valid for a wide range of M_{Moes} and L_{Moes} , even though the h_{min} calculation is less accurate than the h_c one from the Chittenden expression [112], according to [38].

IV.1.3 Operating conditions

This section provides the tribological study of the base oil and a selection of polymer solutions. The PAMA-C was selected since it was identified as the most efficient VII studied in this work, with an almost Newtonian behavior along the experimental conditions studied (from 200 MPa to 400 MPa and below 60 °C). Similarly, the OCP-LE was also chosen since it was considered as a thickener rather than a VII, with a strong shear-thinning behavior. Both PAMA-L and PISH-S were picked as they exhibit intermediate properties.

The experimental conditions are detailed in Table 15 below. Pure rolling conditions were chosen, meaning that the slide-to-roll ratio (SRR) is equal to zero.

$$SRR = 2 \frac{U_{ball} - U_{disc}}{U_{ball} + U_{disc}} \quad \text{Eq. (41)}$$

	Disc Cr		Disc SiO ₂	
Temperature (°C)	25	75	25	75
Entrainment speed U_e (m/s)	0.35 – 5.14	1.90 – 6.49	0.02 – 0.77	0.10 – 3.83
Load W (N)	27		27	
Hertzian pressure p_H (GPa) (see Appendix 12)	0.5		0.5	
SRR	0		0	

Table 15: Experimental conditions for film thickness measurements

The two discs previously described were used, the “disc Cr” to cover central film thicknesses between 100 and 600 nm, and the “disc SiO₂” for thin films below 200 nm. The experiments on “disc SiO₂” were run twice. The film thickness is obtained by matching the measured intensities to the calibration curve, of five different interferograms at each entrainment speed. Moreover, the important pressure variations within the contact induce a density elevation. Therefore, the lubricant refractive index n_0 at atmospheric pressure changes and involves a modification of the optical path length [103]. The central film thickness must thereby be corrected as follows:

$$h(p) = \frac{n_0}{n(p)} h_0 \quad \text{Eq. (42)}$$

Where $h(p)$ and $n(p)$ are respectively the film thickness and the lubricant refractive index at the pressure p and h_0 is the film thickness at atmospheric pressure. Only the central film thickness is here adjusted. Indeed, the corrected central film thickness is lowered by 6 % compared with the non-corrected value under the applied load of 27 N (i.e. a Hertzian pressure of 500MPa), whereas the minimum film thickness is not impacted as the pressure at the side lobes region is assumed to be close to atmospheric pressure. The refractive index $n(p)$ is corrected using the Lorentz-Lorentz formula [113]:

$$\frac{1}{\rho(p)} \frac{n(p)^2 - 1}{n(p)^2 + 2} = \frac{1}{\rho_0} \frac{n_0^2 - 1}{n_0^2 + 2} \quad \text{Eq. (43)}$$

Where ρ_0 is the mass density at atmospheric pressure. At a given temperature, the mass density $\rho(p)$ at pressure p follows the Dowson Higginson equation, defined below:

$$\rho(p) = \rho_0 \frac{5.9 \cdot 10^8 + 1.34p}{5.9 \cdot 10^8 + p} \quad \text{Eq. (44)}$$

IV.2 Film thickness results

This section deals with the film thickness results obtained on the Jerotrib test-rig and their comparison to the analytical predictions by the previously described model. The actual influence of polymers on the film thicknesses generated by different lubricants is then discussed.

IV.2.1 Tribological response of the base oil

The following log-log graphs show the evolution of the experimental central and minimum film thicknesses against the entrainment speed at 25 °C and 75 °C, for the base oil only. The three different run are presented, apart from the results at 75 °C as only one experiment with the “disc SiO₂” is available. Analytical predictions are also plotted to provide visual comparison. The Chittenden solution [25] for h_c is plotted as a black line, whereas the red line stands for the Moes and Chevalier [26][27] predictions for h_{min} .

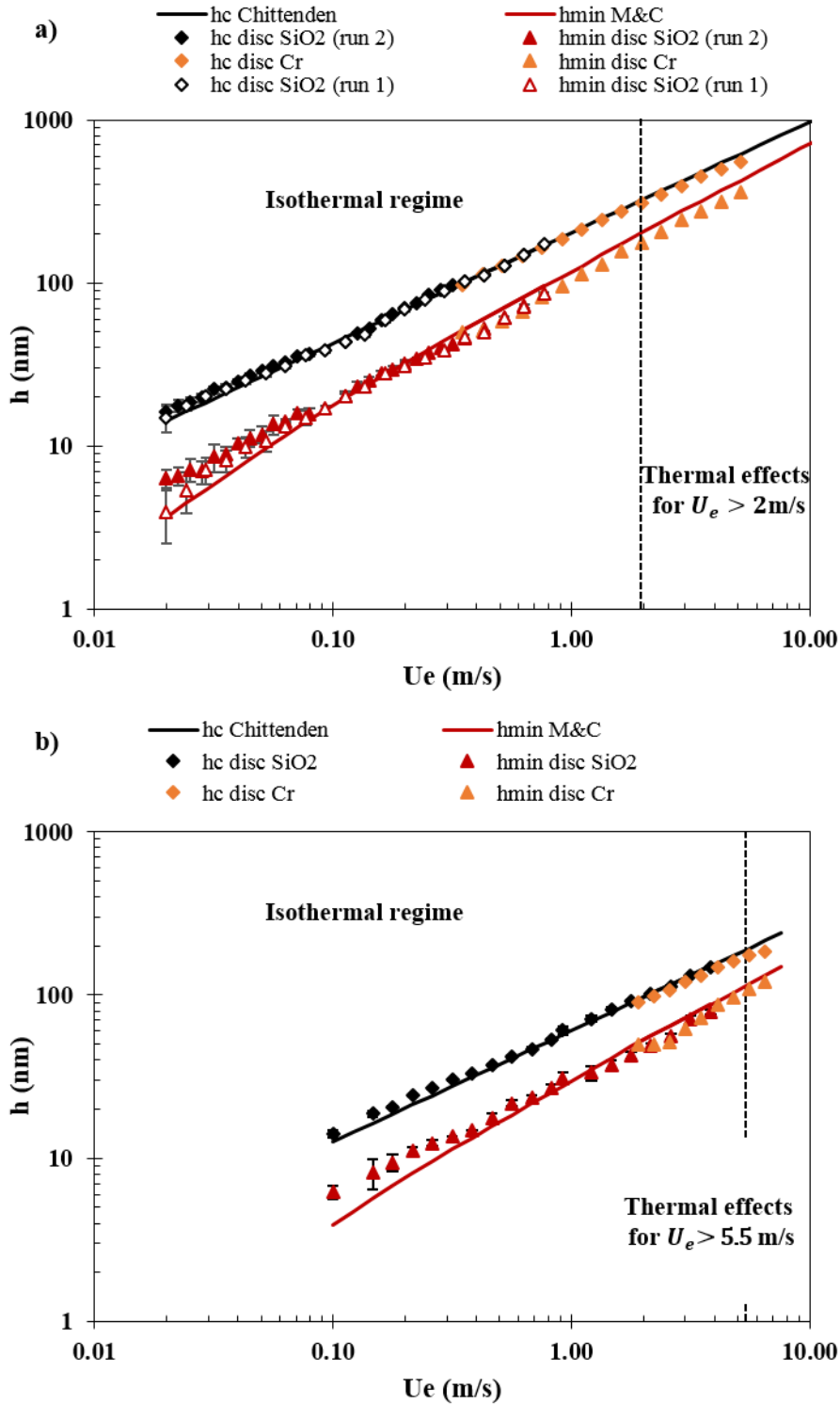


Figure 49: Experimental and analytical central and minimum film thicknesses of the base oil at – a) 25 °C; b) 75 °C.

At 25 °C and 75 °C, the experimental film thicknesses are in good agreement with the analytical predictions (Newtonian, isothermal). Nonetheless, thermal effects may occur at high speed due to the intense shearing at the contact inlet. A thermal factor was proposed by Cheng [114] to evaluate the occurrence of thermal effects at the contact inlet. The value of 0.96 was identified as the critical one, below which shear-heating affects significantly the lubricant properties [115] and thus film thickness.

In the base oil experiment, this value is reached for entrainment speed above 2 m/s at 25 °C and above 5.5 m/s at 75 °C, where the lubricant flow cannot be considered isothermal anymore. Both isothermal regime and thermal areas are indicated in Figure 49. The Newtonian behavior of the base oil is also confirmed, since it is one of the specific assumptions to apply the classical EHL analytical models. Furthermore a good continuity and consistency between the different run is here highlighted. Henceforth, only the results obtained on the “disc SiO₂” will be shown for the polymer solutions, in order to focus on film thicknesses below 200 nm.

IV.2.2 Tribological behavior of polymer solutions

The experimental central and minimum film thicknesses are plotted in log-log scale at 25 °C and 75 °C for the OCP-LE, PISH-S, PAMA-C and PAMA-L solutions (Figure 50 to Figure 53). Likewise the base oil diagram in Figure 49, the Chittenden solution and Moes and Chevalier predictions are plotted for the central h_c and minimal h_{min} film thicknesses, respectively. The low shear viscosity η_0 at atmospheric pressure and the pressure-viscosity coefficient α^* are calculated from the WLF model (see II.2, p. 58) to establish analytical predictions for each solution. The experimental base oil data are also reported on the graphs (dashed lines) in order to picture the polymer effect on the base oil properties. As mentioned previously, only results below 200 nm are here presented. At such film thickness, no thermal effects due to the shear-heating at the contact inlet is encountered for all solutions [114][115]. Comments are made on h_c only, whose characterization is more reliable than for h_{min} .

Power regressions have also been performed on all experimental curves of central film thicknesses h_c (below 200 nm) against entrainment speed U_e , at 25 °C and 75 °C. The power exponents (i.e., the slopes in log-log plots) and the corresponding pre-factors are listed for all solutions in Table 16. It is recalled that the Chittenden equation assumes isothermal conditions and fluids to be Newtonian. In order to provide a reasonable comparison, one should verify that the pre-factors are close, which means that only the dimensionless speed parameter is compared. The speed exponent of the equation is equal to 0.68 for h_c , a value whom the experimental power exponent should be close to. As mentioned previously, no thermal effects occur at the considered speeds. Therefore, any discrepancies on the power exponent may be attributed to a change of lubrication conditions, in which the assumptions of the EHL analytical models cannot be applied anymore [42]. Comments on each solution are provided further. The entrainment speed range, in which the regression is performed, was chosen in regards to the maximal correlation coefficient possible.

In Figure 50, the film thicknesses of the OCP-LE solution differ from the analytical predictions by 35% at 25 °C and 25 % at 75 °C. However, the slope of h_c stays constant all along the explored conditions (see Table 16) and close to the expected value of 0.68. This result reflects a typical non-Newtonian behavior [112]. Moreover, the addition of polymer does have an influence on the solution properties. The addition of OCP-LE increases indeed by 16 % the film thickness of the solution at both 25 °C and 75 °C. Increasing the temperature does not impact the polymer contribution, which tends to comply with the thickener properties of the OCP-LE, highlighted in II.3, p. 63.

Products	Temperature (°C)	Ue (m/s)	Power exponent	Prefactor	Correlation coefficient
Base oil	25	0.02 - 3.5	0.65	198.2	1.000
	75	0.10 - 3.51	0.65	62.0	0.998
OCP-LE solution	25	0.02 - 3.11	0.65	230.6	0.999
	75	0.10 - 3.16	0.64	72.3	0.997
PISH-S solution	25	0.05 - 3.10	0.69	214.9	0.999
	75	0.20 - 3.83	0.63	68.2	0.998
PAMA-C solution	25	0.13 - 3.10	0.65	206.7	0.998
		0.10 - 0.35	0.49	58.2	0.999
	75	0.35 - 3.16	0.64	69.1	0.998
PAMA-L solution	25	0.02 - 0.06	0.51	146.8	0.995
		0.28 - 1.62	0.66	221.2	0.997
	75	0.10 - 0.35	0.41	62.5	0.998
		0.35 - 3.83	0.62	74.5	0.992

Table 16: Power law parameters for the log-log plot of h_c for all solutions

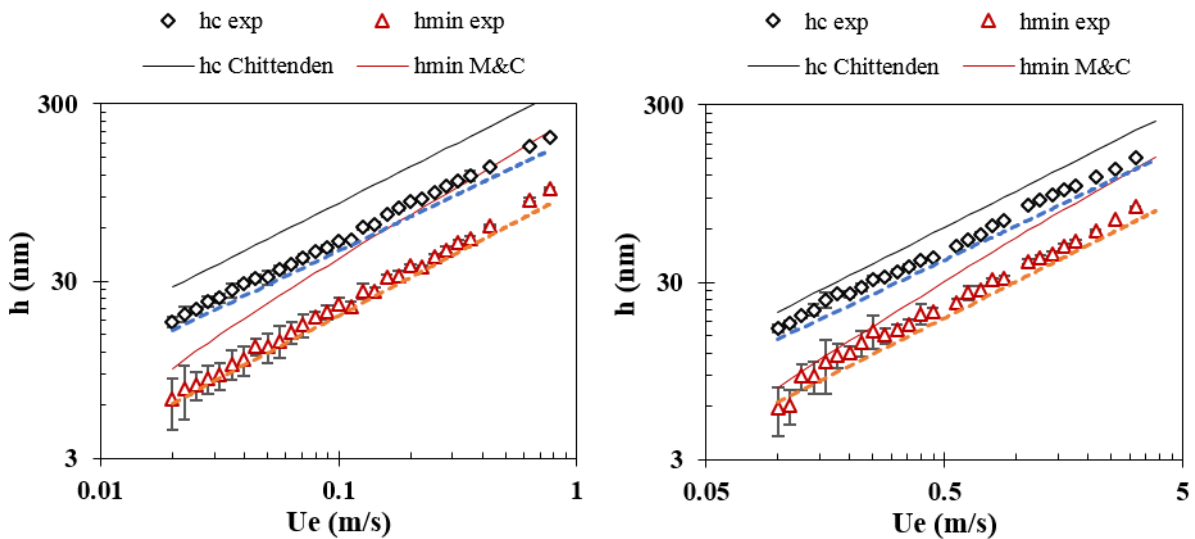


Figure 50: Experimental and analytical central and minimum film thicknesses of the OCP-LE solution at 25 °C (left) and 75 °C (right), along with the base oil film thicknesses (colored dashed lines)

Similarly, the film thicknesses of the PISH-S solution deviates by 30 % at 25 °C and 25 % at 75 °C from the analytical predictions. Again, as the slope of h_c remains stable at both temperatures and close to the theoretical power exponent (see Table 16), this deviation can be explained by the shear-thinning of the PISH-S solution. The addition of PISH-S only affects the solution properties at high temperature, with the film thicknesses increasing by about 5 % at 75 °C. The VII properties of the PISH-S may explain this response since the viscosity plays a major role on the film thickness. Indeed, the polymer contribution to the lubricant viscosity rises with temperature – evidenced by the variations of the PISH-S specific viscosity in II.3.1 (p. 63). Only affecting the tribological behavior of the solution at higher temperature is an interesting property and the interest of VIIs, as it may limit viscous friction at low temperature.

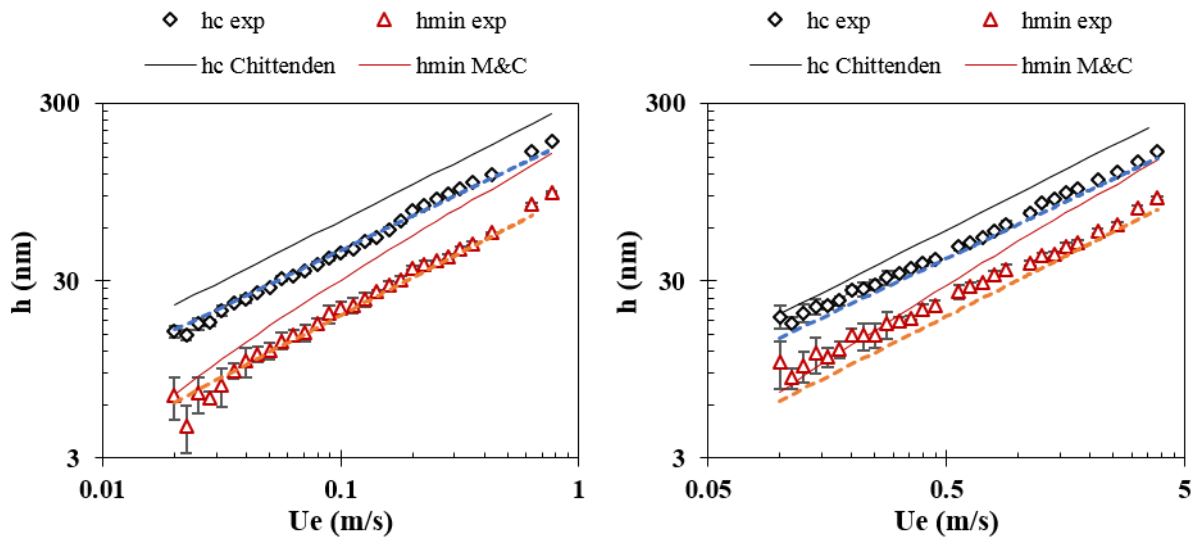


Figure 51: Experimental and analytical central and minimum film thicknesses of the PISH-S solution at 25 °C (left) and 75 °C (right), along with the base oil film thicknesses (colored dashed lines)

Both PAMA responses differ from the PISH-S and OCP-LE solutions. In Figure 52, the PAMA-C solution displays central film thicknesses deviated by +13 % at 25 °C from the Newtonian predictions, and its film thickness slope remains steady. However, this is not the case at 75 °C. The central film thicknesses differ from the analytical calculations by 17 % for entrainment speed above 0.35 m/s. The h_c power exponent is in this case equal to 0.64, close to the Chittenden power exponent (see Table 16) and the observed gap from the analytical predictions may be attributed to the shear-thinning of the PAMA-C solution. However, this is not the case for speeds below 0.35 m/s (corresponding to central film thicknesses of about 40 nm), where a change of slope is observed. This difference cannot be attributed to thermal effects as the Cheng factor [114] is equal to 0.99 at these low film thicknesses. This slope change (more noticed on the minimum film thicknesses than on the central one) rather indicates that the standard EHL theory does not apply anymore in such conditions [42]. The last section of this chapter addresses thin film lubrication regime to explain these observations, where molecular considerations are no longer negligible to the film forming capacity when compared to hydrodynamic contributions.

On other considerations, the PAMA-C addition only affects the base oil properties at high temperature. Similarly to the PISH-S solution, the central film thicknesses h_c (above 40 nm, in the EHD regime) is increased by 10 %, whereas it does not vary at 25 °C (less than 1 %). A more important contribution of the PAMA-C may have been expected compared to the PISH-S, since the PAMA-C is the most efficient VII studied in this work. It must be recalled however that the PAMA-C efficiency was linked to the swelling of its polymer coils above 80 °C, in II.4.2 (p. 69). At 75 °C, the PAMA-C effect on the base oil viscosity is thus rather limited. Experiments conducted at 100 °C should assess this assumption.

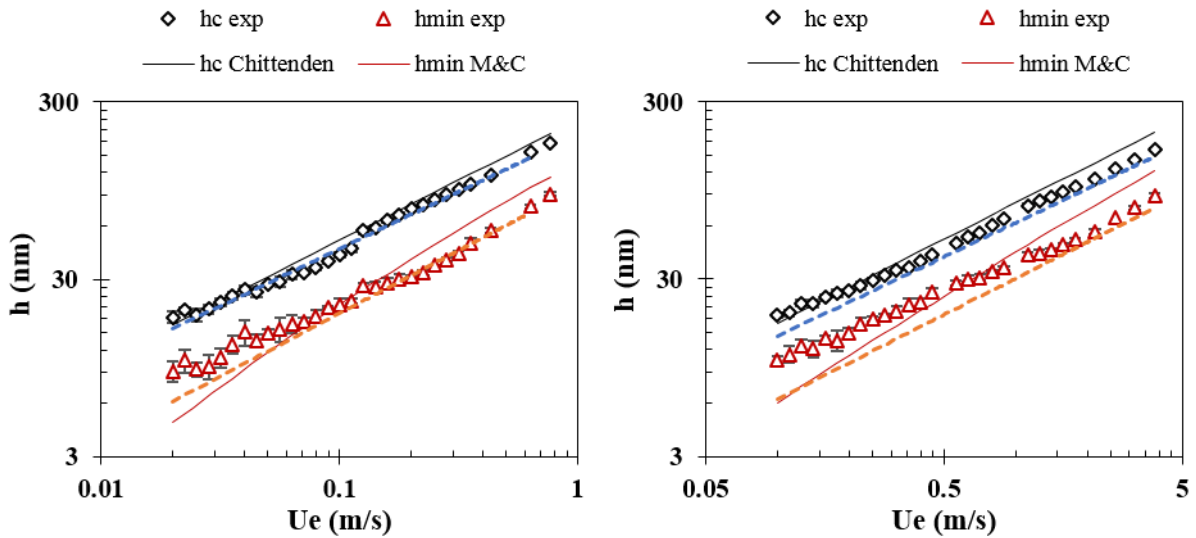


Figure 52: Experimental and analytical central and minimum film thicknesses of the PAMA-C solution at 25 °C (left) and 75 °C (right), along with the base oil film thicknesses (colored dashed lines)

The PAMA-L solution displays a peculiar tribological response, as can be seen in Figure 53. Likewise the PAMA-C results, changes of slope or transitions are observed on both central and minimum film thicknesses. However, these variations are noticed at both 25 °C and 75 °C for the PAMA-L solution. At entrainment speeds above 0.25 m/s at 25 °C and 1.78 m/s at 75 °C, the power exponent of h_c is close to the theoretical value (see Table 16). In such conditions, the experimental film thicknesses of the PAMA-L differ from the analytical predictions by 30 % and can again be explained by the shear-thinning of the solution [112]. At lower speeds, other phenomena occur – including concentration gradient or presence of adsorbed molecules at the surfaces – that can explain the differences with the analytical predictions. These observations are discussed in the last section of this chapter.

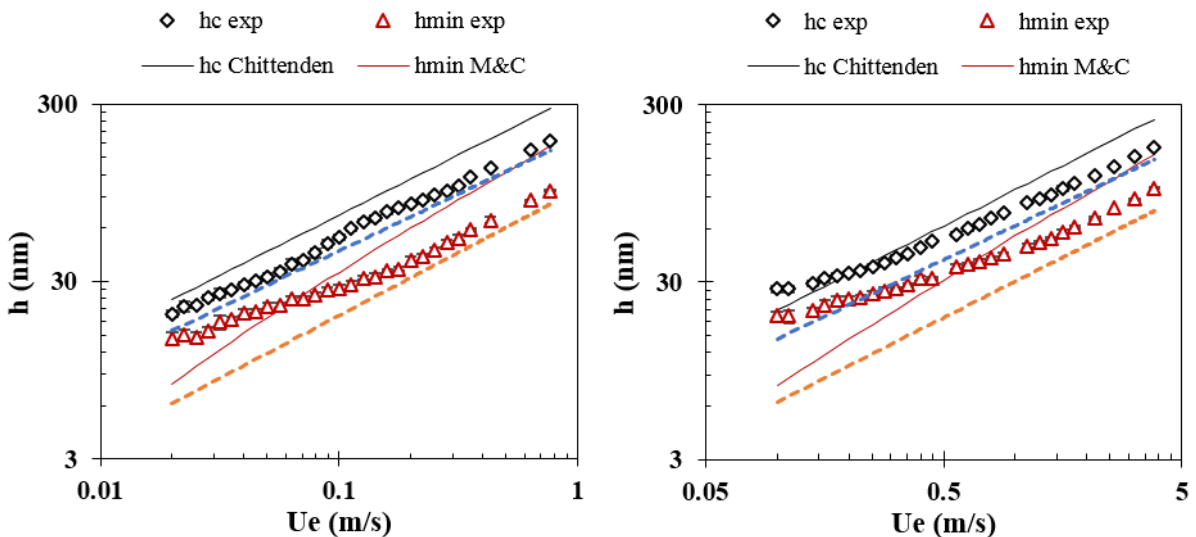


Figure 53: Experimental and analytical central and minimum film thicknesses of the PAMA-L solution at 25 °C (left) and 75 °C (right), along with the base oil film thicknesses (colored dotted lines)

It definitely can be seen that the addition of PAMA-L affects the base oil tribological properties. The film thickness is indeed increased by 10 % at 25 °C and by 20 % at 75 °C, considering conditions where the shear-thinning prevails (above 0.25 m/s at 25 °C and 0.35 m/s at 75 °C). At lower speeds, the film thickens more and it is particularly noticed at high temperature. However, it is difficult to confirm whether or not that this temperature effect is only linked to the VII properties of the PAMA-L. Indeed, the regime is not fully dominated by the elastohydrodynamic factors (including the viscosity) and molecular considerations must be taken into account.

All the presented curves highlight the different polymer contribution to the central h_c and minimum h_{min} film thickness of the solution. It is however surprising that the polymers addition only has a tiny influence on the base oil tribological response, whereas these additives impact on the base oil rheology is significant. Previous work (between 100 and 600 nm) conducted by Mary [10] also presented similar results. The action of these additives within the contact is hence an unresolved point. Indeed, it is questionable to consider if macromolecules, whose size may be about the film thickness, actually go through the contact. Moreover, if they do enter the contact, the shearing at the inlet is so important that degradation of the macromolecules may occur resulting in a permanent loss of viscosity (I.4.2, p. 43). The polymer effect on the base oil properties would thus be limited.

Another assumption is to consider the shear-thinning behavior of the solution. The shearing may be so important at the contact inlet that the solution viscosity may be close to the second Newtonian plateau, thus close to the base oil viscosity. This hypothesis may explain the slight influence of polymer addition on the film thickness and it is the most conceivable regarding our results. At 25 °C, the drop in film thickness is indeed of the same order of magnitude as the drop of viscosity determined in III.1.2 (p. 80) – 40% for the OCP-LE, 30 % for the PISH-S, 10 % for the PAMA-C and 30 % for the PAMA-L. The actual viscosity at the inlet η_{inlet} is calculated from the experimental data h_c in the EHD regime (above 50 nm) and the Chittenden analytical equation (Eq. (37), p. 102), to assess the non-Newtonian behavior. The Table 17 below gives the comparison of η_{inlet} to the low shear stress viscosity η_0 predicted by the WLF model (Eq. (26), p. 47) [14] at 0.63 m/s at 25 °C and 3.83 m/s at 75 °C.

Products	Temperature (°C)	η_{inlet} (mPa.s)	$\eta_{0,WLF}$ (mPa.s)	Relative deviation (%)
Base oil	25	27.6	26.8	3
	75	5.8	5.6	4
OCP-LE solution	25	32.8	64.4	-50
	75	6.7	11.4	-41
PISH-S solution	25	30.2	48.1	-37
	75	5.7	11.1	-49
PAMA-C solution	25	29.8	33.3	-10
	75	6.7	9.2	-28
PAMA-L solution	25	32.6	56.3	-42
	75	7.1	11.0	-39

Table 17: Comparison between the actual viscosities at the inlet determined, from the Chittenden equation and h_c measurements and the low shear viscosity from the modified WLF-Yasutomi model

For the base oil, η_{inlet} is close to the viscosity predicted by the WLF-Yasutomi equation at both 25 °C and 75°C, which validates its Newtonian behavior in such conditions. For all polymer solutions, the gap between η_{inlet} and η_0 illustrates a drop of viscosity due to shear-thinning, as no thermal effects occur at the chosen conditions.

However, the shear-thinning cannot alone explain the observed deviations at low film thicknesses (below 40 nm) and the changes of slope noticed for the PAMA solutions. These deviations from the EHD regime could not be attributed to a transition to the mixed lubrication regime since the parameter λ (Eq. (2), p. 24)[40] is above 2.5 at the considered film thicknesses and indicates a full separation in EHD regime. Contributions, other than hydrodynamic ones, must thus also be taken into account.

IV.3 Thin film lubrication regime

IV.3.1 Approach

In the present tribological study, the operating conditions were chosen to study the solution response in the elastohydrodynamic lubrication regime and at its boundary towards very low film thickness. Given the fluids studied here, at film thicknesses below ten or tens of nanometer, molecular behaviors in the different nano/regions prevail on the lubricant film dynamics [42][116]. The lubrication regime is thus called thin film lubrication (TFL in the following) [36][42] in which the film thickness still varies with the entrainment speed but deviates from the prediction of classical EHL theory. Classical TFL models consider the formation of monomolecular layers of adsorbed molecules on the solids surfaces to explain this deviation [23][42]. In [43], Smeeth indicated that these adsorbed films were desirable since they could reduce friction and wear between sliding surfaces. However, the formation of those thin layers may not be observed for all solutions: this point will be discussed in this section.

The tribological responses of each polymer solution are here examined and linked to the polymer chemistry and structure. The specific viscosity at the inlet $\eta_{sp,inlet}$ is first determined to estimate the variations of viscosity with the central film thickness h_c and the Chittenden equation. Inlet means here the location where the properties of the lubricant determine the film thickness generation, i.e. upstream of the contact area.

$$\eta_{sp,inlet} = \frac{\eta_{solution,inlet} - \eta_{solvent,inlet}}{\eta_{solvent,inlet}} \quad \text{Eq. (45)}$$

Here, the $\eta_{solution,inlet}$ and the $\eta_{solvent,inlet}$ stands for the actual viscosities at the inlet of the polymer solution and the base oil respectively calculated with the Chittenden equation (Eq. (37), p. 102).

The variations of $\eta_{sp,inlet}$ with h_c is a mean to evaluate the occurrence of a fluid layer at the surfaces [23]. Even though the deviations from EHD predictions are more noticed on the minimum film thicknesses h_{min} , no similar considerations of specific viscosity are performed on h_{min} since i) their results are not as reliable as those on h_c and ii) h_{min} prediction is less accurate than the central film thickness one, which could have generated irrelevant uncertainties. If no layer is formed, $\eta_{sp,inlet}$

should remain constant with a change of film thickness. If at low h_c this viscosity increases, this supports the fact that an adsorbed layer of thickness h' is present. Indeed, as the film gets closer to the size of the adsorbed molecules, the composition of the lubricant change. The concentration of polymer may/might vary with the solvent volume decreasing, which should result in a rise of viscosity. It is however difficult to know a priori how this layer is distributed between the two surfaces since they are made of different materials (100C6 steel ball and a glass S-BSL7 disc coated with SiO₂) [23].

Afterwards, another method to have access to the inlet viscosity η_{inlet} is applied. The mean shear strain rate at the contact inlet $\dot{\gamma}_{inlet}$ is evaluated from the experimental film thicknesses at different entrainment speeds for all solutions, apart from the OCP-LE. It must be mentioned that increasing the surfaces speed as well as the temperature lead to higher $\dot{\gamma}_{inlet}$. The minimum and maximum $\dot{\gamma}_{inlet}$ are reached at the minimum and maximum entrainment speed respectively. The viscosity of each solution can then be calculated with the Carreau-Yasuda model provided previously [16] (III.1.2, p. 80) and are detailed in the

Table 18 below. Similar $\dot{\gamma}_{inlet}$ are reached for all products. The PISH-S $\dot{\gamma}_{inlet}$ are thus chosen for the OCP-LE results as these polymer solutions have similar rheological responses, except at 75 °C where the calculated viscosity for the OCP-LE gets lower than the base oil one at the maximum considered $\dot{\gamma}_{inlet}$.

New analytical predictions of the central and minimum film thicknesses are performed using the viscosities derived from $\dot{\gamma}_{inlet}$ and the Carreau-Yasuda model. The adsorbed layer h' is then evaluated, if present. All those considerations are discussed to highlight the relationship between, rheology, tribology and physico-chemistry of the studied polymers.

	Temperature (°C)	$\dot{\gamma}_{inlet}$ (s ⁻¹)		$\eta_{inlet,CY}$ (mPa.s)	
		minimal	maximal	at $\dot{\gamma}_{inlet}$ minimal	at $\dot{\gamma}_{inlet}$ maximal
OCP-LE	25	2.88E+05	2.43E+06	39.2	30.5
	75	1.22E+06	3.00E+06	5.8	5.3
PISH-S	25	2.88E+05	2.43E+06	28.2	25.9
	75	1.22E+06	6.07E+06	6.1	5.8
PAMA-C	25	2.23E+05	2.26E+06	31.1	29.3
	75	1.15E+06	6.20E+06	8.3	7.9
PAMA-L	25	2.23E+05	2.01E+06	40.0	35.9
	75	8.47E+05	6.27E+06	8.5	7.7

Table 18: Actual viscosity calculated at the inlet with the Carreau-Yasuda model $\eta_{inlet,CY}$ at the minimal and maximal shear strain rate evaluated at the inlet.

IV.3.2 Discussion on the PAMA-L in TFL

The PAMA-L tribological response (whose both central and minimum film thicknesses variations against the surfaces speed present a change of slope) is a good illustration of the transition from EHD to TFL regimes. It is important to recall that the PAMA-L is a polar polyalkylmethacrylate synthesized

with a polar dispersant function. In Figure 54, its specific viscosity (Eq. (45), p. 111) calculated at the inlet is plotted against the central film thickness h_c , at 25 °C and 75 °C.

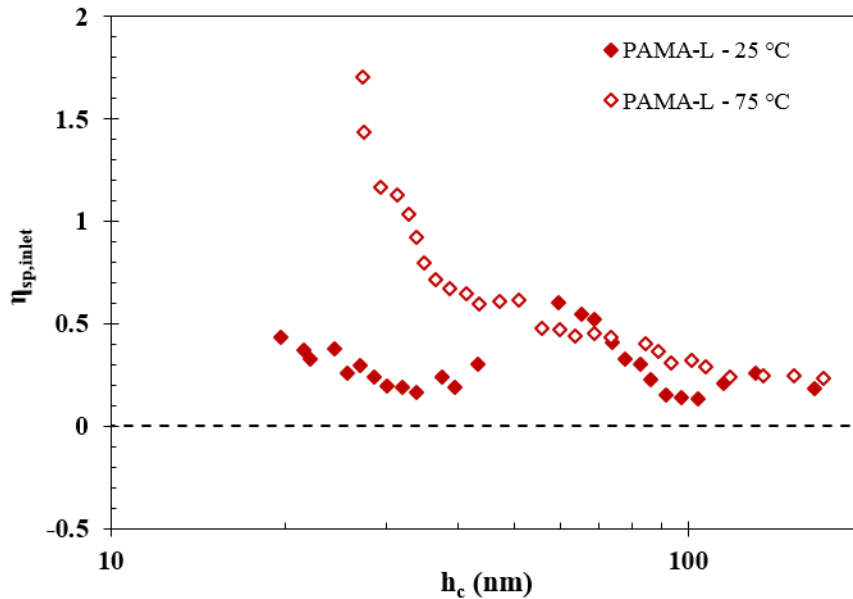


Figure 54: Specific viscosity at the inlet against the central film thickness for the PAMA-L solution at 25 °C and 75 °C.

First of all, the temperature affects the PAMA-L response as the visible increase of $\eta_{sp,inlet}$ (from the high speed to the low speed) is more pronounced at higher temperature (+630 % at 75 °C against +100 % at 25 °C). Moreover, the results at 75 °C clearly illustrate the beginning of the transition from EHL to TFL for thicknesses below 90 nm at which the $\eta_{sp,inlet}$ starts rising before increasing more significantly below 40 nm. The variations at 25 °C are more complex, with the observation of a “beading” between 40 and 90 nm. This phenomenon, which has been shown to be reproducible, may be explained by variations of the solution concentration due to the beginning of the TFL transition [23]. Between 40 and 90 nm, accumulation of polymers molecules at the contact inlet may occur, leading to an increase of the apparent concentration of additives. The diminution of $\eta_{sp,inlet}$ before stabilization might be linked to the passage of a fluid of stable and unknown composition, within the contact.

In Figure 55, the experimental central and minimum film thickness of the PAMA-L solution are plotted against the entrainment speed in log-log scale at 25 °C and 75 °C, along with their Chittenden predictions and Moes and Chevalier calculations. The analytical film thicknesses are here calculated using the viscosity predicted by the Carreau-Yasuda model (see

Table 18) instead of the low shear stress viscosity, at both the minimum and maximum shear strain rates present at the contact inlet. The experimental data fairly follow the analytical predictions obtained with this viscosity, above 30 nm at 25 °C and 40 nm at 75 °C. Combining results from the high pressure rheology and classical EHL analytical equations allow thus a good evaluation of the film thickness of non-Newtonian solutions. Below these conditions, the deviations to the EHD predictions are attributed to the transition to the TFL regime, in which the lubrication mechanisms are dominated by molecular considerations.

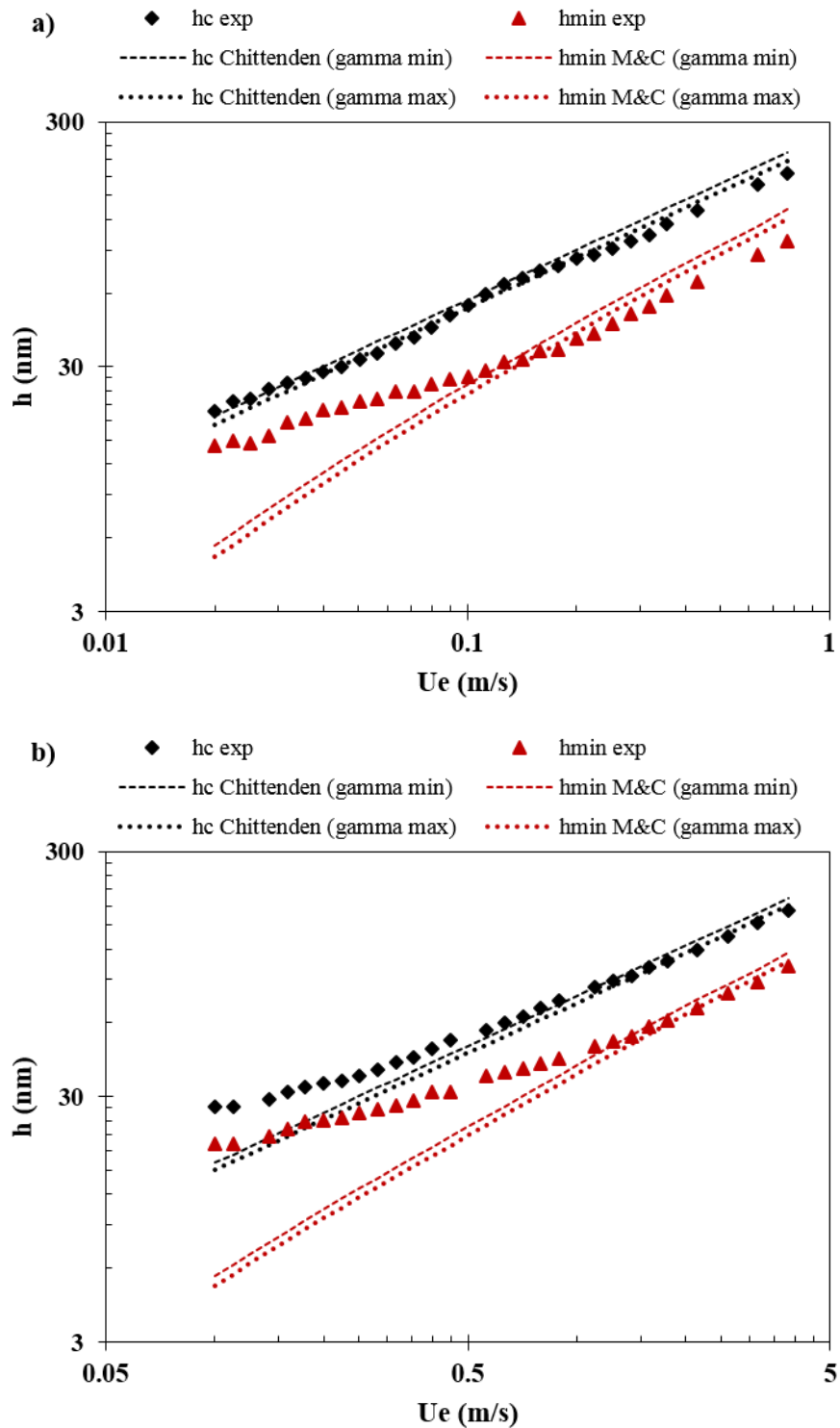


Figure 55: Experimental h_c and h_{min} of the PAMA-L solution shown along with their analytical predictions using the η_{inlet} calculated with the Carreau-Yasuda model, at either the minimal or maximal shear rate encountered at the inlet – a) at 25 °C; b) at 75 °C.

The presence of the adsorbed layer h' is especially noticed on the minimum film thickness and can be evaluated at zero speed by a third degree polynomial regression and extrapolation on the experimental data [117]. The regression is not performed on the “beading” observed on h_c at 25 °C. The fluid layer estimations h' on both central and minimum film thickness are detailed in Table 19 and are about 14 nm at 25 °C and between 17 and 20 nm at 75 °C. It should be mentioned that h' is independent on the regression performed on either h_c and h_{min} . As both sets of experimental data provide similar values, the h' results are reliable. Previous studies have shown that these thin adsorbed layers are linked to gyration radii R_g of the polymers [117], as the latter tend to adsorb on the surfaces as coils [118]. Thus, R_g are determined from the hydrodynamic radii R_h calculated with the Einstein’s law (Eq. (11), p. 41) [10][11] at the considered temperature and pressure, within the contact, i.e. at 500 MPa. The adsorbed layers sizes are about twice those of the radii of gyration of the PAMA-L. Hence, polymer coils must adsorb on both sliding surfaces. However, these results must be considered cautiously since no analysis of the surfaces were performed during or after the experiments.

IV.3.3 Discussion on the PAMA-C in TFL

The results on the comb polyalkylmethacrylate PAMA-C also depict a transition to the TFL regime. Figure 56 below presents the variation of the specific viscosity at the inlet against the central film thickness at 25 °C and 75 °C.

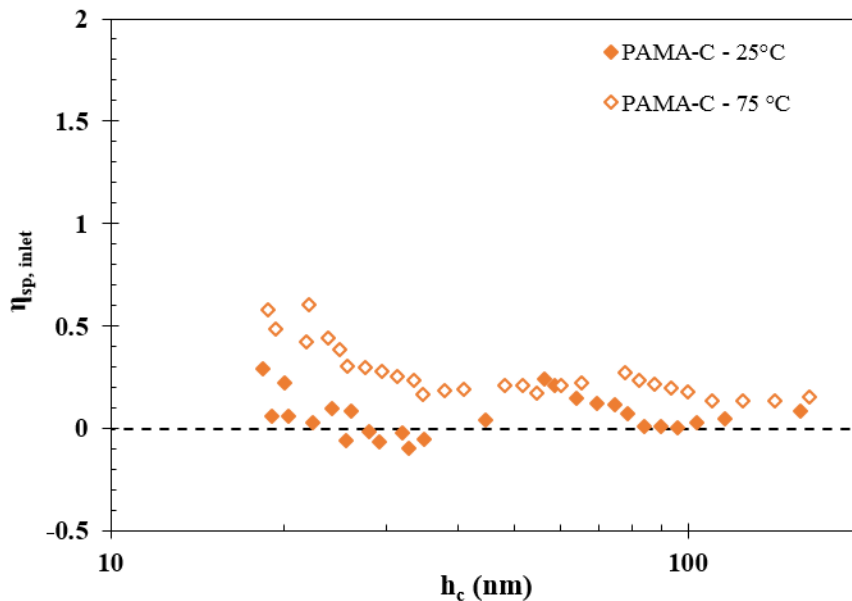


Figure 56: Specific viscosity at the inlet against the central film thickness for the PAMA-C solution at 25 °C and 75 °C.

The variations of the PAMA-C $\eta_{sp,inlet}$ are really similar, though their amplitude is lower, to those of the PAMA-L. It should be mentioned that uncertainties on the viscosity calculations explain the negative $\eta_{sp,inlet}$. Again the temperature affects the polymer properties as the $\eta_{sp,inlet}$ rises with the former is increased. Moreover, the $\eta_{sp,inlet}$ PAMA-C is minimal at 25 °C and only rises at high temperature. This result reflects the minimal impact of the PAMA-C to the base oil viscosity at low temperature and higher contribution of the polymer to the solution viscosity with a temperature rise: this

is actually the desired effect of a VII. However, the PAMA-C was identified as a better VII than the PAMA-L in II.2 (p. 58): rheological considerations only cannot then fully explain the performance of the PAMA-L compared to the PAMA-C. The onset of the transition from EHL to TFL is again visible at 75 °C for film thicknesses below 40 nm at which the $\eta_{sp,inlet}$ rises significantly. As for the PAMA-L, a “beading” is noticed at 25 °C but here between 35 nm and 80 nm and less significant. Again, it may be explained by variations of the solution concentration due to the beginning of the TFL transition [23]. The formation of an adsorbed layer is thus also considered for the PAMA-C solution.

In Figure 57, both experimental data and analytical predictions are plotted against the entrainment speed at 25 °C and 75 °C. As for the PAMA-L, the calculated film thicknesses with Carreau-Yasuda viscosities are in good agreement with the experimental data, at 25 °C on h_c and above 30 nm at 75 °C, *i.e.* in the EHL regime. The transition to TFL is here more difficult to notice as it happens at lower speeds than the PAMA-L ones. The onset of the TFL regime may however be seen on the minimum film thickness at 25 °C, below 30 nm where a change of slope is noticed. Applying the regression method previously described - besides the central film thickness at 25 °C - leads to the adsorbed layer thicknesses h' provided in Table 19. The PAMA-C h' is here evaluated at 7-8 nm at 25 °C and 75 °C, close to one gyration radius of the polymer. As both contacting bodies are made of different materials, it is thus possible that PAMA-C coils only adsorb on a unique surface, likely the steel ball. This assumption is also supported by our learning from the film thickness experiments. Indeed, the cleaning of the disc was more laborious after the PAMA-L experiments than for the PAMA-C ones, which might be explained by the adsorption on the disc of PAMA-L coils. Again, these conclusions must be taken cautiously.

	Temperature (°C)	on h_c		on h_{min}		R_g (nm)
		h' (nm)	Correlation coefficient	h' (nm)	Correlation coefficient	
PAMA-L	25	14.0	1.000	13.2	0.997	7.5
	75	20.3	0.999	17.2	0.998	9.0
PAMA-C	25	-	-	7.0	0.993	6.9
	75	11.9	1.000	8.2	0.996	8.6

Table 19: Comparison of fluid layer thicknesses to hydrodynamic radii R_g at 25 °C and 75 °C for PAMA solutions

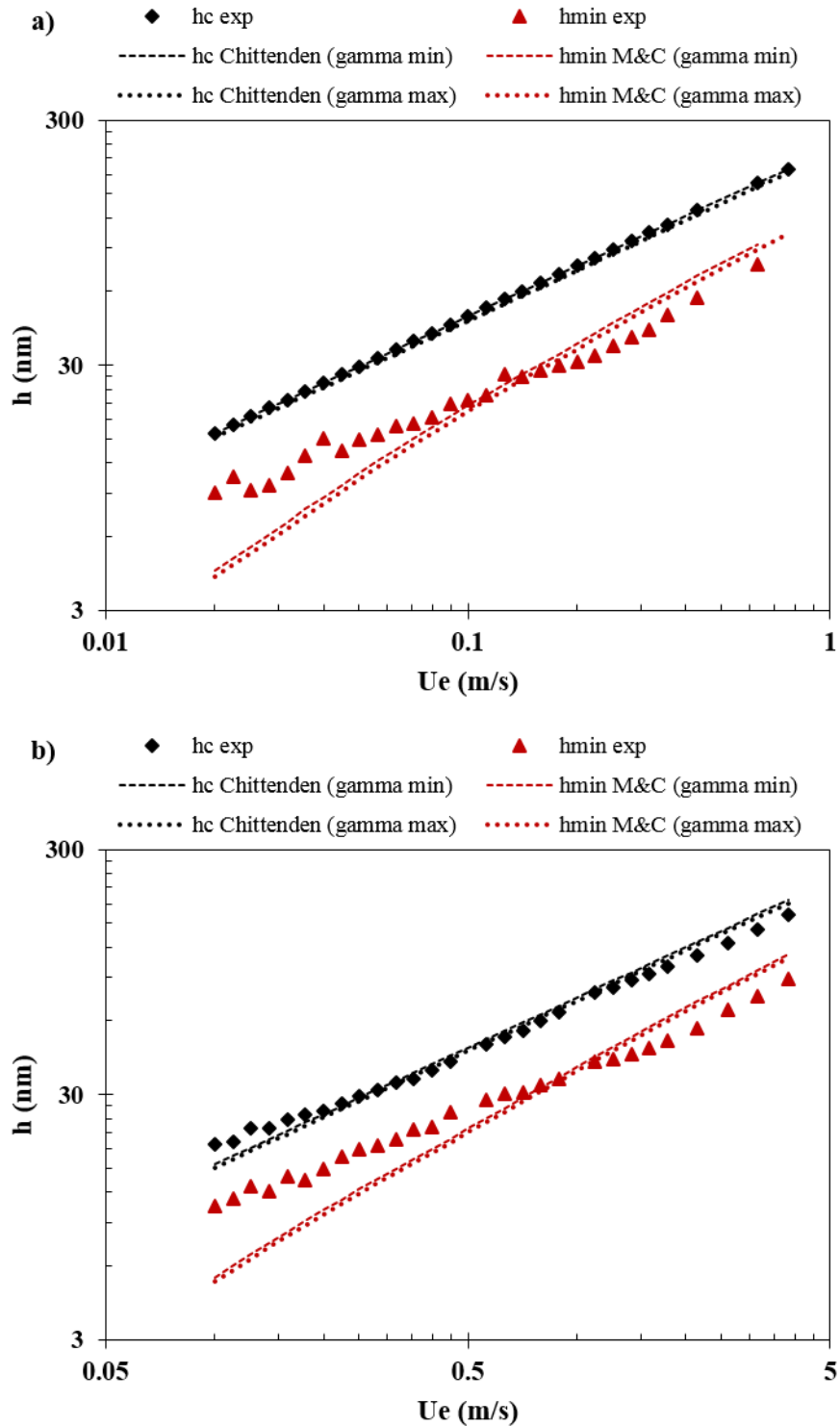


Figure 57: Experimental h_c and h_{min} of the PAMA-C solution shown along with their analytical predictions using the η_{inlet} calculated with the Carreau-Yasuda model, at either the minimal or maximal shear rate encountered at the inlet – a) at 25 °C; b) at 75 °C.

IV.3.4 Discussion on the OCP-LE and parameters influencing the thin layer formation

As for the PAMA, the specific viscosity of the OCP-LE solution at the inlet is plotted against the central film thickness at 25 °C and 75 °C in the Figure 58. No variations of $\eta_{sp,inlet}$ with h_c are here noticed. Henceforth, OCP-LE coils do not adsorb on the surfaces. Moreover, the polymer does thicken the solution since its $\eta_{sp,inlet}$ remains strictly positive, but with no effect of the temperature on its performance. This result is expected of a thickener such as the OCP-LE. In Figure 59, both experimental data and analytical predictions are plotted against the entrainment speed at 25 °C and 75 °C. The experimental data fairly follow the calculated film thicknesses with Carreau-Yasuda viscosities at both temperature. No adsorbed layer or transition to a TFL regime are here noticed.

The structure and chemistry of PAMA and OCP-LE solutions can explain what drives the formation of a thin layer. The polymer polarity is the first factor to consider. Polar molecules like PAMA would indeed adsorb on the surfaces, whereas non polar polymers such as the OCP-LE would not be able to form a thin layer at low speeds. This result is well known in the literature [119][120][121]. Several studies have indeed highlighted the thin layer formation of various polyalkylmethacrylates and the influence from the physico-chemistry point of view. Both studied PAMAs present different properties. The PAMA-C is a comb polyalkylmethacrylate of high molecular weight with long carbonyl side chains, which form rather low thin film and seems to only adsorb on one surface. The PAMA-L is a polyalkylmethacrylate of lower molecular weight with smaller side chains and presenting a polar dispersant function. The functionalization of the PAMA-L explains actually its ability to form thicker and stronger films at low speed. Indeed, the adsorption of non-functionalized PAMA at the surface relies on the polymer polarity and Van der Waals forces [28], whereas functionalized polar molecules can form stronger bonds. This may explain the adsorption on only one surface of the PAMA-C, opposed to the PAMA-L on both surfaces. This particularity have been highlighted by Spikes in [119], in which he studied what parameters affected the polymer response.

The ideal targeted PAMA would then be functionalized, whose polar functional group should be by block rather than randomly distributed in the polymer [119]. The polymer must also have medium to high molecular weight [119]. However, non-functionalized PAMA could also be considered. Muraki and Nakamura studied several non-functionalized PAMA and they concluded that polymers of high molecular weight and shorter side chains were more efficient [121]. This goes against the conclusion on the VII performance, where a comb PAMA, with long side chains, is desirable. A compromise must then be found.

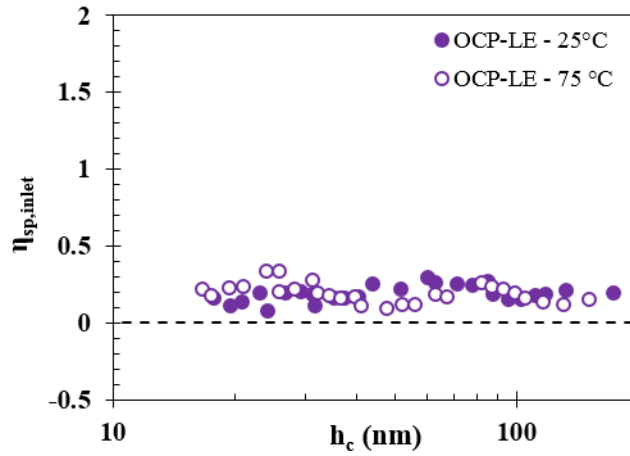


Figure 58: Specific viscosity at the inlet against the central film thickness for the OCP-LE solution at 25 °C and 75 °C.

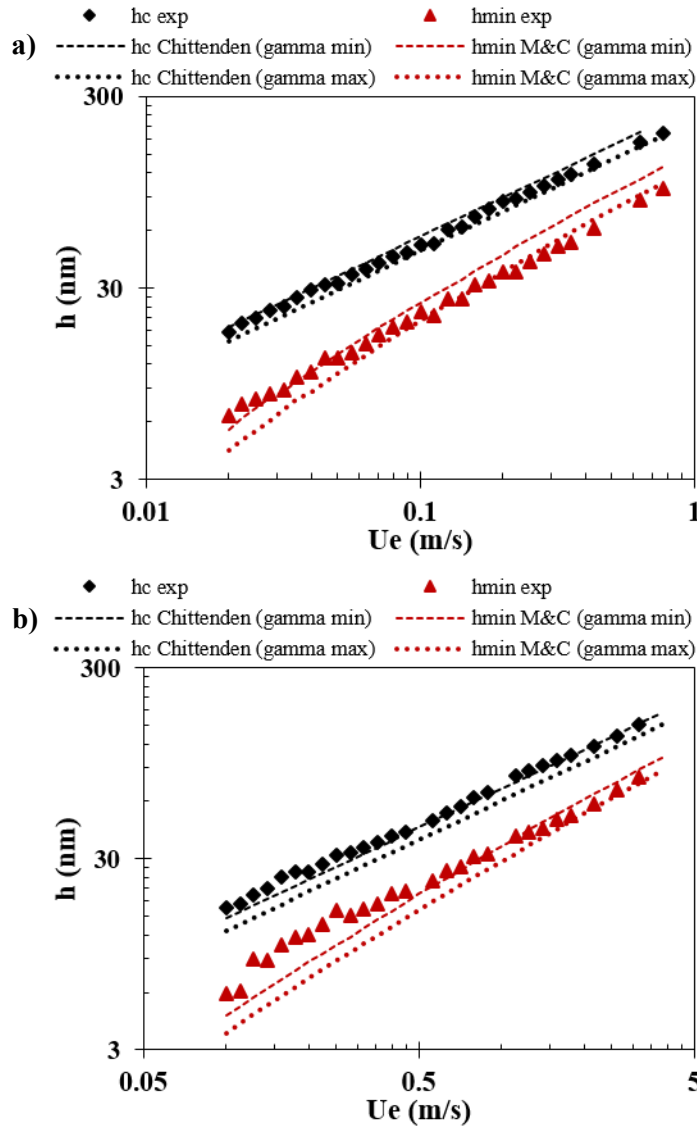


Figure 59: Experimental h_c and h_{min} of the OCP-LE solution shown along with their analytical predictions using the η_{inlet} calculated with the Carreau-Yasuda model, at either the minimal or maximal shear rate encountered at the inlet – a) at 25 °C; b) at 75 °C.

IV.3.5 Discussion on the PISH-S limitations

The PISH-S results are the last to be discussed as they lead to recommendations for future works. In Figure 60, the specific viscosity of the PISH-S, at the inlet of the contact, is plotted along its central film thickness. The increase at 75 °C of the $\eta_{sp,inlet}$, at film thickness below 30 nm, is not significant and cannot be attributed to the formation of an adsorbed layer, which is thus not considered. The PISH-S being a non-polar polymer, this result complies with previous comments. Moreover, the $\eta_{sp,inlet}$ is close to zero all along the considered h_c range. Hence in these conditions the PISH-S addition does not affect the base oil viscosity, at both 25 and 75 °C.

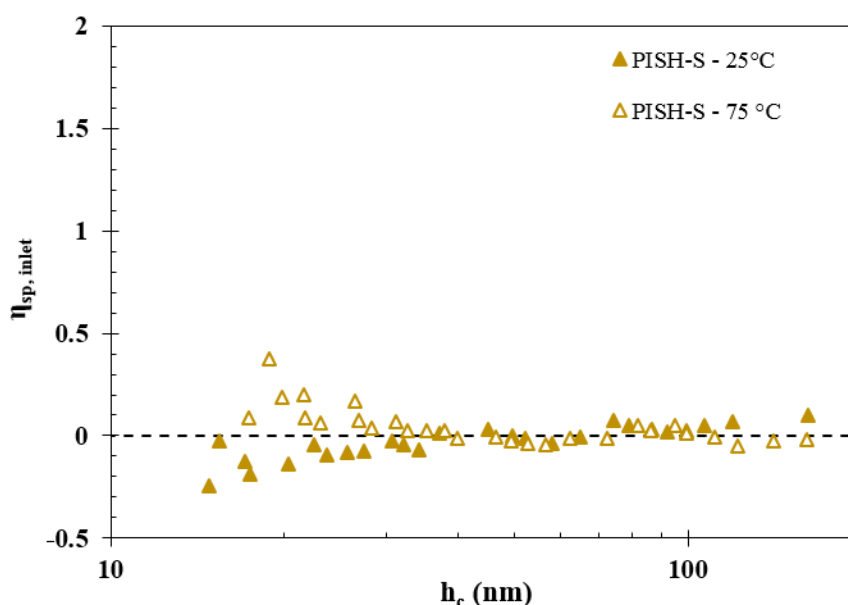


Figure 60: Specific viscosity at the inlet against the central film thickness for the PISH-S solution at 25 °C and 75 °C.

In Figure 61, both experimental data and analytical predictions of the PISH-S solution are plotted against the entrainment speed at 25 °C and 75 °C. The experimental data fairly follow the calculated film thicknesses with Carreau-Yasuda viscosities at both temperature. One should notice that central film thicknesses down to 15nm are measured and even lower are reached on the minimum film thickness. It was also highlighted in II.4.2 (p. 69), that the PISH-S molecules were the biggest studied and their gyration radii are about 20 nm, at 25 °C and 75 °C. It must be then questioned that whether or not these molecules (that cannot adsorb on the surface) enter the contact, especially after considering the previous comment on the PISH-S contribution to the base oil viscosity (see Figure 60). They may also be degraded leading to permanent shear-thinning (I.4.2, p. 43) In situ experiments using spectroscopic methods (Raman [122] or infra-red [123] for instance) should be thus performed on all solutions to visualize the molecules travelling or not through the contact, but also their profile, their alignment and the adsorbed layer at the surface.

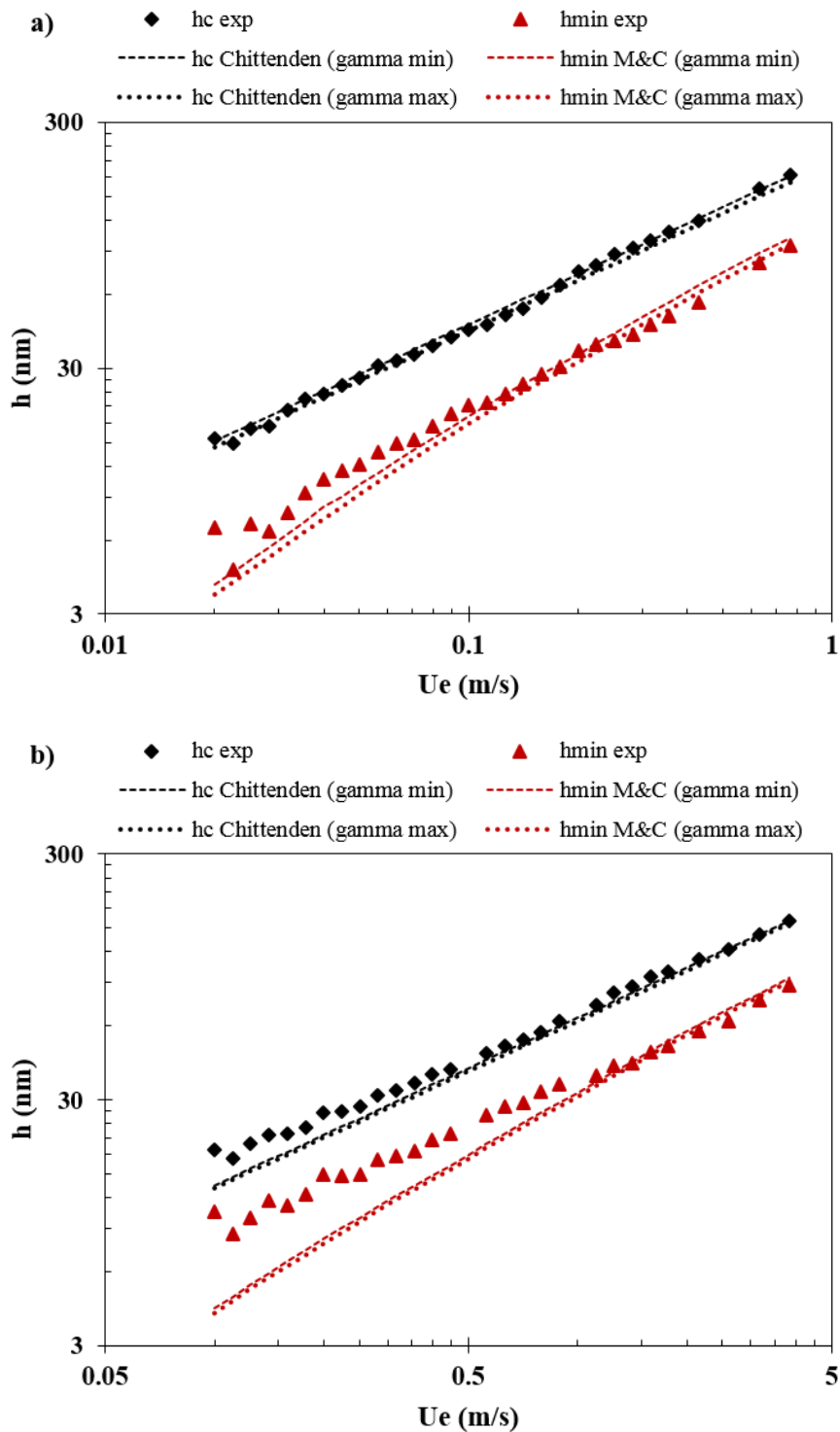


Figure 61: Experimental h_c and h_{min} of the PISH-S solution shown along with their analytical predictions using the η_{inlet} calculated with the Carreau-Yasuda model, at either the minimal or maximal shear rate encountered at the inlet – a) at $25\text{ }^\circ\text{C}$; b) at $75\text{ }^\circ\text{C}$.

IV.4 Conclusion

In this chapter, the tribological behavior of the base oil and polymer solutions in an EHD circular contact was investigated.

Film thickness measurements were first compared to classical EHL analytical models in pure rolling conditions. Deviations between the analytical predictions and the experimental results were highlighted for all polymer solutions and were attributed to the occurrence of shear-thinning. Indeed, the Newtonian predictions overestimate the real film thicknesses, which reveal the importance of using adequate rheological models in film thickness calculations.

However, the shear-thinning of the polymer solutions alone could not explain the film thickness deviations from the EHD analytical predictions of the PAMA solutions at low speed. These discrepancies were attributed to the transition from the EHL to the TFL regimes, in which molecular considerations must be taken into account. The polarity of the molecules was highlighted as a key factor since only the formation of an adsorbed layer was observed for the two polar PAMA. However, the PAMA-L formed thicker adsorbed layer than the PAMA-C. The PAMA-L performance was explained by the functionalization of the molecule, which was confirmed in the literature. Figure 62 offers a schematic representation of the TFL regime for PAMA solutions.

The present results highlighted the influence of the polymers on the base oil tribological response, apart from the PISH-S solution. Generally speaking our results raised the questions of the passage through the contact of large macromolecules, of possible variation of their concentration or of their possible degradation.

To conclude, the polymers rheology, as well as their physico-chemistry, could finally be linked to their tribological response. All conclusions are of main interest for formulators as they can select the optimal polymer in function of the desired tribological performance.

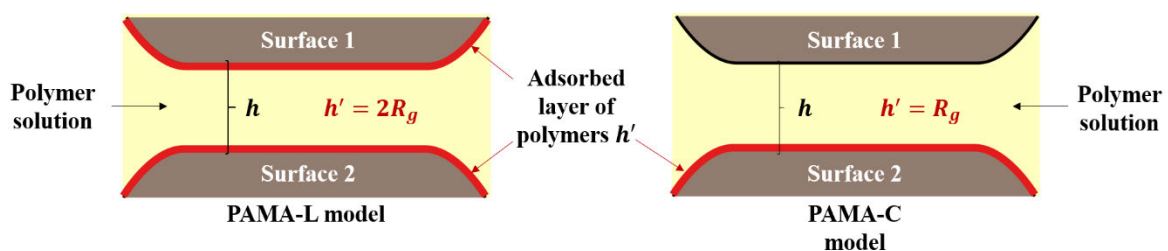


Figure 62: Schematic representation of the PAMA solutions in thin film regime

Summary and conclusion

In the general introduction, the major role of lubricants on friction reduction and engine performance was presented. The motor oil viscosity was highlighted as an essential parameter to control in order to limit friction losses in car engines. In this aim, the former may be adjusted by the addition of polymeric viscosity index improvers (VII). The goal of this work was then to link the molecular scale analysis to the laboratory scale study, from physico-chemistry to tribology through rheology. This approach helps the formulators to select the optimal VII that comply with car manufacturer's requirements without running full-scale engine tests.

Following this introduction, a literature overview on engine lubrication, high pressure rheology and polymer solutions was provided. Basic notions on friction and lubrication regimes were introduced. Then, the complex composition and various role of engine lubricants were specified. The studied additives, the VIIs, were extensively described since they play a major role on the lubricant viscosity. Generalities on the physico-chemistry of polymers and polymer solutions were explained to understand the behavior of these additives in solution, as well as providing the adequate elements for the discussion on how the polymers structure affects their rheological and tribological responses. The rheology of lubricants was then introduced, followed by the description of the rheological models used in this work. Finally, the studied products composed of a hydrocracked mineral base oil and several polymers of different natures were depicted.

Chapters II and III were dedicated to the rheological study of all solutions in realistic engine conditions. In chapter II, the temperature dependence of the solution was fitted by a VTF model and allowed the determination of the glass transition temperature at atmospheric pressure. The temperature-pressure-viscosity dependence of simplified lubricants was then accurately characterized and fitted by a modified WLF-Yasutomi equation up to 800 MPa. Distinction between VII and thickeners were possible by considering the variations of the specific viscosity of the solutions against temperature and pressure, as well as their thickening factor Q . Both OCPs were identified as thickeners, whereas the PAMAs and PISH-S were considered as VII. Moreover, the PAMA-C was highlighted as the most efficient VII studied in this work, whereas the PISH-L polymer has the singularity to present the properties of a thickener at low pressure and of a VII at high pressure.

The polymer efficiency was then illustrated by the variations of their hydrodynamic radius with temperature and pressure. The Einstein's law applied at high pressure was one of the various methods employed to determine the polymer radii. Several tendencies were observed and linked to the polymer physico-chemistry. The PAMA-C's efficiency was attributed to the rise of its hydrodynamic radius with temperature, which was explained by its amphiphilic nature and solvency variations with temperature. The PISH-S was considered as a weaker VII, whose polymer coils slightly swell with an increase of temperature. It was again explained by the increasing solubility of its styrene block in these conditions. Both PAMA-L and PISH-L had similar properties, even though their chemistry and macrostructure were really different. The PISH-L singularity was linked to its ability to form micelles when solvated. A decrease of the hydrodynamic radii of the OCPs was noticed. In summary, solubility and conformation considerations have then explained the rheological response of polymer solutions at high temperature and high pressure.

In chapter III, the viscosity of base oil and polymer solutions were acquired over a large range of shear stresses from 40 °C to 60 °C and from 200 MPa up to 400 MPa. The dependence of the viscosity on shear stress was represented by different rheological models, a modified Carreau-Yasuda expression and the Zhang equation, with a reasonable agreement to the experimental data.

Different rheological behaviors were noticed regarding each polymeric additive. All polymer solutions shear-thinned, apart from the PAMA-C solution. The almost Newtonian behavior of the PAMA-C was explained while taken into account size and/or conformation effects. At comparable size, conformation effects prevail and explain the different behaviors of both PAMAs and OCP-LE solutions. The PAMA-C was a comb polymer, less stretchable than the linear OCP-LE since the comb macromolecule presented strong steric hindrance and intramolecular bonding. The PAMA-L represented an intermediate case, as it had shorter side chains and a more flexible conformation. At comparable steric hindrance, size considerations prevailed. Both PISH-S and PAMA-C polymers presented similar steric hindrance. The PISH-S solution however displayed a large shear-thinning response since its molecules were larger and more shear-sensitive than the PAMA-C ones.

An assumption was proposed to highlight the limit of application of the Carreau-Yasuda model. Since the PAMA-C coils swell with temperature, its larger macromolecules should be more shear-sensitive. A shear-thinning response might be expected above the swelling temperature of a VII which induced a variable ratio between the two Newtonian plateaus. The Carreau-Yasuda model may not be applied anymore. An alternative was proposed with the Zhang model and the results were promising.

Finally, Chapter II and III showed how the high rheological response of simplified lubricants could be linked to the polymer physico-chemistry.

The last chapter linked the rheology and physico-chemistry of the polymer solutions to their tribological response in EHL and TFL regimes. Film thicknesses between 15 and 200 nm were measured by differential colorimetric interferometry and compared to the results determined from EHL analytical models, such as Chittenden, Moes and Chevalier. The good agreement observed for the base oil confirmed its Newtonian behavior in the studied conditions, whereas deviations between analytical predictions and experimental data were observed for all polymer solutions. These gaps were first attributed to the shear-thinning response of the polymer solutions. It was indeed noticed that the deviations were more important for polymers with larger shear-thinning behaviors. Moreover, the film thicknesses calculated with the Carreau-Yasuda viscosity at high shear rate instead of the Newtonian viscosity showed fairly good agreement with the experimental data on the central film thickness, apart from the PAMAs below 50 nm. Combining results from high pressure rheology and classical EHD equations allowed thus a good evaluation of the film thickness of non-Newtonian solutions.

However, rheological considerations alone could not explain the PAMAs response at film thicknesses of the same order of magnitude than the polymer coils. Molecular considerations could explain the presence of adsorbed polymers at the surfaces of the contacting bodies and illustrated the transition to the TFL regime. The adsorbed layer was linked to the gyration radii R_g of the PAMAs, and was equal to one R_g for the PAMA-C and to two R_g for the PAMA-L. The PAMA-L capacity to form thicker adsorbed layer was explained by the polar dispersant function implemented in its backbone.

Finally, the base oil tribological response was affected by the addition of all polymers, apart from the PISH-S whose results raised the question of the size of macromolecules actually travelling through the contact. Nonetheless, the polymer rheology, as well as their physico-chemistry, could finally

be linked to their tribological response. All conclusions should be helpful to the formulators to find new improvement possibilities for fuel-economy lubricants.

A targeted polymer for VII application may be considered in view of the conclusions from this work. The optimal engine lubricant must be viscous enough to fully support the load and separate the contacting bodies, shear-thin for its extensive use as a fuel economy lubricant, and maintain all these properties at high temperatures and pressures.

The swelling of polymer coils with temperature have been shown to enhance the VII properties. The polymer must present a low solubility in the base oil at low temperature and be in “theta conditions” in such conditions. It would have a high molecular weight and a high extensibility (with weak or few intramolecular bonds). This behavior is achieved with comb polyalkylmethacrylate, which is an amphiphilic polymer. Its properties can be adjusted by varying the lengths of its alkyl side chains. The PISH-S, a star shape polyisoprene, presents interesting properties also linked to its solubility variations in the base oil.

The shear-thinning response is indeed an essential property. Even though, the best VII properties were reached for the comb PAMA, this polymer did not shear-thin significantly. The star shape polyisoprene appeared to be a good alternative, as the PISH-S solution displayed a large shear-thinning response with VII properties.

However, the tribological study highlighted the PAMAs capacity to form adsorbed layer at the surfaces since they are polar molecules. Moreover, functionalized PAMAs, such as the PAMA-L, were known to form thicker adsorbed layer.

The targeted VII must thus be a polar polymer, such as a polyalkylmethacrylate, and presents polar functional groups that enhance the polymer adsorption at the surface. The chosen conformation would be the comb one, even though the PAMA-C did not exhibit a large shear-thinning behavior. However, it was assumed that this polymer would shear-thin at high temperature once its polymer coils would be fully swelled and may be then appealing for engine lubricants.

Recommendations for future works

The role and functions of Viscosity Index Improvers on the behavior of engine lubricants was widely investigated in this work. However, several questions were raised and may lead to possible future works.

First of all, several investigations on the polymer solutions would be required to assess the hypothesis made in this study. The high pressure rheological characterization of polymer solutions was improved through this thesis but still lacked information on the viscosity response of solution at very high shear stresses. Improvement of the current rheological models are also required to accurately describe the possible shear-thinning of PAMA-C solution at high temperature. The comparison of results with molecular dynamics simulations would also be of highly interest for the understanding of molecular mechanisms and their effect on the rheological response.

The question of the degradation of polymers or their passage within the contact was raised by the PISH-S results in chapter IV. Permanent shear-thinning might be then studied by running several cycles on Jerotrib or on the high pressure rheometers to approach the engine conditions. In addition, in situ experiments using spectroscopy techniques (Raman, Infra-Red or fluorescence) would be of first interest to visualize the trajectory of VII through the contact in EHL conditions.

Surface analysis could be performed to confirm the polymer adsorption assumed in chapter IV. Moreover, friction measurements linked to film thickness results are also essential to validate the interest of PAMAs in the TFL conditions. The final step of this characterization would be to run numerical simulations including the rheological models determined in chapter II and III, to accurately determine the film thickness and friction coefficient of the polymer solutions in realistic engine conditions.

Next, the study of different polymer solutions should be performed to develop a better understanding of the relationship between the molecular scale, the rheology and the tribology responses. A polar base oil could be studied, since the interactions between the polymer and the base oil drives the polymer behavior in solutions. In chapter II, the swelling of the polymer coils was indeed linked to the solubility variations with temperature of polar molecules within a non-polar solvent. In a polar base oil, the PAMA-C should be in better solvent conditions. Its coils would be fully swelled and a desired shear-thinning response may then occur. However, would the size of the PAMA-C coils still increase since the polymer is more soluble at low temperature? It is not possible to answer since the amphiphilic nature of comb PAMA may also influence the polymer response in polar solvent.

Another possible investigation would be to mix friction modifiers with VII and see how the tribological response of the VII, especially PAMA, would be affected. Indeed, friction modifiers, briefly described in chapter I, reduce friction in the contact thanks to polar compounds which adsorb on the sliding surfaces. The presence of PAMA molecules at the surface may annihilate the friction modifiers efficiency.

Other polymers could be studied. Other conformations of PAMAs would be interesting since polyalkylmethacrylates offer a large variety of structure. A star shape PAMA of high molecular weight, with a polar functional group, could be investigated as no information on its high pressure rheology are currently available. If this polymer exhibits a large shear-thinning response with VII properties, it would be an appealing additive for VII applications.

References

- [1] K. Holmberg, P. Andersson, and A. Erdemir, “Global energy consumption due to friction in passenger cars,” *Tribol. Int.*, vol. 47, pp. 221–234, 2012.
- [2] K. Holmberg and A. Erdemir, “Influence of tribology on global energy consumption, costs and emissions,” *Friction*, vol. 5, no. 3, pp. 263–284, 2017.
- [3] D. Berthe and P. Vergne, “High pressure rheology for high pressure lubrication: A review,” *J. Rheol. (N. Y. N. Y.)*, vol. 34, no. 8, pp. 1387–141, 1990.
- [4] P. M. Lugt and G. E. Morales-Espejel, “A Review of Elasto-Hydrodynamic Lubrication Theory,” *Tribol. Trans.*, vol. 54, no. 3, pp. 470–496, 2011.
- [5] S. Bair, *High Pressure Rheology for Quantitative Elastohydrodynamics*, First edit. Amsterdam: Elsevier, 2007.
- [6] W. Habchi, P. Vergne, S. Bair, O. Andersson, D. Eyheramendy, and G. E. Morales-Espejel, “Influence of pressure and temperature dependence of thermal properties of a lubricant on the behaviour of circular TEHD contacts,” *Tribology Int.*, vol. 43, pp. 1842–1850, 2010.
- [7] T. Doki-Thonon *et al.*, “A Dual Experimental/Numerical Approach for Film Thickness Analysis in TEHL Spinning Skewing Circular Contacts,” *Tribol Lett.*, vol. 50, pp. 115–126, 2013.
- [8] I. Krupka, P. Kumar, S. Bair, M. M. Khonsari, and M. Hartl, “The effect of load (pressure) for quantitative EHL film thickness,” *Tribol. Lett.*, vol. 37, no. 3, pp. 613–622, 2010.
- [9] T. W. Selby, “The Non-Newtonian Characteristics of Lubricating Oils,” *A S L E Trans.*, vol. 1, no. 1, pp. 68–81, Jan. 1958.
- [10] C. Mary, “Physico-chemistry, high pressure rheology and film forming capacity of polymer-base oil solutions in EHL,” PhD thesis. Institut National des Sciences Appliquées de Lyon. N° d’ordre: 2014ISAL0013, 2014.
- [11] P.-G. de Gennes, *Scaling concepts in polymer physics*. Ithaca, NY: Cornell University Press, 1979.
- [12] C. A. Angell, “Formation of Glasses from Liquids and Biopolymers Author (s): C . A . Angell Published by : American Association for the Advancement of Science Stable,” *Science*, vol. 267, no. 5206, pp. 1924–1935, 1995.
- [13] S. Yasutomi, S. Bair, and W. O. Winer, “An Application of a Free Volume Model to Lubricant Rheology I—Dependence of Viscosity on Temperature and Pressure,” *J. Tribol.*, vol. 106, no. 2, pp. 291–312, 1984.
- [14] S. Bair, C. Mary, N. Bouscharain, and P. Vergne, “An improved Yasutomi correlation for viscosity at high pressure,” *Proc. Inst. Mech. Eng. Part J J. Eng. Tribol.*, vol. 227, no. 9, pp. 1056–1060, 2013.
- [15] R. I. Tanner, *Engineering rheology*, Second edition. Oxford: Oxford University Press, 2000.
- [16] S. Bair, “A Rough Shear-Thinning Correction for EHD Film Thickness,” *Tribol. Trans.*, vol. 47, pp. 361–365, 2004.
- [17] B. Zhang, “A Novel Model of the Equivalent Viscosity of Simple Viscoelastic Fluids,” *J. Tribol.*, vol. 138, no. 2, pp. 21802, Nov. 2015.
- [18] A. J. Barlow, A. Erginsav, and J. Lamb, “Viscoelastic Relaxation in Liquid Mixtures,” *Proc. R. Soc. A Math. Phys. Eng. Sci.*, vol. 309, no. 1499, pp. 473–496, 1969.
- [19] M. J. Covitch and K. J. Trickett, “How Polymers Behave as Viscosity Index Improvers in

References

- Lubricating Oils,” *Adv. Chem. Eng. Sci.*, vol. 5, no. April, pp. 134–151, 2015.
- [20] D. Chaveroux, “Relation Structure-Propriétés Des Polymères Améliorants De Viscosité Dans Les Lubrifiants Moteur,” PhD thesis. Université du Maine Le Mans - Laval. Unpublished, 2015.
- [21] I. Larue, “An Investigation into the Morphologies of Polystyrene-b-Polyisoprene Micelles,” PhD Thesis. University of North Carolina, 2006.
- [22] C. Mary *et al.*, “New insight into the relationship between molecular effects and the rheological behavior of polymer-thickened lubricants under high pressure,” *Tribol. Lett.*, vol. 52, no. 3, pp. 357–369, 2013.
- [23] J. Molimard, “Etude expérimentale du régime de lubrification en film mince - application aux fluides de laminage,” PhD thesis. Institut National des Sciences Appliquées de Lyon. N° d’ordre: 99ISAL0121, 1999.
- [24] M. Hartl *et al.*, “Thin Film Colorimetric Interferometry,” *Tribol. Trans.*, vol. 44, no. 2, pp. 270–276, 2001.
- [25] R. J. Chittenden, D. Dowson, J. F. Dunn, and C. . Taylor, “A theoretical analysis of the isothermal elastohydrodynamic lubrication of concentrated contacts - Part II. General case, with lubricant entrainment along either principal axis of the Hertzian contact ellipse or at some intermediate angle,” *Proc. R. Soc. Lond.*, vol. A 397, pp. 271–294, 1985.
- [26] G. Nijenbanning, C. H. Venner, and H. Moes, “Film thickness in elastohydrodynamically lubricated elliptic contacts,” *Wear*, vol. 176, pp. 217–229, 1994.
- [27] F. Chevalier, “Modélisation des conditions d’alimentation dans les contacts élastohydrodynamiques ponctuels,” PhD Thesis. Institut National des Sciences Appliquées de Lyon, 1996.
- [28] H. A. Spikes and P. M. Cann, “The thickness and rheology of boundary lubricating films,” in *Proc. ITC Yokohama*, 1995, pp. 1089–1094.
- [29] IEA Energy Technology Perspectives, “Scenarios and Strategies to 2050,” Paris, France, 2010.
- [30] “Introduction,” *ENSPM Formation Industrie*. IFP Training, pp. 1–13, 2006.
- [31] Habot, “What causes engine oil contamination?,” 2014. [Online]. Available: <http://habotmarketing.blogspot.fr/2014/07/what-causes-engine-oil-contamination.html>. [Accessed: 11-Oct-2017].
- [32] R. Taylor and B. de Kraker, “Shear rates in engines and implications for lubricant design,” *Proc. Inst. Mech. Eng. Part J J. Eng. Tribol.*, vol. 231, no. 9, pp. 1106–1116, 2017.
- [33] M. B. Dobrica and M. Fillon, “Mixed Lubrication,” in *Encyclopedia of Tribology*, Boston, MA: Springer US, 2013, pp. 2284–2291.
- [34] R. C. Coy, “Practical applications of lubrication models in engines,” *Tribol. Int.*, vol. 31, no. 10, pp. 563–571, 1998.
- [35] D. Dowson and P. Ehret, “Past, present and future studies in elastohydrodynamics,” *Proc. Instn. Mech. Engrs., Part J J. Eng. Trib.*, vol. 213, no. 5, pp. 317–333, 1999.
- [36] L. Ma and J. Luo, “Thin film lubrication in the past 20 years,” *Friction*, vol. 4, no. 4, pp. 280–302, 2016.
- [37] J. Molimard, M. Querry, and P. Vergne, “New tools for the experimental study of EHD and limit lubrications,” *Tribol. Ser.*, vol. 36, pp. 717–726, 1999.
- [38] J.-D. Wheeler, P. Vergne, N. Fillot, and D. Philippon, “On the relevance of analytical film thickness EHD equations for isothermal point contacts: Qualitative or quantitative predictions?”

- Friction*, vol. 4, no. 4, pp. 369–379, 2016.
- [39] M. Priest and C. M. Taylor, “Automobile engine tribology—approaching the surface,” *Wear*, vol. 241, no. 2, pp. 193–203, 2000.
- [40] F. Wiltord, “Lubrification du laminage à froid de l’aluminium: Action des huiles de base et des additifs,” PhD thesis. Institut National des Sciences Appliquées de Lyon. N° d’ordre: 2005ISAL0034, 2005.
- [41] J. Luo, X. Lu, and S. Wen, “Developments and unsolved problems in nano-lubrication,” *Prog. Nat. Sci.*, vol. 11, no. 3, pp. 173–183, 2001.
- [42] J. Luo, S. Wen, and P. Huang, “Thin film lubrication Part I: Study on the transition between EHL and thin film lubrication using a relative optical interference intensity technique,” *Wear*, vol. 194, pp. 107–115, 1996.
- [43] S. Günsel, M. Smeeth, and H. Spikes, “Friction and Wear Reduction by Boundary Film-Forming Viscosity Index Improvers,” in *SAE International Fall Fuels and Lubricants Meeting and Exhibition*, 1996.
- [44] Y.-Z. Hu and S. Granick, “Microscopic study of thin film lubrication and its contributions to macroscopic tribology,” *Tribol. Lett.*, vol. 5, pp. 81–88, 1998.
- [45] D. Savio, N. Fillot, and P. Vergne, “A molecular dynamics study of the transition from ultra-thin film lubrication toward local film breakdown,” *Tribol. Lett.*, vol. 50, pp. 207–220, 2013.
- [46] “Engine Oil Licensing and Certification System, Appendix E.” API Base oil Interchangeability Guidelines, API 1509, 2007.
- [47] “Huiles de base minérales,” *ENSPM Formation Industrie*. IFP Training, pp. 1–44, 2006.
- [48] J. Ayel, “Lubrifiants - Constitution,” *Tech. l’Ingénieur*, vol. BM 5 341, pp. 1–17, 1997.
- [49] ASTM D2270, “Calculating viscosity index from kinematic viscosity at 40 and 100 °C.”
- [50] J. Ayel, M. Born, and F. Germain, *Lubrifiants et fluides pour l’automobile*, Ed. Technip. 1998.
- [51] J. Ayel, “Lubrifiants - Additifs à action physique ou physiologique,” *Tech. l’Ingénieur*, pp. 1–18, 2002.
- [52] L. R. Rudnick, *Lubricant additives : chemistry and applications*. Boca Raton, US: CRC Press, 2009.
- [53] J.-M. Georges, *Frottement, usure et lubrification: la tribologie ou science des surfaces*. Paris: Eyrolles, 2000.
- [54] N. Canter, “Viscosity Index Improvers,” *Tribol. Lubr. Technol. STLE*, vol. 67, no. 9, pp. 10–22, 2011.
- [55] C. D. Neveu, R. Sondjaja, T. Stöhr, and N. J. Iroff, “Lubricant and Fuel Additives Based on Polyalkylmethacrylates,” *Polym. Sci. A Compr. Ref.*, vol. 10, pp. 453–478, 2012.
- [56] H. G. Müller, “Mechanism of action of viscosity index improvers,” *Tribol. Int.*, vol. 11, no. 3, pp. 189–192, 1978.
- [57] D. LaRiviere, A.-F. Asfour, A. Hage, and J. Gao, “Viscometric Properties of Viscosity Index Improvers in Lubricant Base Oil over a Wide Temperature Range. Part I: Group II base oil,” *Lubr. Sci.*, vol. 12, pp. 133–143, 2000.
- [58] G. Totten, S. Westbrook, and R. Shah, *Fuels and Lubricants Handbook: Technology, Properties, Performance, and Testing*. Glen Burnie, MD: ASTM publisher, 2003.
- [59] R. L. Stambaugh and B. G. Kinker, “Viscosity Index Improvers and Thickeners,” in *Chemistry*

References

- and Technology of Lubricants*, Dordrecht: Springer Netherlands, 2009, pp. 153–187.
- [60] T. Senninger, “Catalyse de Polymerisation,” *Tech. l’Ingénieur*, vol. J 1 260, pp. 1–21, 1998.
- [61] H. Eschwey and W. Burchard, “Star polymers from styrene and divinylbenzene,” *Polymer*, vol. 16, no. 3, pp. 180–184, 1975.
- [62] J. Omeis and H. Pennewiss, “Comb polymers based on olefin copolymer macromonomers,” US 5,565,130, 1996.
- [63] R. J. Young and P. A. Lovell, *Introduction to polymers*, Third edit. Boca Raton: CRC Press, 2011.
- [64] M. Chanda, *Introduction to polymer science and chemistry : a problem-solving approach*, Second edi. Boca Raton, US: CRC Press, 2013.
- [65] M. D. Hersey and R. F. Hopkins, “Viscosity of lubricants under pressure,” 1954.
- [66] R. F. T. Stepto, “Dispersity in polymer science,” *Pure Appl. Chem.*, vol. 81, no. 2, pp. 351–353, 2009.
- [67] M. Daoud and J. P. Cotton, “Star shaped polymers : a model for the conformation and its concentration dependence,” *J. Phys.*, vol. 43, no. 3, pp. 531–538, 1982.
- [68] P. J. Flory, *Principles of polymer chemistry*, First edit. New-York, US: Cornell University Press, 1953.
- [69] N. S. Davidson, L. J. Fetters, W. G. Funk, N. Hadjichristidis, and W. W. Graessley, “Measurement of chain dimensions in dilute polymer solutions: a light scattering and viscometric study of linear polyisoprene in cyclohexane,” *Macromolecules*, vol. 20, no. 10, pp. 2614–2619, Oct. 1987.
- [70] J. des Cloiseaux and G. Jannink, *Les polymères en solution: leur modélisation et leur structure*. Les Ulis: EDP Sciences, 1987.
- [71] E. Zhang, X. Dai, Z. Dong, X. Qiu, and X. Ji, “Critical concentration and scaling exponents of one soluble polyimide - from dilute to semidilute entangled solutions,” *Polymer*, vol. 84, pp. 275–285, 2016.
- [72] B. A. Wolf, “Polyelectrolytes Revisited: Reliable Determination of Intrinsic Viscosities,” *Macromol. Rapid Commun.*, vol. 28, no. 2, pp. 164–170, 2007.
- [73] M. Rubinstein and R. Colby, *Polymers Physics*. Oxford: ed. Oxford University Press, 2003.
- [74] M. A. Meyers and K. K. Chawla, *Mechanical Behavior of Materials*, Second edi. Cambridge: Prentice Hall, 2009.
- [75] J. C. Maxwell, “On the dynamical theory of Gases,” *Philos. Trans. R. Soc. London*, vol. 157, pp. 49–88, 1867.
- [76] T. Ree and H. Eyring, “Theory of Non-Newtonian Flow. II. Solution System of High Polymers,” *J. Appl. Phys.*, vol. 26, no. 7, pp. 800–809, 1955.
- [77] H. A. Barnes, J. F. Hutton, and K. Wlaters, *An introduction to rheology*, 1st edition. Amsterdam: Elsevier Science Publishers B.V., 1989.
- [78] J. E. Glass, D. N. Schulz, and C. F. Zukoski, *Polymers as Rheology Modifiers*. York, PA, 1991.
- [79] E. N. da C. Andrade, “The Viscosity of Liquids,” *Nature*, vol. 125, no. 3148, pp. 309–310, 1930.
- [80] H. Eyring, “Viscosity, Plasticity, and Diffusion as Examples of Absolute Reaction Rates,” *J. Chem. Phys.*, vol. 4, no. 4, pp. 283–291, 1936.

- [81] C. A. Angell, "Perspective on the glass transition," *J. Phys. Chem. Solids*, vol. 49, no. 8, pp. 863–871, 1988.
- [82] X. Paredes, J. Fernández, A. S. Pensado, and M. J. P. Comuñas, "How Pressure Affects the Dynamic Viscosities of Two Poly(propylene glycol) Dimethyl Ether Lubricants," *J. Chem. Eng. Data*, vol. 55, no. 9, pp. 4088–4094, 2010.
- [83] M. L. Williams, R. F. Landel, and J. D. Ferry, "The Temperature Dependence of Relaxation Mechanisms in Amorphous Polymers and Other Glass-forming Liquids," *J. Amer. Chem. Soc.*, vol. 77, no. 14, pp. 3701–3707, 1955.
- [84] P. W. Bridgman, "The Effect of Pressure on the Viscosity of Forty-Three Pure Liquids," *Proc. Am. Acad. Arts Sci.*, vol. 61, no. 3, p. 57, 1926.
- [85] P. W. Bridgman, "Viscosities to 30,000 Kg/Cm," *Proc. Am. Acad. Arts Sci.*, vol. 77, pp. 117–128, 1949.
- [86] H. Block, "Inverse problems in hydrodynamic lubrication and design directives for lubricated flexible surfaces," in *Proceedings International Symposium on Lubrication and Wear*, 1963, pp. 1–151.
- [87] P. Vergne, "Comportement rhéologique des lubrifiants et lubrification: approches expérimentales," HdR. Institut National des Sciences Appliquées de Lyon., 2002.
- [88] C. M. Roland, "Characteristic relaxation times and their invariance to thermodynamic conditions," *Soft Matter*, vol. 4, pp. 2316–2322, 2008.
- [89] M. M. Cross, "Rheology of Non-Newtonian fluids: a new flow equation for pseudoplastic systems," *J. Colloid Sci.*, vol. 20, pp. 417–437, 1965.
- [90] D. M. Meter and R. B. Bird, "Tube Flow of Non-Newtonian Polymer Solutions: Part I. Laminar Flow and Rheological Models," *A.I.Ch.E J.*, vol. 10, no. 6, pp. 878–881, 1964.
- [91] P. J. Carreau, "Rheological Equations from Molecular Network Theories," *Trans. Soc. Rheol.*, vol. 16, no. 1, pp. 99–127, Mar. 1972.
- [92] ASTM D4741, "Standard Test Method for Measuring Viscosity at High Temperature and High Shear Rate by Tapered-Plug Viscometer." .
- [93] P. Cusseau, N. Bouscharain, L. Martinie, D. Philippon, P. Vergne, and F. Briand, "Rheological considerations on polymer-based engine lubricants: viscosity index improvers versus thickeners – generalized Newtonian models," *Tribol. Trans.*, vol. In press, no. DOI: 10.1080/10402004.2017.1346154, pp. 1–11, 2017.
- [94] S. Bair, "Generalized Newtonian viscosity functions for hydrodynamic lubrication," *Tribol. Int.*, vol. 117, pp. 15–23, 2018.
- [95] I. Larue, M. Adam, M. Pitsikalis, N. Hadjichristidis, M. Rubinstein, and S. S. Sheiko, "Reversible Morphological Transitions of Polystyrene-b-polyisoprene Micelles," *Macromolecules*, vol. 39, pp. 309–314, 2006.
- [96] D. Lariviere, A.-F. A. Asfour, A. Hage, and J. Z. Gao, "Viscometric properties of viscosity index improvers in lubricant base oil over a wide temperature range. Part I: Group II base oil," *Lubr. Sci.*, vol. 12, no. 2, pp. 133–143, 2000.
- [97] U. S. Ramasamy, S. Lichter, and A. Martini, "Effect of Molecular-Scale Features on the Polymer Coil Size of Model Viscosity Index Improvers," *Tribol. Lett.*, vol. 62, no. 2, 2016.
- [98] S. Bair and W. O. Winer, "A New High-Pressure, High-Shear Stress Viscometer and Results for Lubricants," *Tribol. Trans.*, vol. 36, no. 4, pp. 721–725, 1993.

References

- [99] M. Yuan, J. A. Galloway, R. J. Hoffman, and S. Bhatt, "Influence of molecular weight on rheological, thermal, and mechanical properties of PEEK," *Polym. Eng. Sci.*, vol. 51, no. 1, pp. 94–102, 2011.
- [100] M. M. Cross, "Polymer rheology: Influence of molecular weight and polydispersity," *J. Appl. Polym. Sci.*, vol. 13, no. 4, pp. 765–774, 1969.
- [101] J. W. Robinson *et al.*, "Probing the molecular design of hyper-branched aryl polyesters towards lubricant applications," *Sci. Rep.*, vol. 6, pp. 18624, 2016.
- [102] S. Bair, "The First Normal Stress Difference in a Shear-Thinning Motor Oil at Elevated Pressure," *Tribol. Trans.*, vol. 58, no. 4, pp. 654–659, 2015.
- [103] T. Doki-Thonon, "Thermal effects in elastohydrodynamic spinning circular contacts," PhD thesis. Institut National des Sciences Appliquées de Lyon. N° d'ordre: 2012ISAL0058, 2012.
- [104] M. Hartl, I. Krupka, and M. Liska, "Differential colorimetry: tool for evaluation of chromatic interference patterns," *Opt. Eng.*, vol. 36, no. 9, pp. 2384–2391, 1997.
- [105] K. L. Johnson, J. A. Greenwood, and J. G. Higginson, "The contact of elastic regular wavy surfaces," *Int. J. Mech. Sci.*, vol. 27, no. 6, pp. 383–396, 1985.
- [106] C. A. Foord, L. D. Wedeven, F. J. Westlake, and A. Cameron, "Optical Elastohydrodynamics," *Proc. Inst. Mech. Eng.*, vol. 184, no. 1, pp. 487–505, 1969.
- [107] F. Guo and P. L. Wong, "A multi-beam intensity-based approach for lubricant film measurements in non-conformal contacts," *Proc. of Inst. Mech. Eng. Part J J. Eng. Tribol.*, vol. 16, no. 5, pp. 281–291, 2002.
- [108] Z. Fu, A. F. Guo, and P. L. Wong, "Theoretical Study on the Interferometry of Thin EHL Film Measurement," *Tribol Lett.*, vol. 31, pp. 57–65, 2008.
- [109] H. Van Leeuwen, "The determination of the pressure-viscosity coefficient of a lubricant through an accurate film thickness formula and accurate film thickness measurements," *Proc IMechE, Part J J Eng Tribol*, vol. 223, no. 8, pp. 1143–1163, 2009.
- [110] H. van Leeuwen, "The determination of the pressure–viscosity coefficient of a lubricant through an accurate film thickness formula and accurate film thickness measurements. Part 2: high L values," *Proc IMechE, Part J J Eng Tribol*, vol. 225, no. 6, pp. 449–464, 2011.
- [111] I. Bernard, J. Hamrock, and D. Dowson, "Isothermal elastohydrodynamic lubrication of point contacts: part III—fully flooded results," *J. Lubr. Tech.*, vol. 99, no. 2, pp. 264–275, 1977.
- [112] J.-P. Chaomleffel, G. Dalmaz, and P. Vergne, "Experimental results and analytical film thickness predictions in EHD rolling point contacts," *Tribol. Int.*, vol. 40, pp. 1543–1552, 2007.
- [113] M. Born and E. Wolf, *Principles of optics: Electromagnetic theory of propagation interference and diffraction light*, Seventh ed. Cambridge, UK: Cambridge University Press, 1965.
- [114] H. S. Cheng, "A Refined Solution to the Thermal-Elastohydrodynamic Lubrication of Rolling and Sliding Cylinders," *ASLE Trans.*, vol. 8, no. 4, pp. 397–410, 1965.
- [115] I. Jubault, J. L. Mansot, P. Vergne, A. A. Lubrecht, and J. Molimard, "In situ pressure measurements in an elastohydrodynamically lubricated point contact using Raman microspectrometry . Comparison with numerical calculations," *Proc. 29th Leeds-Lyon symp. Tribol. Leeds, D.Dowson al Elsevier 2003*, pp. 663–673, 2002.
- [116] Y.-Z. Hu and S. Granick, "Microscopic study of thin film lubrication and its contributions to macroscopic tribology," *Tribol. Lett.*, vol. 5, pp. 81–88, 1998.
- [117] P. M. Cann and H. A. Spikes, "The Behavior of Polymer Solutions in Concentrated Contacts:

- Immobile Surface Layer Formation,” *Tribol. Trans.*, vol. 37, no. 3, pp. 580–586, 1994.
- [118] P.-G. de Gennes, *Simple views on condensed matter*, Third edition. River Edge, NJ: World Scientific, 2003.
- [119] Müller, Michael, K. Topolovec-Miklozic, A. Dardin, and H. A. Spikes, “The Design of Boundary Film-Forming PMA Viscosity Modifiers,” *Tribol. Trans.*, vol. 49, pp. 225–232, 2006.
- [120] I. Krupka and M. Hartl, “The influence of thin boundary films on real surface roughness in thin film, mixed EHD contact,” *Tribol. Int.*, vol. 40, pp. 1553–1560, 2007.
- [121] M. Muraki and K. Nakamura, “Film-forming properties and traction of non- functionalized polyalkylmethacrylate solutions under transition from elastohydrodynamic lubrication to thin-film lubrication,” *Proc Instn Mech Engrs, Part J J. Eng. Tribol.*, vol. 224, no. 1, pp. 55–63, 2010.
- [122] S. Zhang, Y. Liu, and J. Luo, “In situ observation of the molecular ordering in the lubricating point contact area Nanoscale flow past a colloidal cylinder confined in a slit channel: Lubrication theory and molecular dynamics analysis Physics of Fluids In situ observation of the molecular ordering in the lubricating point contact area,” *J. Appl. Phys. J. Appl. Phys. J. Appl. Phys.*, vol. 116, no. 1, pp. 14302, 2014.
- [123] P. M. Cann and H. a. Spikes, “In Lubro Studies of Lubricants in EHD Contacts Using FTIR Absorption Spectroscopy,” *Tribol. Trans.*, vol. 34, no. 2, pp. 248–256, 1991.
- [124] PCS Instruments, “USV (Ultra Shear Viscometer).” [Online]. Available: <https://pcs-instruments.com/product/usv-ultra-shear-viscometer/>. [Accessed: 17-Jan-2018].
- [125] K. R. Harris and S. Bair, “Temperature and Pressure Dependence of the Viscosity of Diisodecyl Phthalate at Temperatures between 0 and 100 °C and at Pressures to 1 GPa” *J. Chem. Eng. Data*, vol. 52, no. 1, pp. 272–278, 2007.
- [126] S. Bair and G. W. Woodruff, “Measurements of real non-Newtonian response for liquid lubricants under moderate pressures,” *Proc. Inst. Mech. Eng. Part J J. Eng. Tribol.*, vol. 215, no. 3, pp. 223–233, 2001.
- [127] H. Hertz, “Über die berührung fester elastischer körper,” *J. reine und angew. Math.*, vol. 92, pp. 156–171, 1881.

Appendix 1 - Physica MCR301 rheometer (Anton-Paar)

Rheometers are laboratory devices measuring stress and deformation history of a liquid, suspension or any flow of matter, in response to applied forces. The measured parameter is the material viscosity, under shear stress or extensional forces. Several rheometers were used in this project, at both atmospheric (see Appendix 1, Appendix 2) and high pressure (Appendix 3, Appendix 4).

The viscosity-temperature profile at atmospheric pressure of the studied solutions is obtained by the Physica MCR301 rheometer, from Anton-Paar (Figure 63). Several rotational geometries are available: plate-plate, cone-plate and coaxial cylinders (Figure 64). The sample is poured into the gap of the chosen geometry – on the plate or into the outer cylinder – specifically designed to impose simple shear flow when rotated. Both plate-plate and cone-plate geometries work in similar ways. These geometries in oscillating mode can give access to the elastic properties of the studied material. In this work, measurements were carried out with the coaxial cylinders geometry only. The viscosity is linked to the dimensions of the cylinders.

$$\eta = \frac{M_t}{4\pi h_i \Omega} \left(\frac{1}{R_i^2} - \frac{1}{R_{ot}^2} \right) \quad \text{Eq. (46)}$$

Here M_t is the torque of the inner cylinder, h_i the height of the inner cylinder, Ω the angular speed, R_i the inner cylinder radius, R_{ot} the outer cylinder radius. The temperature is regulated by a Peltier system and the shear rate is imposed by an electrically commutated motor.

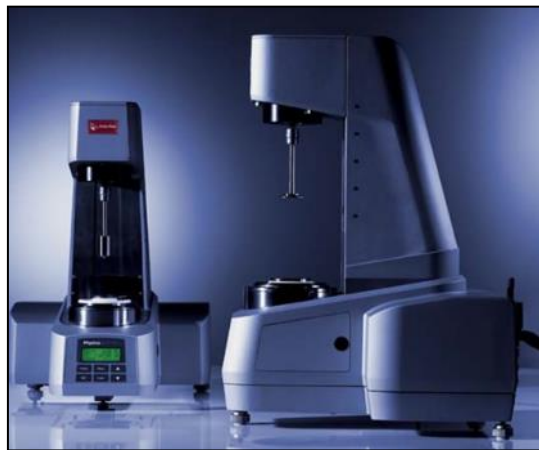


Figure 63: Physica MCR301 rheometer (Anton-Paar) [10]

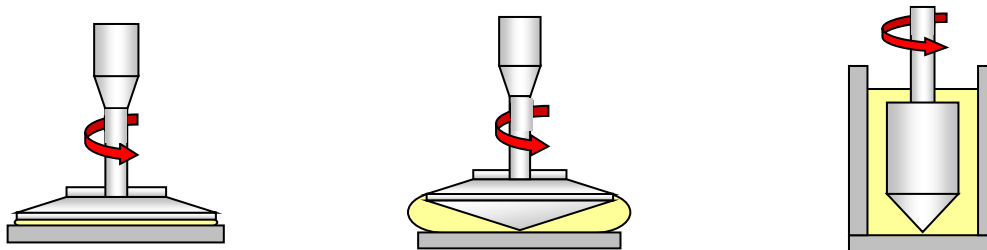


Figure 64: Anton-Paar geometries (plate-plate; cone-plate, coaxial cylinders) [10]

Appendix 2 - Ultra-Shear Viscometer (USV)

The Ultra-Shear Viscometer (USV) (Figure 65) from PCS Instruments [124] is a Couette viscometer, whose shearing gap is about 1 μm and allowing viscosity measurements at shear rates between 10^6 and 10^7 s^{-1} (equivalent to shear stresses from 4 kPa to 20 kPa). Experiments are run from 40 $^\circ\text{C}$ to 150 $^\circ\text{C}$, at atmospheric pressure.



Figure 65: Picture of the USV from PCS Instruments [10]

Rotation of the inner cylinder is ensured by an engine driving speeds greater than 20 000 rotations per minute. The inner cylinder is rotated during a short time (close to 30 ms) to limit shear-heating. The torque is measured by a piezoelectric force sensor connected to the stator. A Peltier system ensure the temperature regulation, which is measured by platinum thermocouples located in the stator and at the bottom of the test chamber.

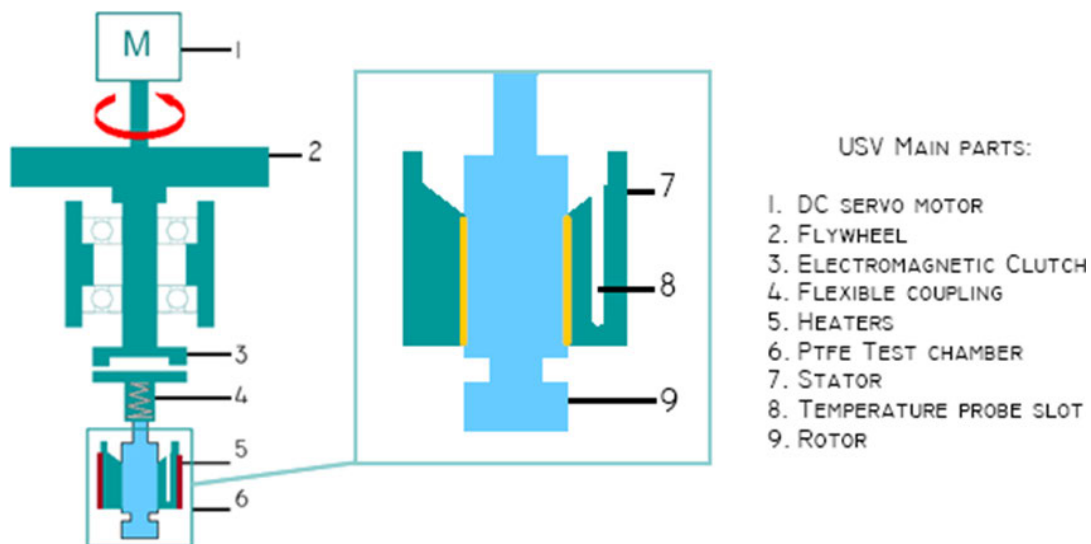


Figure 66: Schematic view of the USV

Appendix 3 – High pressure falling-body viscometer

The high pressure falling body viscometer (Figure 67) is used to obtain the viscosity-temperature-pressure dependence of all solutions. This viscometer, fully described in [98] measures the viscosity of the simplified lubricants over a wide pressure and temperature range, up to 800 MPa and 150 °C. Several sinkers (cup, solid and hollow) are available to cover a range of shear stresses between 1.5 and 70 Pa. The viscosity at low shear stress η_0 is linked to the falling time t of a stainless steel sinker into the cartridge filled with the fluid under study. The position of the magnetic sinker is followed by a LVDT (Linear Variable Differential Transformer) system and is transferred on an oscilloscope screen.

$$\eta_0 = C \cdot t \cdot \frac{\rho_s - \rho}{\rho_s} \quad \text{Eq. (47)}$$

Where ρ_s and ρ are the volumetric mass density of the sinker and the fluid respectively. The constant C is determined through the calibration with a reference fluid, such as the diisodecylphthalate (DIDP), sample C [125].

The pressure is manually applied by a pressuring pump thanks to a hydraulic liquid and an intensifier. The accuracy on the pressure is about 1 %. Regarding the temperature, the latter is adjusted by the circulation of heated air through the vessel and measured by a type K thermocouple, whose precision on the sample temperature is ± 0.3 °C. The statistical uncertainty on the viscosity is always below 5 %.

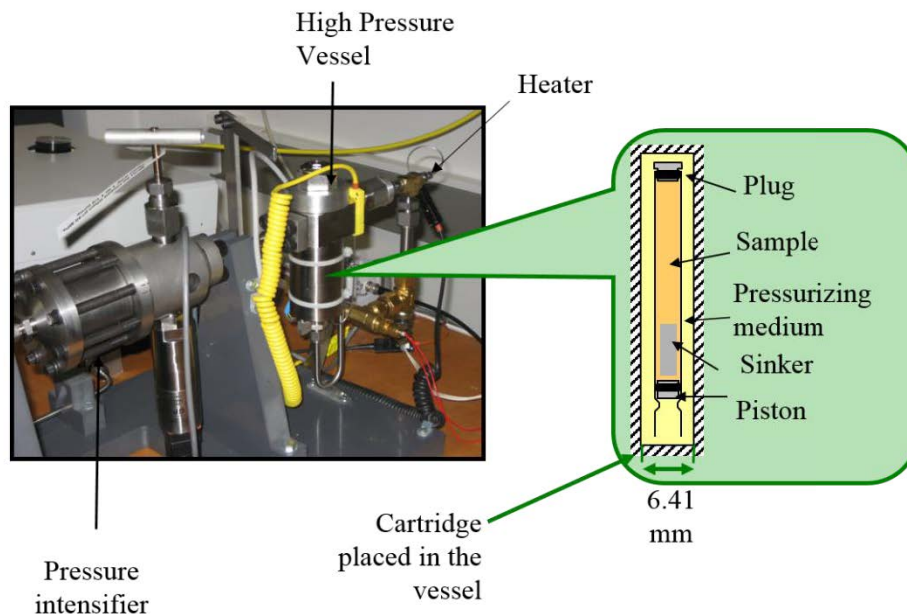


Figure 67: Description of the high pressure viscometer

Appendix 4 - High pressure Couette rheometer.

The high pressure Couette rheometer, designed by Dr. Scott Bair and is fully described in [126], is used to measure the shear stress influence on viscosity of all solutions, at pressures from 200 MPa to 400 MPa. No measurements are possible at atmospheric pressure, owing to the occurrence of cavitation and inadequate torque sensitivity. This rheometer is a rotational rheometer using a coaxial cylinders geometry. The sample is poured between the two concentric cylinders. It is sheared by the rotation of the inner cylinder, thanks to a stepper motor by means of a drive shaft. The torque is measured by strain gages connected to the outer cylinder. Three cylinders sets are used here to cover a large range of shear stresses from 0.5 kPa up to 100 kPa.

	“Low”	“Middle”	“High”
			
Gap (μm)	13.5	7.72	4.53
Resulting τ (kPa)	0.1 to 10	1 to 10 ²	10 to 10 ³

Table 20: Shearing gaps and resulting shear stresses range covered of the cylinders sets

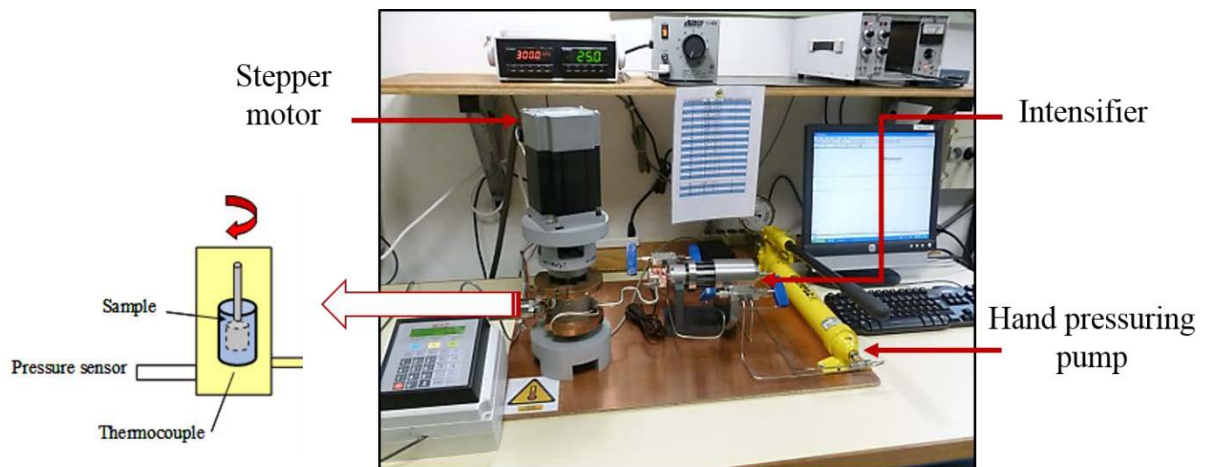


Figure 68: Description of the high pressure Couette rheometer

Thermal softening of the solution may occur in such small gaps and high shear rates and viscosities. The Nahme-Griffith number Na is thus used to evaluate the occurrence of this undesired effect [5]:

$$Na = \frac{\beta_{Na} \tau^2 h^2}{k\eta} \quad \text{Eq. (48)}$$

Where β_{Na} is the temperature-viscosity coefficient, k is the liquid thermal conductivity and h is the film thickness. The values of β_{Na} and k are 0.1 K⁻¹ and 0.1 W.m⁻¹.K⁻¹ respectively. The pressure is applied by a pressuring hand pump and an intensifier, through a solution of perfluorinated octane FC770 + 10%

of Fomblin, of much larger density and lower viscosity than the fluid studied. Most lubricants are not miscible with this solution, therefore they unlikely mix with it. The temperature is ensured by four copper cartridges enclosing the vessel and is measured with a type T thermocouple. The pressure accuracy is assessed at 1 %, whereas the temperature precision is judged to be ± 0.1 °C. The statistical uncertainty on the viscosity values is below 10 %.

Appendix 5 – Analytical tools

Differential Scanning Calorimetry (DSC)

Differential scanning calorimetry (DSC) is a thermoanalytical device in which the heat transfer required to increase the temperature of a sample and reference, is measured as a function of temperature. Specific temperatures, such as crystallization temperature, melting point or glass transition temperature T_g can be determined. When the sample undergoes a physical change of state, less or more heat flow to the sample regarding the physical transition being exothermic (crystallization) or endothermic (melting). Both the sample (with a well-defined heat capacity) and the reference are kept at the same temperature throughout the experiment. Measurements were carried out with a DSC NETZSCH (model 204 F1) on polymer solutions. The temperature ramp was as follow: introduction of the sample at ambient temperature, decrease of temperature to -80 °C at 1 °C/min, decrease to -120 °C at 10 °C/min, isotherm at -120 °C during 5 minutes, rise of T to 50 °C at 10 °C/min. The determination of the glass transition temperature occurs during the heating phase.

Size Exclusion Chromatography (SEC)

Size-exclusion chromatography (SEC) is a chromatographic method in which molecules in solution are separated by their size rather than their chemical affinity. SEC works by trapping the smaller molecules within the pores of a column. Larger molecules go through the column more quickly, present the shorter retention time and are thus first detected. Experiments were run on a Prominence HPLC system from Shimadzu equipped with a quadruple detector: a flow refractive index (RI) detector (RID10A from Shimadzu), a miniDAWN TREOS static light scattering (LS) detector from Wyatt, operating at three scattering angles 49°, 90°, 131° and at a wavelength of 658 nm, a viscometer detector (Viscostar II from Wyatt) and a UV detector (spectra system UV 1000 de spectra physics analytical, at $\lambda = 254$ nm). The samples were analyzed in THF at room temperature using a flow rate of 1 mL.min⁻¹ and were injected at a concentration of ~ 1 g.L⁻¹ in THF after filtration through a 0.2 μ m pore-size membrane. A guard column and two Agilent PL columns (one mixed D column and one uniform 50) (both 5 μ m, 300 x 7.5 mm). Both average molecular weights M_n and M_w as well as the polydispersity indexes were acquired from the RI signal and the LS signal using the adequate value of the specific refractive index increment for each polymer. These increments were equal to 0.075 for OCP, 0.110 for PISH and 0.079 for PAMA. Average hydrodynamic radii were obtained from static LS and viscometry detectors.

Appendix 6 – Viscosity-pressure dependence of all solutions

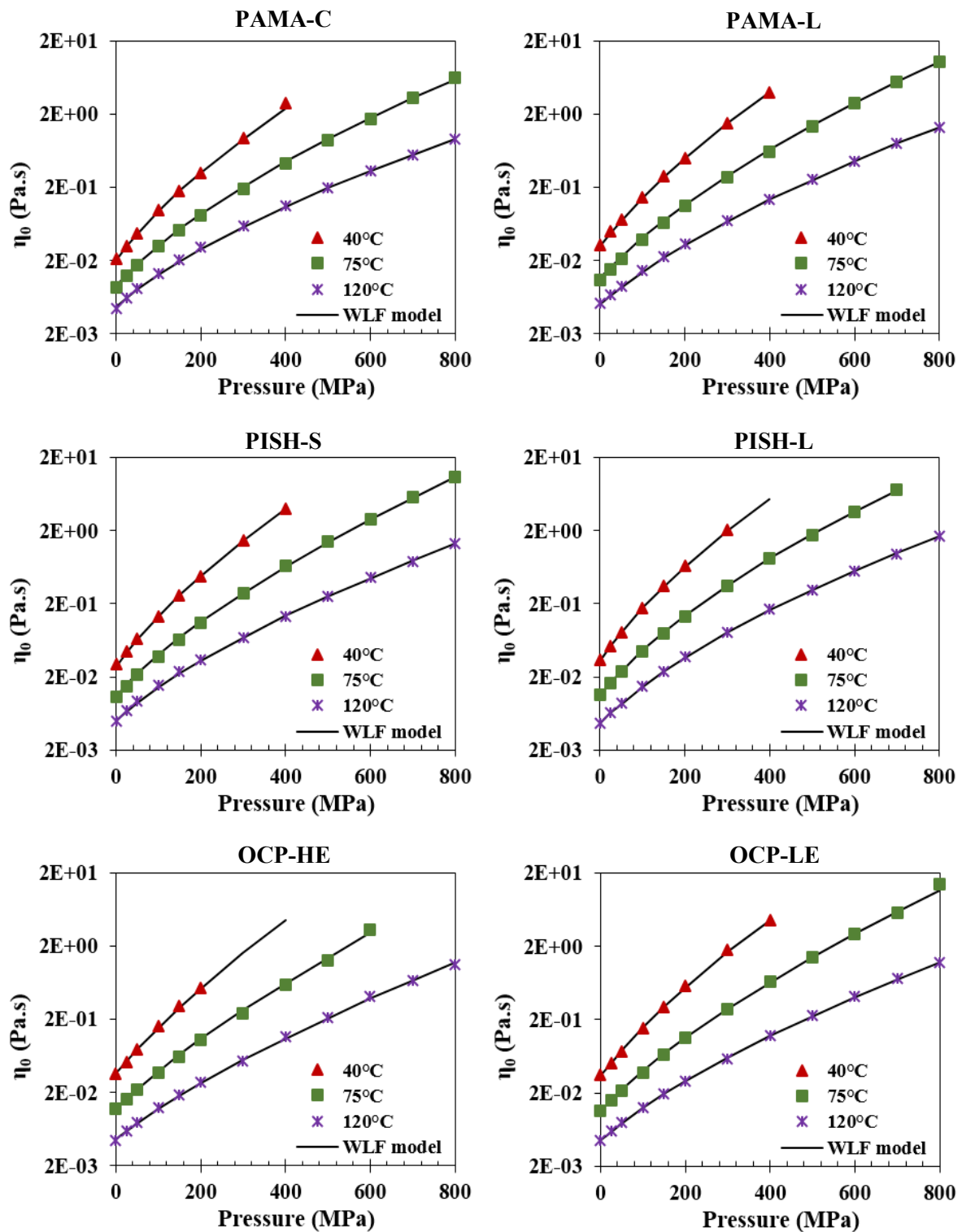


Figure 69: Viscosity-pressure dependence of all solutions at different temperatures

The piezoviscous behavior of all solutions is here presented. Experiments on the high pressure viscometer along with the computed viscosity with the WLF-Yasutomi model (Eq. (26), p. 47)[14] are reported in Figure 69. Again, the modified WLF-Yasutomi model fits well the experimental data. The polymer addition affects the state diagram of the base oil. Indeed, solidification occurs below 300 MPa at 40 °C for the OCP-HE, whereas it happens above 400 MPa at 40 °C for the PAMAs. Extrapolated values must thus be taken cautiously.

Appendix 7 - Reduced viscosity variations against temperature and pressure for all solutions

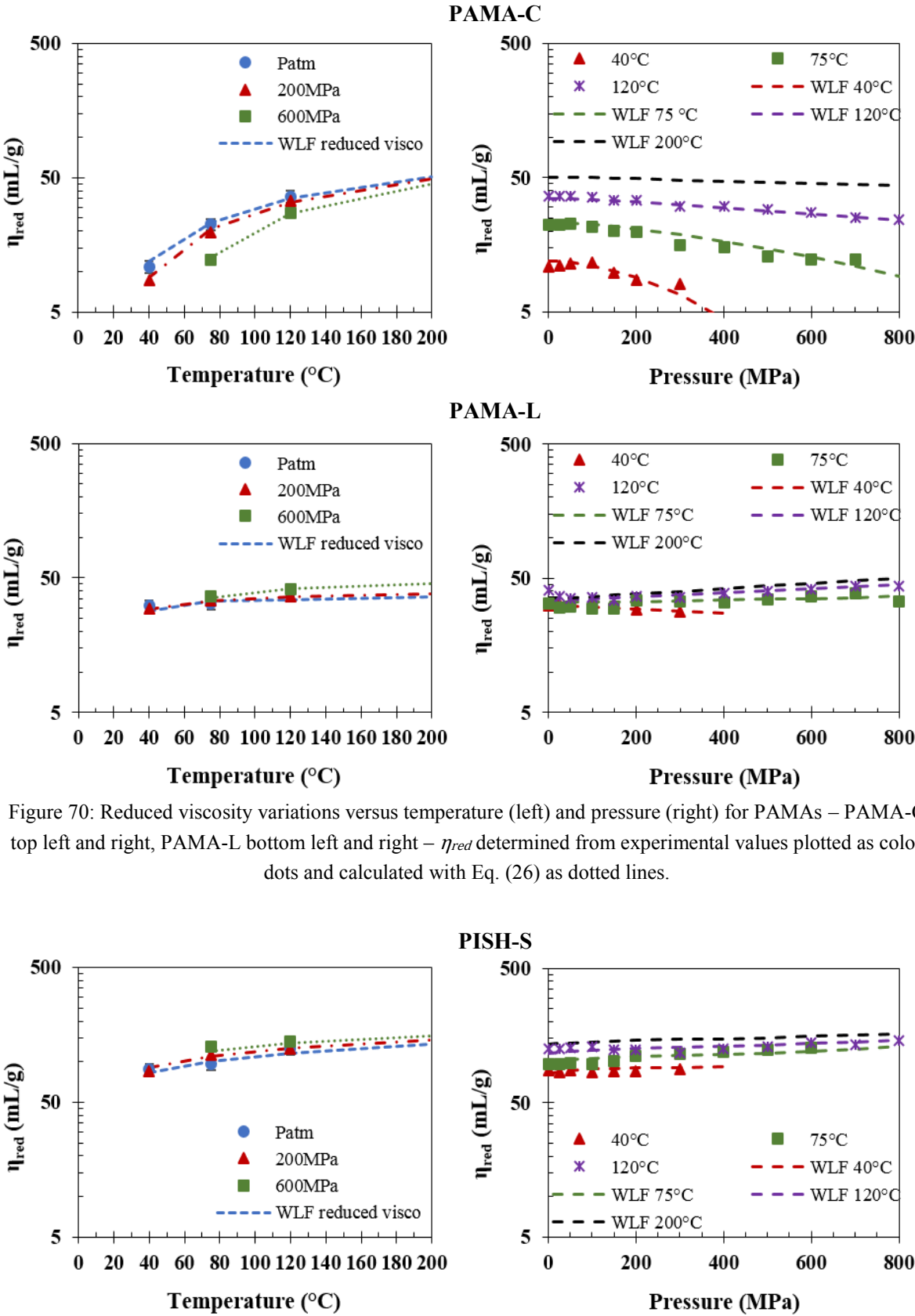


Figure 70: Reduced viscosity variations versus temperature (left) and pressure (right) for PAMAs – PAMA-C top left and right, PAMA-L bottom left and right – η_{red} determined from experimental values plotted as color dots and calculated with Eq. (26) as dotted lines.

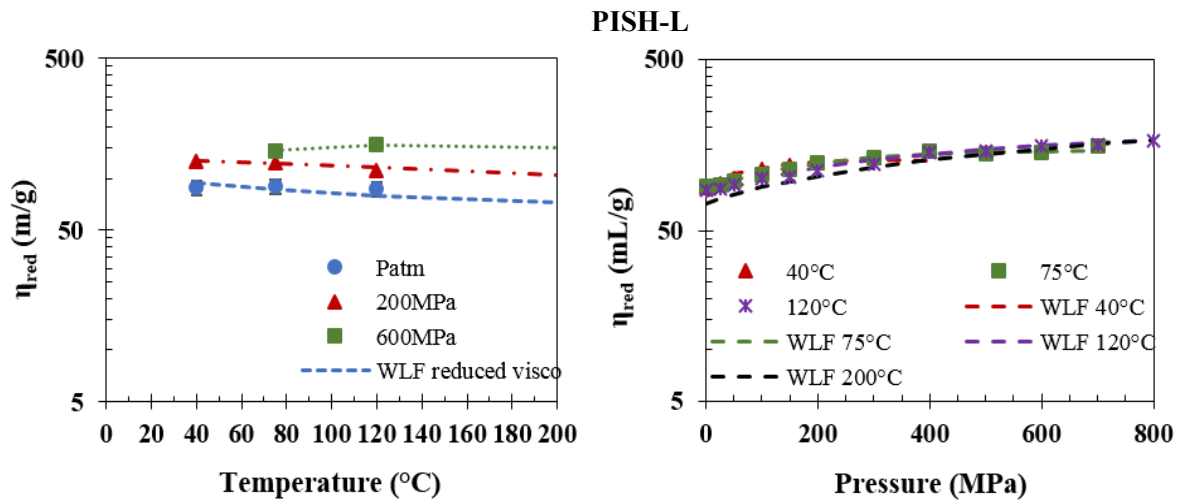


Figure 71: Reduced viscosity variations versus temperature (left) and pressure (right) for PISH-S – PISH-S top left and right, PISH-L bottom left and right - η_{red} determined from experimental values plotted as color dots and calculated with Eq. (26) as dotted lines.

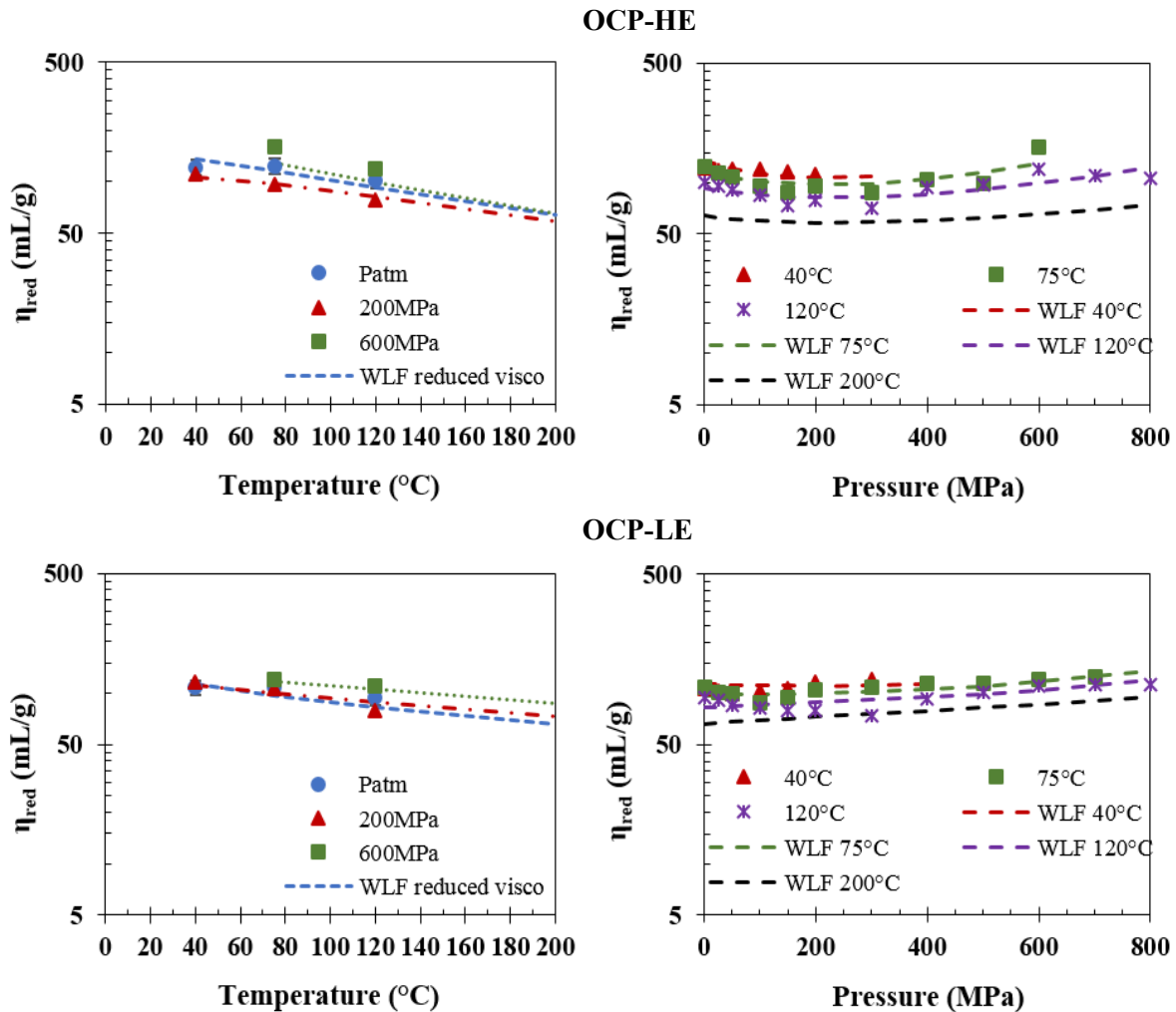


Figure 72: Reduced viscosity variations versus temperature (left) and pressure (right) for OCPs – OCP-HE top left and right, OCP-LE bottom left and right - η_{red} determined from experimental values plotted as color dots and calculated with Eq. (26) as dotted lines.

This appendix presents the variations of experimental and calculated viscosity η_{red} (Eq. (17), p. 43) against temperature and pressure, at low shear stress and for all solutions (Figure 70 to Figure 72). An increase of η_{red} with temperature evidences a more important contribution of the polymer to the base oil viscosity at high temperature, which is the effect sought for VII applications.

Three polymers - PAMA-C, PAMA-L, PISH-S - presents the expected effect of a VII, with an increase of their contribution at high temperature, while both OCP are thickeners. The PAMA-C appears to be the most interesting product for VII application, at low shear stress. The PISH-L behavior is peculiar as it behaves as VII only above a certain pressure.

These results were discussed in *II.3.1* (p. 63) and linked to the hydrodynamic radii variations with temperature and pressure of the polymer, in order to understand the relationship between the molecular scale and the rheological response of polymer solutions.

Appendix 8 - Rheological study of the “PAMA-C low”

In chapter III, the question of applying the Carreau-Yasuda model (Eq. (31), p. 48)[16] to polymer whose coils swell with temperature was raised. Indeed, such product may present a shear-thinning response that varies with temperature since larger particles have been highlighted to be more shear-sensitive. Since the Carreau-Yasuda expression relies on rather strong assumptions, particularly keeping the ratio between the first Newtonian plateau η_0 and the second Newtonian plateau η_2 constant at any temperature and pressure, its application to VII, such as the PAMA-C, above their swelling temperature may be inaccurate and lead to unsatisfactory film thickness predictions.

Unfortunately, this hypothesis could not be tested as the swelling temperature of PAMA-C is above the device capabilities (above 60 °C). Another comb polyalkylmethacrylate whose swelling temperature is about 60 °C, was thus investigated. This appendix is dedicated to the study of this polymer called PAMA-C low. This polymer has a chemistry and structure close to the PAMA-C (see Table 21). The PAMA-C low is thus expected to present a similar behavior and to display a size variations of its polymer coils with temperature. The aim of this study is to see if the swelling of the polymers at 60 °C induces a variation of the polymer shear-thinning response.

	PAMA-C	PAMA-C low
Molecular structure	comb	comb
M_w (g.mol⁻¹)	678 800	807 600
PDI	3,16	2,79

Table 21: Main characteristics of the two comb polyalkylmethacrylates

A complete rheological response was thus performed on the PAMA-C low solution. The temperature influence on the viscosity at atmospheric pressure and low shear stress was first investigated to determine the polymer glass transition temperature T_g (0) (as in II.1, p. 55). Its T_g (0) is rather higher than the PAMA-C one (Table 22). However, this was attributed to a temperature study performed on a restricted experimental range, since no experiments could be run at temperature below -10 °C. In a second time, the temperature-pressure-viscosity dependence was characterized thanks to the high pressure viscometer device and the WLF-Yasutomi equation (Eq. (26), p. 47)[14] was fitted to the experimental data. The model parameters for both comb PAMA are detailed in Table 22, as well as the viscosity index (VI), and are really similar. Then, the hydrodynamic radii of the PAMA-C variations against temperature and pressure is plotted in Figure 73. These results confirm the swelling of polymer coils with temperature.

Finally, experiments are run on the high pressure Couette rheometer from 40 °C to 60 °C and for pressures from 200 MPa up to 400 MPa. The experimental viscosities are plotted in log-log scales against shear stress in Figure 74. The Newtonian viscosity is also drawn as a dotted line to appreciate the drop in viscosity. However, the results are not compelling. Indeed, lower shear stresses are reached as the temperature increase. If present, the onset of the shear-thinning may thus not be reached. It is thus not possible to validate or rebut our assumption by this study.

Material	PAMA-C	PAMA-C low
A_1 (°C)	55.46	144.65
A_2 (GPa ⁻¹)	0.866	0.118
b_1 (GPa ⁻¹)	7.72	6.92
b_2	-0.550	-0.640
C_1	15.54	15.46
C_2 (°C)	17.99	16.77
η_g (Pa.s)	10 ¹²	10 ¹²
$T_g(0)$ (°C)	-92.4	-84.2
rms (%)	4.19	3.72
$\alpha_{40^\circ C^*}$ (GPa ⁻¹)	14.4	14.2
$\alpha_{100^\circ C^*}$ (GPa ⁻¹)	9.9	9.9
$\eta_0(40^\circ C, p_{atm})$ (mPa.s)	21.28	24.23
$\eta_0(100^\circ C, p_{atm})$ (mPa.s)	6.11	6.84
VI	306	264

Table 22: Parameters of the WLF, reciprocal asymptotic isoviscous pressure coefficients computed from the WLF model and VI of comb polyalkylmethacrylates

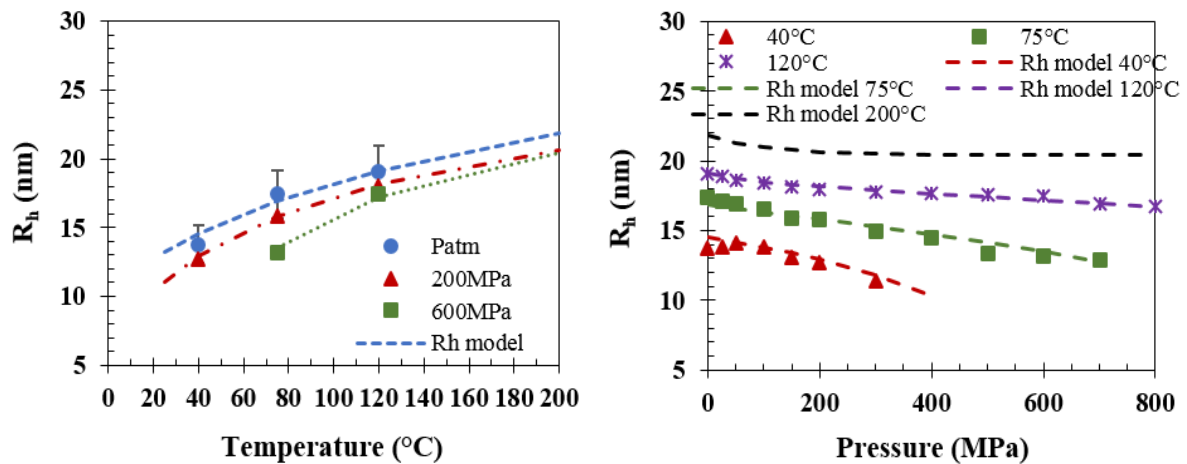


Figure 73: Hydrodynamic radius variations versus temperature (left) and pressure (right) for PAMA-C low

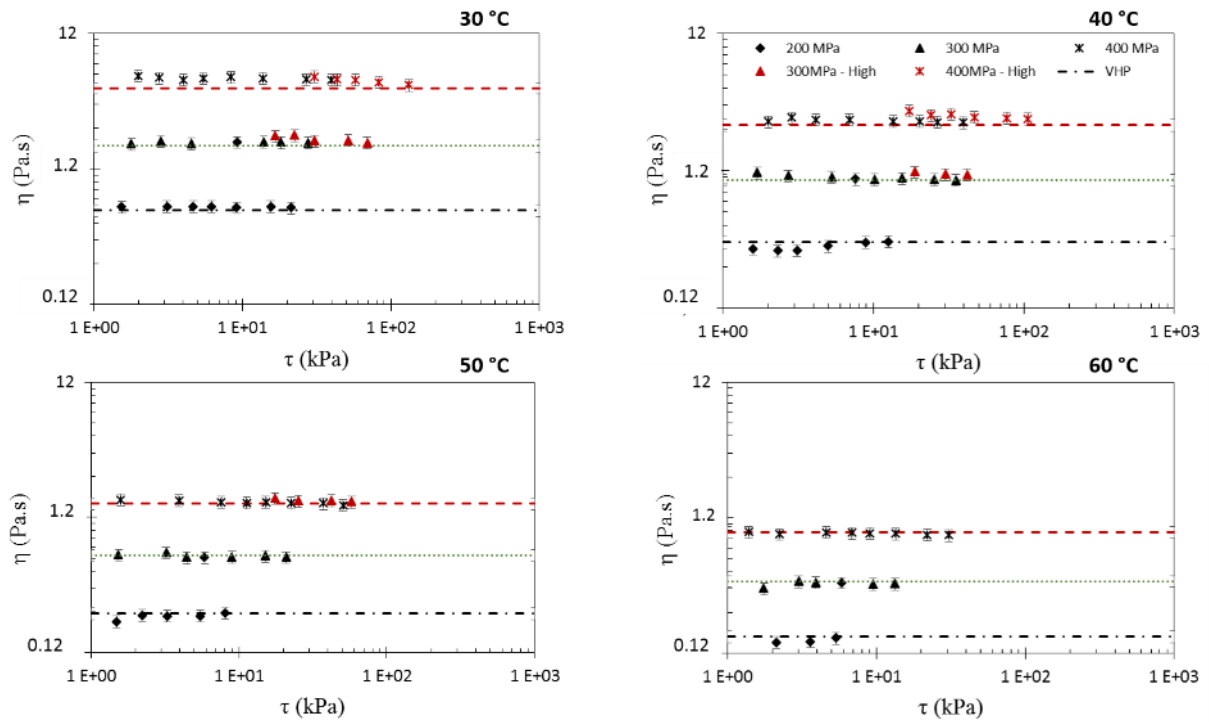


Figure 74: Viscosity of the PAMA-C low solution versus shear stress from 40 °C to 60 °C and from 200 MPa to 400 MPa, along with the Newtonian viscosity at the considered temperature and pressure (colored dotted line)

Appendix 9 - Zhang results

This appendix presents the Zhang results (Eq. (32), p. 49)[17] for the OCP-LE (Figure 75), PISH-L (Figure 76), PAMA-C (Figure 77) and PAMA-L (Figure 78). The experimental dynamic viscosities η are plotted against shear strain rate at 40 °C and from 200 to 400 MPa. The computed viscosity with the Zhang model is drawn as a black line.

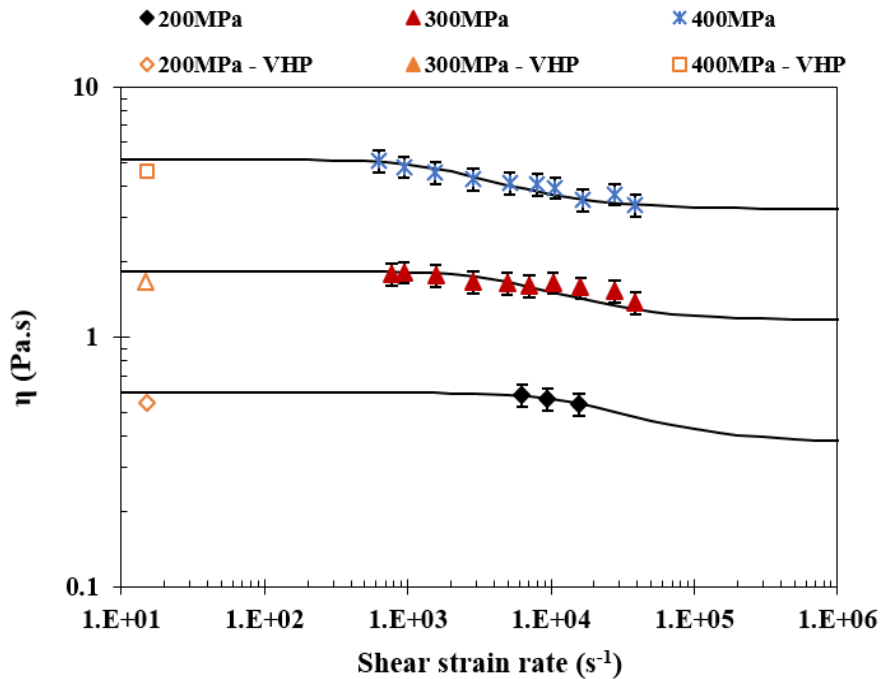


Figure 75: Viscosity of the OCP-LE solution versus shear strain rate at 40 °C, from 200 MPa to 400 MPa and fitted by the Zhang model (black line)

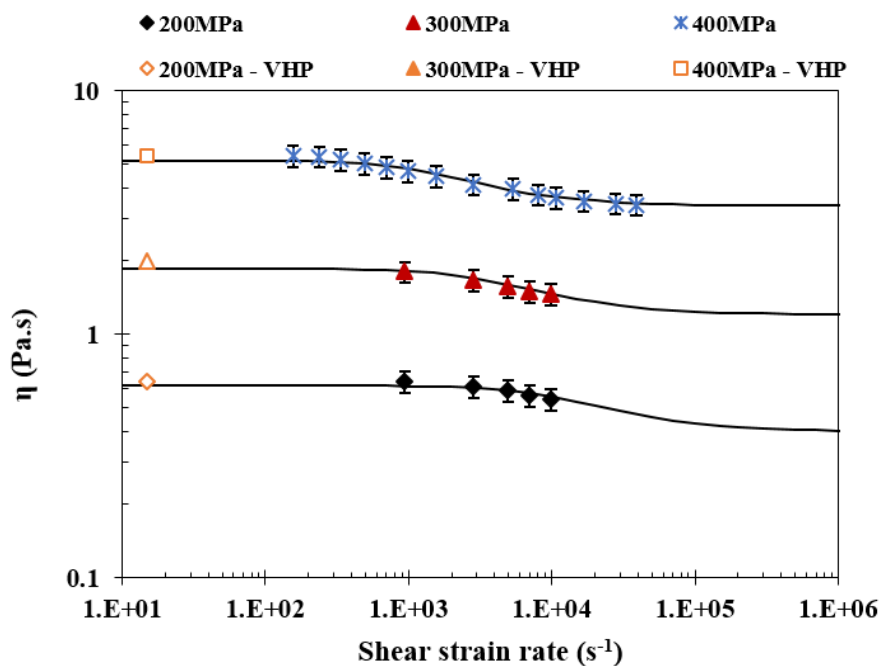


Figure 76: Viscosity of the PISH-L solution versus shear strain rate at 40 °C, from 200 MPa to 400 MPa and fitted by the Zhang model (black line)

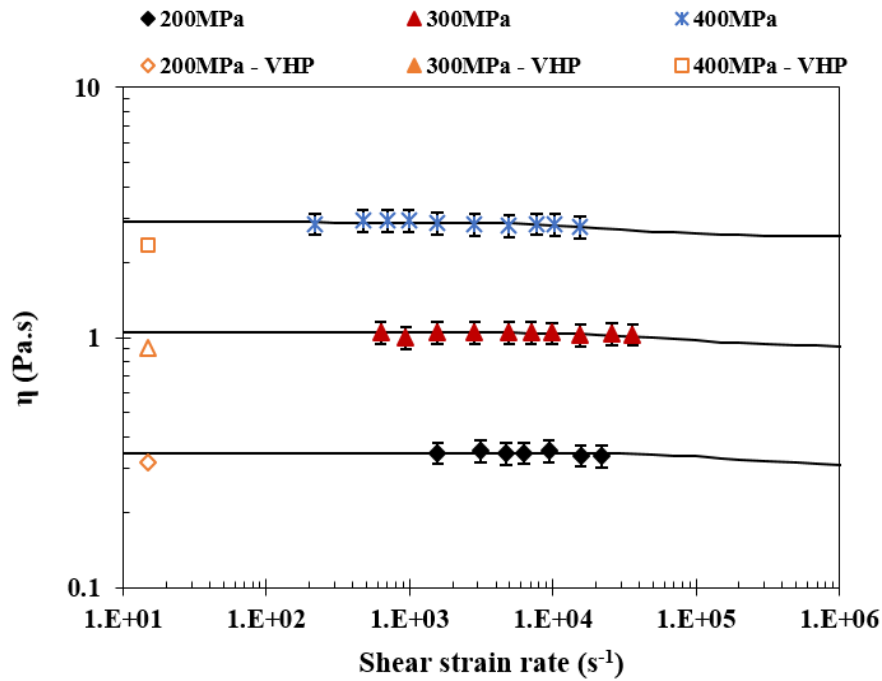


Figure 77: Viscosity of the PAMA-C solution versus shear strain rate at 40 °C, from 200 MPa to 400 MPa and fitted by the Zhang model (black line)

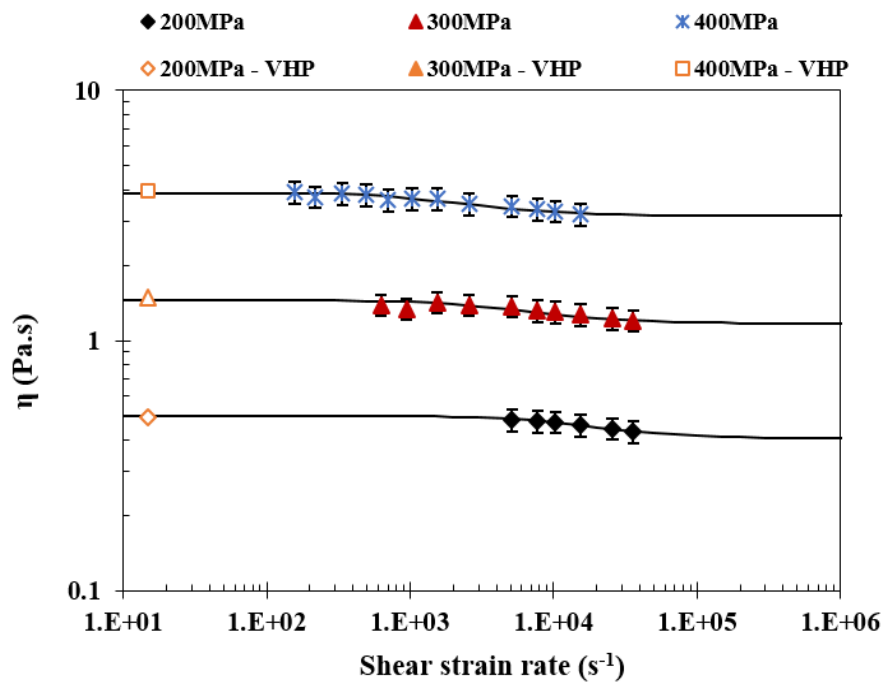


Figure 78: Viscosity of the PAMA-L solution versus shear strain rate at 40 °C, from 200 MPa to 400 MPa and fitted by the Zhang model (black line)

A good agreement is observed between the experimental data and the calculated viscosities. The Zhang parameters were provided for all solutions in *III.3.1* (p. 91). It should be mentioned however that a second Newtonian plateau is always present when fitting data with the Zhang equation due to its construction. The shear-thinning response of polymer solutions may be then underestimated.

Appendix 10 - Comparison Carreau-Yasuda and Zhang modeling

In III.2.4 (p. 89), the strong assumptions behind the Carreau-Yasuda model (Eq. (31), p. 48)[16] lead us to propose a more appropriate relationship which takes into account the viscoelastic properties of the lubricants, the Zhang equation (Eq. (32), p. 49)[17]. Comparison between the two models predictions were provided for the PAMA-C and OCP-LE solutions considering the master curves of the viscosity (III.3.2, p. 92). This appendix provides results for other solutions, including PAMA-L (Figure 79), PISH-S (Figure 80) and PISH-L (Figure 81). These master curves are obtained by dividing the viscosity of the fluid by its viscosity at low shear stress. This normalized viscosity is then plotted in log-log scale against shear stress.

Both models present a good agreement to the experimental data, though extrapolated viscosities are different regarding the considered models. This results highlight one of the limitations of the viscosity calculations due to experimental constraints. The lack of data at very high shear stress and the characterization of the viscosity at the second plateau does not allow us to conclude on whether or not the viscosity drop is over or underestimated by either of the models.

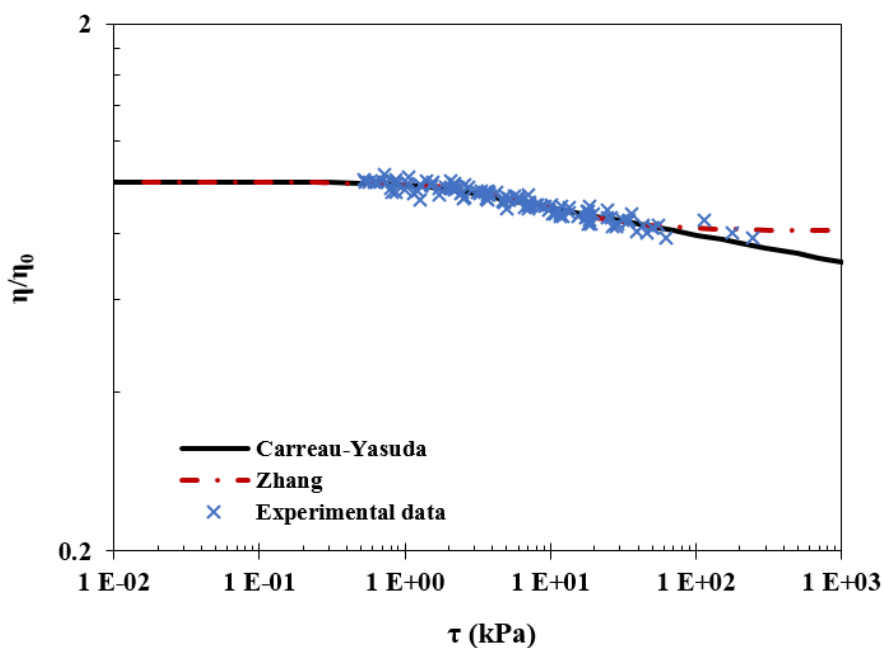


Figure 79: Comparison of Carreau-Yasuda predictions and Zhang's results for the PAMA-L solution by looking at the master curve and experimental results obtained at different temperatures and pressures.

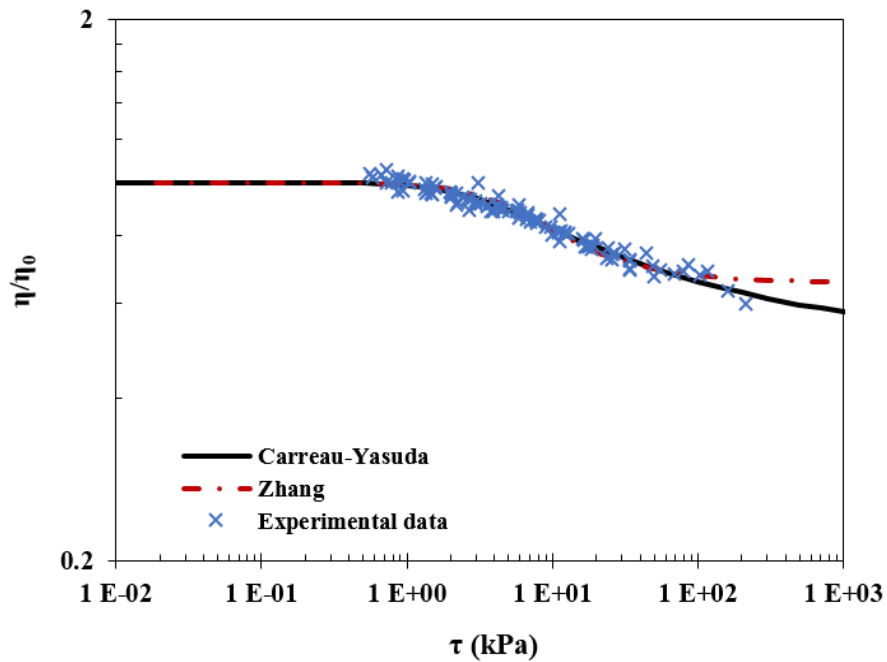


Figure 80: Comparison of Carreau-Yasuda predictions and Zhang's results for the PISH-S solution by looking at the master curve and experimental results obtained at different temperatures and pressures

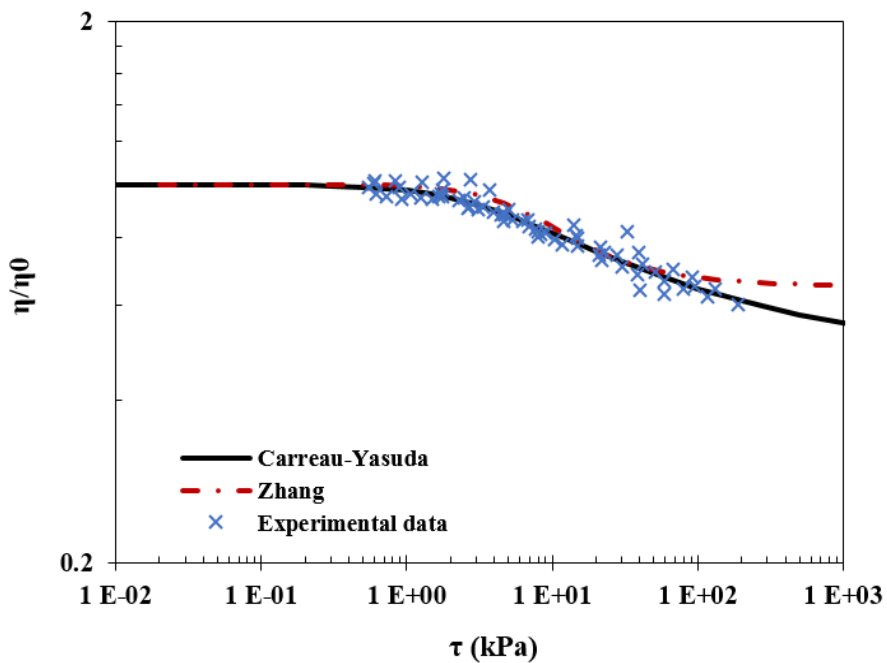


Figure 81: Comparison of Carreau-Yasuda predictions and Zhang's results for the PISH-L solution by looking at the master curve and experimental results obtained at different temperatures and pressures

Appendix 11 - Jerotrib test-rig description

The Jerotrib device is a ball-on-disc tribometer developed by Molimard [23] at LaMCoS. This test-rig allows the measurement of both film thicknesses and traction coefficients, using white light optical interferometry and multi-directional sensors respectively. The ball and disc are driven independently by two separate motors, at different slide-to-roll ratio (SRR). The ball bottom is immersed in a reservoir filled with the lubricant, and its rotation brings the studied fluid within the contact ensuring fully-flooded conditions. The temperature is well controlled as both reservoir and two shafts are insulated and heated by an external bath. The solution temperature is measured by a platinum temperature, whose accuracy on the sample is within ± 0.1 °C. The normal load is applied on the ball spindle through a static force sensor. The device operating ranges and accuracy are detailed below:

Parameters	Range	Accuracy
Speed	0.01 to 7 m.s-1	0.002 %
Slide-to-roll ratio	0 to ± 400 %	<1.2 %
Temperature	-10 to 100 °C	0.1 °C
Normal load	up to 300 N	0.8 %
Friction Force	up to 40 N	0.3 %
Hertz Pressure	up to 3 GPa	
Film thickness	Few to 1500 nm	Typically 2 – 5 nm
Materials	Glass – Sapphire	σ_{RMS} : 2 – 8 nm
	Ceramics	σ_{RA} : 40 nm
	Steel – Tungsten Carbide	σ_{RMS} : 5 – 20 nm
Contact configuration	Slender – Circular – Large elliptical	

Table 23: Jerotrib operating ranges and accuracy

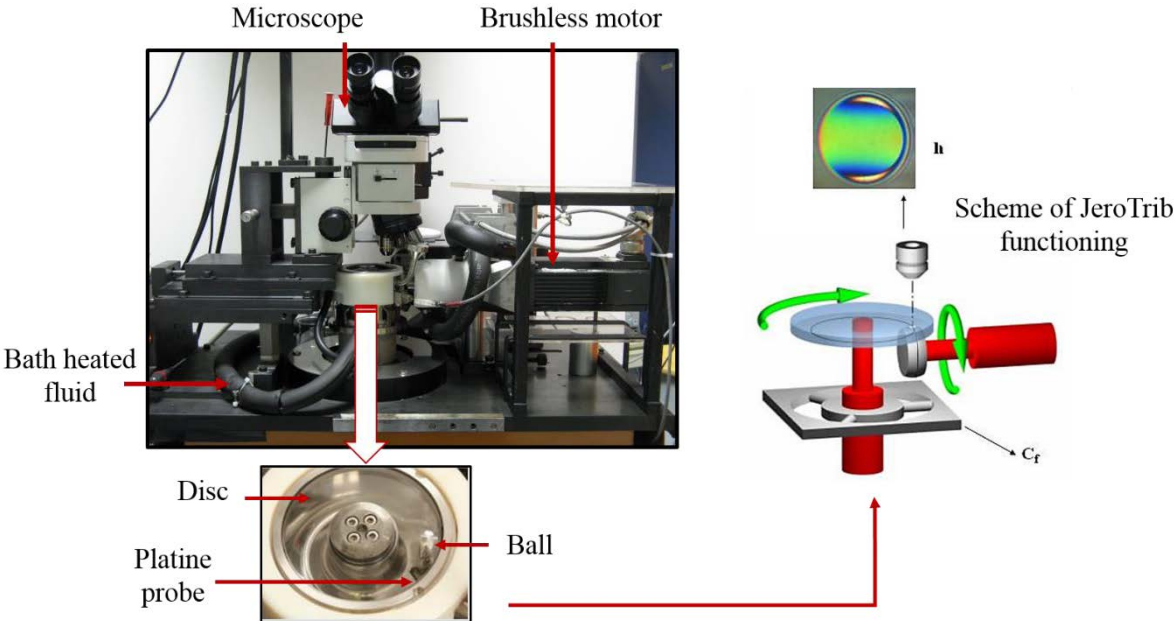


Figure 82: Picture of the Jerotrib test-rig along with its scheme while running

The calibration curve below establishes the dependence of the film thickness h upon the RGB intensity triplet (intensity of the Red, Green and Blue wavelengths respectively).

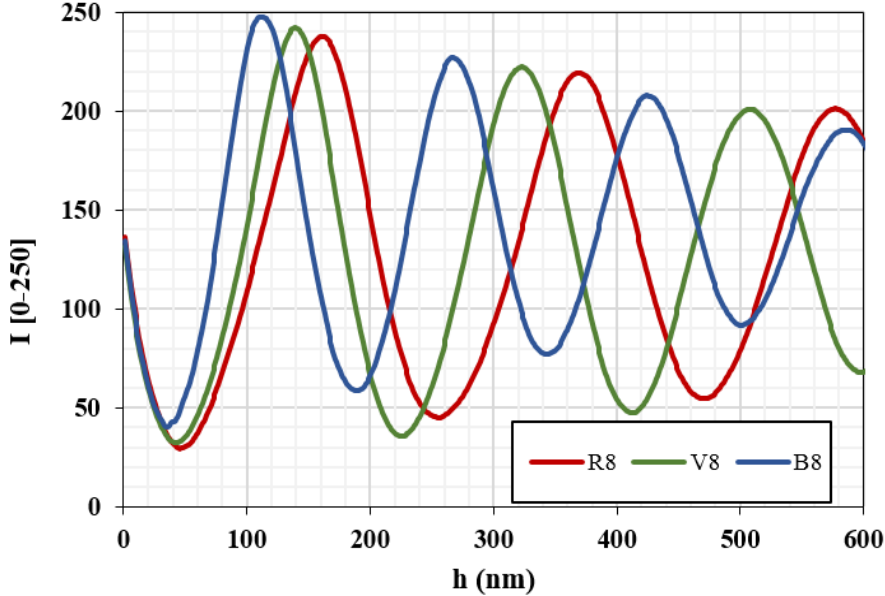


Figure 83: Typical calibration curve used for the interferogram acquired with the Jerotrib test-rig

Appendix 12 - The Hertz theory

The Hertz [127] theory evaluates the deformation of non-adhesive semi-infinite elastic bodies, under dry contact conditions as well as their profile and geometry. Hertzian contact problems assume continuous, frictionless and non-conforming surfaces. The strain must also be small and within the elastic limit. The surfaces curvature radii are respectively R_1 and R_2 . The following parameters are dimensionless and coming from the Hertz theory. For a circular contact, the Hertzian pressure profile is:

$$p(x, y) = \begin{cases} p_H \sqrt{1 - \left(\frac{x}{a_H}\right)^2 - \left(\frac{y}{a_H}\right)^2} & \text{if } \sqrt{x^2 + y^2} \leq a_H \\ 0 & \text{otherwise} \end{cases} \quad \text{Eq. (49)}$$

Where p_H is the maximum Hertzian pressure and a_H is the radius of the contact circle. Both parameters are described below along with the reduced radius of curvature R_{eq} and the reduced Young elastic modulus E_{eq} :

$$p_H = \frac{3W}{2\pi a_H^2} \quad a_H = \sqrt[3]{\frac{3WR_{eq}}{2E_{eq}}} \quad \text{Eq. (50)}$$

$$R_{eq} = \frac{1}{\frac{1}{R_1} + \frac{1}{R_2}} \quad E_{eq} = \frac{2}{\frac{1-\nu_1^2}{E_1} + \frac{1-\nu_2^2}{E_2}} \quad \text{Eq. (51)}$$

Where W is the external applied load, E_1, ν_1 and E_2, ν_2 are the material properties (Young's moduli and Poisson's coefficients) of the solids 1 and 2 respectively.

Finally, Eq. (52) gives the deformed shape of a sphere against a flat surface, with R_{ball} the radius curvature of the ball and r the distance from the contact center:

$$h(r) = \frac{r^2}{2R_{ball}} - \frac{a^2}{R_{ball}} + \frac{1}{\pi R_{ball}} \left[(2a^2 - r^2) \arcsin\left(\frac{a}{r}\right) + r^2 \left(\frac{a}{r}\right) \sqrt{1 - \left(\frac{a}{r}\right)^2} \right] \quad \text{for } r \geq a \quad \text{Eq. (52)}$$



INSA

FOLIO ADMINISTRATIF

THESE DE L'UNIVERSITE DE LYON OPEREE AU SEIN DE L'INSA LYON

NOM : CUSSEAU

DATE de SOUTENANCE : 23/03/2018

Prénoms : Pauline, Isabelle

TITRE :

The role of polymer additives on the behavior of engine lubricants in elastohydrodynamic and thin film regimes: from rheology to tribology

NATURE : Doctorat

Numéro d'ordre : 2018LYSEI020

Ecole doctorale : MEGA

Spécialité : Mécanique

RESUME :

Le développement de lubrifiants haute performance pour réduire le frottement dans les moteurs et limiter la consommation de carburant, demeure un défi majeur pour les fabricants d'huiles. Les améliorants d'indice de viscosité (VII) sont des polymères couramment utilisés pour réduire la dépendance en température de la viscosité du lubrifiant, afin de maintenir une lubrification hydrodynamique acceptable à haute température. Ce travail se concentre sur la compréhension du rôle des VII dans les lubrifiants moteur afin de relier leur réponse tribologique et leur comportement rhéologique. Des lubrifiants simplifiés sont étudiés, composés de divers polymères de différents poids moléculaires et conformations, ajoutés à une huile de base minérale.

Premièrement, la dépendance de la viscosité à la température et la pression de ces lubrifiants est étudiée. Il est montré que leur comportement rhéologique résulte de mécanismes se produisant à l'échelle moléculaire, en considérant les notions de solubilité, rayon hydrodynamique et d'effets de conformation.

Ensuite, la dépendance viscosité-cisaillement est discutée en fonction de la structure des polymères et prédite sur une large gamme de températures et de pressions à travers un modèle conventionnel. Cependant, les hypothèses qui sous-tendent ce modèle nous amènent à proposer une relation plus appropriée prenant en compte la viscoélasticité des lubrifiants.

Enfin, des mesures d'épaisseur de film sont effectuées pour explorer comment l'addition de polymère affecte la réponse du lubrifiant dans les régimes élastohydrodynamique et thin film. Elles sont comparées aux prévisions analytiques basées sur les modèles rhéologiques établis précédemment. Il est montré i) une bonne adéquation entre les prévisions et les données expérimentales dans le régime EHD et ii) la présence d'une épaisseur critique pour certains polymères à partir de laquelle les résultats s'écartent significativement des prévisions. Ce régime thin film, aux faibles épaisseurs, est expliqué par le comportement non newtonien des lubrifiants et l'adsorption des polymères aux surfaces.

MOTS-CLÉS : polymère, améliorant d'indice de viscosité, lubrifiant, rhéologie, pression, tribologie, comportement non-Newtonien, modèles rhéologiques, rayon hydrodynamique, lubrification élastohydrodynamique, lubrification thin film.

Laboratoire (s) de recherche : LaMCoS

Directeur de thèse: P Vergne, D Philippon

Président de jury :

C Chassenieux

Composition du jury :

J Fernandez, M Fillon, L Martinie, P Vergne, D Philippon, F Briand